

Is white matter the weakest link?
Early detection of white matter changes with MRI

Stéfanie A. Tremblay

A Thesis
in the Department
of
Physics

Presented in Partial Fulfillment of the
Requirements For the Degree of
Doctor of Philosophy (Physics)

at Concordia University
Montreal, Quebec, Canada

August 2024

© Stéfanie A. Tremblay, 2024

Abstract

Is white matter the weakest link? - Early detection of white matter changes with MRI

Stéfanie A. Tremblay, Ph.D.
Concordia University, 2024

White matter (WM) tracts play a crucial role in enabling efficient neural transmission, which is essential for optimal brain function. Once overlooked, WM is now recognized for its constant remodeling throughout life, responding to both enriching and adverse factors. These alterations in WM microstructure can enhance cognitive and motor performance through more efficient transmission, or conversely, contribute to functional decline. Notably, WM changes are among the earliest alterations observed in neurodegenerative disorders such as Alzheimer's disease (AD) and other dementias, highlighting the potential for WM as a target for early interventions.

However, our current knowledge is limited regarding: 1) the time scales at which plastic changes occur and 2) the biological mechanisms driving microstructural changes. This is largely due to the physiological non-specificity of commonly used neuroimaging techniques and the predominantly univariate focus of most studies in the field.

This Ph.D. thesis presents four original studies focused on investigating early WM changes in health and disease. The first study examines longitudinal plastic changes in WM following short-term motor learning in young, healthy participants, providing insights into activity-dependent WM remodeling. The second study introduces MVComp, an open-source toolbox developed to compute a multivariate distance metric—the Mahalanobis distance (D2). MVComp allows the integration of various imaging features, yielding individualized scores of deviation from a reference.

The latter half of the thesis focused on the investigation of early pathological changes in WM among older adults at risk of dementia, using the multivariate framework developed in study two. The third study explored the relationship between WM alterations and cardiometabolic risk factors in older adults with a family history of AD. Individuals at higher genetic risk of AD (Apolipoprotein E (ApoE) ϵ 4) displayed a distinct pattern where LDL-cholesterol negatively impacted WM health, with myelination changes as the primary underlying mechanism. Finally, the fourth study assessed WM deviations in coronary artery disease patients, linking higher D2 scores in specific arterial territories to lower fitness levels and poorer cognition.

Together, these findings underscore the dynamic nature of WM changes and demonstrate that multivariate approaches offer a comprehensive characterization, shedding light on the biological mechanisms at play.

Acknowledgements

First and foremost, I would like to express my deepest gratitude to my supervisor, Claudine. You truly are the best mentor one could wish for. Your dedication, attentiveness and openness helped me grow into the researcher I am today. Thank you for letting me wonder, taking extra courses and workshops and attending different conferences that allowed me to explore different career possibilities. Not only you are an amazing researcher, but you are also very humane and understanding. You made me feel truly supported, even in the hard times, and gave me the confidence to keep moving forward. Much of this work would not have been possible without the help of Christopher Steele. Thank you for your patience in teaching me the basics of diffusion MRI preprocessing and python. Your hands-on support in those first months gave me the foundations I needed to then expand my expertise in white matter imaging. I'm also very grateful for the many collaboration opportunities you gave me.

I would like to extend my sincere thanks to my supervisory committee: Dr Christophe Grova and Dr Brandon Helfield. Thank you for your input and guidance throughout my PhD.

I would also like to acknowledge the Canadian Institutes of Health Research for funding my PhD work. Thank you also to the Public Scholar program for providing additional financial support, countless career development opportunities, as well as a community of peers with a shared passion for knowledge dissemination.

I'm also incredibly thankful for the many collaborators I had the chance to work with during my PhD: Anna, Amir, Zacharie, Chris, and Yasser. These collaborations not only enriched the quality of my work, but they also kept me feeling motivated, making the whole PhD experience a lot less lonely. Special thanks to Zaki with whom I spent countless hours working on many different projects and who was always there to reassure me and help me see things in a more positive light when I felt like everything was going wrong.

My lab mates have also been a significant source of support, helping with coding, data collection, stats, or even just being a good listening ear.

I would like to express my deepest gratitude to everyone who contributed to the CIRM project data collection and recruitment: Paule Samson, Thomas Vincent, Julie Lalongé, Hakima Benhalima, Milla Shakleva, Victoria D'Amours, Agathe Godet, Stephanie Beram, Roni Zaks, Robert Hovey, Catherina Medeiros, and Zineb Rouabah. Thank you also to the laboratories of Dr Louis Bherer and Dr Mathieu Gayda for their help with cognitive assessments and exercise testing. Lastly, I would like to thank our research participants without whom this study would not have been possible.

On a more personal note, I would like to thank my parents. You have supported me in such a way that I always felt able to take risks and go after my dreams, whether it was pursuing a high-level athletic career or an academic career in a field that I know always felt very foreign and abstract to you.

To all my friends, thank you for being there for me throughout this whole journey, but especially during the past few months that have been particularly challenging. Celebrating the successes and milestones and feeling loved and supported through the hardships really meant a lot to me.

Last but not least, thank you to my amazing wife. Reflecting on this whole journey makes me realize how much we have been through in the past 5 and a half year. Through all the challenges, the transitions, and the different phases, we have always been each other's pillar. This marks another transition and I'm excited for what's next knowing you'll be by my side to support me in the good and in the hard times.

Contribution of authors

This thesis was authored by myself under the supervision of Dr Claudine Gauthier. The thesis consists of four original research articles, three of the articles are applications research article and one is methodological (software toolbox paper). The contribution of each co-author is detailed below.

Chapter I: General Introduction

Writing: Stéfanie A. Tremblay

Editing: Claudine J. Gauthier

Chapter II: Short-term white matter plasticity in young adults

Published in Brain Structure and Function. DOI: 10.1007/s00429-021-02267-y

Title: White matter microstructural changes in short-term learning of a continuous visuomotor sequence

Authors: Stéfanie A. Tremblay, Anna-Thekla Jäger, Julia Huck, Chiara Giacosa, Stephanie Beram, Uta Schneider, Sophia Grahl, Arno Villringer, Christine L. Tardif, Pierre-Louis Bazin, Christopher J. Steele*, Claudine J. Gauthier*

*Contributed equally.

Writing: Stéfanie A. Tremblay

Editing: Claudine J. Gauthier, Anna-Thekla Jäger, Pierre-Louis Bazin, Chiara Giacosa, Christopher J. Steele, and Claudine J. Gauthier.

Visualization: Stéfanie A. Tremblay

Formal analysis: Stéfanie A. Tremblay, Anna-Thekla Jäger, Stephanie Beram, Chiara Giacosa, and Sophia Grahl.

Conceptualisation: Christine L. Tardif, Pierre-Louis Bazin, Arno Villringer, Christopher J. Steele, and Claudine J. Gauthier.

Methodology: Christine L. Tardif, Pierre-Louis Bazin, Christopher J. Steele, and Claudine J. Gauthier.

Software: Pierre-Louis Bazin, Christopher J. Steele, and Julia Huck.

Data collection: Pierre-Louis Bazin, Uta Schneider, Sophia Grahl, Anna-Thekla Jäger, and Julia Huck.

Funding acquisition: Arno Villringer

Supervision: Christopher J. Steele, and Claudine J. Gauthier.

Chapter III: Development of a toolbox for multivariate analysis

Published in Aperture Neuro. DOI: 10.52294/001c.118427

Title: MVComp toolbox: MultiVariate Comparisons of brain MRI features accounting for common information across measures

Authors: Stéfanie A. Tremblay*, Zaki Alasmar*, Amir Pirhadi, Felix Carbonell, Yasser Iturria-Medina, Claudine J. Gauthier, Christopher J. Steele

*Contributed equally.

Writing: Stéfanie A. Tremblay, Zaki Alasmar

Editing: Claudine J. Gauthier, Christopher J. Steele, Felix Carbonell, Yasser Iturria-Medina

Visualization: Stéfanie A. Tremblay, Zaki Alasmar

Formal analysis: Zaki Alasmar

Conceptualisation: Stéfanie A. Tremblay, Zaki Alasmar, Yasser Iturria-Medina, Claudine J. Gauthier, and Christopher J. Steele.

Methodology: Stéfanie A. Tremblay, Zaki Alasmar, Amir Pirhadi, Felix Carbonell, Yasser Iturria-Medina, and Christopher J. Steele.

Software: Stéfanie A. Tremblay, Zaki Alasmar, Amir Pirhadi, and Christopher J. Steele.

Data curation: Stéfanie A. Tremblay, Zaki Alasmar, and Amir Pirhadi.

Funding acquisition: Christopher J. Steele and Yasser Iturria-Medina.

Supervision: Christopher J. Steele, and Claudine J. Gauthier.

Chapter IV: Multivariate white matter in pre-clinical Alzheimer's disease

Submitted to eLife. BioRxiv DOI: 10.1101/2024.08.21.608995

Title: Sex and APOE4-specific links between cardiometabolic risk factors and white matter alterations in individuals with a family history of Alzheimer's disease

Authors: Stefanie A. Tremblay, R. Nathan Spreng, Alfie Wearn, Zaki Alasmar, Amir Pirhadi, Christine L. Tardif, Mallar M. Chakravarty, Sylvia Villeneuve, Ilana R. Leppert, Felix Carbonell, Yasser Iturria-Medina, Christopher J. Steele, Claudine J. Gauthier, for the PREVENT-AD Research Group

Writing: Stéfanie A. Tremblay

Editing: Claudine J. Gauthier, Christopher J. Steele, R. Nathan Spreng, Alfie Wearn, Zaki Alasmar, Yasser Iturria-Medina, Christine L. Tardif, Sylvia Villeneuve

Visualization: Stéfanie A. Tremblay, Alfie Wearn

Formal analysis: Stéfanie A. Tremblay

Conceptualisation: Stéfanie A. Tremblay, Zaki Alasmar, Yasser Iturria-Medina, Claudine J. Gauthier, and Christopher J. Steele.

Methodology: Stéfanie A. Tremblay, Zaki Alasmar, Amir Pirhadi, Christine L. Tardif, Mallar M. Chakravarty, Ilana R. Leppert, Felix Carbonell, Yasser Iturria-Medina, and Christopher J. Steele.

Software: Stéfanie A. Tremblay, Zaki Alasmar, Amir Pirhadi, Ilana R. Leppert, and Christopher J. Steele.

Investigation: Mallar M. Chakravarty, Sylvia Villeneuve, and Ilana R. Leppert.

Funding acquisition: R. Nathan Spreng, Sylvia Villeneuve, Christopher J. Steele, Yasser Iturria-Medina, and Claudine J. Gauthier.

Supervision: Claudine J. Gauthier.

Chapter V: White matter microstructure in older adults with cardiovascular disease

In preparation.

Title: Multivariate white matter microstructure alterations link to fitness and cognition in older adults with coronary artery disease

Authors: Stefanie A. Tremblay*, Zacharie Potvin-Jutras*, Dalia Sabra, Ali Rezaei, Safa Sanami, Christine Gagnon, Brittany Intzandt, Amélie Mainville-Berthiaume, Lindsay Wright, Ilana R. Leppert, Christine L. Tardif, Mathieu Gayda, Christopher J. Steele, Josep Iglesias-Grau, Anil Nigam, Louis Bherer, Claudine J. Gauthier

*Contributed equally.

Writing: Stéfanie A. Tremblay and Zacharie Potvin-Jutras.

Editing: Claudine J. Gauthier.

Data collection: Stéfanie A. Tremblay, Zacharie Potvin-Jutras, Dalia Sabra, Safa Sanami, Ali Rezaei, Brittany Intzandt, Amélie Mainville-Berthiaume, and Lindsay Wright.

Visualization: Stéfanie A. Tremblay and Zacharie Potvin-Jutras.

Formal analysis: Stéfanie A. Tremblay and Zacharie Potvin-Jutras.

Conceptualisation: Stéfanie A. Tremblay, Zacharie Potvin-Jutras, and Claudine J. Gauthier.

Investigation: Christine Gagnon, Josep Iglesias-Grau, Mathieu Gayda, Louis Bherer, and Anil Nigam.

Methodology: Stéfanie A. Tremblay, Christopher J. Steele, Ilana R. Leppert, Christine L. Tardif and Claudine J. Gauthier.

Resources: Christopher J. Steele

Funding acquisition: Claudine J. Gauthier and Louis Bherer.

Supervision: Claudine J. Gauthier and Louis Bherer.

Chapter VI: General discussion

Writing: Stéfanie A. Tremblay

Editing: Claudine J. Gauthier

Chapter VII: Conclusion

Writing: Stéfanie A. Tremblay

Editing: Claudine J. Gauthier

TABLE OF CONTENTS

LIST OF FIGURES	XV
LIST OF TABLES	XVIII
CHAPTER I: GENERAL INTRODUCTION	1
1.1 EXECUTIVE SUMMARY.....	1
1.2 WHITE MATTER PHYSIOLOGY	4
1.3 WHITE MATTER IMAGING	5
1.3.1 Overview	5
1.3.2 Diffusion-weighted imaging.....	7
PRINCIPLES OF DIFFUSION IMAGING	7
DWI ACQUISITION	8
DIFFUSION TENSOR IMAGING	10
NEURITE ORIENTATION DISPERSION AND DENSITY IMAGING	13
CONSTRAINED SPHERICAL DECONVOLUTION.....	16
1.3.3 Magnetization transfer imaging.....	19
PRINCIPLES OF MAGNETIZATION TRANSFER IMAGING	19
MTI ACQUISITION	21
MAGNETIZATION TRANSFER RATIO	21
MAGNETIZATION TRANSFER SATURATION.....	22
1.3.4 Multi-parametric mapping	24
PRINCIPLES OF MULTI-PARAMETRIC MAPPING	24
QUANTITATIVE MAPS.....	26
1.3.5 Integrating multiple MRI measures with multivariate approaches.....	27
1.4 WHITE MATTER CHANGES AS AN EARLY PATHOLOGICAL PROCESS IN AGE-RELATED DISEASE	29
1.4.1 Dementia	31
1.4.2 High blood pressure.....	32
1.4.3 Obesity	33
1.4.4 Cholesterol	34
1.4.5 Elevated glucose	36
1.4.6 APOE genotype.....	37
1.4.7 Coronary artery disease.....	38
1.4.8 Protective factors.....	39
1.5 EARLY INTERVENTION TO PREVENT AGE-RELATED DISEASES.....	40
CHAPTER II: SHORT-TERM WHITE MATTER PLASTICITY IN YOUNG ADULTS.....	42
PREFACE	42
2.1 ABSTRACT.....	43
2.2 INTRODUCTION.....	44
2.3 METHODS	46
2.3.1 Participants	46
2.3.2 Motor Sequence Learning Task.....	47
2.3.3 Experimental Design	49
2.3.4 MRI Acquisitions.....	49
2.3.5 Image Preprocessing.....	50
2.3.6 Statistical Analyses.....	52
2.4 RESULTS.....	56
2.4.1 Performance improvement in the SPFT	56
2.4.2 WM microstructural changes across learning stages.....	58
2.4.3 WM microstructural changes associated with functional changes.....	61
2.5 DISCUSSION	63

2.5.1 Changes in the LRN group.....	63
2.5.2 Changes in both groups	69
2.5.3 Relationships between behavioural and WM microstructural changes.....	70
2.5.4 Limitations and Future Considerations	71
2.6 CONCLUSION.....	72
CHAPTER III: DEVELOPMENT OF A TOOLBOX FOR MULTIVARIATE ANALYSIS	74
PREFACE	74
3.1 ABSTRACT.....	75
3.2 INTRODUCTION.....	77
3.3 METHODS	81
3.3.1 General framework.....	81
Comparisons between an individual and a group (reference).....	82
Comparisons within an individual	83
3.3.2 Data preparation	86
3.3.3 Computing the reference mean and covariance matrix	86
Comparisons between an individual and a group (reference).....	86
Comparisons within an individual	87
3.3.4 Computing D2	88
Comparisons between an individual and a group (reference).....	88
Comparisons within an individual	89
3.3.5 Statistical analysis.....	90
Comparisons between an individual and a group (reference).....	90
Comparisons within an individual	90
3.3.6 Determining feature importance	91
Comparisons between an individual and a group (reference).....	91
Comparisons within an individual	92
3.3.7 Experiments.....	92
Data Description	92
Preprocessing	92
Experiment 1: Comparisons between an individual and a group (reference)	96
Experiment 2: Comparisons within an individual	97
3.4 RESULTS.....	98
3.4.1 Experiment 1: Comparisons between an individual and a group	98
3.4.2 Experiment 2: Comparisons within an individual.....	99
3.5 DISCUSSION	100
3.5.1 D2 reflects the underlying microstructure of WM	101
3.5.2 D2 in the study of pathologies	102
3.5.3 Limitations.....	103
3.6 CONCLUSION.....	104
CHAPTER IV: MULTIVARIATE WHITE MATTER IN PRE-CLINICAL ALZHEIMER'S DISEASE.....	106
PREFACE	106
4.1 ABSTRACT.....	107
4.2 INTRODUCTION.....	108
4.3 METHODS	110
4.3.1 Participants	110
4.3.2 MRI Protocol.....	112
4.3.3 Preprocessing	113
4.3.4 Computing multivariate distance metric (D2)	116
4.3.5 Blood samples	118
4.3.6 Body composition and physiological measures	118
4.3.7 APOE4 genotyping	118
4.3.8 Cognitive assessment.....	119

4.3.9 Statistical analyses.....	119
4.4 RESULTS.....	121
4.4.1 Relationships between WM microstructure and risk factors in each sex.....	121
4.4.2 Relationships between WM microstructure and risk factors in each APOE4 group.....	124
4.4.3 Determining feature importance in regions of interest.....	128
4.4.4 Relationships between deviations in WM microstructure and cognition.....	132
4.5 DISCUSSION.....	132
4.5.1 Sex-related effects.....	132
4.5.2 APOE4-dependent effects of LDL.....	133
4.5.3 Role of myelin and other components.....	135
4.5.4 Strengths and limitations.....	135
4.6 CONCLUSION.....	136
CHAPTER V: WHITE MATTER MICROSTRUCTURE IN OLDER ADULTS WITH CARDIOVASCULAR DISEASE.....	137
PREFACE.....	137
5.1 ABSTRACT.....	138
5.2 INTRODUCTION.....	139
5.3 METHODS.....	140
5.3.1 Participants.....	140
5.3.2 MRI Protocol.....	143
5.3.3 Preprocessing.....	143
5.3.4 Computing multivariate distance metric (D2).....	147
5.3.5 Extracting D2 in arterial territories.....	150
5.3.6 Cardiorespiratory fitness assessment.....	150
5.3.7 Cognitive assessment.....	150
5.3.8 Statistical analyses.....	152
5.3.9 Determining features contribution to D2.....	152
5.4 RESULTS.....	153
5.4.1 Group differences.....	153
5.4.2 Features contribution to D2.....	154
5.4.3 Links between WM D2, fitness, and cognition.....	156
5.4.4 Differential effects in patients vs controls.....	158
5.4.5 Links between WMH, fitness and cognition.....	158
5.5 DISCUSSION.....	159
5.5.1 WM microstructural alterations in CAD patients.....	159
5.5.2 Links with fitness.....	160
5.5.3 Links with cognition.....	161
5.5.4 Biological mechanisms underlying WM alterations.....	161
5.5.5 Limitations & Future directions.....	162
5.6 CONCLUSION.....	163
CHAPTER VI: GENERAL DISCUSSION.....	164
6.1 CONTRIBUTIONS OF THIS THESIS.....	167
6.1.1 Studying white matter with a multivariate approach.....	167
6.1.2 Dynamic white matter changes in health and disease.....	168
6.1.3 Comparing AD- and vascular-related impairments in white matter.....	170
6.2 FUTURE DIRECTIONS.....	171
6.2.1 Studying white matter longitudinally.....	171
6.2.2 Expanding beyond white matter.....	171
6.2.3 Assessing the entire health-disease continuum.....	172
6.2.4 Expanding beyond biology.....	173
CHAPTER VII: CONCLUSION.....	175

BIBLIOGRAPHY	177
APPENDIX I – SUPPLEMENTARY MATERIAL STUDY 1	235
APPENDIX II – SUPPLEMENTARY MATERIAL STUDY 2	236
APPENDIX III – SUPPLEMENTARY MATERIAL STUDY 3	237

List of figures

Chapter I: General Introduction

Figure 1. Isotropic and anisotropic diffusion in different brain compartments.

Figure 2. Representation of angular sampling in diffusion-weighted imaging (DWI).

Figure 3. Diffusion ellipsoid of the diffusion tensor imaging (DTI) model.

Figure 4. Crossing fibers representation in different DWI modelling approaches.

Figure 5. Sample of orientation dispersions from the Watson distribution in the neurite orientation dispersion and density imaging (NODDI) model.

Figure 6. NODDI maps are contrasted with fractional anisotropy and principal direction maps.

Figure 7. Ellipsoids from the DTI model are contrasted with fiber orientation density (FOD) functions from spherical deconvolution.

Figure 8. Tractography from DTI and from spherical deconvolution.

Figure 9. FODs showing the orientation and density of every fiber population in a voxel.

Figure 10. Fiber-specific metrics from multi-tissue constrained spherical deconvolution.

Figure 11. Schematic representation of excitation of the macromolecular pool in magnetization transfer imaging (MTI).

Figure 12. Basic acquisition scheme for MTI.

Figure 13. Diagram showing how the magnetization transfer ratio (MTR) is calculated.

Figure 14. MT saturation map.

Figure 15. Histograms of MTsat and MTR showing separation between tissue types.

Figure 16. T1 recovery curve and T2 decay curve.

Figure 17. Quantitative maps from multi-parametric mapping.

Figure 18. Health – disease continuum and potential interventions.

Chapter II: Short-term white matter plasticity in young adults

Figure 1. Sequential pinch force task (SPFT) and experimental design.

Figure 2. DWI data processing workflow.

Figure 3. Regions of interest (ROIs) in white matter created from grey matter ROIs.

Figure 4. Behavioral results. Temporal deviation for each group and each task across training days and retention session.

Figure 5. Longitudinal changes in FA from voxel-wise analyses.

Figure 6. Changes in WM microstructure in the ROI underlying the right supplementary motor area.

Chapter III: Development of a toolbox for multivariate analysis

Figure 1. Implementations of the D2 framework in neuroimaging studies.

Figure 2. D2 workflow for two example cases. Voxel-wise comparisons between a subject and a reference and within-subject comparisons between all WM voxels and a reference ROI.

Figure 3. Results of voxel-wise comparisons between each subject and the reference.

Figure 4. Results of within-subject voxel-voxel comparisons.

Chapter IV: Multivariate white matter in pre-clinical Alzheimer's disease

Figure 1. Methodological framework.

Figure 2. Relationships between D2 in WM and risk factors in each sex.

Figure 3. Relationships between D2 in WM and risk factors in each APOE4 group.

Figure 4. Features contribution to D2 in each significant cluster from PLS analyses in females and males.

Figure 5. Features contribution to D2 in each significant cluster from PLS analyses in APOE4+ and APOE4-.

Chapter V: White matter microstructure in older adults with cardiovascular disease

Figure 1. Workflow for computing D2.

Figure 2. Arterial territories within the WM mask, overlaid on the group average MPRAGE T1w image.

Figure 3. Mean and median D2 for each group and relative contribution (%) of each MRI metric to D2 in each region (whole WM and arterial territories).

Figure 4. Associations between VO2max and D2 in whole WM and in the left PCA in the whole sample.

Figure 5. Associations between D2 in the left MCA and processing speed in the whole sample.

Figure 6. Associations between WMH volumes and MoCA in the whole sample.

List of tables

Chapter II: Short-term white matter plasticity in young adults

Table 1. Demographic data in each group.

Table 2. Clusters in which significant changes in FA were found.

Chapter IV: Multivariate white matter in pre-clinical Alzheimer's disease

Table 1. Demographics data for each sex and for the sex-balanced reference group that was used for D2 calculation (mean \pm standard deviation).

Table 2. Cluster information (PLS analyses in each sex).

Table 3. Cluster information (PLS analyses in each APOE4 group).

Chapter V: White matter microstructure in older adults with cardiovascular disease

Table 1. Demographic data of the cohort.

CHAPTER I: General Introduction

1.1 Executive Summary

The brain's white matter (WM) microstructure is shaped by our experiences – the sports we play, the things we learn, and the social connections we form – and this capacity for plasticity is maintained throughout the lifespan (Sampaio-Baptista & Johansen-Berg, 2017). WM microstructure is also highly sensitive to exposure to stressors and insults (Bartzokis, 2004a). With age, the increasing vulnerability of myelin formed by later-differentiating oligodendrocytes, along with the accumulation of exposures to stressors, result in myelin and axonal breakdown. Several factors impact the trajectory of myelin degeneration, influencing whether someone will age successfully or develop a neurodegenerative disorder (Bartzokis, 2004a, 2011). These include genetic factors, such as possessing one or more $\epsilon 4$ alleles of the Apolipoprotein E (ApoE) gene, as well as modifiable risk factors (e.g., education, hypertension, dyslipidemia, hyperglycemia, obesity, cardiovascular disease) (Bartzokis et al., 2007; Livingston et al., 2024). This vulnerability has made WM an early target in the pathological course of neurodegenerative diseases such as dementia (N. Adluru et al., 2014; Agosta et al., 2011; Araque Caballero et al., 2018; Maier-Hein et al., 2015). Importantly, the fact that WM retains its plastic potential into adulthood also means that improvements to WM microstructural health may be used as targets in interventions aimed at preventing neurocognitive disorders (Concha, 2014; Sampaio-Baptista & Johansen-Berg, 2017).

Measuring WM microstructural properties may thus offer a promising avenue for the early detection of abnormalities, as well as for monitoring progression and assessing improvements in response to interventions. However, we lack a basic understanding of the time scales at which plastic changes in WM can occur, and of the alterations that occur at different stages of learning, even in healthy adults. This gap was addressed in Study 1.

Furthermore, because most studies in the field rely on neuroimaging techniques that are physiologically non-specific and on predominantly univariate analysis methods, we lack a comprehensive understanding of the factors that impact WM microstructure and of the biological mechanisms driving these changes. We tackled these issues by developing a toolbox (Study 2) that allows the integration of several neuroimaging metrics into a multivariate distance score – the

Mahalanobis distance – and applying this framework to the study of two populations at risk of dementia: older adults with a familial history of Alzheimer’s disease (Study 3) and those with coronary artery disease (Study 4).

In Chapter 1, I first provide a brief background on WM physiology (Section 1.2), followed by an overview of commonly used WM imaging techniques (i.e., diffusion-weighted imaging [DWI], magnetization transfer imaging [MTI]), several of which were used in this work (Section 1.3). The concept that WM alterations constitute an early pathological event in age-related diseases is then introduced, and literature on the impact of several risk factors on WM microstructure is reviewed (Section 1.4). Lastly, I discuss potential interventions aimed at promoting neuroplasticity and preventing cognitive decline and dementia (Section 1.5).

The body of the dissertation contains four original manuscripts. In the first manuscript (Chapter 2), I investigated changes in WM across learning stages in a cohort of healthy young adults. The data used for this study were acquired at 7 Tesla at the Max Planck Institute for Cognitive and Brain Sciences in Leipzig. I analyzed the DWI data using the diffusion tensor model (DTI) and conducted all analyses. I also collaborated with a PhD student from Germany (Anna-Thekla Jäger, second author on manuscript 1) to relate longitudinal structural changes in WM to the changes in resting-state functional connectivity she found in the same cohort (Jäger et al., 2021).

The second manuscript (Chapter 3) describes the MultiVariate Comparison (MVComp) toolbox (<https://github.com/neuralabc/mvcomp>) that I co-created in collaboration with Zaki Alasmar (co-first author), Amir Pirhadi (third author), and Christopher Steele (senior author). The toolbox allows the computation of the Mahalanobis distance (D2) from neuroimaging data. My main contributions were in developing the conceptual framework, defining the potential applications of the toolbox, and writing the manuscript, while my collaborators, Zaki Alasmar and Amir Pirhadi, focused on the technical implementation (i.e., writing the code in Python and preparing for public release on GitHub). The open-source Human Connectome Project (S1200) dataset was used in the validation experiments of this study. I preprocessed the DWI data of more than a thousand participants and fitted advanced models which yielded 10 microstructural maps. To our knowledge, MVComp is the only available toolbox for computing D2 from imaging data.

In the third manuscript (Chapter 4), I investigated the sex-specific and APOE genotype-related relationships between alterations in WM microstructure, quantified using the MVComp framework, and multiple risk factors in a cohort of older adults with a familial history of Alzheimer's disease. This project was a collaboration with the PREVENT-AD Research Group who recruited the participants and collected the data used in this study (Tremblay-Mercier et al., 2021). I preprocessed all data (DWI and multi-parametric mapping; MPM) and conducted all analyses for this manuscript.

Finally, the fourth manuscript (Chapter 5) leveraged the D2 framework to assess WM deviations from a healthy reference in coronary artery disease patients. The links between WM alterations in atlas-based arterial territories, fitness, and cognition were also explored. As the coordinator for this study since the beginning of my PhD (January 2019), I have been involved in all stages of this project, from obtaining ethics approval to recruitment and collecting data in over 100 participants at the Montreal Heart Institute. I have been involved in all aspects of data collection, including the MRI acquisition, maximal cardiopulmonary exercise testing (VO₂max), and the administration of cognitive assessments. This study is a collaboration with Zacharie Potvin-Jutras (co-first author) who preprocessed the MTI data and performed segmentations of WM hyperintensities and registrations of an arterial territories atlas. I was responsible for preprocessing the DWI data, computing D2 and performing registrations to bring all maps into a common space. I also did most of the formal analyses and of the writing.

In the final chapter (Chapter 6), I highlight and discuss the contributions of this thesis to advancing our understanding of how the brain's WM microstructural health is altered in individuals at risk of dementia. I also emphasize the importance of studying WM with a multivariate approach, demonstrating how the open-source toolbox we developed can facilitate the broader adoption of these methods, thus making a significant contribution to the field. Lastly, future directions for this work are outlined.

1.2 White matter physiology

Efficient neural transmission is crucial for normal function as communication between brain regions, as well as between the brain and spinal cord, supports virtually all physiological functions and behaviors from the most basic to the most complex tasks (Susuki, 2010). Conduction of neural signals through axons must occur at very high speeds to allow for the integration and processing of large amounts of information in a coordinated manner. Myelin, a lipid-rich membranous sheath that surrounds most long-range axons in the central nervous system, increases the speed of neural transmission, enabling efficient information processing by optimizing neural timing (Baumann & Pham-Dinh, 2001; Paus, 2010; Waxman, 1975). Axons and their myelin, along with glial cells (i.e., oligodendrocytes, astrocytes, and microglia), form the brain's white matter (WM). WM is located deep within the brain beneath the cortical grey matter and is named after the characteristic color of lipid-rich myelin. Long thought of as passive tissue that carries impulses between neurons, the importance of WM in coordinating information transmission is now widely recognized (Fields, 2008b).

White matter undergoes a long developmental process that extends well beyond that of grey matter, continuing until the end of the fifth decade of life (Bartzokis, 2004b; Sowell et al., 2003). The extent of myelination in the human brain is unique and has been posited as one of the most important features differentiating humans from other mammals (Bartzokis, 2004b). The human brain is unique in the amount of WM it contains compared to other species, but also in its "heterochronologic" development, that is, the fact that myelination in different regions follows different time courses. Primary motor and sensory regions myelinate early in life, while prefrontal and other association areas (temporal and parietal lobes) continue myelinating until the fifth decade (peaking at about 45 years of age) (Bartzokis, 2004b, 2011). Oligodendrocytes that differentiate later in life wrap thin myelin sheaths around a large number of axons of small diameters, whereas those that differentiate earlier ensheath thicker myelin around larger axons (Bartzokis, 2004b).

According to the myelin model, this extensive myelination underlies not only our exceptional abilities, but also our unique vulnerability to various stressors, predisposing humans to age-related neurodegenerative disorders such as Alzheimer's disease (Bartzokis, 2011). Age-related WM degeneration tends to follow a pattern that reverses the developmental pattern, with fibers that myelinated last (i.e., axons of smaller diameters with thinner myelin sheaths) being the first ones

to break down when degeneration begins (Bartzokis, 2004b, 2011; Braak & Braak, 1996). This “disconnection” results in cognitive decline, especially in higher order functions and in the formation of new memories, functions that require widely distributed neural networks (Bartzokis, 2004b). Several factors can impact the trajectory of WM development and accelerate its breakdown. WM damage is thus a common feature of several neurological disorders including multiple sclerosis, Alzheimer’s disease, and other forms of dementia, and is also commonly reported in metabolic disorders such as hypertension, diabetes, and cardiovascular disease (Alfaro et al., 2018; Alotaibi et al., 2021; Bae et al., 2020; Santiago et al., 2015).

Myelination follows an age-dependent developmental pattern that is influenced not only by adverse factors, but also by learning and training (Fields, 2015; Scholz et al., 2009). Myelination is thus an activity-dependent process as WM microstructure adapts to the demands imposed on itself in order to perform frequently-repeated tasks more efficiently (Deng et al., 2018). The long developmental timeline of WM means that a portion of oligodendrocytes precursor cells that have the capacity to differentiate into oligodendrocytes and produce myelin remain in adulthood (Sampaio-Baptista & Johansen-Berg, 2017). WM thus retains its capacity for experience-induced plasticity, supporting learning throughout life. Plastic changes in WM, which also involve changes in axon diameter and in internodal length in addition to myelin (Sampaio-Baptista & Johansen-Berg, 2017), occur even following short periods of training, attesting to its capacity for rapid remodelling (Hofstetter et al., 2013).

Because axons were traditionally thought of as passive passageways, WM has long been overlooked and has thus received much less attention than neurons and synapses (Fields, 2008b; Sampaio-Baptista & Johansen-Berg, 2017). There is now growing recognition that WM changes are highly dynamic and that its trajectory of development (and degeneration) can be altered through exposure to both enriching and adverse experiences throughout the lifespan.

1.3 White matter imaging

1.3.1 Overview

Given the utmost importance of neuronal conduction and its reliance on WM microstructure, several magnetic resonance imaging (MRI) techniques have been designed to characterize properties of the brain’s WM *in vivo*. Diffusion-weighted imaging (DWI), one of the most

commonly used techniques, relies on the bulk motion of water molecules to indirectly probe WM microstructure (Le Bihan et al., 1988, 2001; Le Bihan & Iima, 2015). DWI provides invaluable information regarding axonal organization and density, yet these techniques alone do not provide a specific measure of myelin content as several other factors impact diffusion MRI metrics (Beaulieu, 2002; Paus, 2010). Myelin-specific imaging techniques, such as magnetization transfer imaging (MTI), should therefore be used alongside DWI to characterize WM more fully as neural transmission velocity and timing depend on both axonal diameter and myelin thickness (Fields, 2008a; Waxman, 1975). Lastly, relaxometry can provide measures of the quantitative T1, T2* and proton density parameters, which allow further specificity by providing measures of iron content in addition to water and myelin (Margaret Cheng et al., 2012). These quantitative parameters can be acquired efficiently using multi-parametric mapping (MPM) imaging protocols (Helms, Dathe, & Dechent, 2008; Weiskopf et al., 2011). This is important given that iron accumulation is frequently observed in neurodegeneration, and it can confound other MRI measures if it is not taken into account. Using the quantitative parameters obtained through MPM, it is possible to determine whether iron is accumulating and whether myelin repair or demyelination is occurring (Callaghan et al., 2014).

WM imaging techniques have numerous important research and clinical applications. These techniques allow the characterization of several aspects of the brain's WM and of how they are altered during development, learning, and aging, as well as in neurological disorders (G. Adluru et al., 2014; Badji et al., 2019; Campbell et al., 2018; Fields, 2008a; Foong et al., 2001; Kado et al., 2001). WM imaging offers the possibility to detect abnormalities and monitor progression in patients suffering from several conditions affecting the brain's WM. For instance, pathological changes occurring in demyelinating disorders such as multiple sclerosis (MS) can be quantified using MTI, allowing for the characterization of the progression of disease and of the effects of treatment on remyelination (Campbell et al., 2018). Furthermore, combining techniques such as DWI, MTI, and MPM allows for more specific interpretations of observed differences or changes as it allows to disentangle changes in myelin, axons, and iron.

The following sections will present MRI techniques that allow the quantification of different aspects of WM microstructure: DWI, MTI, and MPM. Each section will introduce the physics principles on which these techniques are based and present some examples of the acquisition schemes and models that can be used, along with the parameters that can be derived from these

models. Lastly, multivariate approaches that aim at integrating several parameters will be discussed.

1.3.2 Diffusion-weighted imaging

PRINCIPLES OF DIFFUSION IMAGING

Diffusion-weighted imaging (DWI) is based on the widely known concept that small particles move in a random fashion as a result of the available thermal energy, a concept termed Brownian motion (Brown, 1828; Einstein, 1905; Le Bihan et al., 2001). DWI exploits this intrinsic physical property, which is not altered by MRI, along with the fact that motion is restricted/hindered by structural boundaries, such as cellular membranes, axons, and macromolecules in the brain (Le Bihan et al., 2001). With a mean displacement of 10 μm during a typical diffusion time (i.e., 50 ms), water molecules, the most frequently imaged molecules, allow for the probing of tissue structure at a microscopic level (i.e., microstructure). As an imaging voxel contains a large number of water molecules, DWI techniques aim at characterizing the displacement distribution of these molecules. The geometric organization of the brain microstructure can thus be inferred through characterization of the displacement distribution at every imaged voxel. Brain tissue at different locations possesses varying levels of anisotropy. In tissues with anisotropic configuration, the mobility of water molecules differs among directions due to physical barriers to diffusion. For instance, in coherently organised WM (i.e., arranged into bundles of parallel axons), diffusion is anisotropic, as water molecules preferentially diffuse in directions parallel to fiber bundles, while in cerebral ventricles filled with cerebrospinal fluid (CSF), diffusion is mostly isotropic (see **Figure 1**). In WM, higher anisotropy values are found in areas where fibers are myelinated. Since axonal membranes are more permeable than myelin, diffusion perpendicular to the axon is restricted to a lesser extent in unmyelinated axons, resulting in lower anisotropy (Le Bihan et al., 2001). Through modeling and the estimation of diffusion metrics, several aspects of biological tissues can be assessed, including the detection of brain ischemia, quantification of WM microstructure, and mapping of fiber organization. Before proceeding to the description of these models and applications, the general DWI acquisition scheme will first be presented.

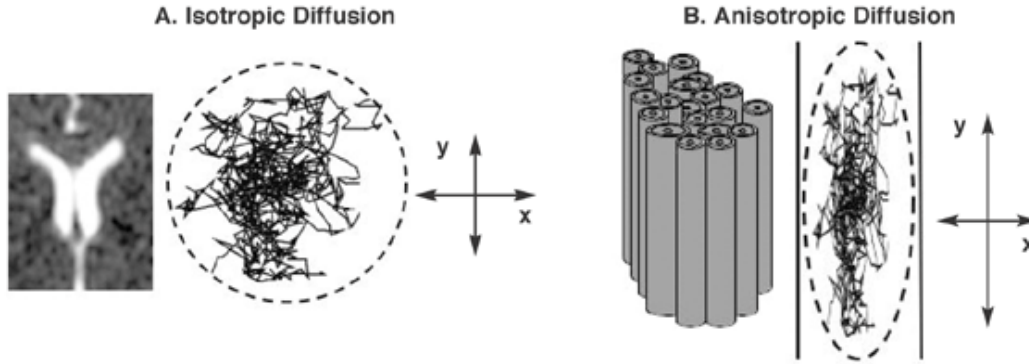


Figure 1. Isotropic (A) and anisotropic diffusion (B) in different brain compartments (lateral ventricles in A; parallel bundle of axons in B). (Rosenbloom et al., 2003).

DWI ACQUISITION

Most commonly, diffusion-weighted images are acquired using a spin-echo sequence, consisting in two radiofrequency pulses of 90° and 180° . Moreover, two diffusion-sensitizing gradient pulses of equal amplitude and duration are applied on each side of the 180° pulse. This sequence, known as the Stejskal-Tanner pulsed gradient spin echo (PGSE) technique, was developed in the 1960's and is still used today with some slight modifications to reduce artifacts (A. L. Alexander et al., 1997; Reese et al., 2003; Stejskal & Tanner, 1965). The first gradient dephases the spins and a second gradient, which has the opposite effect on the spins (because of the 180° pulse), then rephases stationary spins. However, moving spins keep accumulating phase between the two gradients and are thus not rephased by the second gradient. This dephasing of the spins causes signal attenuation, which is how diffusion is measured in DWI. Echo planar imaging (EPI) then allows for a quick readout after the second gradient, minimizing the effects of bulk motion (Le Bihan et al., 2001). In order to compute signal attenuation, a T2-weighted image, consisting in the same spin-echo sequence but without diffusion gradients, must also be obtained to serve as a baseline (i.e., non-diffusion weighted) (Le Bihan et al., 2001). DWI acquisitions require long repetition times ($TR \sim 10$ s), reducing T1 contributions, and long echo time ($TE \sim 75$ ms). Thus, the image contrast of DWI images is due to differences in transverse relaxation between tissue types (i.e., T2-weighted), as well as in attenuation due to diffusion.

The signal measured (S) is a function of the attenuation (A) of the baseline signal S_0 , which depends on the gradient strength used (b) and on the amount of diffusion (D) present in tissue, and can be expressed by the following equations:

$$A = \exp(-bD), \quad (\text{Eq. 1})$$

$$S(b, D) = S_0 \exp(-bD), \quad (\text{Eq. 2})$$

where D is the diffusion coefficient (in mm^2/s) and b is the b-value (in s/mm^2), representing the strength of the gradient pulses, which depends on the amplitude (G), duration (δ), and shape of the pulses, as well as on the gyromagnetic ratio γ of the imaged nucleus (42.58 MHz/T for hydrogen) (Le Bihan et al., 1986). The b-value can be expressed with the following equation: $b = \gamma^2 G^2 \delta^2 (\Delta - \delta/3)$, where Δ is the interval between gradient pulses. Thus, the gradient amplitude, duration and time interval can be manipulated to achieve a given b-value. However, an important element to keep in mind is that the maximum G that can be used is limited by both the hardware and safety limits (i.e., the maximum specific absorption rate; SAR). Therefore, in some settings, it may be preferred to manipulate the duration of the gradient pulses to change the b-value (Descoteaux, 2015). Low b-values, acquired with weaker/shorter gradients, are sensitive to faster diffusion, which takes place in the extracellular compartment (Le Bihan et al., 2001). On the other side, larger b-values measure slower diffusion and result in more signal attenuation, as spins dephase to a greater extent when stronger gradients are applied. A DWI image provides a window

into the diffusion process occurring along a single direction (i.e., the direction in which the diffusion gradient was applied) (see **Figure 2**). Therefore, the DWI acquisition must be repeated with gradients applied in different directions to obtain a complete picture of the three-dimensional diffusion process. Three orthogonal diffusion images (x, y, z) are sufficient to estimate the apparent diffusion coefficient (ADC), but at least six images are required for the diffusion tensor (DTI) model (Descoteaux, 2015). More complex models and applications, such as fiber tracking, require a much greater number of directions. The concept of q -space must be introduced here for a better visual representation of angular sampling in DWI (see top

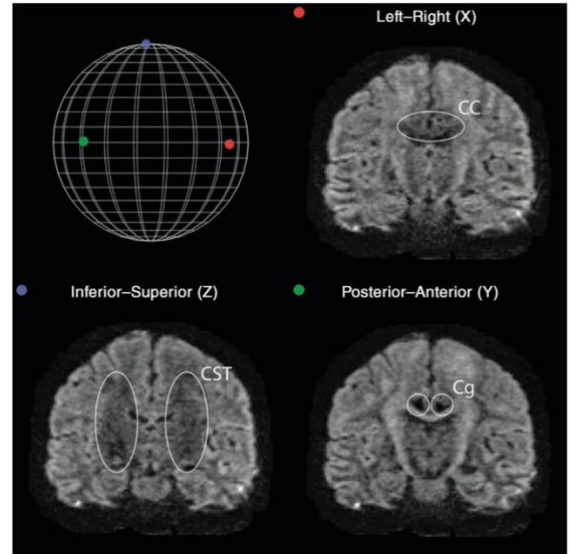


Figure 2. Top left: Representation of the q -space showing sampling in 3 orthogonal directions (x direction = red; y = green; z = blue). Top right: Corpus callosum, a fiber tract oriented from left-right is dark (signal attenuated) on the x -direction image. Bottom left: Corticospinal tracts, oriented superior-inferior are dark on z -direction image. Bottom right: Cingulum, oriented post-ant, on the y -direction image. (Descoteaux, 2015).

left panel of **Figure 2**). In a similar way as phase- and frequency-encoding gradients (i.e., G_y and G_x) allow to travel k -space to acquire information at different spatial frequencies, diffusion gradients allow to navigate the diffusion space (i.e., q -space) to probe the diffusion process in different directions. Applying diffusion gradients in a large number of directions thus provides a rich sampling of q -space. Higher angular sampling provides several advantages but requires increased scanning time, making the use of acceleration techniques such as parallel imaging very important for DWI (Descoteaux, 2015). With an increasing number of directions, more baseline images ($b = 0$) are required (i.e., the acquisition of one b-zero image is recommended for every 10 directions), which further increases scan time (Descoteaux, 2015).

DIFFUSION TENSOR IMAGING

The diffusion tensor (DTI) model was created to model the diffusion process in biological tissues (Basser et al., 1994a, 1994b). Indeed, unless diffusion is perfectly isotropic, it cannot be represented by a single scalar D (Le Bihan et al., 2001). The tensor is a 3x3 symmetric matrix representing diffusion along nine directions:

$$\mathbf{D} = \begin{pmatrix} D_{xx} & D_{xy} & D_{xz} \\ D_{yx} & D_{yy} & D_{yz} \\ D_{zx} & D_{zy} & D_{zz} \end{pmatrix}, \quad (\text{Eq. 3})$$

Therefore, the following equation, which is an extension of Eq. 2, must be solved for six unknown diffusion coefficients (D_{xx} , D_{yy} , D_{zz} , D_{xy} , D_{xz} and D_{yz}), as the matrix is symmetric, (i.e., $D_{xy} = D_{yx}$):

$$S = S_0 \exp(-b_{xx}D_{xx} - b_{yy}D_{yy} - b_{zz}D_{zz} - 2b_{xy}D_{xy} - 2b_{xz}D_{xz} - 2b_{yz}D_{yz}), \quad (\text{Eq. 4})$$

where D_{xx} , for instance, is an element of the diffusion tensor matrix and b_{xx} is the corresponding term of the \mathbf{b} matrix, the diffusion coefficient and the gradient pulse strength along the x-direction (i.e., left-right), respectively. A minimum of six diffusion-weighted images in different, uniformly spaced, directions is required to solve for the six unknown coefficients (D_{ij}) of Eq. 4 using weighted least-squares methods, with weights based on signal intensities (Basser et al., 1994a; Descoteaux, 2015; Le Bihan et al., 2001). Since Eq. 4 must be solved at every voxel, tensor computation yields a 4D image, or a series of six 3D volumes each containing the diffusion

coefficients D_{xx} , D_{yy} , D_{zz} , D_{xy} , D_{xz} and D_{yz} at each voxel (Descoteaux, 2015). The tensor can then be diagonalized, that is the frame of reference can be changed to a frame where the tensor is reduced to its diagonal terms (D_{xx} , D_{yy} and D_{zz}), allowing to simplify the signal equation to:

$$S = S_0 \exp(-b_{x'x'}D_{x'x'} - b_{y'y'}D_{y'y'} - b_{z'z'}D_{z'z'}), \quad (\text{Eq. 5})$$

where x' , y' and z' indicate the diagonalized frame of reference, which is aligned to the main diffusion directions. Diagonalization is also referred to as *eigenvalue decomposition* as it yields three eigenvectors ($\mathbf{\epsilon}$), the main directions of diffusion, and three eigenvalues (λ), the diffusivities in each of those directions, where $\lambda_1 > \lambda_2 > \lambda_3$ (Descoteaux, 2015; Le Bihan et al., 2001). The principal orientation of the tensor ($\mathbf{\epsilon}_1$) is thus given by the direction of the largest eigenvalue, λ_1 . Diffusion at each voxel can be represented visually as an ellipsoid where the main axis indicates the main direction of diffusion $\mathbf{\epsilon}_1$ and the length of each axis, the displacement distance in that direction during the diffusion time T_d (**Figure 3**) (Le Bihan et al., 2001). Importantly, the shape of the ellipsoid shows the degree of anisotropy; the more elongated the ellipsoid the higher the anisotropy of diffusion, and the higher the orientation coherence of the underlying microstructure in that voxel (Descoteaux, 2015; Le Bihan et al., 2001). On the other hand, a spherical shape indicates a voxel where diffusion is isotropic and diffusivities are equal in all directions ($\lambda_1 = \lambda_2 = \lambda_3$).

These different aspects describing the diffusion process (i.e., overall molecular displacement, or diffusivity, degree of anisotropy, and main direction of diffusion), can be quantified by deriving scalar metrics from the tensor image (Le Bihan et al., 2001).

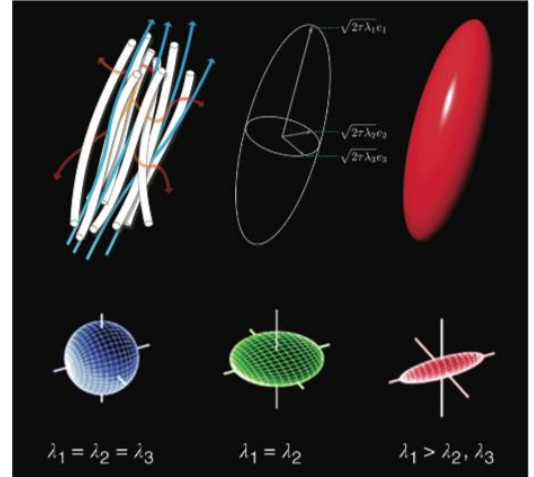


Figure 3. Diffusion ellipsoid of the DTI model. The red ellipsoid of the top panel represents a tensor with a fractional anisotropy (FA) value of approximately 0.7 (coherently organised WM fibers as shown on the top left). The bottom part of the figure illustrates different possible tensor configurations (blue= isotropic, green= oblate, red = prolate). (Descoteaux, 2015).

Mean diffusivity (MD), the spatial extent of random motion at a given voxel, is computed by averaging the three eigenvalues: $MD = (\lambda_1 + \lambda_2 + \lambda_3)/3$. This measure is very useful in clinical applications such as detecting early brain ischemia as diffusion drops almost immediately in ischemic regions due to intracellular swelling (Descoteaux, 2015; Le Bihan et al., 2001). In

ischemia (e.g. stroke), the increased intracellular volume, and accompanying decrease in extracellular volume, in a given voxel leads to greater restriction for molecular motion as DWI is sensitive mainly to the extracellular compartment, where diffusion occurs at higher speeds (especially at low b values) (Le Bihan et al., 2001).

Diffusion anisotropy is most frequently quantified using fractional anisotropy (FA) (A. L. Alexander et al., 2000). FA ranges from 0 to 1; values near zero describe isotropic diffusion while values above 0.7 are found in voxels containing fibers organised with high coherence (e.g., corpus callosum). FA images thresholded at 0.2 are often used as maps of WM since voxels with $FA > 0.2$ tend to be located in WM while lower values are typically found in grey matter and CSF.

$$FA = \frac{3}{2} \sqrt{\frac{(\lambda_1 - \lambda_2)^2 + (\lambda_1 - \lambda_3)^2 + (\lambda_2 - \lambda_3)^2}{\lambda_1^2 + \lambda_2^2 + \lambda_3^2}}, \quad (\text{Eq. 6})$$

Two other commonly used metrics, axial and radial diffusivities (AD and RD), provide information on diffusivity along the principal direction ($AD = \lambda_1$) and in the plane perpendicular to ϵ_1 ($RD = (\lambda_2 + \lambda_3)/2$) (Descoteaux, 2015). Lastly, fiber orientation can be tracked by aligning the principal direction vectors, ϵ_1 , at each voxel, allowing to map the connective architecture of the brain *in vivo*.

DTI is now widely used in clinical settings, to detect brain ischemia, as well as in research to investigate WM changes due to aging, pathology, and learning (Le Bihan et al., 2001). However, there are several limitations to the DTI model as metrics derived from DTI are sensitive but non-specific (H. Zhang et al., 2012a). For instance, different tissue configurations, such as an area of crossing fibers and an area where diffusion is truly isotropic (i.e., ventricles) can lead to similar FA values (see **Figure 4**) (Descoteaux, 2015). Furthermore, DTI models the diffusion process as either Gaussian (e.g., water molecules in the extra-cellular space) or non-Gaussian (e.g., restricted diffusion in the intra-cellular space) and can thus only model one fiber population per voxel (Descoteaux, 2015; H. Zhang et al., 2012a). The Gaussian assumption is violated most of the time as over two thirds of WM voxels have multiple fiber populations with different orientations (Descoteaux, 2015). These limitations have led to the emergence of new, higher order, models that

require acquisitions of higher angular resolution and multiple b-values (i.e., shells) (Descoteaux, 2015).

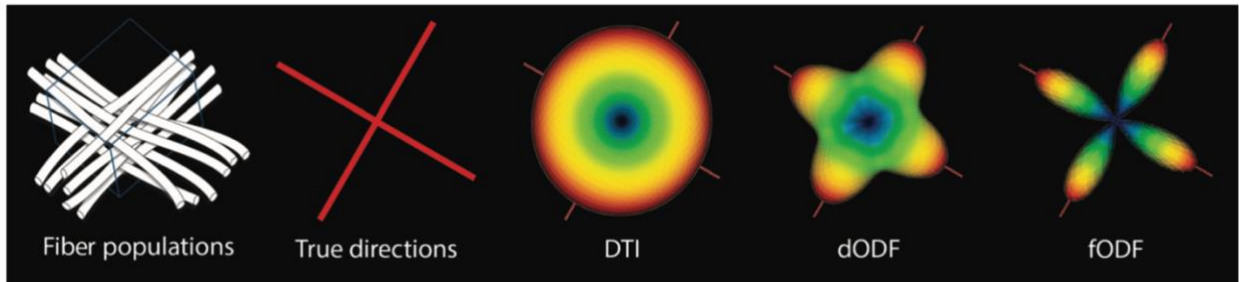


Figure 4. Crossing fibers at an imaging voxel are represented by a sphere in DTI, and thus as isotropic. The true configuration can be resolved with more advanced modeling approaches which yield orientation dispersion functions (ODFs). Modified from Descoteaux, 2015.

NEURITE ORIENTATION DISPERSION AND DENSITY IMAGING

In order to resolve crossing fibers and to distinguish changes in axonal density from changes in fiber organization, more advanced modelling approaches have been developed (Descoteaux, 2015; H. Zhang et al., 2012a). As these models involve complex mathematics and more degrees of freedom than DTI, a higher number of diffusion-weighted images must be acquired. The number of acquired directions (i.e., angular resolution), the number of b-values (i.e., shells), or both can be increased (Descoteaux, 2015). Several models were developed to overcome the limitations of DTI (e.g., composite hindered and restricted water diffusion model; CHARMED, minimal model of white matter diffusion; MMWMD and neurite orientation dispersion and density imaging; NODDI). These models integrate more compartments (i.e., 3 or 4) than the DTI model, providing a more realistic representation of tissue organization. However, some of these models (e.g., CHARMED and MMWMD) represent axons as parallel cylinders, an assumption that is rarely met outside the highly coherent WM tracts such as the corpus callosum.

The NODDI model requires high angular sampling resolution of one or multiple shells (i.e., single-shell HARDI and multi-shell HARDI) (Descoteaux, 2015; H. Zhang et al., 2012a). NODDI is a three-compartment tissue model that comprises an intracellular compartment, where diffusion is restricted, an extracellular compartment, where diffusion is hindered by surrounding neurites (i.e., “projections of neurons”, comprising axons and dendrites), and a CSF compartment, where diffusion is isotropic (H. Zhang et al., 2012a). The following equation describes the total normalized signal:

$$A = (1 - v_{iso})(v_{ic}A_{ic} + (1 - v_{ic})A_{ec}) + v_{iso}A_{iso}, \quad (\text{Eq. 7})$$

where A_i and v_i are the signal and volume fraction of each compartment and the *iso*, *ec* and *ic* subscripts denote the isotropic (i.e., CSF-filled), extracellular, and intracellular compartments, respectively.

The development of NODDI builds on other advanced DWI models with a higher number of compartments, but the NODDI model, unlike CHARMED and MMWMD, does not assume a parallel fiber orientation (H. Zhang et al., 2012a). Instead, a Watson distribution is used to model the orientation distribution of nonparallel axons, with organizations ranging from high to low dispersions (H. Zhang et al., 2011, 2012a). The intracellular compartment is represented as sticks of zero radius, to model the highly restricted diffusion perpendicular to the axon and the unhindered diffusion along the axon (H. Zhang et al., 2012a). These sticks are oriented at varying degrees of dispersion around a mean orientation (μ). The orientation dispersion index (OD) is a measure of the extent of dispersion around μ that ranges from 0 to 1, where an OD = 0 indicates perfectly parallel cylinders and OD = 1 indicates perfectly isotropic diffusion. A sample of orientation dispersions, from the Watson distribution, is illustrated in **Figure 5**, with different OD around the mean orientation (represented by the vertical axis). Diffusion in the extracellular compartment is hindered by surrounding neuronal structures and is thus modelled as a Gaussian anisotropic process (H. Zhang et al., 2012a). Lastly, diffusion in CSF-filled spaces (d_{iso}) is modelled as a Gaussian isotropic process (H. Zhang et al., 2012a). The intracellular diffusivity parallel to the axon (d_{\parallel}) and isotropic diffusivity (d_{iso}) can be approximated from known typical *in vivo* values (i.e., $3.0 \times 10^{-9} \text{ mm}^2\text{s}^{-1}$ and $1.7 \times 10^{-9} \text{ mm}^2\text{s}^{-1}$, respectively), and are thus input as fixed parameters in the model (H. Zhang et al., 2012a). Reducing the number of unknown parameters enables estimation of other parameters by ensuring the system is well-determined.

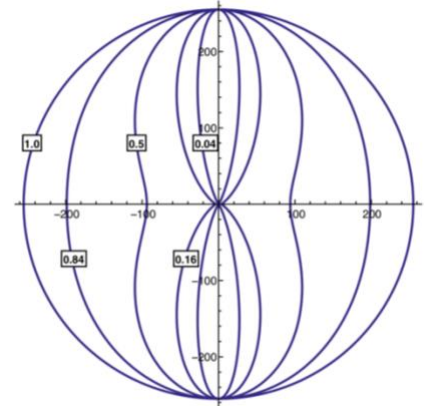


Figure 5. Sample of OD from the Watson distribution, with OD ranging from low to high dispersion around the mean orientation μ , represented by the vertical axis (OD \in {0.04, 0.16, 0.5, 0.84, 1.0}). From Zhang et al., 2012.

Two metrics derived from NODDI are of particular interest: neurite density, given by v_{ic} , and the orientation dispersion index (OD). In coherently organized WM tracts, such as the corpus callosum, v_{ic} is high and OD is low (which corresponds to high FA) (H. Zhang et al., 2012a). In areas of fanning and crossing fibers however, OD values are higher while v_{ic} values remain similar, as neurite density shows very little variation across healthy WM, though it may decrease in age and disease (e.g., Gozdas et al., 2021). These two metrics thus allow to distinguish changes in WM fiber density from changes in fiber organization (see **Figure 6**). This is highly pertinent in the investigation of learning-induced neuroplasticity, as well as in investigating changes associated with aging and different disorders affecting WM (Kodiweera et al., 2016; Schneider et al., 2017; Tavor et al., 2013). While FA is affected to a greater extent by OD (i.e., strong negative correlation with FA), changes in v_{ic} alone (i.e., weak positive correlation with FA), or in combination with changes in OD, may also lead to alterations in FA. This highlights the importance of specific metrics, such as OD and v_{ic} , to disentangle factors contributing to FA. In grey matter, OD is higher and neurite density lower than in WM. In CSF-filled cavities such as ventricles, the diffusivity corresponds to d_{iso} , OD is very high (i.e., near 1) and v_{iso} is high, while other volume fractions are low (H. Zhang et al., 2012a).

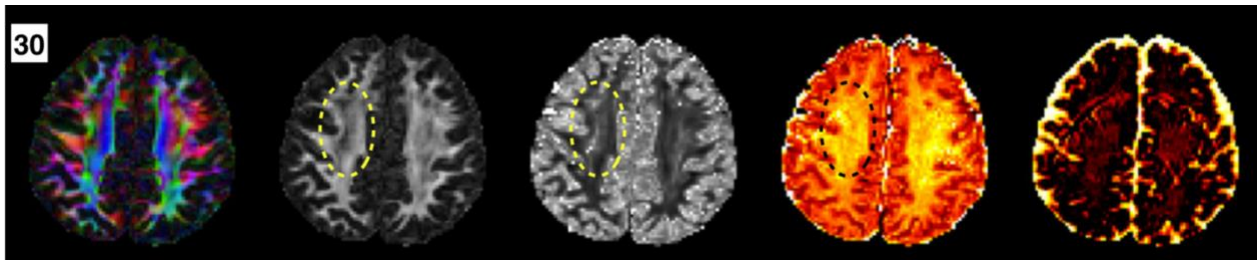


Figure 6. From left to right: Principal direction color map, FA, OD, v_{ic} , and v_{iso} maps. Area of crossing fibers in the centrum semiovale (in region encircled by yellow and black dashed lines) showing lower FA values corresponding to higher OD values, while v_{ic} remains high at that location (encircled by black dashed line). Modified from Zhang et al., 2012.

The NODDI model provides WM metrics of greater sensitivity and specificity than DTI (G. Adluru et al., 2014; Kodiweera et al., 2016; Pines et al., 2020; Schneider et al., 2017; H. Zhang et al., 2012a). Histology has shown that NODDI provides accurate measures of orientation dispersion and neurite density, even in areas of crossing fibers (Jespersen et al., 2010, 2012; Seppehrband et al., 2015). NODDI aims at quantifying neurite density and orientation dispersion but not axonal diameter, which is entirely absent from this model since it assumes sticks of zero radii (H. Zhang et al., 2012a). Zhang and colleagues (2012) have however showed that this simplification does not impact the accuracy of neurite density and orientation dispersion estimations and allows for shorter

acquisition and computational times. Another limitation of NODDI is that a single mean orientation (and a single summary measure of neurite density) can be estimated per voxel. For this reason, NODDI is not the preferred method for tractography or if fibre-specific information is desired, in which case methods such as spherical deconvolution should be used instead (Daducci et al., 2014, 2015).

CONSTRAINED SPHERICAL DECONVOLUTION

Spherical deconvolution (SD) methods use high angular resolution imaging (HARDI) to model multiple fiber orientations per voxel, overcoming one of the main limitations of DTI and NODDI: the crossing fibers “problem” (see **Figure 7**) (Dell’Acqua & Tournier, 2019). Initially thought of as an issue affecting just a few problematic areas, the extent of WM voxels in which more than one fiber populations are present has recently been estimated at about 70-90% of the entire WM (Jeurissen et al., 2013; Riffert et al., 2014). The capacity to model multiple fibers is thus essential to

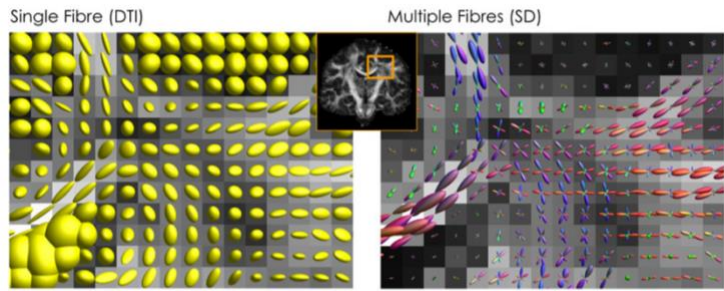


Figure 7. On the left, ellipsoids from the DTI model provide directional information for a single orientation per voxel. On the right, fiber orientation density functions (fODFs) from spherical deconvolution (SD) model multiple fiber directions. From Dell’Acqua & Tournier, 2019.

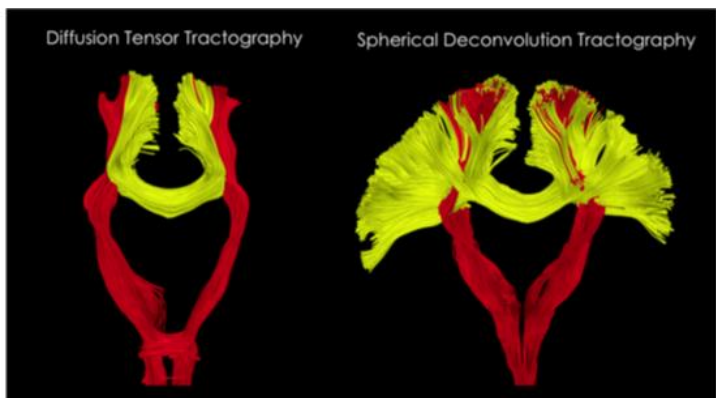


Figure 8. Tractography performed with DTI (left) and SD (right) is shown. From Dell’Acqua & Tournier, 2019.

accurately estimate microstructural parameters and to map complex fiber organization with tractography (see **Figure 8**) (Dell’Acqua & Tournier, 2019). SD methods rely on the principle that the DWI signal reflects the ensemble of fiber populations present in a voxel (Jeurissen et al., 2014). The DWI signal can be expressed by the convolution of the fiber orientation density function (fODF) and of the response function, which is the typical DW signal profile of a given tissue type:

$$DW \text{ signal} = \text{response fct} * fODF, \text{ (Eq. 8)}$$

where $*$ denotes a convolution. Spherical deconvolution of the response function from the measured DWI signal can thus be performed to obtain the fODF. The response function is estimated directly from the DW signal, using a brain segmentation to define volume fractions of each tissue type at each voxel. SD can estimate all the fiber populations present in a voxel, regardless of the number (Jeurissen et al., 2014). Spherical harmonic basis functions, which are functions defined on the surface of a sphere, are frequently used to in SD. When performing SD, coefficients in this SH basis are obtained and stored in the “Fiber orientation distribution (FOD) image”. Similar to the ellipsoid from DTI, a representation of the fiber populations can be visualized (see **Figure 9**).

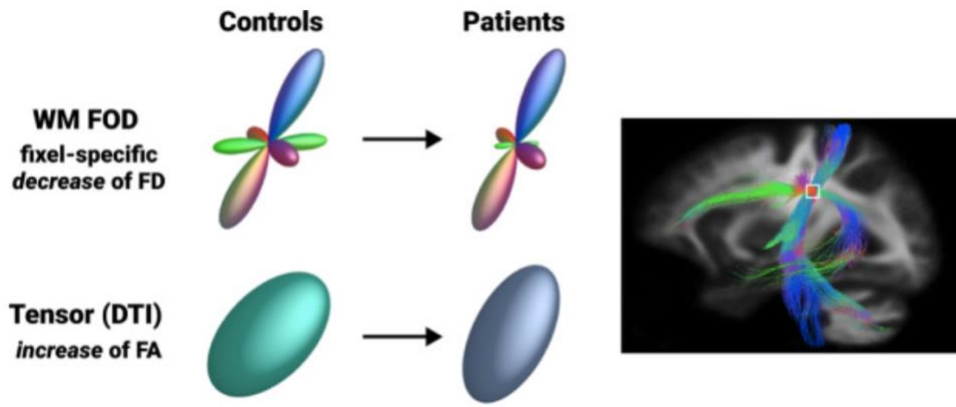


Figure 9. The WM FOD, which shows the orientation and density of every fiber population in a voxel, is illustrated. The impact of lower fibre-specific FD in patients vs controls is shown in both the WM FOD and the ellipsoid from DTI. The higher FA in patients could be interpreted as higher white matter “integrity” if only DTI is used, even though patients experienced a loss in density in a fiber running orthogonal to the main direction. From Dhollander et al., 2021.

Initially, SD techniques could only be applied to single-shell DWI data and yielded fODFs that were only accurate in voxels containing pure WM (Jeurissen et al., 2014). In voxels with partial voluming, inaccuracies occur because the WM response function does not reflect the signal profile of other tissues such as GM and CSF. Recently, the method has been expanded to multi-shell data, taking advantage of the b-value dependency of each tissue to estimate tissue-specific ODFs. This method is called multi-shell multi-tissue CSD (MSMT-CSD). The signal equation then becomes:

$$DW \text{ signal} = (WM \text{ response fct} * fODF) + (GM \text{ response fct} * GM \text{ ODF}) + (CSF \text{ response fct} * CSF \text{ ODF}), \quad (\text{Eq. 9})$$

Because SD is an ill-posed problem, a non-negativity constraint is added to reduce noise sensitivity, giving rise to constrained SD, or CSD (Tournier et al., 2007). CSD has led to improvements in tractography as well as the introduction of new quantitative measures of WM microstructure such

as apparent fibre density (AFD), which is proportional to the intra-axonal volume (Jeurissen et al., 2014). A minimum of 3 shells (including a b-zero shell) is required to model the three main tissue types (WM, GM, and CSF). A fourth shell allows to also compute subcortical GM. Because low diffusion gradients are mostly sensitive to the extra-axonal space, one of the shells should have a value of $\geq 2500\text{-}3000\text{s/mm}^2$ to ensure that the AFD estimated accurately reflects the intra-axonal volume (Jeurissen et al., 2014). Other metrics such as fiber cross-section (FC) and a combined measure of fiber density and cross-section (FDC) were also introduced (see **Figure 10**) (Dhollander, Clemente, et al., 2021; Raffelt, Tournier, et al., 2017). Most importantly, CSD can provide information at a sub-voxel resolution, yielding measures for each fiber population (*fixel*; or fiber element) within voxels. The fibre-specific measures obtained through this framework, called *fixel-based analysis*, are thus highly specific.

In a popular implementation of MSMT-CSD, tissue-specific response functions are computed from the multi-shell DWI data and tissue segmentations (typically obtained from a T1-weighted structural image) (Jeurissen et al., 2014; S. M. Smith, 2002). Multi-tissue CSD of the response functions from the DWI data is then performed to obtain FODs (Eq. 9). A population template is created from the subjects' FODs, and subject's FODs are then registered and warped to the template space (Dhollander, Clemente, et al., 2021; Raffelt, Tournier, et al., 2017). *Fixels* are segmented from the

FOD template, where each peak is interpreted as a fiber population. This determines the *fixel grid*. The WM FOD of each subject is then segmented to identify *fixels*' location and their AFD (which will subsequently be referred to as FD). FD is defined by the amplitude of the FOD (FOD lobe integral) and is a measure of microstructural axonal loss/gain. Individual subjects' *fixels* are then reoriented and mapped to the *fixel grid*. The cross-sectional size of the bundle (FC) is then estimated from the warps computed in the previous step (Raffelt, Tournier, et al., 2017). FC can be

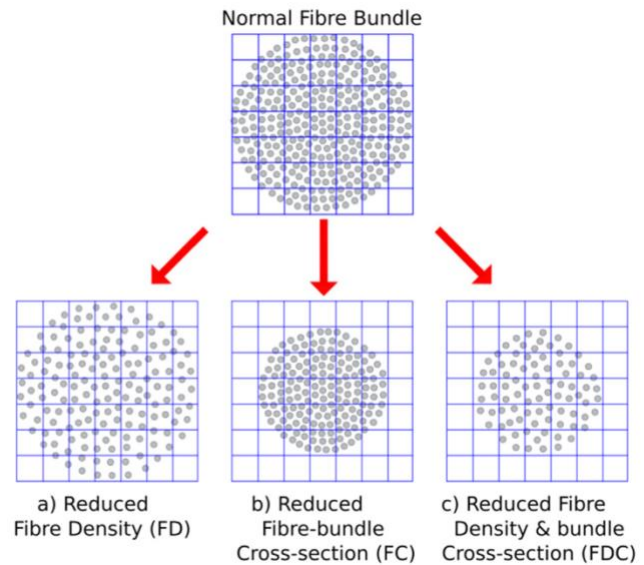


Figure 10. Axons (grey circles) comprised in a fiber bundle within a voxel (grid) are illustrated. In the bottom left, a loss in the number of axons results in decreased FD. In the middle, FC is decreased. In the bottom right, both FD and FDC are decreased, which is reflected by reduced FDC. From Raffelt et al., 2017.

conceptualized as the amount of expansion or contraction orthogonal to the fibre direction necessary to align to the template. It is a measure of macroscopic differences that would result from atrophy or tract swelling for instance. Lastly, a combined measure of fibre density and cross-section (FDC), calculated as $FD \cdot FC$, yields a measure that represents the total information carrying capacity. It has been shown to be more sensitive than FD or FC alone, although a complete picture can only be obtained by using all three metrics together. For instance, edema without axonal loss would result in increased FC, decreased FD, and unchanged FDC (Raffelt, Tournier, et al., 2017). In this example, edema could not be captured using the FDC metric alone.

The *fixel-based analysis* (FBA) framework has emerged in recent years as a solution to the main problems of DTI which yields metrics that are highly unspecific. In addition to being much more specific, FBA metrics have also been shown to be more sensitive (Adanyeguh et al., 2018), especially in crossing fibres regions (Raffelt et al., 2015). Further, since MSMT-CSD requires multiple shells and high b-values, the intra-axonal compartment can be directly estimated and the impact of other compartments (i.e, GM and CSF) is explicitly taken into account, resulting in more accurate fibre estimations (Jeurissen et al., 2014). NODDI also allows modeling of the intra-axonal compartment, providing more specific information than DTI, but like DTI, a single fibre orientation can be estimated at each voxel. MSMT-CSD thus provides highly specific information on each individual fibre bundle contained in a voxel. However, FBA metrics cannot differentiate changes in axon count from changes in axon diameters. Like other DWI techniques, CSD is also not specific to myelin (Jeurissen et al., 2014). The following section introduces myelin-sensitive techniques.

1.3.3 Magnetization transfer imaging

PRINCIPLES OF MAGNETIZATION TRANSFER IMAGING

Magnetization transfer imaging (MTI) allows for the indirect estimation of myelin content in the brain *in vivo* using the binary spin-bath model (i.e., two pools model). Because of their ultra-short transverse relaxation times ($T_2 < 100 \mu\text{s}$), macromolecules such as myelin cannot be imaged directly (Campbell et al., 2018; Sled & Pike, 2001). However, myelin can be imaged indirectly by

saturating the macromolecular pool (i.e. bound protons), which will then interact with free water protons, producing an effect on the MR-visible pool (Sled & Pike, 2001; Wolff et al., 1991). In a typical MRI sequence, the radiofrequency excitation pulse applied at Larmor frequency (ω_0) targets the free water pool. Conversely, in MTI, a specially designed off-resonance RF pulse, termed the MT pulse, is used to excite the macromolecular pool, causing its saturation (see **Figure 11**) (Helms, Dathe, Kallenberg, et al., 2008; Seeger et al., 2003). The saturated macromolecular pool then releases energy to the “lattice”, which, in this case, is the unexcited nuclei in the free water pool. This drives the free pool to a higher energy state which results in a greater number of spins down and thus in decreased net magnetization. This magnetization transfer from the saturated “bound” pool to the free water pool occurs through dipole-dipole interactions and chemical exchange, collectively referred to as cross-relaxation (Wolff et al., 1991; Yarnykh & Yuan, 2004). An on-resonance RF pulse is then applied to the free water pool, which now has a reduced net magnetization. This results in reduced signal compared to the same pulse sequence without a saturation pulse (Helms, Dathe, Kallenberg, et al., 2008). Because macromolecular content varies substantially across the brain, MTI offers high contrast between tissues (De Boer, 1995). MT contrast is more sensitive to lipids (the main constituent of myelin, axonal membranes, neurofilaments, and glial cells), than to proteins (Kucharczyk et al., 1994; Laule et al., 2007). For this reason, MTI is most commonly used to measure myelin content. The greater the macromolecular content in tissue, the greater the degree of interaction, or exchange, with the free water pool (i.e., MT effect), which is observed as a reduction in MR signal (De Boer, 1995).

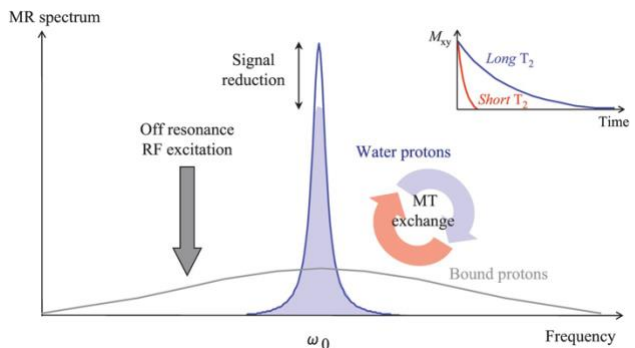


Figure 11. Schematic representation of excitation of the macromolecular pool, which has a short T_2 and a broad resonance line shape, with an off-resonance pulse. ω_0 = Larmor frequency. From McRobbie et al., 2017.

MTI ACQUISITION

The basic acquisition scheme in MTI (see **Figure 12**) involves the combination of preparatory MT pulses with either a gradient echo (GE) or spin-echo sequence (Helms, Dathe, Kallenberg, et al., 2008; Pike, 1996; Pike et al., 1993). As each MT pulse only partially saturates the bound pool, pulses

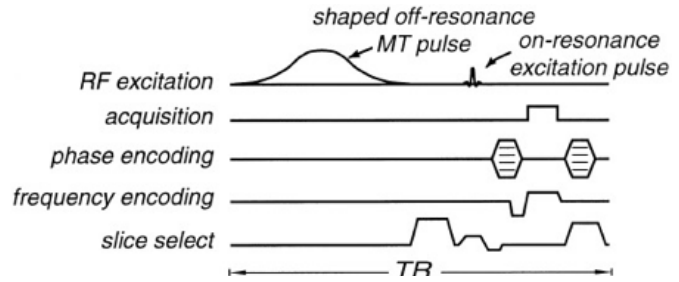


Figure 12. Basic acquisition scheme: first a shaped off-resonance MT pulse is applied, followed by a spoiled gradient echo sequence. From Sled & Pike, 2001.

must be repeated at a frequency high enough, relative to the cross relaxation rate, to achieve saturation (Pike, 1996). Most commonly, a spoiled GE sequence is used (SPGE or FLASH; Fast Low Angle Shot), allowing for a fast acquisition (Helms, Dathe, Kallenberg, et al., 2008; Melki & Mulkern, 1992; Pike, 1996). The FLASH sequence employs a small flip angle ($\alpha < 15^\circ$) and short TR ($TR \ll T1$) to induce a steady-state signal with minimal T1-weighting (Helms, Dathe, Kallenberg, et al., 2008). Spoiling is used to remove steady-state magnetization remaining in the transverse plane (M_{xy}), allowing for more magnetization to be available (i.e., in the longitudinal plane) for the next excitation, thus resulting in higher signal (Helms, Dathe, Kallenberg, et al., 2008; Pike, 1996; Pike et al., 1993). In order to measure the magnitude of the MT effect, an acquisition with a preparatory MT pulse (MT-w) and one without MT pulse (proton density weighted; PD-w) are required (Lema et al., 2017; Wolff et al., 1991).

Several MTI techniques have been developed over the years and allow for the calculation of various MT-based parameters. Two approaches will be described in the following sections: the MT ratio (MTR) and the MT saturation index.

MAGNETIZATION TRANSFER RATIO

The MTR metric provides a measure of the magnitude of the MT effect, and thus of macromolecular content in tissue (Wolff et al., 1991). The advantage of this MT-based parameter is that only two SPGE acquisitions are necessary – a MT-on and a MT-off (PD-w) image. The ratio can then be calculated simply by subtracting the signal of the MT-w acquisition (S_{MT}) from the signal of the PD-w acquisition (S_0) and dividing by S_0 (see Eq. 10) (Lema et al., 2017). This is also illustrated in **Figure 13**.

$$MTR = (S_0 - S_{MT})/S_0, \quad (\text{Eq. 10})$$

Higher macromolecular content leads to more signal attenuation (S_{MT}) which results in a higher MTR (Helms, Dathe, Kallenberg, et al., 2008). MTR has been found to increase during development as fiber tracts undergo myelination (Rademacher et al., 1999) and to decrease in demyelinating disorders such as MS, indicating myelin loss in both normal-appearing WM (NAWM) and lesions (Filippi et al., 1995; Lema et al., 2017). The interpretability of the MTR is however limited because of its dependence on longitudinal

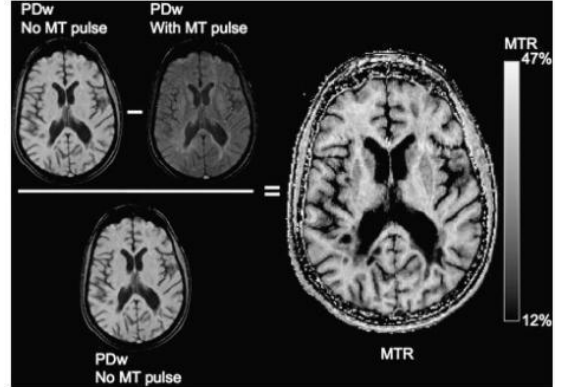


Figure 13. Diagram of how MTR is calculated from a PD-weighted image and a MT-weighted image. The resulting MTR map is shown on the right. From Fox et al., 2011.

relaxation (T_1), B_1 inhomogeneities, and the choice of MT pulse parameters (frequency offset, shape, and bandwidth) (Helms, Dathe, Kallenberg, et al., 2008). For instance, increases in T_1 due to edema in some MS lesions can mask myelin loss, since T_1 and macromolecular content have opposite effects on the MTR (Levesque et al., 2005). For these reasons, more complex metrics that take those confounding effects into account have been developed.

MAGNETIZATION TRANSFER SATURATION

The MT saturation (MTsat) index is another MT-based parameter in which RF inhomogeneities and T_1 dependence are reduced. The MTsat index represents the percentage of saturation transmitted by one MT pulse during the TR (Helms, Dathe, Kallenberg, et al., 2008). To compute this index, a T_1 -w image must be acquired in addition to the two SPGE acquisitions (MT-on and MT-off). A B_1 map may also be acquired to correct for B_1 inhomogeneities (Helms, Dathe, Kallenberg, et al., 2008). The saturation term (δ), the reduction in steady-state signal caused by the saturation effect of one MT pulse, can be calculated from the following signal equation (S_{MT}):

$$S_{MT} \cong A \alpha \frac{R_1 TR}{\alpha^2/2 + \delta + R_1 TR}, \quad (\text{Eq. 11})$$

where A , the amplitude of the signal when fully relaxed longitudinally, and R_1 , the relaxation rate, can be calculated from the signal of the non-MT-w sequences (S_{PD} and S_{T1}) of different flip angles and TR. The metric of interest, δ , a dimensionless value typically expressed as a percentage, is then calculated with the following equation:

$$\delta_{app} = \left(\frac{A_{app}\alpha}{S_{MT}} - 1 \right) R_{1app}TR - \alpha^2/2, \quad (\text{Eq. 12})$$

Since the flip angle and relaxation rate (R_1) are taken into account separately in the signal equation, the MTsat index is independent of those parameters and is thus a more specific measure of the magnetization exchange occurring between the bound and free water pool due to macromolecular content (e.g., myelin) (Helms, Dathe, Kallenberg, et al., 2008; Lema et al., 2017). Another advantage of this parameter is that it yields maps with improved contrast between WM and grey matter (GM), where δ values are highest in WM, lower in GM and close to zero in CSF-filled spaces such as ventricles (**Figures 14 and 15**). For this reason, Helms and colleagues (2008) have suggested that MTsat maps may be used for brain segmentation. MTsat is clinically feasible and has been shown to be more sensitive than MTR in assessing tissue damage in MS patients (Helms, Dathe, Kallenberg, et al., 2008; Lema et al., 2017). An MS study comparing these MTI-based metrics has found that disability scores correlate with MTsat in NAWM and in lesions, in both the brain and spinal cord, while MTR correlated to disability only in brain lesions, but not in NAWM nor in any cervical regions (Lema et al., 2017).

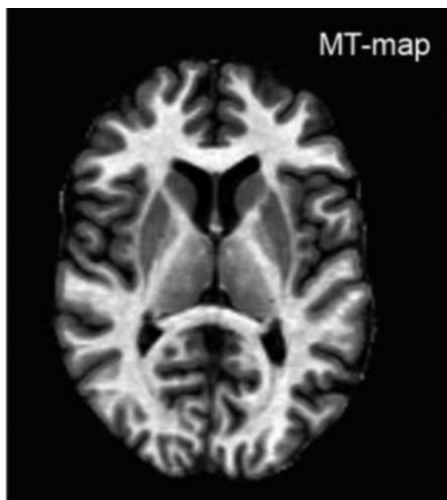


Figure 14. MTsat map shows good contrast between WM and GM. The contrast is especially improved for the U-fibers, and for the WM tracts connecting to the globus pallidus and thalamus (internal capsule). Modified from Helms et al., 2008.

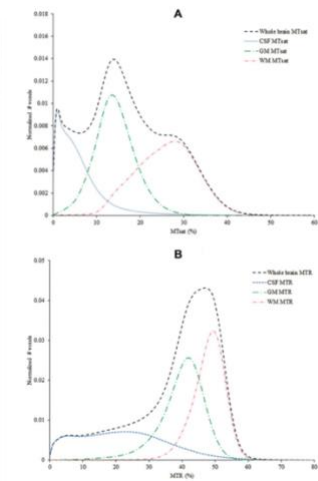


Figure 15. The histogram of the top panel shows clear separation between the WM (red) and GM (green) modes in MTsat, evidenced by a deeper trough compared to the MTR histogram (bottom panel). From Lema et al., 2017.

However, a limitation of this model is that the MTsat index represents only a fraction of the bound spins since this metric measures the effect of a single MT pulse while several pulses are necessary

to saturate the entire macromolecular pool (Helms, Dathe, Kallenberg, et al., 2008). Furthermore, even though the impact of RF inhomogeneities and T_1 relaxation are mitigated, MT_{sat} is still dependent on some sequence parameters, especially those relating to the MT pulse. For instance, MT saturation increases with the energy of the MT pulse, which depends on its flip angle and duration. However, particular attention must be paid in order not to exceed the specific absorption rate (SAR) limits when using MT pulses of high energy. The choice of MT pulse frequency offset also influences measures of MT_{sat} (Helms, Dathe, Kallenberg, et al., 2008). MT pulses of low frequency offsets (i.e., 1 kHz) generate greater saturation, but direct RF energy absorption (i.e., by the free water pool) may occur. Ensuring the frequency of the MT pulse is far enough from Larmor frequency is therefore important to prevent direct absorption as the effects of direct saturation cannot be distinguished from magnetization transfer. However, if the frequency offset is too large, the amount of saturation is reduced. A frequency offset of 2.2 kHz is considered optimal and is thus typically used (Helms, Dathe, Kallenberg, et al., 2008; Lema et al., 2017).

1.3.4 Multi-parametric mapping

PRINCIPLES OF MULTI-PARAMETRIC MAPPING

Multi-parametric mapping (MPM) uses an optimized protocol consisting in the acquisition of multi-echo data with different weightings to derive four quantitative maps of tissue microstructure: proton density (PD), (effective) transverse relaxation rate $R2^*$, longitudinal relaxation rate $R1$, and MT_{sat} . Relaxometry principles are leveraged to estimate relaxation rates and PD. Relaxometry is a technique whereby multiple measurements with different parameters (i.e., different echo times for T_2 and different inversion times for T_1) allow the characterization of signal relaxation after the RF pulse and thus estimation of relaxation times (and rates). Longitudinal (T_1) relaxation refers to the magnetization returning toward its initial position (M_z), precessing around the static B_0 field, and occurs due to energy transfer with the surrounding “lattice” (i.e., spin-lattice relaxation) (Westbrook & Talbot, 2018). T_1 is the time it takes for the net magnetization to reach about 63% of M_z (**Figure 16**). On the other hand, transverse relaxation refers to the dephasing of transverse components of magnetization due to interactions with neighboring spins (i.e., spin-spin relaxation). T_2 is the time it takes for transverse magnetization (M_{xy}) to decay to about 37% of the initial M_{xy} (**Figure 16**). Once relaxation times are estimated, relaxation rates can easily be calculated (e.g., $R1=1/T1$). Proton density (PD) refers to the number of hydrogen protons per unit volume and is a

measure of the total amount of available signal (Westbrook & Talbot, 2018). The last parameter, MT_{sat} , is the attenuation resulting from one MT pulse and is proportional to the size of the macromolecular pool (Helms, Dathe, Kallenberg, et al., 2008). MT has been discussed in detail in the previous section.

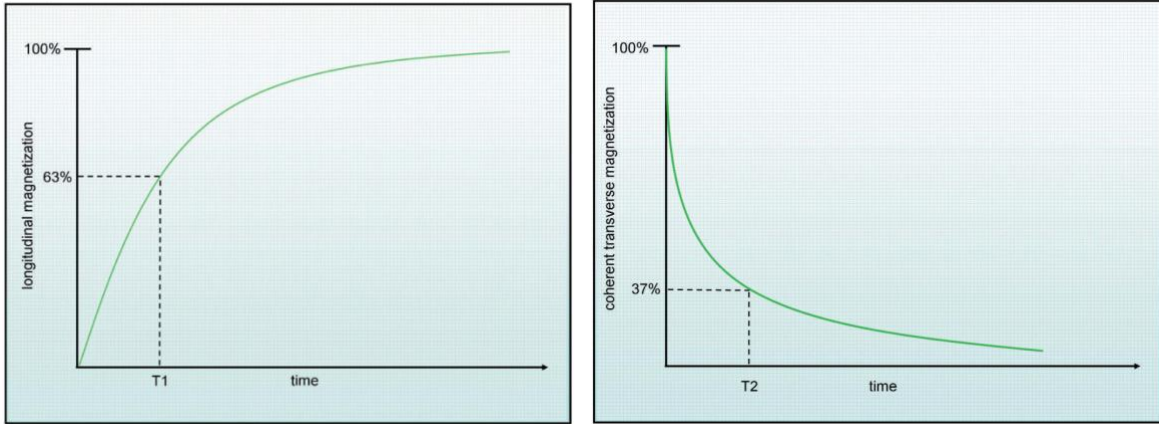


Figure 16. Left: T_1 recovery curve. Right: T_2 decay curve. From Westbrook & Talbot (2011).

MPM ACQUISITION AND PARAMETERS ESTIMATION

Three spoiled multi-echo 3D fast low angle shot (FLASH) acquisitions with predominant PD (8 equidistant echoes), T_1 (6 echoes), and MT weighting (6 echoes) are required for MPM (Weiskopf et al., 2011). The repetition time (TR), and flip angle (α) are manipulated to obtain different weightings. A RF transmit field map (B_1) and a static magnetic (B_0) field map are also acquired to correct for field inhomogeneities. As described in the section on MT_{sat} above, an MT pulse is applied prior to excitation to achieve MT-weighting.

The R_2^* map is calculated by performing a linear regression from the logarithm of the signal intensities at different echo times (using the 8 PD-weighted echoes) (Weiskopf et al., 2013). The six first echoes of each scan are averaged to increase SNR. The three average images are then used to calculate MT_{sat} , the signal amplitude (A), and apparent R_1 using the Ernst equation that describes FLASH signals. Effective PD^* is obtained by correcting the signal amplitude (A) for global and local receive sensitivity differences. The PD map obtained is said to be effective because, since the average across multiple echoes was used (effective TE = 8.45ms) to calculate PD, and it was not extrapolated to TE=0, the PD measure obtained is still partly dependent on R_2^* .

PD* maps are scaled to standardize the mean PD* in WM to the published value of 69%. This step ensures PD* maps are comparable across participants. Quantitative R1 maps are calculated by correcting the apparent R1 maps for local RF transmit field inhomogeneities and for imperfect RF spoiling. Lastly, MTsat maps, computed from the averaged MT-w and PD-w scans, are corrected for local RF transmit field (i.e., flip angle).

QUANTITATIVE MAPS

MPM yields quantitative parameters that are highly specific to macromolecular, myelin and iron content (**Figure 17**) (Callaghan et al., 2014; Weiskopf et al., 2013). R1 depends mainly on the mobility of water, it is thus higher in WM regions that have higher myelin content (bound pool of low mobility) but is also increased by iron, especially in iron-rich subcortical regions (Callaghan et al., 2014). PD*, the amount of observable free water, shows the opposite pattern with low PD* values in WM, especially in highly myelinated regions. R2* is specific to iron content. Iron accumulation, observed as increased R2* is frequently reported in the basal ganglia and hippocampus in aging (Bartzokis et al., 2007; Callaghan et al., 2014; Rodrigue et al., 2013). Myelin content is most accurately quantified by MTsat. However, myelination is a complex process that also involves iron as the cells responsible for myelin production and repair, oligodendrocytes, contain a high level of iron and require iron to sustain their metabolism. The concurrent use of all four parameters is thus highly pertinent in disentangling these aging-related processes (Callaghan et al., 2014). For instance, increased R2* with normal or maintained R1 levels may indicate an increased concentration in iron-rich oligodendrocytes as oligodendrocytes are actively working to maintain myelin levels. On the other hand, increased R2* with reduced MTsat suggest higher iron levels are rather a result of iron being released from damaged oligodendrocytes which then leads to impaired myelination. Lastly, a reduction in R2*, R1, and MTsat is likely to reflect later-stage loss of oligodendrocytes (and of its iron) and demyelination as R1 is dependent on both myelin and iron (Callaghan et al., 2014).

MPM yields measures that are comparable across sites and time points, making longitudinal studies and data harmonization in multi-center studies more reliable (Weiskopf et al., 2013). Long scan times (~20 min) are however required, which may be challenging for some populations. Further, MPM acquisition requires high gradient performance and multi-channel RF receive coils (Weiskopf et al., 2013).

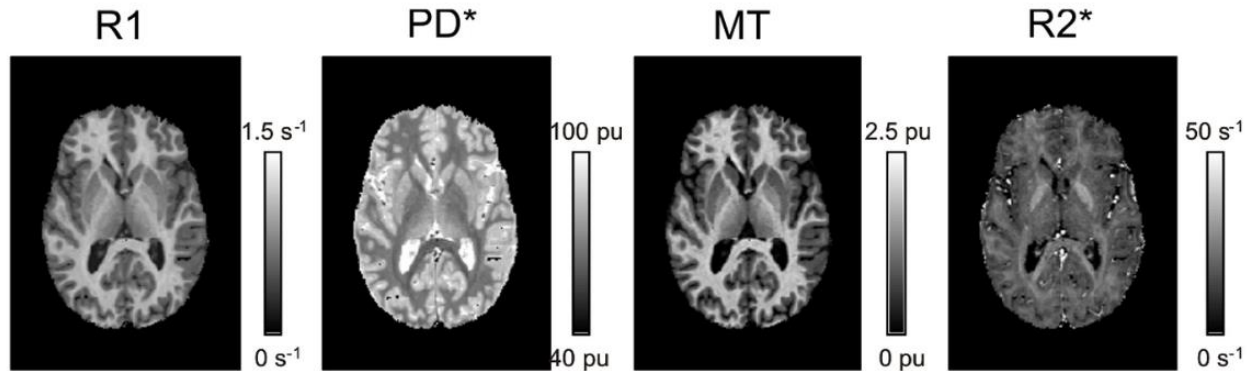


Figure 17. Quantitative maps from MPM. R1: longitudinal relaxation rate; PD*: effective proton density; MT: magnetization transfer saturation index; R2*: effective transverse relaxation rate.

1.3.5 Integrating multiple MRI measures with multivariate approaches

As shown in previous sections, each WM imaging technique can provide some insight into the underlying microstructure, but each technique also suffers from its own limitations. For instance, DWI techniques are sensitive to several aspects of the brain’s WM, including axonal density, diameter, and organization, as well as myelination. However, although changes in myelin content alter the DWI signal, as myelin constitutes an additional barrier to diffusion, these techniques cannot measure the water trapped in myelin sheaths because of its short transverse relaxation time. This limitation of DWI is what makes myelin-sensitive techniques relevant. Using MTI in conjunction with diffusion MRI provides rich information on myelin thickness as well as on axonal properties, which are both important for optimal neural conduction in the central nervous system. Lastly, using MPM, in addition to MTI and diffusion MRI techniques, allows to disentangle myelin and axonal changes, as well as detect the presence of iron, which is useful in monitoring pathological progression in age-related neurological disorders and assessing the efficacy of treatments.

Further, biophysical models used to map tissue microstructure to the MRI signal (e.g., DTI, NODDI) comprise a certain set of assumptions (Novikov et al., 2018). The metrics derived from each of these models are thus imperfect representations of the underlying tissue properties, biased by these assumptions. Because a perfect one-to-one mapping between tissue property and MRI metric does not yet exist (i.e., a change in myelin will be reflected by a change in FA, R1, and MTsat, and conversely, a change in FA could be due to a change in fiber dispersion or in fiber density), multi-modal imaging has emerged as a potential avenue to address the lack of specificity

of imaging-derived metrics (Tardif et al., 2016). Using several MRI metrics from different WM imaging models it is possible to leverage the strengths of each approach while mitigating their weaknesses and allowing for a more holistic and mechanistic characterization of tissue microstructure. However, to avoid multiple comparisons problems and retain statistical power, reducing data dimensionality through multivariate approaches is necessary (Avants, Duda, et al., 2008; Naylor et al., 2014; Owen et al., 2021).

Multivariate approaches that combine MRI metrics have been used in various contexts. At the group level, partial least squares (PLS) analyses and their variants assess the covariance between multiple measures (Khedher et al., 2015; Nestor et al., 2002). Other group-level multivariate techniques include principal component analysis (PCA), Sparse Group Lasso, independent component analysis (ICA), and non-negative matrix factorization (Calhoun et al., 2001; Chamberland et al., 2019; Khedher et al., 2015; Plitman et al., 2020; Richie-Halford et al., 2021; W. Yang et al., 2011). At the individual level, interregional correlations of multiple measures can be used to create individual-specific network maps based on morphometric similarity, which can then be linked to behavior (Seidlitz et al., 2018). These individualized network maps offer a comprehensive structural mapping that captures both biological complexity and individual variability by integrating multiple MRI features (Vandekar et al., 2016; Whitaker et al., 2016).

However, in some of these approaches, the shared covariance between MRI measures is not accounted for (e.g., [Seidlitz et al., 2018](#)). This has the potential to bias inferences made from such analyses, as there is significant covariance among commonly used imaging parameters (Carter et al., 2022; Uddin et al., 2019). Various multivariate approaches address this issue, including multivariate linear regression (Naylor et al., 2014; Young et al., 2010), machine-learning (Calhoun et al., 2001; Carbonell et al., 2020; C. Chen et al., 2019; Guberman et al., 2022; Khedher et al., 2015; W. Yang et al., 2011), and Hotelling's T2 test (Avants, Duda, et al., 2008; Hotelling, 1947). Many of these methods, including multivariate linear regression and machine learning, are computationally expensive and some require making subjective decisions (Alexopoulos, 2010; Gyebnár et al., 2019; Hayasaka et al., 2006; Naylor et al., 2014). Hotelling's T2 test, a multivariate extension of a two-sample t-test, is a simple yet powerful option for group comparisons (Avants, Duda, et al., 2008; Hotelling, 1947), though it provides little insight at the individual level.

In contrast, the Mahalanobis distance (D2) offers an individual-level measure of deviation relative to a reference distribution, accounting for covariance between features (e.g., imaging metrics). Developed by P. C. Mahalanobis in 1936 to quantify racial similarities based on anthropometric skull measurements, D2 can be viewed as a multivariate z-score that accounts for metric-metric covariance (P. N. Taylor et al., 2020). D2 has been widely used in outlier detection, cluster analysis, and classification applications (Ghorbani, 2019; Kritzman & Li, 2010; Xiang et al., 2008). In neuroimaging, D2 has been used to detect lesions in neurological disorders (Gyebnár et al., 2019; Lindemer et al., 2015), and to evaluate abnormality in patients' brains relative to controls (Dean et al., 2017; Guerrero-Gonzalez et al., 2022; Owen et al., 2021; P. N. Taylor et al., 2020), as well as to study healthy WM development (Kulikova et al., 2015).

Despite their potential, these approaches are not frequently used to study WM changes in health and disease, likely due to their complexity and higher computational demands compared to univariate analyses (Alexopoulos, 2010; Gyebnár et al., 2019; Hayasaka et al., 2006; Naylor et al., 2014).

1.4 White matter changes as an early pathological process in age-related disease

WM changes have been reported as one of the earliest pathological processes in several age-related neurological disorders (N. Adluru et al., 2014; Araque Caballero et al., 2018; Bartzokis et al., 2003, 2004; Bronge et al., 2002; de la Monte, 1989; Roher et al., 2002). The myelin breakdown model posits that the disproportionately high WM volume and the very long myelination period of human brains could underlie the unique vulnerability of our species to neuropsychiatric and neurodegenerative disorders (Bartzokis, 2004b). Oligodendrocytes are particularly vulnerable to various insults due to the high metabolic demands of producing and maintaining myelin, which increases with age as the need for repair grows (Connor & Menzies, 1996; Wiggins, 1982). The capacity of oligodendrocytes to continually repair damaged myelin is a double-edged sword as iron-related toxicity increases with increased oligodendrocytes activity (Bartzokis, 2011). Because oligodendrocytes contain a high amount of iron, which is essential for its differentiation (Sow et al., 2006), increased myelin repair leads to higher brain iron levels and myelin breakdown results in iron release, in turn leading to greater toxicity (Bartzokis, 2011; Callaghan et al., 2014).

Myelination also depends on brain cholesterol levels since cholesterol is one of the main constituents of myelin (Bartzokis, 2004b). The dependence of the myelination process on such a wide array of factors (e.g., iron, cholesterol, and energy supply) means that any change in the supply or metabolism of these compounds, often due to environmental insults that can be exacerbated by some genetic variants, can start altering myelin's production and repair cycles and ultimately accelerate breakdown (Bartzokis, 2004b, 2011). This, along with the capacity of oligodendrocytes to continuously repair myelin through life, producing increasingly more fragile myelin sheaths, has been posited to underlie the particular vulnerability of oligodendrocytes and myelin. In this model, myelin is thus regarded as the “weakest link”, where myelin breakdown would result in network disconnection in addition to increased neurotoxicity that lead to further damage (Bartzokis, 2011; Lynch et al., 2000).

WM health declines with normal aging, but the damage is more pronounced in individuals with neurodegenerative diseases such as Alzheimer's disease (AD) and other types of dementia (Mayo et al., 2017). In AD and cerebral small vessel disease, factors such as iron overload, oxidative stress, and endothelial dysfunction disrupt oligodendrocyte function, leading to demyelination and axonal loss (Tranfa et al., 2024). The presence of WM abnormalities in AD is now well established, with several brain imaging studies reporting macrostructural (i.e., reduced WM volume) (Chaim et al., 2007; Hua et al., 2010; Im et al., 2008) and microstructural changes (i.e., decreased axonal diameter, axonal density and myelination) in AD patients (Bozzali et al., 2002; Huang et al., 2012; P.-N. Wang et al., 2012). We now know that pathological changes start occurring decades before symptom onset and diagnosis of AD (Beason-Held et al., 2013; Perl, 2010). Conditions such as hypertension, diabetes, and dyslipidemia, as well as risk factors such as physical inactivity and smoking, have been associated with more subtle changes in WM integrity and may thus constitute an earlier stage along the health – disease continuum (**Figure 18**) (Alfaro et al., 2018; Foley et al., 2014; Mole et al., 2020; R. Wang et al., 2015; O. A. Williams et al., 2019). Furthermore, genetic factors, and other non-modifiable risk factors that increase the likelihood of developing AD (e.g., female sex), also impact WM microstructure (Heise et al., 2011; Honea et al., 2009; Toschi et al., 2020). Characterizing the impact of these risk factors on the brain's WM has important implications in understanding the early phase of the disease which can aid in the design of more effective intervention strategies to prevent or slow down the progression of AD.

1.4.1 Dementia

Dementia (“de-”: deprivation or loss, “ment-”: mind, “ia”: state), as its etymological meaning suggests, is characterized by a loss of function, particularly cognitive functions like memory, as well as changes in behaviors and personality (H. D. Yang et al., 2016). Dementia is an umbrella term designating a collection of symptoms that can be caused by several different brain diseases. Alzheimer’s disease (AD) is the most common form of dementia, followed by vascular, Lewy body, frontotemporal, and Parkinson’s disease-related dementia (Cao et al., 2020; Ritchie & Lovestone, 2002). There is however a great amount of overlap in the neuropathology and predisposing factors between different dementia types (Fierini, 2020; Korczyn, 2002; Ritchie & Lovestone, 2002). In fact, it has been argued that cases of pure AD are rather rare and that dementia most often presents as a mixed pathology (Fierini, 2020). Evidence of a vascular contribution in the pathogenesis of AD supports this view (Fierini, 2020; Iturria-Medina et al., 2016). Many have thus embraced a more multi-factorial view of dementia, where a different set of pathologies can be present in different individuals diagnosed with the same type of dementia and similar pathologies can occur in individuals with different diseases.

In one of the predominant theories of Alzheimer’s disease, the disease is defined by the accumulation and deposition of amyloid- β (A β) plaques that are toxic to the brain (Kung, 2012). However, the presence of amyloid deposition in cognitively normal individuals, the lack of association between amyloid and cognitive performance, and the limited success of therapeutic approaches targeting amyloid that are only effective in specific subgroups and have several side effects, suggest amyloid is not the only etiology (Duchesne et al., 2024). Rather, AD would be caused by multiple concomitant and interacting factors (Iturria-Medina et al., 2017; Sheikh et al., 2013). The numerous pathological changes present in AD have given rise to just as many hypotheses and theories of AD. These include: amyloid- β and tau deposition, cerebrovascular changes, inflammation, oxidative stress, metabolic and mitochondrial dysregulation, as well as white matter degeneration (Duchesne et al., 2024). Genetic factors also come into play with the E4 allelic variant of the apolipoprotein E (APOE) gene being the strongest risk factor for AD after age (Yamazaki et al., 2019). In light of this, there has been a push for reframing AD as a complex and heterogenous disease with a multi-factorial etiology (Duchesne et al., 2024; Iturria-Medina et al., 2017).

Vascular risk factors (e.g., hypertension, hyperglycemia, dyslipidemia, etc.) have garnered a large amount of interest as they predispose not only to vascular dementia but also to Alzheimer's disease and other dementias (Z.-C. Chen et al., 2022; Fierini, 2020). Moreover, our relatively advanced knowledge on prevention and treatment of vascular conditions, makes them promising targets for interventions aimed at preventing dementia (Konwar et al., 2023; Korczyn, 2002). Because WM is less perfused than GM, and owing to the particularly high metabolic demands of oligodendrocytes, WM is particularly vulnerable to changes in perfusion and metabolism (Bartzokis, 2011; Connor & Menzies, 1996; Inoue et al., 2023; Wiggins, 1982).

The effect of the main AD risk factors – with an emphasis on cardiometabolic factors – on WM microstructure will be detailed in the following subsections.

1.4.2 High blood pressure

Hypertension is a known risk factor for AD and other forms of dementia, and several studies have documented its impact on WM, both at the macro- and microstructural levels (Gons et al., 2012; X. Li et al., 2015; Z. Li et al., 2023; Maillard et al., 2012; Rosano et al., 2015). Microstructural changes with hypertension are most often found in long-range fibers such as the anterior thalamic radiation (ATR) and inferior fronto-occipital fasciculus (IFOF), and WM lesions typically occur in the periventricular area (Z. Li et al., 2023). Importantly, reductions in WM integrity, often quantified as reduced FA and increased MD, in hypertensive individuals have been related to impairments in global cognition (Gons et al., 2012). These alterations in WM microstructure are also often accompanied by changes in the functional connectivity of networks connected by the affected tracts (X. Li et al., 2015). In a study by Li and colleagues (2015), altered WM microstructure in the bilateral superior longitudinal fasciculus was associated with impaired executive function, an association that was mediated by functional connectivity in the frontoparietal network. WM abnormalities associated with hypertension thus impact cognitive functions in a spatially-specific manner, likely through disruptions of neuronal communication and therefore functional connectivity in the affected networks (Gons et al., 2012; Z. Li et al., 2023).

It was demonstrated that a history of high systolic blood pressure (SBP) in older adults was more predictive of lower WM integrity than high SBP at the time of imaging (Rosano et al., 2015). Although long-term exposure to high BP has been found to be more predictive of WM microstructure than BP at a single time point (Rosano et al., 2015), the effects of high blood

pressure are already detectable in young adults (Maillard et al., 2012), suggesting WM changes due to hypertension may start accumulating as early as the fourth decade of life. Interestingly, the study by Rosano and colleagues (2015) reported no relationship between SBP and grey matter, consistent with the idea that WM is particularly susceptible to the deleterious effects of vascular risk factors.

1.4.3 Obesity

Midlife obesity is associated with earlier onset of AD and higher AD pathology load at autopsy (Chuang et al., 2016). One of the mechanisms through which obesity may accelerate brain aging and precipitate AD onset is through alterations to WM microstructural health. Studies have reported changes in DTI metrics thought to reflect loss in WM integrity (\downarrow FA) with obesity, especially in WM tracts of the limbic system and in tracts connecting the temporal and frontal lobes (corpus callosum, fornix, cingulum and corona radiata) (Daoust et al., 2021; Kullmann et al., 2015; Stanek et al., 2011). Studies using more advanced techniques have reported decreased myelin content (\downarrow R1), increased water content (\downarrow R1 and \uparrow PD*) and altered iron content in the superior longitudinal fasciculus, anterior thalamic radiation, internal capsule, and corpus callosum (Kullmann et al., 2016). The impact of obesity on myelin was also found to be dependent on genetic risk where only individuals with a family history of AD who carry the APOE4 genotype showed an association between waist-to-hip ratio and reduced myelin (macromolecular proton fraction) (Mole et al., 2020). Moreover, this association was found to be moderated by blood pressure and inflammation. As a host of cardiometabolic factors often co-occur with obesity, disentangling the individual effect of obesity from the effects of inflammation, hypertension, insulin resistance, diabetes, and dyslipidemia is difficult. Furthermore, those factors seem to work together in accelerating brain aging (García-García et al., 2022).

On the other hand, other studies have reported beneficial effects of obesity on WM (i.e., higher FA and lower diffusivities) (Birdsill et al., 2017), something that has been termed “the obesity paradox” (Qizilbash et al., 2015). Growing evidence however points to methodological issues as the culprits behind the so-called paradox (Ades & Savage, 2010; Banack & Stokes, 2017; Donini et al., 2020). For instance, the use of BMI as a proxy for obesity is not ideal. Furthermore, the study reporting a beneficial effect of obesity on WM microstructure relied on DTI metrics, which are difficult to interpret, especially in regions of crossing fibers (as many as 63-90% of voxels contain

crossing fibers) (Jeurissen et al., 2013; Riffert et al., 2014). A reduction in FA thus does not always indicate a loss in WM integrity and may instead reflect increased complexity (e.g., development of a secondary fiber population in a different direction as the main fiber population). In conclusion, substantial evidence indicates that midlife obesity is detrimental to overall health including brain health. However, it is important to note that a body weight that is too low also comes with health risks, including reduced life expectancy and higher dementia risk (C. M. Lee et al., 2020; Minagawa & Saito, 2021; Qu et al., 2020).

1.4.4 Cholesterol

There is growing evidence that dysfunction in lipid metabolism is involved in the pathogenesis of AD and other neurodegenerative diseases (Area-Gomez & Schon, 2024; Di Paolo & Kim, 2011; Shobab et al., 2005; Vitali et al., 2014). This has sparked a large amount of interest in studying the impact of serum cholesterol on the brain and the potential of lipid-lowering medications in preventing and treating neurocognitive disorders (Alfaro et al., 2018; Di Paolo & Kim, 2011; Shobab et al., 2005). While most of the brain's cholesterol is synthesized endogenously by astrocytes and oligodendrocytes, brain cholesterol is not fully independent from the periphery. Studies demonstrate that cholesterol from the circulation can enter the brain under the form of an oxidized oxysterol, 27-hydroxycholesterol, which has the ability to pass the blood-brain barrier (Vitali et al., 2014). HDL and LDL particles can also enter the brain via a multi-ligand receptor called the scavenger receptor class B type I (SR-BI). Considering that most of the brain's cholesterol is contained in myelin, abnormal cholesterol profiles as well as factors that affect its metabolism and transport (e.g., APOE4 and other lipid-related genes) may impact WM.

Several DTI studies report associations between serum cholesterol and WM microstructure, but findings are somewhat contradictory (Cohen et al., 2011; Iriundo et al., 2021; Warstadt et al., 2014; V. J. Williams et al., 2013). While evidence points to a well-established protective effect of HDL on cognition and brain structure (Iriundo et al., 2021; Van Exel et al., 2002; Vitali et al., 2014; Warstadt et al., 2014), the impact of peripheral LDL and total cholesterol on the brain is less clear (Alfaro et al., 2018; Lamar et al., 2020; Lv et al., 2016; Ma et al., 2017; Warstadt et al., 2014; Yaffe et al., 2002; Z.-X. Yin et al., 2012). Some studies report changes in DTI metrics that are typically associated with worse microstructural health in individuals with higher LDL (Cohen et al., 2011; Iriundo et al., 2021; V. J. Williams et al., 2013), whereas others report a positive association

between WM integrity and total cholesterol (Warstadt et al., 2014). Similarly, both negative (Lv et al., 2016; Z.-X. Yin et al., 2012) and positive (Elias et al., 2005; Lamar et al., 2020; Ma et al., 2017; Manolio et al., 1993; Yaffe et al., 2002) associations have been reported between cholesterol levels (both LDL and total cholesterol) and cognition. These discrepancies may be due to the unknown contribution of oxidized LDL to total LDL in these studies. Indeed, it has been shown that oxidized LDL, which shows an enhanced production in inflammatory conditions when oxidative stress is high, is a better predictor of atherosclerosis and cardiovascular disease than LDL itself (Hecht & Harman, 2003; Holvoet et al., 2003, 2004; Nishi et al., 2002). As previously mentioned, LDL can pass the blood-brain barrier (BBB) in its oxidized form and it has also been suggested that plasma oxysterols could damage the BBB, increasing its permeability and thus impacting brain health (Dias et al., 2014). Studies also report associations between oxidized LDL and neuronal death (Draczynska-Lusiak et al., 1998; Keller et al., 2002), ischemic damage in the brain (Uno et al., 2005), and cognitive impairments (A. Wang et al., 2018). It has thus been hypothesized that the beneficial effects of statins may be due to decreased LDL oxidation and consequently lower oxidized LDL in plasma (Anderson et al., 1996; Ndrepepa et al., 2005; Sasaki et al., 2002; Vasankari et al., 2001).

On the other hand, HDL has been consistently associated with positive cognitive outcomes, where lower levels of HDL are associated with poorer cognition, both cross-sectionally and longitudinally (Singh-Manoux et al., 2008; Vitali et al., 2014). Low HDL cholesterol has also been associated with higher dementia risk (Reitz et al., 2010; Van Exel et al., 2002). Several mechanisms may underlie this protective effect of HDL. Namely, the antioxidant and anti-inflammatory properties of HDL could reduce inflammation in the brain and HDL-mediated reverse cholesterol transport could contribute to decreasing atherosclerosis in cerebral blood vessels (Vitali et al., 2014). In addition, HDL has a beneficial effect on endothelial function (Vitali et al., 2014). The antioxidant property of HDL may also contribute to preventing LDL oxidation as HDL concentrations have been reported to be inversely related to the concentrations of oxidized LDL (Holvoet et al., 2004; Sigurdardottir et al., 2002).

Interactions with obesity (Cohen et al., 2011) and APOE4 genotype (Ye et al., 2024) may complicate the relationships between cholesterol and WM. Cohen and colleagues (2011) have found that abnormal cholesterol profiles were associated with WM alterations only in obese adults. Further, APOE4 was found to moderate the relationship between WM microstructure and LDL,

where elevated LDL was detrimental in APOE4 carriers, but showed the opposite pattern in non-carriers (Ye et al., 2024). Because APOE4 has a role in LDL metabolism and influences antioxidant concentrations, this negative impact of LDL on WM in APOE4 carriers may be due to increased LDL oxidation (Dias et al., 2014). Together, this highlights the complex interplay in the effects of multiple risk factors on WM.

1.4.5 Elevated glucose

Diabetes affects nearly all organs in the body and the brain is not spared. The risk of Alzheimer's disease and other forms of dementia is higher in individuals with diabetes (Barbiellini Amidei et al., 2021). Alterations in cerebral blood flow, metabolism and structure associated with type 2 diabetes can precipitate cognitive impairments, potentially culminating in the onset of dementia (Biessels, 2023; Gaspar et al., 2016). WM microstructural changes characterized using DTI have been observed in diabetes patients, mostly in frontal, temporal and limbic tracts, and these alterations were found to correlate with cognitive performance (Alotaibi et al., 2021; Moran et al., 2017; Sanjari Moghaddam et al., 2019) Even sub-clinically elevated glucose (i.e., without a diagnosis of diabetes) can lead to changes in cognition and brain structure, including changes in WM microstructure and increased WM hyperintensity volume (Biessels et al., 2014; Garfield et al., 2021; Moran et al., 2017; Repple et al., 2021; Segura et al., 2009). This highlights the importance of assessing levels of blood glucose, even in non-diabetic individuals, as deleterious changes likely start occurring before the diagnostic threshold for diabetes is reached (Repple et al., 2021).

Diabetes risk, which can be indexed using glycated hemoglobin (HbA1c), was shown to be negatively associated with FA in later myelinating WM tracts (Foley et al., 2014), which are known to be particularly vulnerable to aging and AD risk factors according to the myelin breakdown model (Bartzokis, 2004b, 2011; Bartzokis et al., 2003, 2004). Interestingly, this association was only seen in older adults with the APOE4 genotype, suggesting glucose dysregulation poses a greater risk to APOE4 carriers (Foley et al., 2014; Irie et al., 2008; Peila et al., 2002). APOE4 is known to influence cerebral blood flow regulation and glucose metabolism (Thambisetty et al., 2010). Thus, the combined effects of elevated glucose and of vascular and metabolic dysregulation in APOE4 carriers could be especially detrimental for the brain. In addition, high HbA1c has been shown to correlate with increased LDL oxidation in a cohort composed of both diabetic and nondiabetic

individuals (Holvoet et al., 2004), further highlighting the complex interactions between risk factors and their impact on WM.

1.4.6 APOE genotype

The apolipoprotein E (APOE) gene encodes the APOE protein that is involved in the transport of cholesterol and other lipids, as well as in glucose metabolism and cerebrovascular function (Yamazaki et al., 2019). The APOE gene has three allelic variants: E2, E3, and E4. Different variants encode proteins of slightly different structures, leading to variations in their lipid-binding properties. As a result, susceptibility to several diseases varies depending on the genotype.

The APOE genotype is, after age, the strongest risk factor for Alzheimer's disease (Yamazaki et al., 2019). Carrying one E4 allele is associated with a 3-4 fold increase in risk, whereas carrying two alleles would increase risk by as much as 9-15 fold (Farrer et al., 1997; Genin et al., 2011). APOE4 has also been associated with a younger age at onset. It has thus been hypothesized that APOE4 may accelerate age-related myelin breakdown, especially in late-myelinating WM regions, thus accelerating cognitive decline (Bartzokis et al., 2006, 2007; Triebswetter et al., 2022). WM differences in individuals of different APOE genotypes have also been observed in healthy older and younger adults (Heise et al., 2011; Honea et al., 2009). The high lipid-binding affinity of APOE4 makes cholesterol transport less efficient, resulting in impaired myelination and repair (Cheng et al., 2022). As a lipid-transporter, APOE thus plays an important role in myelination, modulating WM microstructure throughout the lifespan (Cheng et al., 2022; Mahley, 2016; Yamazaki et al., 2019).

Further, as was mentioned in previous sections, the APOE4 genotype amplifies the effects of other risk factors on the brain's WM (Foley et al., 2014; Irie et al., 2008; Mole et al., 2020; Peila et al., 2002; R. Wang et al., 2015; O. A. Williams et al., 2019; Ye et al., 2024). Studies looking at the combined effects of vascular risk factors (e.g., hypertension, obesity, dyslipidemia, and diabetes) report reduced WM integrity (lower FA and higher MD) in older adults who have multiple risk factors, especially in those with the APOE4 genotype (Alfaro et al., 2018; R. Wang et al., 2015; O. A. Williams et al., 2019). The fact that APOE4 increases the deleterious impact of risk factors on WM also means APOE4 carriers may benefit to a greater extent from interventions aimed at modifying these risk factors. For instance, physical activity has been shown to be more effective in reducing amyloid burden, maintaining WM integrity, and reducing cognitive decline in APOE4

carriers compared to non-carriers (Head et al., 2012; L Woodard et al., 2012; Luck et al., 2014; Raffin et al., 2021; J. C. Smith et al., 2013, 2016).

1.4.7 Coronary artery disease

Cardiovascular disease, representing a higher vascular burden along the health – disease continuum (see **Figure 18**), also increases the risk of dementia (Justin et al., 2013). In fact, several risk factors for cardiovascular disease also increase the risk of dementia (Livingston et al., 2020). In coronary artery disease (CAD), one of the most common form of heart disease, the risk of cognitive impairment or dementia is 1.45 times greater than in those without CAD (Deckers et al., 2017). Furthermore, patients with both diabetes and CAD were found to be at even greater risk of both Alzheimer's (adjusted hazard ratio; aHR= 1.41) and vascular dementia (aHR = 2.03), with a greater risk for the vascular type (Olesen et al., 2024).

Atherosclerosis, the build-up of plaque inside artery walls that can lead to narrowing of the artery, is a major feature of coronary artery disease. When plaque ruptures, dislodged pieces obstruct the coronary artery causing ischemia of the heart muscle cells (i.e., myocardium) that results in cell death (Libby & Theroux, 2005). This is what constitutes a myocardial infarction (MI) and is commonly referred to as a heart attack. When part of the heart muscle cells dies in MI, the heart's pumping capacity, along with circulation to the rest of the body, can be impaired. Furthermore, the presence of atherosclerosis is rarely confined to the coronary arteries alone, and plaques will typically also be found in the carotid arteries, as well as in small cerebral arteries, a condition termed cerebral small vessel disease (Kovacic et al., 2012). In small vessel disease, arterioles, capillaries and small veins that supply and drain WM and deep brain structures are most affected (Chojdak-Łukasiewicz et al., 2021). This results in reduced cerebral blood flow/perfusion, hypoxia, blood-brain barrier disruptions, vascular inflammation, and impaired A β clearance (Bell & Zlokovic, 2009; Inoue et al., 2023; Justin et al., 2013), which lead to pathological changes in several types of brain cells.

Studies report lower WM, GM and total brain volume, as well as more cerebral infarcts, microbleeds and WM lesions in CAD patients (Vidal et al., 2010). CAD patients are also more likely to have lower cognitive scores and the relationship between atherosclerotic burden and cognition has been shown to be mediated by brain pathology (Vidal et al., 2010). WM is particularly vulnerable to decreases in blood flow as WM is already less perfused compared to GM,

especially in border zones between arterial territories, regions known as the watershed areas (Inoue et al., 2023). The high metabolic demand of oligodendrocytes may also contribute to the vulnerability of WM to changes in perfusion (Bartzokis, 2011; Connor & Menzies, 1996; Wiggins, 1982).

Although WM macrostructural changes have been well-studied in CAD patients (Vidal et al., 2010; Vuorinen et al., 2014), fewer studies focus on microstructural changes that likely precede lesions and atrophy. In a recent study, WM alterations (decreased FA and increased MD) that go beyond aging-related changes were found in patients with ischemic heart disease (Poirier et al., 2024). Moreover, a study showed that WM microstructural integrity (FA) was associated with executive function and processing speed in cognitively unimpaired CAD patients, suggesting that WM microstructure alterations may underlie early subtle cognitive changes (Santiago et al., 2015). Importantly, changes to WM microstructure, as opposed to lesions, are reversible and WM health can be improved through exercise-based cardiac rehabilitation (Poirier et al., 2024).

1.4.8 Protective factors

In addition to the adverse risk factors of dementia discussed above, there are also protective factors. These include physical activity, cognitive and social engagement throughout life. Physical activity (PA) likely decreases dementia risk through mitigation of cardiometabolic risk factors such as diabetes, hypertension, obesity, and dyslipidemia (W. Xu et al., 2017). Other possible mechanisms through which PA may decrease dementia risk include increased neuroplasticity (i.e., neurogenesis, angiogenesis and synaptic plasticity) and improved A β clearance (Andrieu et al., 2015; Varma et al., 2015).

Cognitive engagement is commonly quantified using the number of years of formal education completed, perhaps because it is relatively easy to quantify. Education, and the cognitive stimulation it entails, is so powerful in protecting against dementia that the sex/gender gap in dementia prevalence that was consistently reported in older studies is now narrowing as women are reaching higher levels of education than in the past (Geraets & Leist, 2023; Wolters et al., 2020). Education is known to contribute to brain development and several MRI studies report greater grey matter volume, cortical thickness, and WM integrity in highly educated individuals (Arenaza-Urquijo et al., 2013; Bartrés-Faz & Arenaza-Urquijo, 2011; Y. Liu et al., 2012; Seyedsalehi et al., 2023; Teipel et al., 2009). Together, these structural properties (i.e., increased

number of neurons, synapses, axons, etc.) are referred to as *brain reserve*, or “the neurobiological capital” (Stern et al., 2020). The brain reserve theory simply states that the more we gain through life experiences, the more we can afford to lose without noticeable functional impairment. Moreover, people with greater education attainments would also have a greater capacity to cope with brain pathology such as A β plaques and tangles, resulting in a lessened risk for cognitive impairment and dementia (Roe et al., 2007). This phenomenon, referred to as cognitive reserve, may be due to greater adaptability and network efficiency as well as other compensatory mechanisms that allow highly educated individuals to maintain high cognitive function despite brain damage (Stern, 2006). In addition to the typical AD pathology markers, the protective effect of education has also been demonstrated with the presence of WM lesions and alterations in WM microstructure (Dufouil et al., 2003; Mortamais et al., 2014; Teipel et al., 2009). In this study by Teipel and colleagues (2009), reduced WM integrity was associated with less cognitive impairment in individuals with more education (Teipel et al., 2009). Social engagement, especially complex social activities, may operate in a similar fashion, boosting cognitive reserve hence reducing dementia risk (Penninkilampi et al., 2018). These protective factors provide several avenues for dementia prevention through individual interventions and public health strategies.

1.5 Early intervention to prevent age-related diseases

The fact that WM retains its capacity for remodeling throughout life also means damage to WM microstructure can potentially be repaired, provided interventions are initiated before damage is too severe and irreversible (see **Figure 18**) (Concha, 2014; Salsone et al., 2021; Sidaros et al., 2008). As was discussed above, several adverse factors impact WM integrity (hypertension, obesity, abnormal cholesterol and glucose levels, etc.). Interventions that target these factors thus hold the potential of promoting WM repair. For instance, exercise-based interventions have been shown to promote neuroplasticity in healthy older adults (Mendez Colmenares et al., 2021) and in patients with prodromal to mild Alzheimer’s disease that have a high vascular burden (Konwar et al., 2023). Exercise-based cardiac rehabilitation has also been associated with WM improvements in patients with ischemic heart disease (Poirier et al., 2024). Further, controlling blood pressure with antihypertensive medications may lead to recovery of normal WM integrity in individuals that were previously diagnosed with hypertension (Haight et al., 2018).

Other interventions such as cognitive training have also proven to be effective in promoting WM plasticity (McPhee et al., 2019) and combining cognitive training with aerobic exercise may be even more effective, especially in older adults with cardiovascular risk factors (Roig-Coll et al., 2024; Stephen et al., 2020). Multi-domain lifestyle interventions for dementia prevention have garnered a large amount of interest in the last decade, following the success of the FINGER (Finnish Geriatric Intervention Study to Prevent Cognitive Impairment and Disability) trial and with the recent launch of a worldwide network (Kivipelto et al., 2020; Ngandu et al., 2015; Stephen et al., 2020). In these trials, several factors including diet, exercise, cognitive training, and vascular risk factors monitoring, are targeted simultaneously (Kivipelto et al., 2020; Ngandu et al., 2015). Importantly, these intervention strategies have been found to positively impact WM health both individually and in combination, and to reduce the risk of cognitive decline (Kivipelto et al., 2020; MCPhee et al., 2019; Ngandu et al., 2015; Roig-Coll et al., 2024; Roy et al., 2022; Stephen et al., 2020). This multi-domain approach thus appears as a promising candidate to reduce the risk of dementia (Kivipelto et al., 2020; Ngandu et al., 2015) and WM plasticity may be an important mechanism contributing to the maintenance of cognitive function in these interventions (Roig-Coll et al., 2024; Stephen et al., 2020).

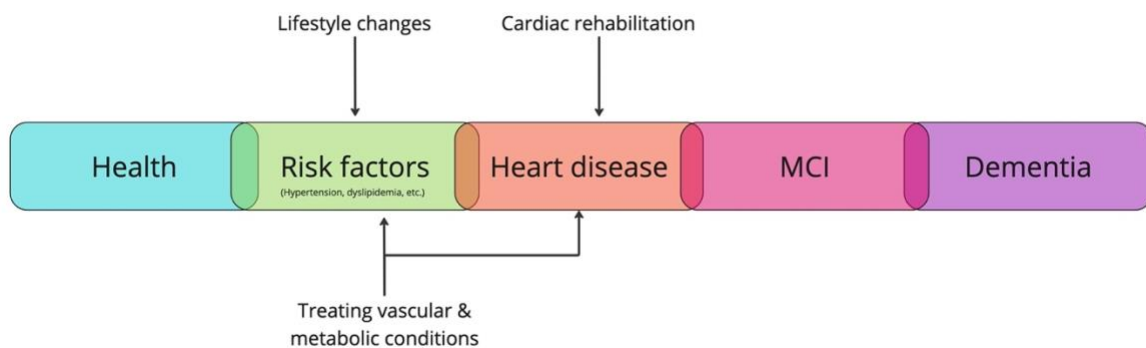


Figure 18. Health – disease continuum and potential interventions that can be initiated to prevent or slow down progression are illustrated. These interventions have also been shown to promote white matter plasticity.

CHAPTER II: Short-term white matter plasticity in young adults

Preface

White matter (WM) retains its capacity for experience-induced plasticity in adulthood (Sampaio-Baptista & Johansen-Berg, 2017). This has important implications for dementia prevention as WM changes that start occurring decades before the onset of neurodegenerative diseases could potentially be reversed through therapeutic interventions that promote neuroplasticity (Concha, 2014; Salzone et al., 2021). We now know WM is remodeled in a highly dynamic manner, with changes observed within hours following the initiation of a new activity (Hofstetter et al., 2013). In addition to changes in WM structure occurring almost immediately when starting to learn a new task, plastic changes can also be maintained for long periods, even when the task that caused these alterations is no longer practiced (Dayan & Cohen, 2011). Since WM properties underlie the efficiency of signal conduction in brain networks, changes in WM microstructure impact the functions subserved by the affected network (Chorghay et al., 2018; Fields, 2015). Plastic changes in WM thus contribute to supporting learning and, potentially, the recovery of cognitive function.

Interventions that promote neuroplasticity are promising strategies in preventing cognitive decline and neurodegenerative diseases such as dementia (Fissler et al., 2017; Stephen et al., 2020; ten Brinke et al., 2017). For instance, cognitive training, physical activity, and interventions that combine multiple modalities have been shown to induce changes in WM microstructure in various populations (Konwar et al., 2023; McPhee et al., 2019; Poirier et al., 2024; Roig-Coll et al., 2024; Stephen et al., 2020). However, because most plasticity studies have used a pre-post design (Hofstetter et al., 2013; Scholz et al., 2009; Steele et al., 2012), we lack a basic understanding of the time scales at which plastic changes in WM can occur, and of the alterations that occur at different stages of learning, even in healthy adults.

Characterizing the dynamic nature of WM plastic changes in healthy adults thus appeared as a natural first step before investigating pathological changes in at-risk individuals.

White matter microstructural changes in short-term learning of a continuous visuomotor sequence

Stéfanie A. Tremblay, Anna-Thekla Jäger, Julia Huck, Chiara Giacosa, Stephanie Beram, Uta Schneider, Sophia Grahl, Arno Villringer, Christine L. Tardif, Pierre-Louis Bazin, Christopher J. Steele, Claudine J. Gauthier

Published in Brain Structure and Function. <https://doi.org/10.1007/s00429-021-02267-y>

2.1 Abstract

Introduction: Efficient neural transmission is crucial for optimal brain function, yet the plastic potential of white matter (WM) has long been overlooked. Growing evidence now shows that modifications to axons and myelin occur not only as a result of long-term learning, but also after short training periods. Motor sequence learning (MSL), a common paradigm used to study neuroplasticity, occurs in overlapping learning stages and different neural circuits are involved in each stage. However, most studies investigating short-term WM plasticity have used a pre-post design, in which the temporal dynamics of changes across learning stages cannot be assessed.

Methods: In this study, we used multiple magnetic resonance imaging (MRI) scans at 7 Tesla to investigate changes in WM in a group learning a complex visuomotor sequence (LRN) and in a control group (SMP) performing a simple sequence, for 5 consecutive days.

Results: Consistent with behavioral results, where most improvements occurred between the two first days, structural changes in WM were observed only in the early phase of learning (d1-d2), and in overall learning (d1-d5). In LRNs, WM microstructure was altered in the tracts underlying the primary motor and sensorimotor cortices. Moreover, our structural findings in WM were related to changes in functional connectivity, assessed with resting-state functional MRI data in the same cohort, through analyses in regions of interest (ROIs). Significant changes in WM microstructure were found in a ROI underlying the right supplementary motor area.

Discussion: Together, our findings provide evidence for highly dynamic WM plasticity in the sensorimotor network during short-term MSL.

2.2 Introduction

The idea that structure determines function, and that function can modulate structure, is a well-known concept governing biology (Kohn et al., 2018). Just like any other organ in the body, the structure of the brain changes in response to changing demands in order to support new functions, in a process termed neuroplasticity (Zatorre et al., 2012). Synaptic changes have been the main focus of early plasticity studies (Rioult-Pedotti et al., 2000; T. Xu et al., 2009), yet recent research now indicates that plastic changes can also involve alterations to neurons, glial cells, and cerebral vessels (Sampaio-Baptista & Johansen-Berg, 2017; Tardif et al., 2016; Zatorre et al., 2012).

The plastic potential of white matter (WM), and the behavioral relevance of changes in the fiber tracts connecting neurons, has long been overlooked. However, growing evidence now shows modifications to astrocytes, microglia, and myelin-producing oligodendrocytes occur as a result of experience-dependent learning (Chorghay et al., 2018; Tardif et al., 2016). There is a large amount of evidence regarding activity-dependent myelination ([Caeyenberghs et al., 2016](#); [Lakhani et al., 2016](#); [Sampaio-Baptista et al., 2020](#); [Sampaio-Baptista & Johansen-Berg, 2017 for review](#)) and some studies have also shown that axonal diameter can change in adult brains (Chéreau et al., 2017; Lazari et al., 2018; S. Lee et al., 2012). Changes to axons and myelin would lead to changes in conduction speed and thus more efficient information processing through optimized timing of neural transmission (Chorghay et al., 2018; Fields, 2015; Sampaio-Baptista & Johansen-Berg, 2017). Given the crucial role of efficient neural transmission for optimal brain function (Fields, 2015; Waxman, 1975), a deeper understanding of the ways in which WM can be altered by experience is of critical importance.

Motor sequence learning (MSL) tasks are a common paradigm used to study neuroplasticity (Doyon et al., 2009; Hikosaka et al., 2002; Nissen & Bullemer, 1987; Penhune & Steele, 2012). MSL occurs in overlapping stages that have been described by various models. As such, motor learning can be divided into an initial fast stage, where a large amount of improvement occurs in a short period of time, followed by a consolidation stage, which solidifies the gains in performance between training sessions, making them resistant to interference. In a final late/slow stage, the learned sequence is fine-tuned to optimize motor parameters such as force, timing and spatial accuracy (Dayan & Cohen, 2011; Doyon et al., 2002; Doyon & Benali, 2005; Karni & Sagi, 1993;

Korman et al., 2003; Luft & Buitrago, 2005). In each case, there is significant evidence from neuroimaging studies that different neural circuits are involved in each stage of learning (Dayan & Cohen, 2011; Halsband & Lange, 2006 for review).

Studying neuroplasticity with magnetic resonance imaging (MRI) allows for the longitudinal investigation of functional and structural reorganization at the network (how are different brain regions connected to each other, i.e., whole-brain level) and microstructural levels (what properties do the fiber bundles that make up these connections have, i.e., voxel level), as whole-brain images can be obtained repeatedly (Tardif et al., 2016). Recent advances in MRI techniques and models, especially in the areas of connectivity and network theory, have created the opportunity for a better understanding of how brain architecture and network efficiency impact information processing and how these are modified through experience (Albert et al., 2009; Guye et al., 2010; Lewis et al., 2009). Changes in connectivity can be defined structurally, with diffusion-weighted imaging (DWI), a technique that probes WM microstructural organization through imaging the bulk motion of water molecules (Abdul-Kareem et al., 2011; Klein et al., 2019; Le Bihan et al., 2001), and functionally, through the measurement of spontaneous activity at rest and the temporal correlation of the blood-oxygen-level-dependent (BOLD) signal between brain regions (resting-state functional MRI) (Albert et al., 2009; Lewis et al., 2009). In parallel, advances in hardware, such as the increasing use of ultra-high field MRI, and improved modeling approaches allow for the characterization and quantification of several properties of brain structures at finer spatial scales (Dumoulin et al., 2018; Frangou et al., 2020; Heidemann et al., 2012). These advances could allow us to bridge the gap between the knowledge gained from animal and human studies, and better define the mechanisms and time course at play when the brain is reshaped through experience (Sampaio-Baptista & Johansen-Berg, 2017; Tardif et al., 2016).

Although the greatest gains in performance occur during the initial stage of learning (Dayan & Cohen, 2011; Halsband & Lange, 2006; Savion-Lemieux & Penhune, 2005), early investigations of WM plasticity mainly focused on the effects of long-term training with cross-sectional studies in musicians and dancers with several years of training (Abdul-Kareem et al., 2011; Bengtsson et al., 2005; Giacosa et al., 2016, 2019; Hänggi et al., 2010). The cross-sectional nature of many of these studies does not allow characterization of the temporal dynamics of learning nor distinguishing training-induced changes from pre-existing differences in WM (Abdul-Kareem et

al., 2011; Bengtsson et al., 2005; Giacosa et al., 2016, 2019; Hänggi et al., 2010; Steele et al., 2012). More recently, longitudinal studies using DWI have shown that WM changes can occur at shorter timescales. For instance, changes to WM microstructure underlying the intraparietal sulcus were observed after 6 weeks of juggling training (Scholz et al., 2009) and another study reported such changes in the fornix as quickly as after a few hours of spatial learning in a car racing game (Hofstetter et al., 2013). However, most studies investigating short-term WM plasticity have used a pre-post design, or a single measurement at the end of learning, in which the temporal dynamics of changes across learning stages cannot be assessed (Hofstetter et al., 2013; Scholz et al., 2009; Steele et al., 2012). Moreover, the control group in some of these studies does not allow to distinguish changes due to sequence-specific learning from those due to motor execution (e.g., Scholz et al., 2009). In this study, we used multiple MRI scans at 7T to investigate changes in WM across learning stages in a group learning a complex visuomotor sequence, and in a control group performing a simple sequence. The DTI model used to derive diffusivity metrics from DWI data yields measures that are highly sensitive to changes in WM microstructure, although physiologically non-specific (Riffert et al., 2014). Moreover, we investigated WM plasticity in regions of interest (ROIs) near areas of change in functional connectivity, assessed with resting-state fMRI (rs-fMRI) data in the same cohort (Jäger et al., 2021).

2.3 Methods

2.3.1 Participants

Forty neurologically normal individuals of 21 to 30 years of age ($M \pm SD$: 24.5 ± 2.44 ; 21 females) and without motor or correctible visual impairments were recruited from the participant database of the Max Planck Institute for Human Cognitive and Brain Sciences in Leipzig, Germany. All participants were task naïve prior to this study and right-handed according to the Edinburgh Handedness Inventory ($M \pm SD$: 83.7 ± 16.9), except for one who was ambidextrous (EHI= 40). The majority of participants had no exceptional musical experience ($M \pm SD$: 8.55 ± 8.83 years), but one participant self-identified as a professional musician and two as having advanced musical experience. Participants had an average sport experience of 5.83 ± 7.15 years and two participants self-identified as professional athletes. After ensuring the participants had no neurological conditions and no contraindication to MRI, they gave written informed consent according to the

declaration of Helsinki. Participants were randomized into two groups: the experimental group (N=20), who learned a complex visuo-motor sequence, and the control group (N=20), who learned a simple repetitive visuo-motor sequence. One participant from the experimental group was excluded from this study due to a large signal drop in DWI data. **Table 1** shows the demographic data for each group. After completion of the study, participants were financially compensated for their time. The study was approved by the ethics review board of the Medical Faculty of the University of Leipzig and all participants provided written informed consent according to the Declaration of Helsinki.

Table 1. Demographic data in each group. LRN= experimental group; SMP= control group; SD= standard deviation; EHI= Edinburgh Handedness Inventory

	Group	Sex	Age	EHI (handedness)	Music yrs (formal)	Sport yrs (formal)
N	LRN	19 Male	9			
		Female	10			
	SMP	20 Male	10			
		Female	10			
Missing	1					
Mean	LRN		25.1	84.8	7.87	4.95
	SMP		23.9	83.0	9.32	6.95
SD	LRN		2.47	18.0	8.29	6.97
	SMP		2.38	16.5	9.66	7.42
Min.	LRN		22	40.0	0	0
	SMP		21	40.0	0	0
Max.	LRN		30	100	28.0	25
	SMP		30	100	29.5	25

2.3.2 Motor Sequence Learning Task

The sequential pinch force task (SPFT) is a complex visuomotor sequence learning task requiring fine force control (Camus et al., 2009; Krakauer et al., 2019), and was previously shown to result in short-term plastic changes in grey matter (Gryga et al., 2012). During the SPFT, participants hold a pressure sensor between the thumb and index finger of their right hand (**Figure 1a**) and are required to exert force on the sensor in order to match the height of a moving reference bar (REF;

blue on **Figure 1b**) displayed on a computer screen. Another moving bar (FOR; yellow), representing the amount of pressure they are exerting on the device, is also displayed on the screen to provide visual feedback. The device samples force continuously throughout the task at a rate of 80 Hz. The change in height of the REF bar follows one of two specific sequences, as illustrated in **Figure 1** (c). In the learning condition (LRN), the bar moves following a complex sequence that is difficult to predict (blue on **Figure 1c**) (Gryga et al., 2012). In the control condition, the bar moves following a simple sinusoidal sequence (SMP) that is learned almost immediately (green). The SMP sequence was designed to match the LRN sequence in terms of the total magnitude of force, duration, and frequency at the maximum level of force. This control condition can be used to distinguish between potential structural alterations related to motor execution (i.e., participants pinch a device in both conditions) from alterations that are specific to learning a sequence. Lastly, in the rest condition (RST), participants were asked to fixate their gaze on the static REF and FOR bars (both at 50% of their maximal height).

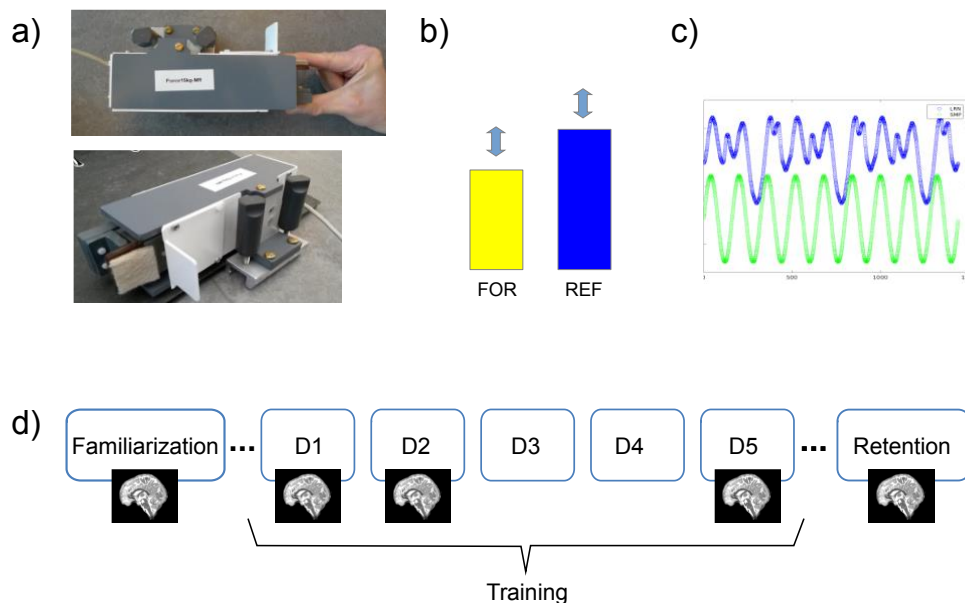


Figure 1. Sequential pinch force task (SPFT) and experimental design. a) SPFT device. Participants hold the pressure sensor between the thumb and index finger. b) They exert force on the sensor to match the height of the reference bar (REF; blue). The FOR bar (yellow) represents the amount of force they are exerting on the device. c) Visual representation of the complex (LRN; blue) and of the simple (SMP; green) sequences. d) Schema of the experimental design. The familiarization session (d0) takes place 2 days before the first day of training (d1) and the retention scan (d17) 12 days after the last training day (d5). All training sessions (d1-d5) take place on consecutive days, Monday to Friday. Participants were in the scanner on d0, d1, d2, d5 and d17.

2.3.3 Experimental Design

The experimental design is illustrated in **Figure 1** (d). Participants performed the SPFT on 5 consecutive days (Monday to Friday). A familiarization session (d0) on the previous Thursday or Friday, 2 days prior to the first day of training, allowed to test the participant's maximum pinch force and calibrate the level of force required in subsequent training sessions in order to avoid fatigue. The minimum bar level corresponded to a force of 5% of the participant's maximum force, while the maximum bar level corresponded to 30% of the participant's maximal force. During this session, participants also became familiar with the device and the task as they performed 9 trials of the SMP sequence. Each training day (d1-d5), participants of the experimental group completed 3 pseudo-randomly presented blocks each consisting of 3 trials of SMP, RST, and LRN, resulting in a total of 9 trials per condition every day. Participants in the control group also performed 3 blocks of training, but LRN trials were replaced by SMP trials. Throughout this manuscript, the experimental group will be referred to as the LRN group and the controls as the SMP group. Each trial lasted 18 seconds and the entire training session lasted 20 minutes as in Gryga et al. (2012). Participants were given feedback on their performance (i.e., average accuracy in matching the height of the REF bar) after the SMP and the LRN trials. A retention session (d17) was conducted approximately 12 days after the last day of training and consisted in the same procedure as the previous training sessions (d1-d5). The task was performed inside the MRI scanner on d0, d1, d2, d5, and d17 and outside the scanner on d3 and d4 (see **Figure 1d**). Both MRI sequences of interest for this study (i.e., DWI and rs-fMRI) were acquired prior to SPFT training. All sessions for all participants took place in the morning to avoid the potential influence of circadian rhythms on our results as the time of the day has been shown to impact the relative volumes of the intra-axonal and extra-axonal spaces in WM (Voldsbekk et al., 2020).

2.3.4 MRI Acquisitions

MRI data was acquired on a Siemens 7 Tesla scanner (MAGNETOM, Siemens Healthcare, Erlangen, Germany) with a 32-channel Nova head coil at the Max Planck Institute in Leipzig, Germany. DWI data, acquired from an Echo Planar Imaging (EPI) sequence (TR= 10100 ms, TE= 62.8 ms, FOV= 192 x 192 mm², slice acceleration factor: 2, slice thickness = 1.2 mm, 102 slices, GRAPPA factor: 2, partial Fourier 6/8, b=1000 s/mm², 20 directions, PE= AP, bandwidth= 1562 Hz/Px, voxel size= 1.2 x 1.2 x 1.2 mm), was used to assess WM microstructure. Rs-fMRI data

were acquired with a blood-oxygen-level-dependent (BOLD) sequence (TR= 1130ms, TE= 22ms, flip angle= 40°, FOV = 192 x 192 mm², slice thickness = 1mm, 102 slices, GRAPPA factor 2, partial Fourier 6/8, bandwidth = 1562 Hz/Px, voxel dimensions = 1.2 x 1.2 x 1.2mm). Participants had their eyes open and were fixating their gaze on a cross during this 10-min acquisition. Rs-fMRI and DWI data were acquired prior to SPFT training. Uniform intensity T1-weighted images (UNI) were also acquired with an MP2RAGE sequence (TR = 5000 ms, TE = 2.45 ms, flip angle 1 = 5°, flip angle 2 = 3°, FOV = 224 x 224 x 240 mm³, slice thickness = 0.7 mm, 240 slices, bandwidth = 250 Hz/Px, voxel size = 0.7 x 0.7 x 0.7 mm) (Marques et al., 2010). Fieldmaps were also acquired (TR = 18ms, TE1 = 4.08ms, TE2 = 9.18ms, flip angle = 10°, FOV = 256 x 256mm², slice thickness = 2mm, 80 slices, bandwidth 1 = 300 Hz/Px, bandwidth 2 = 300 Hz/Px, voxel dimensions = 2 x 2 x 2mm) to correct distortions in BOLD images due to field inhomogeneities. As indicated above, one subject from the LRN group was excluded because of a large DWI signal drop in the temporal lobe.

2.3.5 Image Preprocessing

DWI data were preprocessed using the MRtrix (3.0) software which performs denoising of the data, corrects for motion and Eddy currents (Eddy tool in FSL 6.0.1), and for susceptibility-induced distortions (topup tool in FSL) using b0 volumes of opposite phase-encoding polarities (PA) (Andersson et al., 2003; Andersson & Sotiropoulos, 2016; Skare & Bammer, 2010; S. M. Smith et al., 2004; Tournier et al., 2019). The gradient scheme containing gradient vectors and b-values (bvecs and bvals) is stored in the header of the MRtrix file format (mif) and automatically reoriented by MRtrix functions. Bvecs and bvals were extracted from the preprocessed image before the next step, which requires the NIFTI format. Bias field correction was performed using the N4 algorithm of ANTs (3.0) within a mask computed using the brain extraction tool (bet) of FSL on the b=0 preprocessed volume (Tustison et al., 2010). A brain extraction of all DWI volumes was then applied using the b=0 mask in order to remove all non-brain voxels. Preprocessed DWI volumes were smoothed anisotropically, a method in which kernels are shaped based on the main directions of fiber tracts, using the 3danisosmooth function in AFNI (19.0.26 'Tiberius') (2 iterations, $\sigma_1=0.5$, $\sigma_2=1.0$) (Ding et al., 2005). This type of smoothing has been shown to preserve directional information, maintaining WM structure boundaries and limiting partial voluming effects (Van Hecke et al., 2010). This method was also shown to decrease the influence of

smoothing parameters, such as kernel size, on voxel-based analysis results (Jones et al., 2005; Moraschi et al., 2010; Van Hecke et al., 2010).

DWI data were fitted to a tensor model with `dwi2tensor` (MRtrix 3.0) and the tensor images were converted to a symmetric matrix in the NIFTI format in the lower-triangular ordering (dxx, dxy, dyy, dxz, dyz, dzz) for ANTs. Spatial normalization was performed in ANTs using high-dimensional non-rigid registration of the tensor images, which uses both spatial and directional tensor information, and was shown to improve alignment of WM tracts and minimize shape confounds on FA outcomes (H. Zhang et al., 2007). Warps were computed at 4 levels: first, using rigid and affine transforms (with mutual information; MI, as similarity metric) to compute the warp from DWI (using the b=0 volume which has the highest contrast) to anatomical space (UNI image from the MP2RAGE T1 acquired in the same session), and then from anatomical (one day) to subject space (across days), from subject to group space, and lastly to MNI space (MNI152) using rigid (MI), affine (MI), and SyN (symmetric normalization; with cross-correlation) transforms with the `antsRegistration` function (Avants, Epstein, et al., 2008; Avants et al., 2009). The first step of the registration process of tensor images takes care of the spatial alignment: all warps were applied to the tensor images in a single step, using `antsApplyTransforms`. Linear interpolation in the log space was used and, since the log of 0 is undefined, the background tensor value was set to 0.0007 (Arsigny et al., 2006). All warps were then combined, and the combined transform was used to reorient the deformed tensor images (`ReorientTensor`), accounting for the orientational aspect of normalization (H. Zhang et al., 2007). Maps of fractional anisotropy (FA), mean diffusivity (MD), axial diffusivity (AD), and radial diffusivity (RD) were then computed on the reoriented tensor images (in MNI space) using `ImageMath` in ANTs. A WM mask was created from the mean FA image thresholded at 0.35 to include only WM voxels in statistical analyses.

Rs-fMRI data was corrected for motion and for magnetic field inhomogeneities using the acquired fieldmaps. Nuisance regression, including 12 motion regressors (3 translations and 3 rotations plus their first derivatives), outlier regressors and physiological regressors, was performed using Nilearn's `NiftiMasker`. A Gaussian smoothing kernel of 2.4mm was then applied before calculating voxel-wise network centrality metrics degree centrality (DC) and Eigenvector centrality (EC) (Wink et al., 2012). DC and EC maps were non-linearly registered to MNI space with ANTs (Avants et al., 2009). DC and EC provide a measure of the degree of connectivity of a node to other

nodes, with each grey matter voxel representing a node. All preprocessing, tissue segmentation and registration scripts, which were implemented in the CBS Tools environment, are openly available at <https://github.com/AthSchmidt/MMPI/tree/master/preprocessing>. Preprocessing of rs-fMRI data is explained in more details in Jäger et al. (2021).

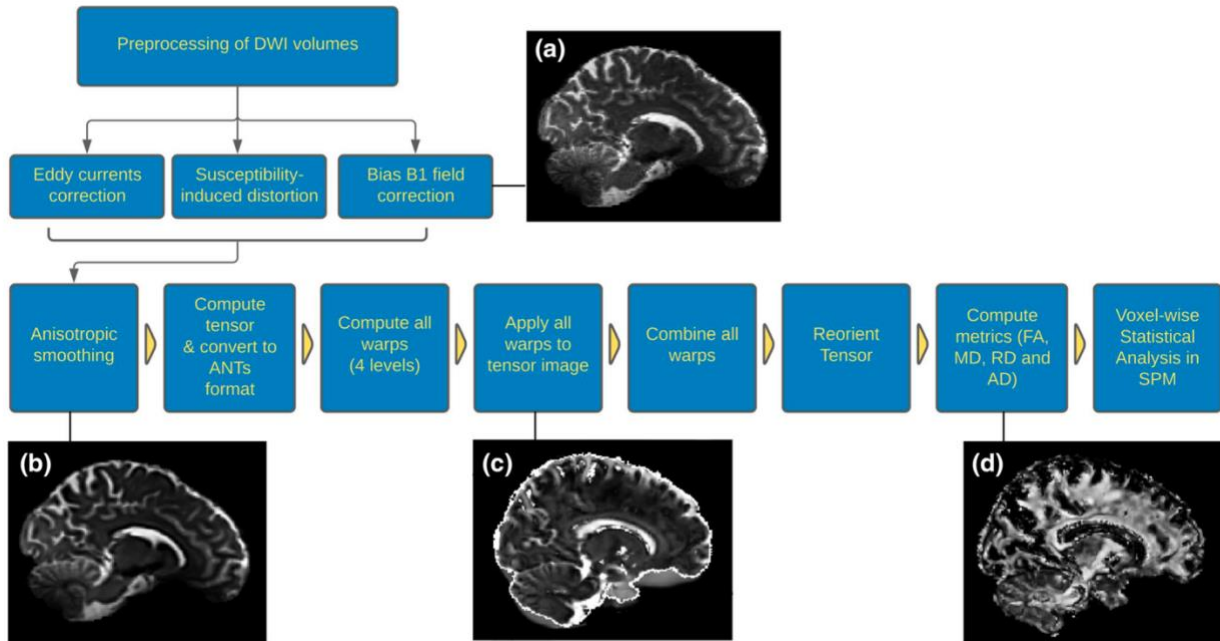


Figure 2. DWI data processing workflow. Preprocessing included correction for motion, Eddy currents, susceptibility-induced distortions, and bias B1 field correction (N4). The preprocessed DWI image ($b=0$ volume) of one participant is shown in a). Preprocessed DWI volumes were then smoothed anisotropically (b), fitted to a tensor model and converted to a symmetric matrix in the lower-triangular ordering ($dx_x, dx_y, dy_y, dx_z, dy_z, dz_z$) for ANTs. Four levels of warps were computed (native to T1, T1 to subject, subject to group, and group to MNI) and applied to the tensor image with linear interpolation in the log space in ANTs (c). All warps were combined, and the combined transform was used to reorient the deformed tensor image. Maps of fractional anisotropy (FA), mean diffusivity (MD), axial diffusivity (AD), and radial diffusivity (RD) were computed on the reoriented tensor images. The FA map of the same participant is shown in d. These maps were analyzed with voxel-wise analyses.

2.3.6 Statistical Analyses

Performance improvement in the SPFT

Performance and improvements in performance over the course of the training sessions were quantified using a measure of temporal synchronization (SYN) calculated using custom-built scripts in MATLAB (Version R2016a, The MathWorks, Inc., Natick, Massachusetts, United States). SYN was defined as the temporal deviation (in ms) between the time of the movement of the REF bar and the time when the FOR bar matches the height of the REF bar most closely. The time of best match between the REF and FOR patterns was determined using cross-correlation.

The time difference (SYN in ms) was then calculated between the time of movement of the REF bar and the time lag with the greatest cross-correlation (i.e., representing the best match between REF and FOR patterns). A SYN score of zero thus indicated perfectly timed performance.

SYN score values of the three trials of each block were averaged for each participant, resulting in three block values per day. Block SYN scores were then averaged, yielding one SYN value per day. A repeated-measures ANOVA was conducted in Jamovi (<https://www.jamovi.org>; <https://cran.r-project.org/>; Lenth et al., 2018; Singmann et al., 2018), to assess the progression in performance, with Group-Task (LRN group-LRN task, LRN group-SMP task and SMP group-SMP task) as a between-subject factor and Day (1-5 and 17) as the repeated-measures factor. Mauchly's tests were conducted to assess sphericity, and the appropriate correction was applied if sphericity was violated (Greenhouse-Geisser if $\epsilon < 0.75$ or Huynh Feldt if $\epsilon > 0.75$). Post-hoc Tukey's tests were then used to assess the specific temporal location of differences in significant effects and interactions (i.e., between which days the improvement in SYN score was significant).

WM microstructural changes across learning stages

We conducted voxel-wise analyses within a WM mask on all diffusion maps (FA, MD, AD, and RD) using a flexible factorial design for longitudinal data from the CAT12 (Computational Anatomy Toolbox: <http://www.neuro.uni-jena.de/cat/>) in SPM12 (Statistical Parametric Mapping software: <http://www.fil.ion.ucl.ac.uk/spm/>) implemented in MATLAB (Version R2019a, The MathWorks, Inc., Natick, Massachusetts, United States). The flexible factorial design accounts for dependency between time points for each participant, and included two factors: Group (LRN and SMP) and Scan (d1, d2, and d5). Based on the MSL literature, putative changes between d1-d2 were interpreted as occurring during the initial fast learning stage, d2-d5 as the subsequent slow learning stage, and d1-d5 as overall learning. The contrasts assessed were the interaction between Group and Scan in the following manner: $d2 > d1$, $d2 < d1$, $d5 > d2$, $d5 < d2$, $d5 > d1$, and $d5 < d1$. These contrasts were assessed in both groups, only within the LRN group, and with the opposite direction of change in the LRN vs SMP group (e.g., $d2 > d1$ in LRN, $d2 < d1$ in SMP), which resulted in a total of 18 contrasts. Results are reported using cluster inference with the SPM default threshold of $p < 0.001$ and FWE correction for multiple comparisons at the cluster level ($p < 0.05$). All analyses were conducted within the WM mask. We defined sequence-specific changes as significant changes in the contrasts of opposite directions between groups, where the LRN group

was driving the interaction (i.e., greater change in LRN). Significant changes in both groups were defined as non-sequence specific and interpreted as related to motor execution of the SPFT. Similar voxel-wise interaction analyses were conducted on rs-fMRI centrality metrics with Group and Scan as factors, allowing to identify clusters of changes in functional connectivity (Jäger et al., 2021), which were used for ROI generation.

WM microstructural changes associated with functional changes

Work from our group focusing on the rs-fMRI data in the same cohort identified functional reorganization of the networks involved in MSL (Jäger et al., 2021). These regions were used to define ROIs in WM tracts associated with these task-relevant functional changes. Specifically, increases in centrality (DC and EC) were found in the right globus pallidus internal segment (GPi) in the initial learning stage (d1-d2) and bilaterally in the superior parietal cortex (SPC) in overall learning (d1-d5). Decreases in the right supplementary motor area (R SMA) and right pars opercularis (R PO) were also observed between d1-d5 in the LRN group. In order to relate structural changes in WM to functional changes, ROIs (**Figure 3**, in blue) were generated from the rs-fMRI clusters in grey matter (**Figure 3**, in red) using the 3dROIMaker function in AFNI (P. A. Taylor & Saad, 2013). The GM ROI was first inflated by two voxels to find where it overlapped WM (within our group WM mask) and then inflated by four voxels to define an ROI within the WM. Inflating parameters were adjusted when creating the R GPi and the R SPC ROIs, in order to yield ROIs of similar sizes, as these clusters were located closer to the WM mask. Resulting ROIs contained 79, 187, 238, 161, and 69 voxels for the R GPi, L SPC, R SPC, R SMA and R PO, respectively. We extracted mean values from each ROI and conducted repeated-measures ANOVAs across timepoints (d1, d2, and d5) in the LRN group, with separate analyses for each diffusion metric (FA, MD, RD and AD) and ROI. Post-hoc Tukey's tests were then conducted on significant effects and interactions to determine the locations of significant changes in WM metrics (i.e., between which days). These analyses focused on participants of the LRN group since ROIs from the rs-fMRI data come from an interaction analysis between groups which showed changes specific to the LRN in these regions.

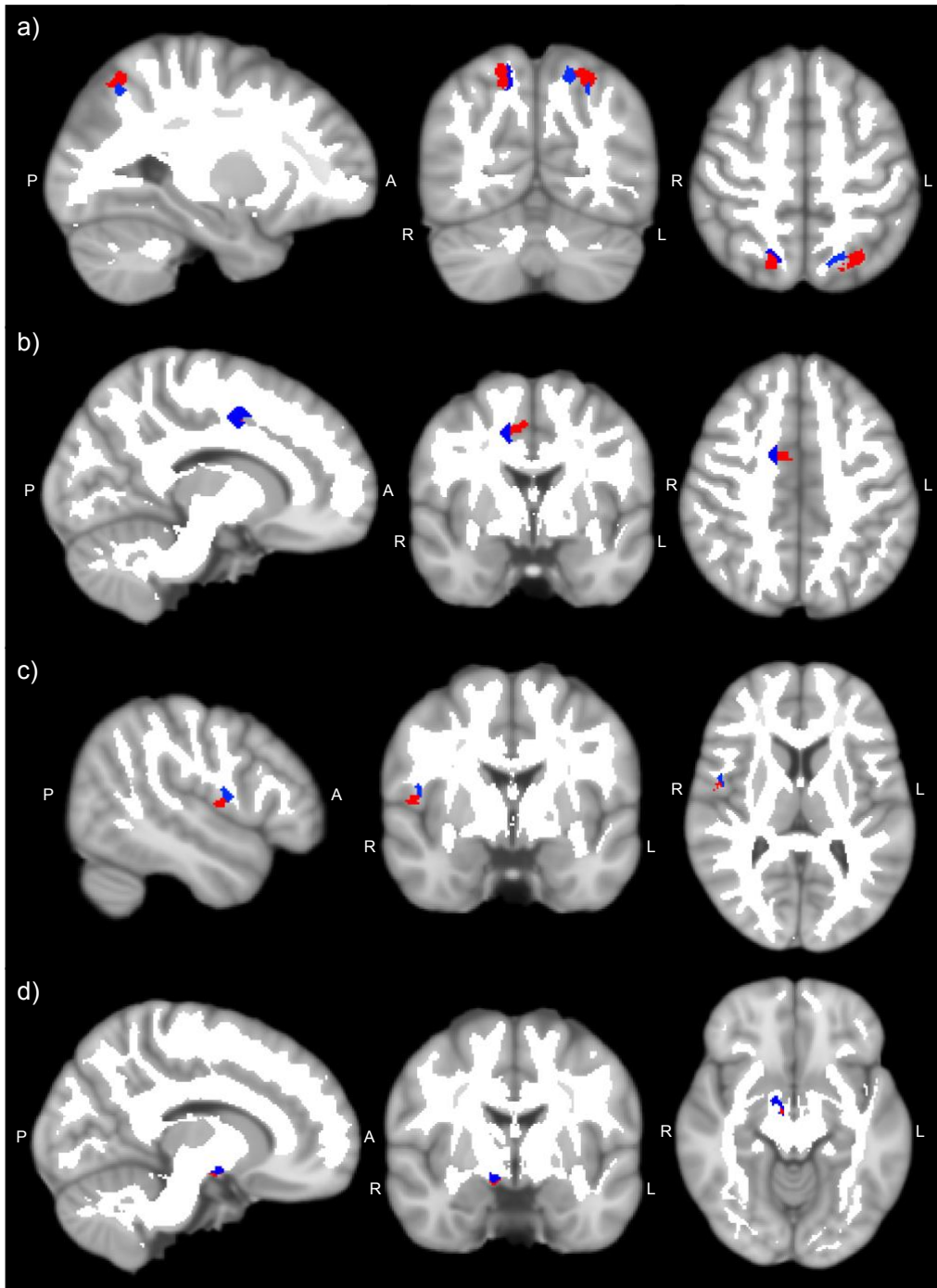


Figure 3. Regions of interest (ROIs) in white matter (blue) created from grey matter ROIs (red) where sequence-specific changes in functional connectivity were found (Jäger et al., 2021). ROIs are displayed on the MNI152 template and WM ROIs are overlaid on a white matter mask created from the group average of FA maps thresholded at 0.35. a) Right and left superior parietal cortex (SPC) ROIs. b) Right supplementary motor area (SMA) ROI. c) Right pars opercularis (PO) ROI. d) Right globus pallidus internal segment (GPi) ROI.

Retention of WM microstructural changes

To assess whether WM microstructural changes were maintained through the retention period, paired t-tests were conducted between mean values at d5 and those at d17 in clusters where significant changes were found during the training period (d1-d5). ROIs used for these analyses consisted in any cluster where a significant change was found with whole-brain voxel-wise analyses, as well as ROIs created from rs-fMRI clusters in which a significant change in WM microstructure was found with repeated-measures ANOVAs. These analyses focused on the LRN group and on the metrics (i.e., FA, MD, RD, or AD) that showed significant changes during the training period. A lack of significant change between mean values at d5 and those at d17 was interpreted as WM microstructural change retention.

Correlation with improvements in performance

Changes in WM metrics were correlated with performance improvements in the initial learning stage (d1-d2) and in overall learning (d1-d5). The slow learning phase (d2-d5) was not assessed since there were no significant behavioural or structural changes during this time period. Improvements in performance were expressed as a relative change from baseline in percent to account for different baseline performance levels (i.e., SYN score at the beginning of d1) across subjects. Relative improvements in SYN (%) were calculated as: $[\text{ABS}(\text{SYNd2} - \text{SYNd1})/\text{SYNd1}] * 100$ for initial fast learning and as: $[\text{ABS}(\text{SYNd5} - \text{SYNd1})/\text{SYNd1}] * 100$ for overall improvement. These analyses aimed at investigating whether the extent of changes in WM metrics during each learning stage was related to the improvements on the task during the same period.

2.4 Results

2.4.1 Performance improvement in the SPFT

Participants in the LRN group learned the complex sequence progressively over the course of the training period as evidenced by the large decrease in temporal deviation (SYN) between the beginning of training (d1 block 1 mean SYN score = 224.01 ± 68.53) and the last block of d5 (89.31 ± 62.67). Moreover, the mean SYN score at the retention session (d17; 109 ± 60.5 ms) indicates that gains in performance were maintained. On the other hand, participants in the control group improved very minimally in performing the SMP task as the sequence was fairly easy and temporal

deviation was already minimal at the beginning of training (mean SYN score at d1 block 1= 33.98 ± 7.31 ; mean SYN at last block of d5= 19.23 ± 5.56). Scores were significantly different between groups; a repeated-measures ANOVA revealed a significant main effect of Group ($F(2,53)= 62.0$, $p < 0.001$) and an effect size (η_p^2) of 0.700, further showing how different the sequences are (see **Figure 4**). There were no significant correlation between performance in the task and sport or musical experience ($p > 0.05$).

There was also a main effect of Day ($F(5,265)= 30.2$, $p < 0.001$, $\eta_p^2= 0.363$) and a significant interaction of Day*Group ($F(5,265)= 20.7$, $p < 0.001$, $\eta_p^2= 0.438$). These main effects and interactions were still significant ($p < 0.001$) after Greenhouse-Geisser correction which was applied because sphericity was violated in this analysis. Consistent with the theories of learning stages, most improvements took place in the first days and then reached a plateau at d4 in the LRN group performing the complex task (LRN); post-hoc Tukey was significant between d1-d2 ($t=7.864$, $p < 0.001$), d2-d3 ($t= 4.367$, $p=0.002$), and nearly significant d3-d4 ($t= 3.497$, $p= 0.054$), but not significant between d4-d5 ($t= -0.774$, $p= 1.000$), nor between d5-d17 ($t= -1.755$, $p= 0.953$) (**Figure 4**). Post-hoc Tukey was also significant between d1-d17 ($t= 13.199$, $p < 0.001$) and d2-d17 ($t= 5.335$, $p < 0.001$), but not between d5-d17 ($t= -1.755$, $p= 0.953$) indicating that performance in the task was maintained after 12 days without practice.

In contrast, participants in the SMP group exhibited little significant improvement over the course of the 5 days of training. None of the pairwise comparisons between consecutive days were significant in this group and Post-hoc Tukey was also non-significant between d1-d5, indicating no significant improvement in the overall learning period. There was no significant difference between the performance of the LRN group and that of the SMP group on the SMP task (Post-hoc Tukey $p > 0.05$ between LRN group-SMP task and SMP group-SMP task at every time point). As expected, SYN scores of both groups performing the SMP task differed significantly from the SYN scores of the LRN task (Post-hoc $p < 0.001$ at every time point). Two participants from the SMP group were excluded from the analysis because their SYN scores on d3, and d4 for one of them, were outliers as they exceeded the mean by more than two SD.

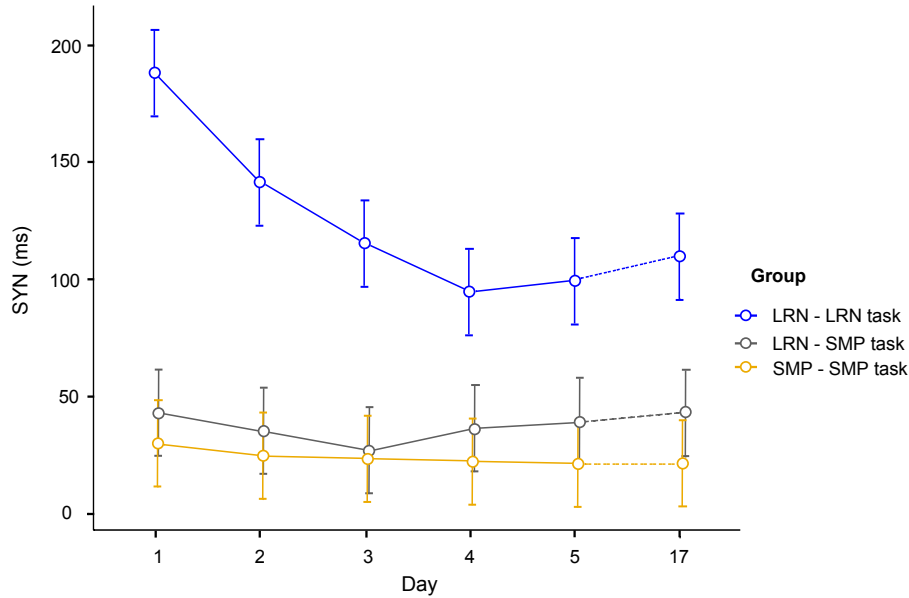


Figure 4. Behavioral Results. Temporal deviation (SYN; in ms) for each group and each task across training days (d1-d5) and retention session (d17), where the SYN value of each day is the mean across blocks. LRN – LRN task: learning group performing the LRN task (in blue); SMP – SMP task: control group performing the SMP task (in orange); LRN – SMP task: learning group performing the SMP task (in grey). Error bars represent the standard error of the mean.

2.4.2 WM microstructural changes across learning stages

Changes of opposite directions in both groups were found in the corticospinal tract, underlying the left primary motor cortex (M1) ($t= 4.20$, $p= 0.002$; **Figure 5b**). FA decreased in LRN, whereas FA increased in this cluster in SMP ($d5 < d1$ in LRN, $d5 > d1$ in SMP). The mean Δ FA in LRN was -0.029 , while FA increased by 0.0395 in the SMP group. Voxel-wise analyses also revealed a decrease in FA ($t= 5.01$, $p= 0.005$; mean Δ FA= -0.176) in the right ascending sensorimotor tract adjacent to the primary somatosensory cortex (S1), in the LRN group only, during overall learning ($d5 < d1$; see **Figure 5a**). Other DTI metrics for these contrasts were non-significant ($p_{FWE} > 0.05$).

There were also changes in FA in the same regions in both groups. These plastic changes were common to both groups and therefore considered non-sequence specific and more related to motor execution. FA had a near significant increase in the frontal inferior longitudinal (FIL) tract underlying the right pars opercularis (PO) in the early stage of learning ($d2 < d1$; **Figure 5c**) in both groups ($t= 4.02$, $p= 0.063$; mean Δ FA in all subjects= 0.115 , mean Δ FA in LRN= 0.125 , mean Δ FA in SMP= 0.104). In overall learning, FA increased significantly in the right anterior corona radiata adjacent to the frontal eye field (FEF; $t= 5.28$, $p= 0.023$; **Figure 5d**) in both groups (mean Δ FA in all subjects= 0.119 , mean Δ FA in LRN= 0.147 , mean Δ FA in SMP= 0.093). Other metrics

for these contrasts, and all other contrasts assessed, were non-significant ($p_{FWE} > 0.05$). The results are summarized in **Table 2**.

Table 2. Clusters in which significant changes in FA were found

	k (#voxels)	p_{FWE}	T	Peak Coordinates in MNI (mm)	Region
d5 < d1 in LRN	38	0.005	5.01	[14, -35, 60]	R ascending sensorimotor tract adjacent to S1 (Figure 5a)
d5 < d1 in LRN; d5 > d1 in SMP	42	0.002	4.20	[-24, -11, 30]	L corticospinal tract adjacent to M1 (Figure 5b)
d2 > d1 in both groups	25	0.063	4.02	[41, 14, 23]	R frontal inferior longitudinal tract adjacent to PO (Figure 5c)
d5 > d1 in both groups	30	0.023	5.28	[17, 29, 41]	R Anterior corona radiata adjacent to FEF (Figure 5d)

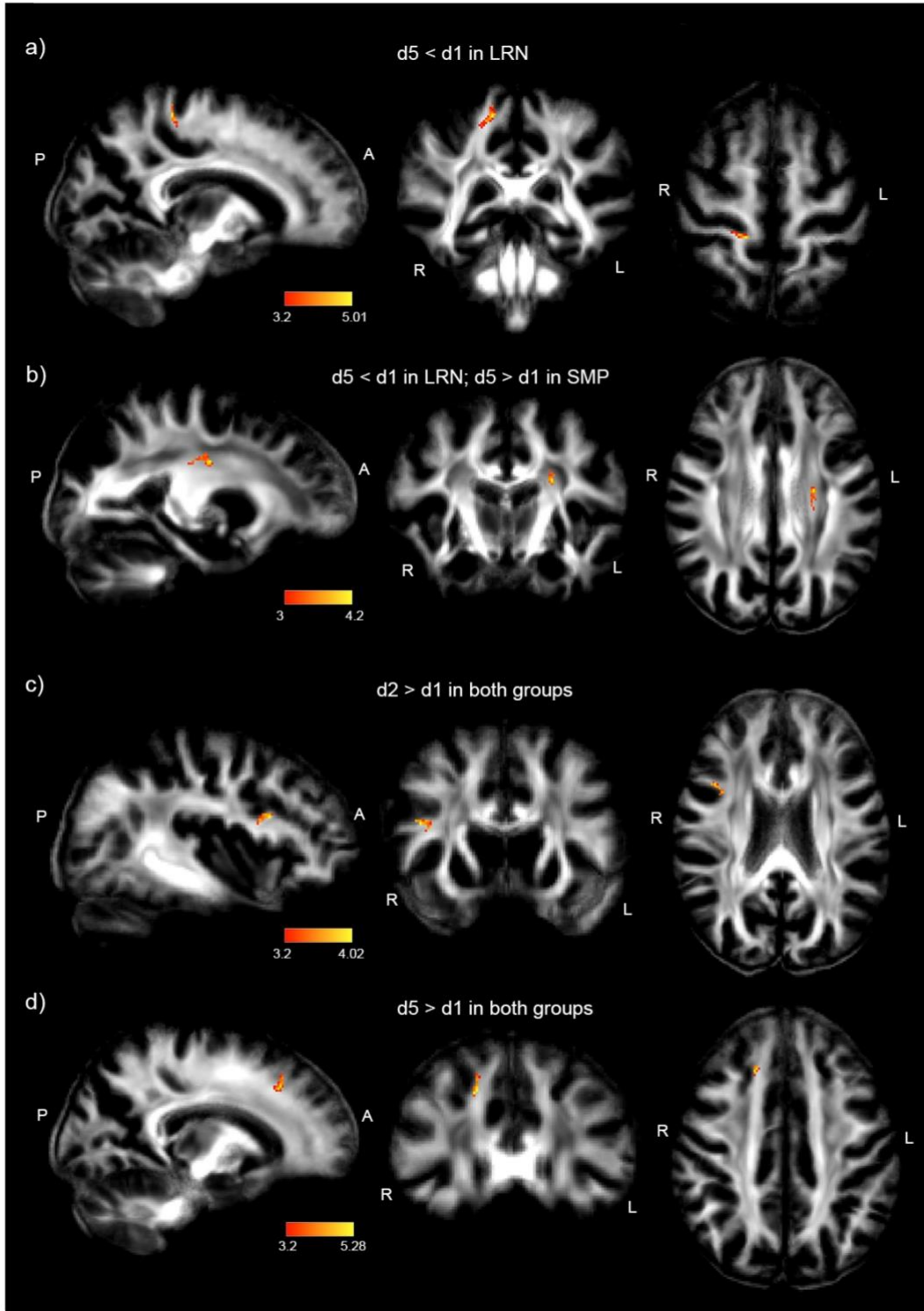


Figure 5. Changes in FA from voxel-wise analyses. *T*-stat maps (maximum intensity projection for better visualization) are overlaid on the mean FA image. a) Decrease in FA in the LRN group between d1-d5 in the right ascending sensorimotor tract connecting to the primary somatosensory cortex (S1). b) Decrease in FA in LRN and increase in FA in SMP between d1-d5 in the left corticospinal tract connecting to the primary motor cortex (M1). c) Increase in FA in both groups between d1-d2 in the right frontal inferior longitudinal (FIL) tract connecting to the pars opercularis (PO). d) Increase in FA in both groups between d1-d5 in anterior corona radiata connecting to the right frontal eye field (FEF).

2.4.3 WM microstructural changes associated with functional changes

WM microstructure in the ROI underlying the right SMA was altered during the training period in the LRN group (**Figure 6a**). FA was found to decrease significantly across days ($F(2, 36)= 5.82$, $p=0.006$, $\eta_p^2= 0.244$; **Figure 6b**) and Tukey's post-hoc test revealed that this decrease was significant between d1-d2 ($t= 3.072$, $p=0.011$) and between d1-d5 ($t= 2.823$, $p=0.021$), but not between d2-d5 ($t= -0.249$, $p=0.966$). There was also a significant decrease in AD (**Figure 6c**) in the R SMA ($F(1.38, 24.91)= 6.27$, $p=0.012$ after Greenhouse-Geisser correction, $\eta_p^2= 0.258$) and post-hoc tests showed that the differences were statistically significant between d1-d2 ($t= 3.300$, $p= 0.006$) and between d1-d5 ($t= 2.763$, $p= 0.024$). RD increased significantly across days ($F(1.44, 25.99)= 3.93$, $p= 0.044$ after Greenhouse-Geisser correction, $\eta_p^2= 0.179$) (**Figure 6d**). This increase bordered on statistical significance in Post-hoc Tukey's tests between d1-d2 ($t= -2.419$, $p=0.053$) and between d1-d5 ($t= -2.438$, $p= 0.051$), but not between d2-d5 ($t= -0.0190$, $p= 1.000$). MD showed no significant change in this ROI ($p > 0.05$). To test whether the DTI metrics changed in the SMP group, the same analyses (RM-ANOVAs) were conducted in that group. Diffusion metrics did not change significantly across days in the SMA ROI in the SMP group ($p > 0.05$).

Diffusion metrics in the other ROIs (L and R SPC, R GPi, and R PO) did not change significantly across days in repeated-measures ANOVA analyses.

Retention of WM microstructural changes

Changes in FA in the right S1 and left M1, which both decreased significantly between d1-d5 in LRNs, were not maintained at the retention session (d17). Paired samples t-tests revealed significant differences between mean FA values at d5 and mean FA at d17 (S1: $t(18)= 2.25$, $p= 0.037$; M1: $t(18)= 2.94$, $p= 0.009$) in the LRN group. There was however no significant difference between mean FA at d5 and at d17 in the WM tract underlying the left M1 in the SMP group ($t(19)= 1.11$, $p= 0.279$). Refer to Supplemental **Figure 1** for the time course of FA changes in S1 and M1.

FA in the right PO was not significantly different between d5-d17 ($t(38)= -1.31$, $p= 0.197$). However, when inspecting the time course of changes relative to baseline (see **Supplemental Figure 1**; Appendix I), we can see that FA slowly decreases after the time point of significant change (d1-d2; in both groups), from d2-d17. Retention did not take place in the right FEF, where

FA, which increased across the overall training period (d1-d5) in both groups, then decreased significantly between d5-d17 ($t(38) = -2.93$, $p = 0.006$).

Changes in all WM metrics were maintained at d17 in the right SMA (**Figure 6**). There were no significant differences between the mean values at d5 and those at d17 for FA and AD, which both decreased in the early stage of training (d1-d2) in the LRN group (FA: $t(18) = 0.035$, $p = 0.972$; AD: $t(18) = -0.174$, $p = 0.863$). The increased RD was also maintained at d17 as evidenced by the non-significant t-test d5-d17 ($t(18) = 0.025$, $p = 0.981$).

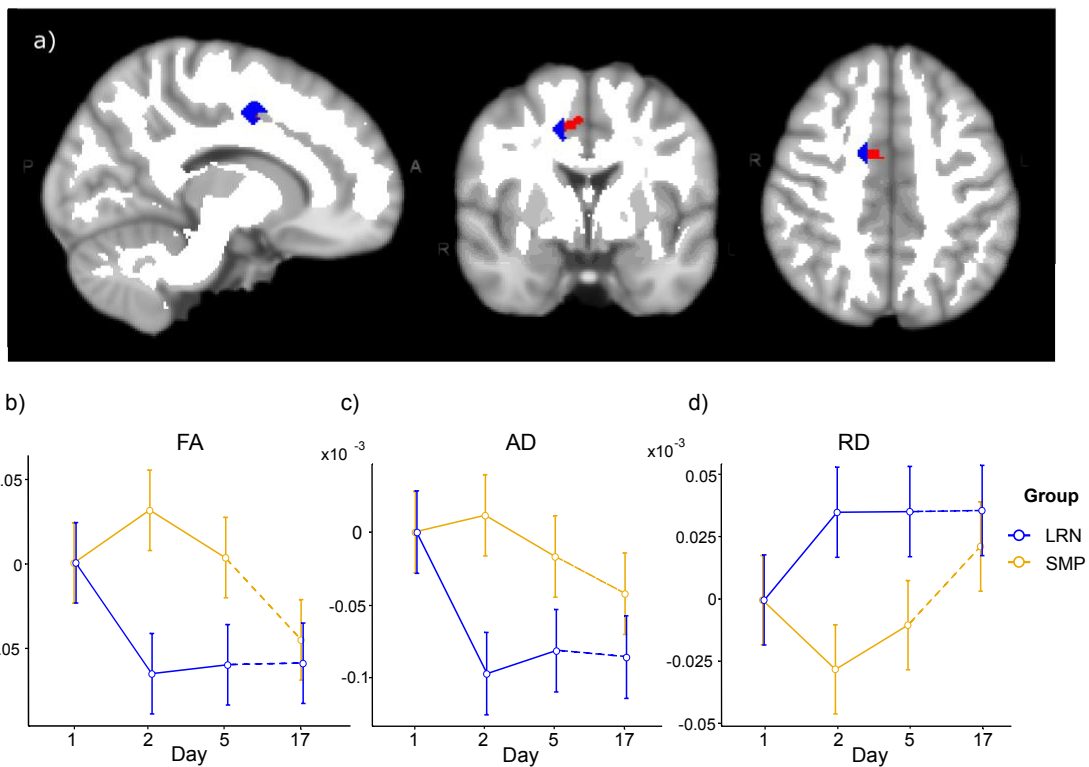


Figure 6. Changes in WM microstructure in the ROI underlying the right supplementary motor area (SMA) in which sequence-specific changes in functional connectivity were found (Jäger et al., 2021). a) The right SMA ROI from resting-state analyses (in red) and the WM ROI (in blue; overlaid on the WM mask in white) are both overlaid on the MNI152 template. Mean change in DTI metrics from baseline (d1) in both groups: b-c) FA and AD decreased in the LRN group (blue lines) between d1 and d2 and remained lower at d5 and d17. d) RD increased between d1 and d2 in LRN and remained higher at d5 and d17. DTI metrics in the right SMA in the SMP group did not change significantly ($p > 0.05$). Error bars represent the standard error of the mean.

Correlation with improvements in performance

No significant correlation between changes in FA and improvement in performance was found ($p > 0.05$).

2.5 Discussion

In this study, we investigated structural changes in WM over the course of 5 training days on a continuous visuomotor sequence task using DTI. Consistent with the behavioral results, where the greatest amount of improvements in temporal synchronization (SYN) were detected between the two first days (see **Figure 4**), we observed structural changes in WM only in the early phase of learning (d1-d2), and when looking at the overall learning period (d1-d5), which suggests a slower, more progressive change. Sequence-specificity was assessed through interaction analyses between the LRN group, who performed a complex sequence, and the control group (SMP), who performed a simple sequence, where the interaction is driven by the LRNs. FA was found to change in opposite directions in both groups in the left corticospinal tract (CST) inferior to the primary motor cortex (M1; **Figure 5b**) during overall learning. However, as the SMP group showed a greater change than the LRNs, we cannot establish that altered FA in WM underlying M1 is due to sequence learning per se. Changes in the right ascending sensorimotor tract (SMT) adjacent to the primary somatosensory cortex (S1) were also observed in the LRN group (**Figure 5a**). Changes underlying M1 and S1 were however not maintained at the retention session, 12 days after cessation of training. WM microstructure was altered during the early phase of learning in the ROI underlying the right supplementary motor area (SMA; **Figure 6**), where sequence-specific changes in functional connectivity were found during overall learning in this cohort (Jäger et al., 2021). Changes in WM microstructure underlying the right SMA were maintained at the retention session. Together, our findings provide evidence for training-dependent white matter plasticity in the sensorimotor network during short-term motor sequence learning.

2.5.1 Changes in the LRN group

Overall Learning - Right Primary somatosensory cortex (S1)

Fractional anisotropy decreased in the right ascending SMT in participants of the LRN group during overall learning (d1-d5; **Figure 5a**). We hypothesize that this decrease in FA in fiber tracts connecting to the right S1 may reflect suppression of activity in S1 ipsilateral to the hand used in the SPFT (Kastrup et al., 2008; Staines et al., 2002). Increased activity in the contralateral S1, and suppression of activity in the ipsilateral S1, as a result of task-relevant somatosensory stimulation and voluntary movements, have been reported in fMRI and EEG studies (Kastrup et al., 2008; Lei

& Perez, 2017; Nirikko et al., 2001; Staines et al., 2002). Blood flow suppression along with inhibition of S1 areas that are not involved in a task (e.g., ipsilateral body parts) from the prefrontal-thalamic system have been suggested as mechanisms to selectively gate sensory inputs (Drevets et al., 1995; Knight et al., 1999; Staines et al., 2002; Yamaguchi & Knight, 1990). In work by Drevets and colleagues (1995), blood flow reductions were observed in S1 ipsilateral to the expected stimulus when participants were anticipating somatosensory stimulation. The fact that changes in the SMT were only found in the LRN group may be due to increased levels of anticipation and attention in participants performing a complex task (Drevets et al., 1995; Halsband & Lange, 2006; Staines et al., 2002). We speculated that the increased attention necessary to perform the complex task would likely require greater activation of the dorsolateral prefrontal cortex. This could lead to greater inhibition of the ipsilateral S1, through the prefrontal-thalamic sensory gating system, as a way to suppress background noise and enhance processing of task-relevant inputs (Corbetta & Shulman, 2002; Halsband & Lange, 2006; Staines et al., 2002; Yamaguchi & Knight, 1990). Participants of the SMP group on the other hand may not need to pay as much attention to the task at hand, and to the associated sensory inputs, and may perform the repetitive sinusoidal sequence in a more automated manner.

This sensory gating, in which behaviorally-irrelevant regions are inhibited in order to effectively suppress unimportant, and potentially disruptive, inputs, may thus contribute to enhancing the responsiveness of the contralateral S1 to stimuli (Staines et al., 2002). Enhanced somatosensory inputs while performing a motor task have been associated with improvements in performance, and disrupting somatosensation during training impairs motor learning (Vidoni et al., 2010; Wei et al., 2018). As participants in this study were holding a pressure sensor between their thumb and index fingers, enhanced somatosensory inputs to the central nervous system due to SPFT training could result in the acquisition of a new task-specific sensory map (Braun et al., 2000; Pascual-Leone et al., 2005). This would provide better sensory feedback when subsequently performing the task, which could translate into improved accuracy in matching the reference bar (Wei et al., 2018).

Overall Learning - Left Primary motor cortex (M1)

FA in the left CST connecting to M1 was found to decrease in the LRN group, while it increased in the SMP group during overall learning (d1-d5; **Figure 5b**), indicating a relatively slow change in this region over the course of the five training days. As the SMP group did not show any

significant improvement in the SPFT, we are cautious in interpreting a change in this group without supporting behavioral evidence. The change in the LRN group on the other hand was accompanied by a change in behavior. We will thus focus the interpretation on the LRN group although we could speculate that any plastic change occurring in the SMP group could mirror changes in the LRNs but occur on a shorter time scale, as the sequences learned by each group have different complexities (Dayan & Cohen, 2011; Hyde et al., 2009; Karni et al., 1995).

Since we expect M1 to be activated when performing a motor task with the contralateral limb, as M1 has a known role in motor execution and the storage of learned sequence representations (Bengtsson et al., 2005; Hardwick et al., 2013; Hyde et al., 2009; Monfils et al., 2005; Penhune & Steele, 2012; Yokoi et al., 2018), this decrease in FA in the group performing a more complex task may seem contradictory. However, activity in M1 was previously shown to progressively decrease as a motor skill is learned (Dayan & Cohen, 2011; Poldrack, 2000; Seidler et al., 2005), possibly reflecting increased efficiency. Moreover, functional connectivity in M1 was found to increase in the LRN group during the early stage of training (Jäger et al., 2021). This suggests an important and active role of this area as we begin to learn a task, but then, as the motor sequence is learned, less neuronal resources would be needed to perform the task which could be reflected by decreased connectivity (Dayan & Cohen, 2011; Poldrack, 2000). In line with this, studies in musicians, experts in sensorimotor control, have also reported lower FA in motor circuits, including the bilateral CST and corona radiata (Imfeld et al., 2009; Penhune & Steele, 2012 for review; Schmithorst & Wilke, 2002). This decrease in anisotropy may be due to increased efficiency, or it may result from changes in the permeability of axonal membranes to water, or to an increased axonal diameter, which would lead to an increase in intracellular radial diffusivity (Beaulieu, 2002; Imfeld et al., 2009; Zatorre et al., 2012). Lastly, the development of a secondary fiber population in areas of crossing fibers is another potential mechanism through which FA could be reduced (Zatorre et al., 2012). Indeed, another study investigating structural changes associated with five days of MSL found that lower FA in the CST on the last training day correlated with better performance on the task (Steele et al., 2012). Since the significant correlation was located in a region where the CST and superior longitudinal fasciculus (SLF) cross, they hypothesized that maturation of the SLF, which would be the secondary fiber population here, drove the reduction in FA and promoted performance, as the SLF connects cortical regions that are involved in this task. The lack of significant changes in other diffusivity metrics in this study however does not allow to

disentangle the extent to which these factors contribute to the reduction in FA observed in the CST. Acquiring a greater number of diffusion gradient directions and strengths, and using more advanced diffusion models such as neurite orientation dispersion and density imaging (NODDI), and tractography, may allow to distinguish the underlying factors leading to altered FA in future studies (Steele & Zatorre, 2018; Tardif et al., 2016; H. Zhang et al., 2012a). However, the increase in functional connectivity observed during the early stage of learning (Jäger et al., 2021), along with the slower decrease in FA found in this study, support the hypothesis of a strong initial M1 involvement, followed by decreased M1 activation as learning progresses, reflecting enhanced network efficiency (Bassett et al., 2015; Costa et al., 2004; Dayan & Cohen, 2011; Finc et al., 2020; Karni et al., 1995; Mohr et al., 2016; Poldrack, 2000).

Fast Learning - Right Supplementary motor area (SMA)

ROI-based analyses were conducted in WM tracts underlying clusters of changes in resting-state centrality metrics, which included bilateral SPC, right GPi, right SMA and right PO (inferior part) (**Figure 3**). These analyses revealed changes in the WM ROI underlying the right SMA, in a fiber pathway we identified as the frontal aslant tract (FAT) (**Figure 6a**). The FAT connects the superior frontal gyrus (SFG), including the supplementary motor area (SMA), to the IFG (Briggs et al., 2018) and is thought to have a role in working memory, motor planning and coordination (Dick et al., 2019; Varriano et al., 2020). This pathway may function to coordinate sequential motor movements, especially in visuo-spatial tasks, to select the appropriate motor outputs (Dick et al., 2019). Moreover, the SMA has been shown to be involved in long-term (Hikosaka et al., 1995, 1996; Jenkins et al., 1994; Shima & Tanji, 2000; Tanji, 1996; van Mier et al., 1998), and short-term MSL (Vollmann et al., 2013), especially in action planning and in the organization of temporal aspects, such as timing and order, in a wide range of domains (e.g., language, working memory, motor sequences) (Cona & Semenza, 2017; Krakauer et al., 2019). A study using the same task provided strong evidence of the implication of the SMA in sequence learning by showing that non-invasive stimulation over the SMA led to improvements in performance of the SPFT (Vollmann et al., 2013).

Considering the known role of the SMA and FAT in sequence processing (Cona & Semenza, 2017; Dick et al., 2019; Krakauer et al., 2019; Shima & Tanji, 2000; Tanji, 1996; Varriano et al., 2020; Vollmann et al., 2013), we may expect connectivity to be enhanced with this type of task. However,

work from our group has found decreases in functional connectivity in the right SMA and right PO during overall learning in the same cohort (Jäger et al., 2021). It was hypothesized that reduced connectivity in these regions may thus reflect increased efficiency, or decreased need for resources to plan and coordinate movements, which would result in segregation of the network. This hypothesis is consistent with the view that the integration of multiple large-scale networks is necessary in the early stages of learning (Finc et al., 2020) and then, as a skill is mastered and becomes nearly automatic, a more easily reachable network, consisting in autonomous segregated modules, is sufficient to execute the task (Bassett et al., 2015; Finc et al., 2020; Mohr et al., 2016). In the present study, we found decreases in FA and AD in the WM ROI underlying the right SMA in the LRN group, during the early stage of learning and in overall learning, which were maintained during the retention period (**Figure 6a-c**). These findings, along with the increase in RD during the same period (**Figure 6d**), suggest a decrease in structural connectivity in the right SMA, which precedes a reduction in functional connectivity in the same region (Jäger et al., 2021). The idea of structure preceding function may seem contradictory, however resting-state connectivity is not assessed online, during task performance. Since WM tracts form the structural basis of connectivity, linking regions within resting-state networks, modulation of the supporting connections may be necessary to allow for greater communication. We could thus hypothesize that WM microstructure is altered in response to increased or decreased activation in a region during task performance (online) (Day & Sweatt, 2011; Fields, 2015; Forbes & Gallo, 2017; Zatorre et al., 2012) and that this then leads to modulations of resting-state networks (offline; rs-fMRI). It is therefore possible that structural changes underlie the subsequent changes in functional connectivity, though future studies would be necessary to fully investigate this hypothesis.

The spatial and temporal patterns of WM structural changes observed in the current study are in line with a theoretical framework describing two networks operating in parallel during MSL with different time courses (Hikosaka et al., 2002). Those two networks would each subserve distinct aspects of MSL: learning spatial coordinates, supported by a prefronto-parietal loop, and learning motor coordinates, which occurs more slowly and is supported by a M1-sensorimotor loop (Dayan & Cohen, 2011; Hikosaka et al., 2002). Both of these loops also receive contributions from different parts of the striatum and cerebellum depending on the learning stage and on the component learned (spatial vs motor) (Hikosaka et al., 2002; Penhune & Steele, 2012). Interestingly, we observed changes only in the motor loop (M1 and S1). This may be due to the

fact that learning spatial coordinates requires less time than learning motor coordinates (Hikosaka et al., 2002; Miller & Cohen, 2001; Penhune & Steele, 2012). This could mean, in the context of the SPFT, that spatial learning took place within the first session, perhaps on the timescale of minutes or hours considering the low complexity of the spatial coordinates to be learned in this task, and did not induce changes in WM that we could detect considering the much longer timescale of our measurements (i.e., days). Moreover, as a sequence is learned, its performance becomes more implicit, and thus relies more heavily on motor mechanisms and very little on attention-demanding spatial mechanisms (Hikosaka et al., 2002; Penhune & Steele, 2012). The SMA, another area in which we observed changes, both functionally (Jäger et al., 2021) and structurally, would provide the link between those two parallel loops, allowing for updated spatial representations to be used by the M1-sensorimotor loop to optimize motor output, according to this framework (Hikosaka et al., 2002). Indeed, Penhune & Steele (2012) emphasized the need for a high degree of interaction between these parallel systems to optimize MSL. The time course of changes in WM tracts underlying the SMA (fast change; d1-d2), and S1-M1 (slower changes; d1-d5), is also in line with the hypothesis that the SMA is involved in converting quickly acquired spatial coordinates to motor coordinates which are then processed by the M1-sensorimotor loop (Hikosaka et al., 2002). Moreover, the retention of WM microstructure alterations in the fiber tracts underlying the SMA points to a lasting role of this region in sequence learning. If the SMA is indeed involved in linking spatial to motor coordinates as has been shown previously (Hikosaka et al., 2002; Penhune & Steele, 2012), effectively mapping spatial representations to the appropriate motor outputs, this lasting change in underlying WM would suggest that these maps between coordinate spaces become part of long-term storage. The SMA is known for its role in sequence-specific learning and has been shown to be involved in the storage of sequence representations (Krakauer et al., 2019). The lasting changes observed in the WM tracts underlying the SMA in our study may thus reflect enhanced sequence storage efficiency in a more segregated, or autonomous, network (Bassett et al., 2015; Mohr et al., 2016).

Our findings are in line with previous literature (Bloechle et al., 2016; Karni et al., 1995; Klein et al., 2019; Lotze et al., 2003; Schmithorst & Wilke, 2002; Zatorre et al., 2012) and point to the highly dynamic plastic processes in WM tracts underlying the SMA-M1-sensorimotor loop, which parallel functional changes. It has been suggested that increases in anisotropy may reflect ongoing

enhancement of fibers organization while decreased FA may be related to increased network efficiency in later stages of learning (Schmithorst & Wilke, 2002).

2.5.2 Changes in both groups

Changes in anisotropy were also observed in both groups, suggesting the involvement of a number of regions in motor execution rather than sequence-specific learning. While no change in performance common to both groups was observed, participants of both groups performed a very similar task, made up of the same movements but ordered in sequences of different complexities, on five consecutive days. The element all participants have in common is thus the execution of these pinching movements daily. We provide a putative interpretation of these results below.

FA increased in WM tracts underlying the inferior frontal gyrus (IFG; opercular part) in the early stage of training (d1-d2; **Figure 5c**), and in the right anterior corona radiata (aCR) adjacent to the right frontal eye field (FEF) during overall learning (d1-d5; **Figure 5d**).

Overall Learning - Right Frontal Eye Field (FEF)

The frontal eye field (FEF) is involved in processing visual inputs and controlling voluntary eye movements and its activation is thought to be dependent on the saliency of the target (i.e., whether the target is behaviorally relevant) (Schall & Bichot, 1998; Vernet et al., 2014). In this task, participants maintained the gaze on the computer screen where the REF and FOR bars (**Figure 1**) provided both instructions (REF) and feedback (FOR) for the SPFT. Maintaining the gaze on a visual target for extended periods of time (~20 min/day for 5 consecutive days) may require high sustained activation in the FEF which could translate into structural changes in fiber tracts connecting this region during the overall learning period. The FEF clearly plays an important role in visually guided tasks, but its role has been investigated mostly in the context of goal-oriented saccadic eye movements (Schall & Bichot, 1998). However, in addition to its role in target selection in saccades, the FEF is also involved in the detection and analysis of visual inputs during periods of fixation of the gaze (Posner, 1980; Schall, 2004; Schall & Bichot, 1998). Non-invasive neurostimulation of the right FEF was shown to enhance visual perception and improve performance in a visual detection task (Chanes et al., 2012). Other studies support the idea that the FEF, especially of the right hemisphere, is involved in shifting visual attention without eye movement (Donner et al., 2000; Grosbras & Paus, 2002). Moreover, the FEF may play a role in

short-term memory of visuo-spatial information (Clark et al., 2012; Gaymard et al., 1999). The high potential for plasticity of the FEF has made this region a target for neurostimulation to increase visuo-spatial attention in healthy and patient populations (Vernet et al., 2014). Our results, showing FA increases in both groups, support the view that the FEF is highly plastic and suggest that this region is relevant in directing visual attention regardless of task complexity.

Fast Learning - Right Pars Opercularis (PO)

Increased FA was also observed in the frontal inferior longitudinal (FIL) tract underlying the dorsal part of the right pars opercularis (PO) between d1-d2 (**Figure 5c**). The FIL tract is a chain of u-shaped fibers connecting the dorsal part of the IFG (including the PO), to the middle frontal gyrus and pre-central gyrus (M1) (Catani et al., 2012). U-fibers of the frontal and parietal lobes have been shown to play an important role in sensorimotor integration (Catani et al., 2012, 2017), and have been hypothesized to coordinate movement planning and execution by linking motor and premotor regions (Catani et al., 2012). Moreover, the right PO has been specifically linked with fine motor control of manual motion (Briggs et al., 2019; Liakakis et al., 2011).

Our findings suggest that high task complexity might not be necessary to recruit the PO and incur structural changes in the underlying WM tracts, as the SMP sequence also requires the integration of sensory information to execute the task, as well as fine motor control in order for the appropriate amount of force to be applied on the device at the right time. Furthermore, the change in fiber tracts underlying the PO was observed in the early stage of learning, which may indicate a greater need for sensorimotor integration at this stage.

2.5.3 Relationships between behavioural and WM microstructural changes

Although the fact that most improvements occurred in the initial stage of learning (d1-d2) is consistent with the time period when changes in WM microstructure were found (d1-d2 and d1-d5), the time courses of behavioural and WM microstructural changes were different. While temporal deviation (SYN) followed an exponential decay across time (i.e., improvement in performance), changes in WM appeared highly dynamic, with early changes which were maintained in some instances (i.e., SMA), as well as slow decreases in FA which were not maintained at the retention session (e.g., S1 and M1). This makes it challenging to relate behavioral to structural changes at the same time point and may explain why significant correlations were not

found in this study. Other longitudinal plasticity studies have shown inconsistent relationships between brain plastic changes and behavioral outcomes with some studies reporting associations (e.g., Takeuchi et al., 2010), while others report no relationship (e.g., Scholz et al., 2009), or relationships in directions opposite to what is expected (for review, Zatorre et al., 2012). It has been suggested that correlations between performance and brain structural changes may be more closely linked to the amount of time spent training than on performance outcomes (Scholz et al., 2009). However, the fact that we did not identify a significant correlation between behavioural change and WM microstructural change is likely due to behaviour being the result of the integration of structural changes in WM and GM, as well as functional changes. Thus, WM changes alone could not predict the extent of performance improvement on the task. However, as some of the significant changes in WM were observed only in the LRN group, the only group showing behavioral change, in regions known for their role in motor sequence learning (i.e., SMA, M1, and S1), we argue that this provides evidence of behavioral relevance. Lastly, our findings showed different brain regions are involved in different stages of learning, suggesting the SMA became involved early in learning and had a persistent role in learning the SPFT, with changes still present 12 days after cessation of training, whereas sensorimotor regions played a more transient role. A better understanding of the relationships between changes in the brain's structure and behavior would thus likely be achieved using multi-parametric models that take into account several aspects of brain plasticity to identify the most relevant parameters.

2.5.4 Limitations and Future Considerations

The main limitation of this study is that the high field strength (7T) may make our findings less generalizable across studies, as 3T is still much more commonly used in research. The high spatial resolution of our acquisition may have also led to a decrease in SNR. Moreover, despite the high spatial resolution of our acquisition, the angular resolution was low, with only 20 directions, and a single diffusion gradient strength was applied (i.e., one shell). The angular sampling, number of diffusion shells and gradient strength were limited due to time constraints, as the study involved the acquisition of several other MRI sequences of long duration. In future studies, DWI acquisitions with higher gradient strengths and a greater amount of directions would allow for tractography to be performed, which would increase certainty when identifying fiber tracts where changes in scalar DTI metrics are observed, and for tract-based quantification of DTI metrics (Mukherjee et al.,

2008; Wakana et al., 2007). Furthermore, with a higher number of shells and directions, more advanced modelling approaches, such as NODDI, can be used, which would allow to disentangle factors such as fiber density and orientation dispersion, especially in areas of crossing fibers (Steele & Zatorre, 2018; Tardif et al., 2016; H. Zhang et al., 2012a). Furthermore, the combination of multiple quantitative MR parameters, such as magnetization transfer saturation (MTsat), proton density (PD) and longitudinal and transverse relaxation rates (R1 and R2*), would allow to specify the contributions of myelination and changes in axon morphology to training-induced WM plastic changes (Caeyenberghs et al., 2016; Deoni et al., 2008; Helms, Dathe, Kallenberg, et al., 2008; Weiskopf et al., 2015).

Another challenge when investigating neuroplasticity in MSL is that high variability in the duration of each learning stage, depending on the complexity of the task, makes it difficult to relate stage-specific findings across studies (Dayan & Cohen, 2011; Hyde et al., 2009; Karni et al., 1995). Moreover, our experimental design did not allow us to distinguish structural changes occurring during consolidation (i.e., offline), from those occurring during training (i.e., online). However, it is unlikely that the techniques used in the current study would have had the sensitivity to detect such subtle differences and the structural changes observed in WM are likely the sum of alterations taking place both during the training session (i.e., online) and in between sessions (i.e., offline).

Lastly, the motor sequence training period was of short duration in the present study which may limit the amount of observable structural changes. A longer training duration may have led to a greater amount of plastic changes in WM tracts which could have provided further insights into MSL-related neuroplasticity.

2.6 Conclusion

Our study provided evidence for white matter plasticity in the sensorimotor network, where the SMA plays a role in linking the spatial and motor aspects, in short-term learning of motor sequences. Our findings also highlighted the time course of plastic changes in this network as we scanned participants not only in the beginning and at the end of training, but also on the second day, allowing for the characterization of changes occurring in the early stage of training. Future ultra-high field MRI studies investigating plasticity in the context of MSL should use a high angular

resolution, and a higher number of diffusion shells of varying strengths. This would provide more precision in localizing areas of change and in characterizing the biological underpinnings of plastic changes in brain white matter.

CHAPTER III: Development of a toolbox for multivariate analysis

Preface

As we have seen in Study 1 (Chapter II), the metrics derived from diffusion tensor imaging (DTI), which is still the most commonly used model in imaging studies focused on WM, lack biological specificity. This makes it difficult to interpret findings as biological underpinnings that underlie WM changes cannot be easily inferred. More advanced models that are based on multi-shell high angular resolution imaging (e.g., NODDI, constrained spherical deconvolution, etc.) are gaining popularity in the field as they provide greater specificity. Although more specific, these models still do not provide a perfect representation of the underlying microstructure. Each of the derived metric consists in an indirect measure linking the MR signal to microstructural properties, and each comprises a set of assumptions and biases (Novikov et al., 2018). Moreover, techniques based on DWI do not yield measures specific to myelin. These limitations, and the necessity to characterize several microstructural properties simultaneously, has led many researchers to adopt multi-modal imaging. The high dimensionality data generated by multi-modal imaging (and/or several DWI models) provides a rich and comprehensive view of the underlying microstructure. However, multivariate approaches are needed to reduce the dimensionality of the data. Such approaches allow to leverage the strengths of each technique while mitigating their weaknesses. They also reduce the amount of multiple comparisons correction required and offer greater statistical power than univariate approaches (Avants, Duda, et al., 2008; Naylor et al., 2014; Owen et al., 2021).

The complexity of several multivariate approaches has been a significant hurdle in their adoption. For the second study of this thesis, I contributed to the development of an open-source toolbox for the computation of a multivariate distance measure (the Mahalanobis distance, or D2) that allows the integration of several MRI metrics. With the release of this toolbox, our aim is to enhance accessibility of the D2 approach for researchers from diverse backgrounds (e.g., those with limited computational skills or resources), thereby promoting its broader adoption in neuroimaging studies.

MVComp toolbox: MultiVariate Comparisons of brain MRI features accounting for common information across measures

Tremblay, Stefanie A*, Alasmar, Zaki*, Pirhadi, Amir, Carbonell, Felix, Iturria-Medina, Yasser, Gauthier, Claudine J, Steele, Christopher J

* Contributed equally to this work.

Published in *Aperture Neuro*. <https://doi.org/10.52294/001c.118427>

3.1 Abstract

Introduction: Multivariate approaches have recently gained in popularity to address the physiological unspecificity of neuroimaging measures and to better characterize the complexity of biological processes underlying behavior. However, commonly used approaches are biased by the intrinsic associations between variables, or they are computationally expensive and may be more complicated to implement than standard univariate approaches. Here, we propose using the Mahalanobis distance (D2), an individual-level measure of deviation relative to a reference distribution that accounts for covariance between measures. To facilitate its use, we introduce an open-source python-based tool for computing D2 relative to a reference group or within a single individual: the MultiVariate Comparison (MVComp) toolbox (<https://github.com/neuralabc/mvcomp>). The toolbox allows different levels of analysis (i.e., group- or subject-level), resolutions (e.g., voxel-wise, ROI-wise) and dimensions considered (e.g., combining MRI measures or WM tracts). Several example cases are presented to showcase the wide range of possible applications of MVComp and to demonstrate the functionality of the toolbox.

Methods & Results: The D2 framework was applied to the assessment of white matter (WM) microstructure at 1) the group-level, where D2 can be computed between a subject and a reference group to yield an individualized measure of deviation. We observed that clustering applied to D2 in the corpus callosum yields parcellations that highly resemble known topography based on neuroanatomy, suggesting that D2 provides an integrative index that meaningfully reflects the underlying microstructure. 2) At the subject level, D2 was computed between voxels to obtain a measure of (dis)similarity. The loadings of each MRI measure (i.e., its relative contribution to D2)

were then extracted in voxels of interest to showcase a useful option of the MVComp toolbox. These relative contributions can provide important insights into the physiological underpinnings of differences observed.

Discussion: Integrative multivariate models are crucial to expand our understanding of the complex brain-behavior relationships and the multiple factors underlying disease development and progression. Our toolbox facilitates the implementation of a useful multivariate method, making it more widely accessible.

Keywords: Multivariate analysis, white matter, covariance, personalized assessment, toolbox, python

3.2 Introduction

In the past decade, there has been exponential growth in the number of modeling approaches that link white matter (WM) microstructural properties and the MR signal (Novikov et al., 2018). Since none of the existing models (e.g., diffusion tensor, neurite orientation dispersion and density imaging (NODDI), etc.) is a perfect representation of the underlying microstructure, choosing a model and contrast for analyses can be challenging, potentially leading to errors in biological interpretation (D. C. Alexander et al., 2019; Novikov et al., 2018). Multi-modal imaging, and multivariate frameworks that combine several parameters derived from different models and modalities, have been suggested as a promising avenue to harness the complementarity of different neuroimaging-derived measures (Bells et al., 2011; Tardif et al., 2016; Uddin et al., 2019).

Multivariate frameworks have the potential to counteract issues arising from the physiologically unspecific nature of commonly used neuroimaging measures and to capture the complexity and heterogeneity of biological properties (Dean et al., 2017; Guberman et al., 2022; Seidlitz et al., 2018; Tardif et al., 2016; P. N. Taylor et al., 2020). Multiple mechanisms give rise to brain structure (e.g., myelination, cell proliferation), support neuroplastic change (Azzarito et al., 2023; Taubert et al., 2012) and behavioral performance (Seidlitz et al., 2018; Thiebaut de Schotten & Forkel, 2022) and are involved in neurological disorders (Iturria-Medina et al., 2017). Interpreting the results of univariate statistical analyses is thus challenging within this context. In addition to capturing a more nuanced picture of the expected mechanisms, multivariate statistical frameworks can offer greater statistical power than multiple univariate analyses as they reduce the amount of multiple comparisons correction required (Avants, Duda, et al., 2008; Naylor et al., 2014; Owen et al., 2021). Lastly, and perhaps most importantly, multivariate frameworks can be leveraged to move away from group comparisons and towards individual-level analyses, an essential step on the road to precision medicine (Chamberland et al., 2021; Marquand et al., 2016; Wolfers et al., 2018).

Multivariate approaches that combine structural MRI measures have been used in a number of promising contexts. At the group level, partial least squares (PLS) analyses and their variants can be used to assess the covariance between multiple measures (Khedher et al., 2015; Nestor et al., 2002). Other multivariate approaches that can be used in group analyses include principal

component analysis (PCA), Sparse Group Lasso, independent component analysis (ICA) and non-negative matrix factorization (Calhoun et al., 2001; Chamberland et al., 2019; Khedher et al., 2015; Plitman et al., 2020; Richie-Halford et al., 2021; W. Yang et al., 2011). At the individual level, inter-regional correlations of multiple measures can be used to create individual-specific network maps based on morphometric similarity that can then be linked to behavior (Seidlitz et al., 2018). Individualized network maps provide a more comprehensive structural mapping that captures both biological complexity and individual variability because they integrate multiple MRI features (Vandekar et al., 2016; Whitaker et al., 2016). However, in this study by Seidlitz et al., (2018), the shared covariance between MRI measures was not accounted for. This has the potential to bias inferences made from such analyses, as there is significant covariance between many commonly used imaging parameters (Carter et al., 2022; Uddin et al., 2019). Various multivariate approaches that can overcome this issue exist, including multivariate linear regression (Naylor et al., 2014; Young et al., 2010), machine-learning (Calhoun et al., 2001; Carbonell et al., 2020; C. Chen et al., 2019; Guberman et al., 2022; Khedher et al., 2015; W. Yang et al., 2011), and Hotelling's T^2 test (Avants, Duda, et al., 2008; Hotelling, 1947). However, many of these approaches (including multivariate linear regression and machine learning) are computationally expensive and some necessitate making subjective decisions (Alexopoulos, 2010; Gyebnár et al., 2019; Hayasaka et al., 2006; Naylor et al., 2014). The Hotelling's T^2 test, a multivariate extension of a two-sample t-test, is a simple yet powerful option for group comparisons (Avants, Duda, et al., 2008; Hotelling, 1947), but provides little insight at the individual level (Guberman et al., 2022).

Here we propose using the Mahalanobis distance (D_2) (Mahalanobis, 1936) for analyzing multimodal MRI measures. D_2 is closely related to Hotelling's T^2 but can also provide an individual-level measure of deviation relative to a reference distribution. It is defined as the multivariate distance between a point and a distribution in which covariance between features (i.e., imaging measures) is accounted for. Initially developed by P. C. Mahalanobis in 1936 to quantify racial similarities based on anthropometric measurements of skulls, D_2 can be thought of as a multivariate z-score where the covariance between features is accounted for (P. N. Taylor et al., 2020).

The D_2 approach has been used extensively in outlier detection, cluster analysis, and classification applications (Ghorbani, 2019; Kritzman & Li, 2010; Xiang et al., 2008). D_2 has also been used in

neuroimaging, mainly in the study of neurological disorders, to detect lesions (Gyebnár et al., 2019; Lindemer et al., 2015), or to evaluate the degree of abnormality in the brains of patients relative to controls (Dean et al., 2017; Guerrero-Gonzalez et al., 2022; Owen et al., 2021; P. N. Taylor et al., 2020; Yeatman et al., 2012), but also to study healthy WM development (Kulikova et al., 2015). Despite promising implementations and its high versatility, D2 has not yet been widely adopted. To facilitate its use, we present here an open-source python-based tool for computing D2 relative to a reference group or within a single individual: the MultiVariate Comparison (MVComp) toolbox. We provide a step-by-step guide to computing D2 using the MVComp tool (<https://github.com/neuralabc/mycomp>) for two distinctive scenarios: a) comparisons between a subject and a reference group, and b) within-subject comparisons between voxels. Lastly, the results of these example cases are presented and the general approach is discussed (Tremblay, Alasmar, et al., 2024a).

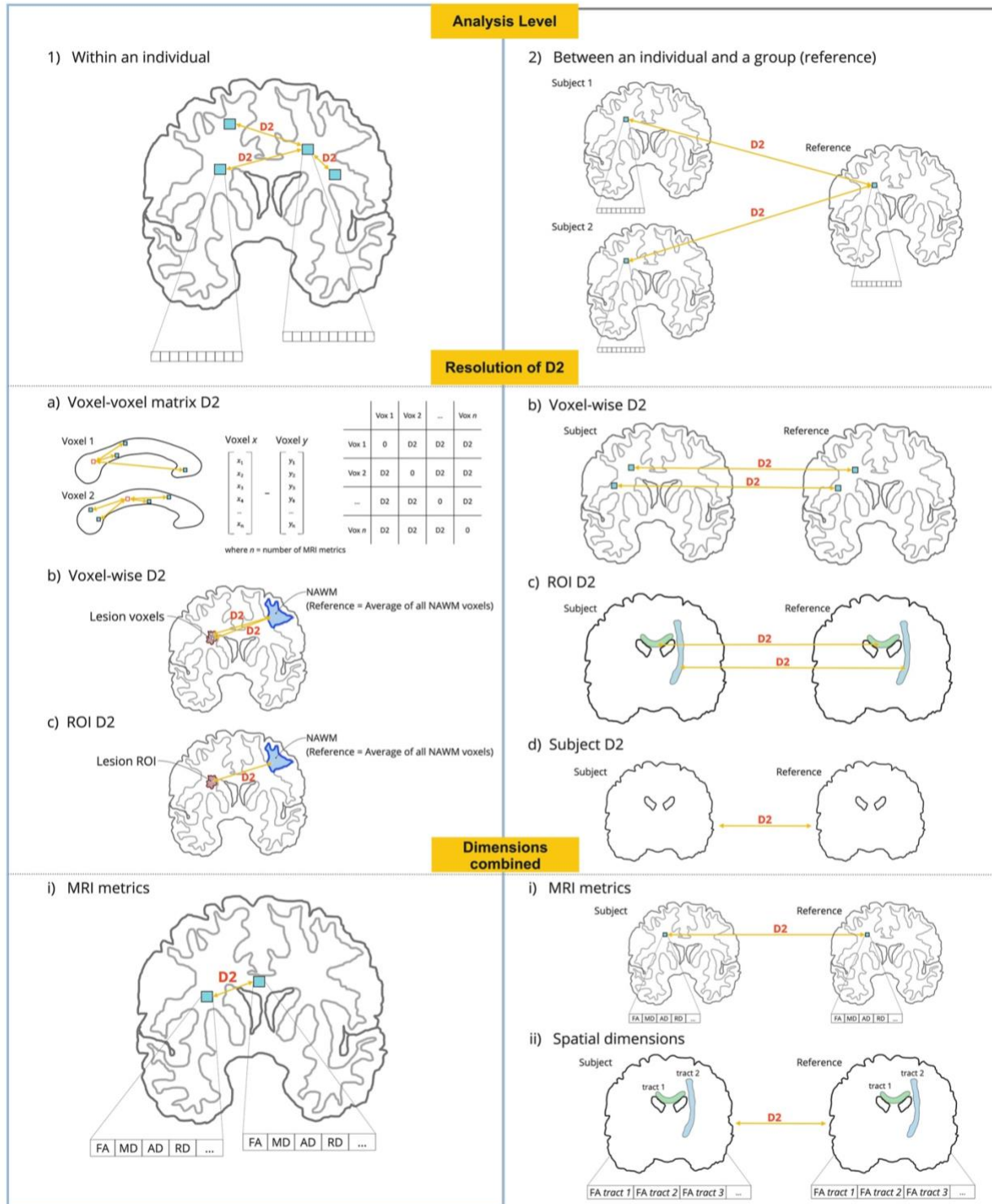


Figure 1. Implementations of the D2 framework in neuroimaging studies. Analysis level: (1) Within an individual (left panel, in light blue): D2 can be computed between different voxels or brain regions (e.g., WM tracts) within a single subject. (2) Between an individual and a group (right panel, in light gray): D2 can be computed between a subject and a reference group (e.g., control group). Resolution of D2: (a) Voxel-voxel matrix D2: D2 can be computed between each voxel and all other voxels in a mask of analysis, resulting in a D2 matrix of size n voxels \times n voxels (only applicable to analyses within an individual). (b) Voxel-wise D2: A D2 value can be computed at each voxel. (c) ROI D2: In this case, a D2 value is obtained for each WM tract, or other brain

region (ROI) defined by the user. (d) Subject D2: A single D2 value can be obtained per subject, resulting in a measure of global brain deviation from the reference (only applicable to analyses between an individual and a group). Dimensions combined: (i) MRI measures: when the dimensions combined through D2 are MRI measures, the length of the vector of data is the number of measures. (ii) Spatial dimensions: when WM tracts, or other parcellated brain regions, are combined through D2, the length of the vector of data is equal to the number of WM tracts (only applicable to analyses between an individual and a group; yields a single D2 value per subject).

3.3 Methods

3.3.1 General framework

Since D2 can be defined relative to virtually any reference of matching features, MVComp has been designed to support a wide range of applications. The first step is to define the set of multivariate data that will serve as the reference for computing D2. This choice depends on the hypothesis of interest, which will determine the *Level of Analysis* (**Figure 1**). D2 can be computed between different brain regions within an individual (with the individual's data also serving as the reference) or between an individual and a group, in spatially correspondent regions. In each case, multiple different *Resolutions* of analysis are possible, including voxel-wise and region of interest-(ROI) based comparisons.

Lastly, the choice of which dimensions to combine, either MRI-derived measures or brain regions (e.g., WM tracts), depends on what we want to capture. Combining brain regions within a multivariate measure allows to capture the degree of deviation from a reference even in the presence of high spatial heterogeneity (Owen et al., 2021; P. N. Taylor et al., 2020), while combining features is useful in the presence of mechanistic heterogeneity (i.e., several concomitant underlying biological mechanisms) and when preserving regional specificity is desirable (Guerrero-Gonzalez et al., 2022; Gyebnár et al., 2019; Lindemer et al., 2015). Both brain regions and MRI measures can be combined, as has been done by Dean and colleagues (2017). See **Figure 1** for a comprehensive view of the possible combinations of levels of analysis, resolutions and with different dimensions combined.

To illustrate the flexibility of the D2 approach, we present 4 examples:

Comparisons between an individual and a group (reference)

Example 1: Computing a voxel-wise D2 map for each individual

Data: Diffusion MRI (dMRI) data in several subjects

Level of Analysis: Between an individual and a group (**Figure 1** right panel)

Feature Resolution: Voxel-wise D2 (in all WM voxels) (**Figure 1b**)

Dimensions combined: dMRI-derived maps (**Figure 1i**)

In this example the reference would be defined as the voxel-wise group average for each dMRI-derived measure (m_1, m_2, m_n , where n is the number of measures) and D2 is computed by comparing the feature values in each voxel of an individual to the corresponding voxel in the reference (see Figure 2a-c). The resulting D2 maps can then be entered into second-level analyses to, for example, identify brain-behavior associations. If two groups are being analyzed (e.g., patients vs controls), the control group could be used as the reference and D2 values computed between each patient and the reference would represent voxel-wise multivariate distance from controls.

Example 2: Computing a single D2 score per individual

Data: dMRI data in several subjects

Level of Analysis: Between an individual and a group (**Figure 1** right panel)

Feature Resolution: Subject D2 (**Figure 1d**)

Dimensions combined: WM tracts (spatial dimensions) (**Figure 1ii**)

A single MRI measure can also be used and combined across multiple ROIs (e.g., mean FA in pre-defined WM tracts). The reference is defined as the group mean of each tract (m_1, m_2, m_n , where n is the number of tracts) and a single D2 value is computed for each individual. In this case, D2 represents a measure of how different an individual's WM microstructure is relative to a reference, across multiple tracts. This workflow can also be used if the user wishes to combine both brain regions and MRI measures. The reference is then defined as the group mean of each MRI measure for each tract ($m_{11}, m_{12}, m_{1n}, m_{i1}, m_{i2}, m_{in}$, where n is the number of MRI measures and i is the number of tracts and the length of the vector is $n \times i$). Again,

a single D2 score is obtained for each subject. These applications are not demonstrated in the present article but have been shown by others (Owen et al., 2021; P. N. Taylor et al., 2020) and can be implemented using MVComp.

To ensure that each subject's data will not bias their D2 values in single sample designs (i.e., where the entire sample is used as a reference) and to allow the evaluation of controls in two-sample designs, a leave-one-subject-out approach is also possible. In this way, the subject under evaluation is excluded from the group mean (reference) and covariance matrix prior to calculating D2.

Comparisons within an individual

Example 3: Computing D2 between lesion voxels and normal appearing WM (NAWM)

Data: dMRI data in one subject

Level of Analysis: within an individual (**Figure 1** left panel)

Feature Resolution: voxel-wise (in lesion voxels) (**Figure 1b**)

Feature Dimensions: dMRI-derived maps (**Figure 1i**)

Here, the level of analysis is within-subject, the dimensions combined are multiple dMRI-derived measures in each voxel, and the reference is the average of all voxels within a region of interest (ROI) for each dMRI measure. To investigate the distance between WM lesions and NAWM, the reference would be defined as the average of all NAWM voxels (m_1, m_2, m_n , where n is the number of measures) and D2 would be computed for each voxel classified as a lesion. Alternatively, the *resolution* could be ROI-wise if the user deems a single D2 value per lesion sufficient. This within-subject approach can also be used as a measure of similarity by computing D2 between all WM voxels and a reference ROI in a specific tract (e.g., voxels in the cortico-spinal tract, as in **Figure 2d**). Voxels within the same WM tract as the reference ROI are likely to have lower D2 values (indicating higher similarity) than voxels in other tracts or in areas of crossing fibers (**Figure 2e**).

Example 4: Computing D2 between each voxel and all other voxels in a mask

Data: dMRI data in one subject

Level of Analysis: within an individual (**Figure 1** left panel)

Feature Resolution: Voxel-voxel D2 matrix (**Figure 1a**)

Feature Dimensions: dMRI-derived maps (**Figure 1i**)

D2 can be calculated between every pair of voxels (voxel x – voxel y) within a mask of analysis to compute a voxel-voxel D2 matrix (see **Figure 1a**). In this case, the reference for computing the covariance matrix would be the data in all voxels contained in the mask.

See Supplementary material for a summary of the workflow for the 4 examples

(<https://mvcomp.readthedocs.io/en/latest/UserGuide/index.html>).

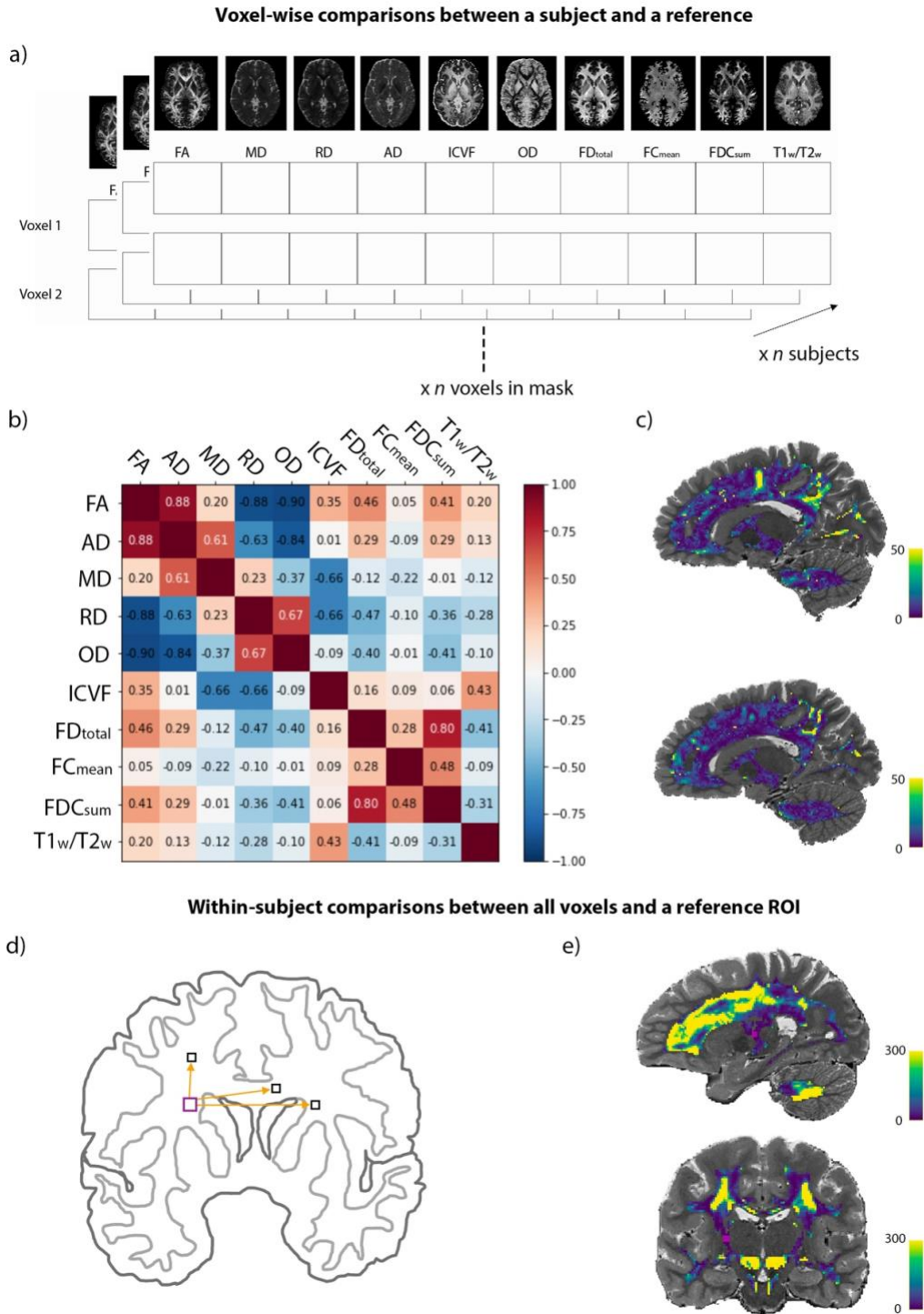


Figure 2. D2 workflow. Voxel-wise comparisons between a subject and a reference. (a) The multivariate space is illustrated here. In this example, we have a vector of 10 dMRI measures at each WM voxel for each subject. (b) The covariance matrix is computed from the reference feature matrix of shape n voxels in WM \times n features. The plot shows the amount of correlation between features in the reference sample (i.e., the whole group). (c) Voxel-wise D2 maps in two example subjects, where bright yellow represents areas of greater deviation from the reference population. Distinct patterns can be seen in the two subjects. Note that the leave-one-subject-out approach was used so that the data of the subject under evaluation was not included in the group mean (i.e., reference)

and covariance matrix prior to D2 calculation. Within-subject comparisons between all WM voxels and a reference ROI. (d) Schematic representation of the multivariate comparisons showing that D2 was computed between all WM voxels and a ROI of 24 voxels in the corticospinal tract (CST). (e) D2 map showing the multivariate distance between all WM voxels and the CST ROI (in pink).

**Data used for these examples will be presented in section 3.3.7.*

3.3.2 Data preparation

In all cases, data for all subjects should be preprocessed and all MRI measures of interest computed and transformed to bring them into the same voxel space. If instead of voxel-wise comparisons the user is interested in performing ROI-based comparisons, summary measures should be calculated for each region of interest (e.g., mean FA in each WM tract of interest) for each subject. Masks should also be generated to restrict analyses to chosen regions (e.g., WM) and these should also be transformed into the same space. Masks can be binary or thresholded at a later step within MVComp.

3.3.3 Computing the reference mean and covariance matrix

In the case of analyses between subject(s) and a reference (**Figure 1** right panel), the reference mean and covariance matrix are derived either from multiple features (**Figure 1i**) or multiple ROIs (**Figure 1ii**) in another group (e.g., control group). The comparison can also be between each individual and the mean of all other individuals if only a single group is available. In the case of analyses within an individual (**Figure 1** left panel), multiple features can be compared between voxels (e.g., **Figure 1 a-b**) or between ROIs (e.g., **Figure 1c**).

Comparisons between an individual and a group (reference)

Combining MRI measures

For this application, the group average of each measure must be computed from the reference group (`mvcomp.compute_average` can be used to perform this task). The `mvcomp.feature_list` function can then be used to create a list of feature names and a list of the full paths of the average maps that were created with the `compute_average` function. The `feature_gen` function extracts the feature matrix from a set of input images. Run on the reference group mean images with a provided mask, it returns the feature matrix (`m_f_mat` of shape n voxels in the mask \times n features), a mask vector (`mat_mask` of shape n voxels) and a nibabel object of the mask (`mask_img`). The mask

array contains zeros at voxels where values are *nan* or *inf* for at least one of the reference average maps in addition to the voxels below the threshold set for the mask. The `norm_covar_inv` function is then used to compute the covariance matrix (`s`) and its pseudoinverse (`pinv_s`) from the reference feature and mask matrices (`m_f_mat` and `mat_mask`). The `correlation_fig` function can be used to generate a correlation matrix from the covariance matrix (`s`), which is informative to verify if expected relationships between features are present.

A leave-one-out approach (where the individual to be compared to the reference is left out of the average) is preferred in cases where the individual subject is also a member of the reference group. This functionality is directly available in the model comparison function (`model_comp`). If the leave-one-out approach is used, it is not necessary to compute the group average nor to use the `feature_gen` and `norm_covar_inv` functions since the average and covariance matrix will be computed within the `model_comp` function from a group that excludes the subject for which D2 is being computed.

Combining spatial dimensions

The reference mean values (e.g., reference group mean FA in each WM tract) and covariance matrix are computed within the `spatial_mvcomp` function described in detail below. See (Owen et al., 2021; P. N. Taylor et al., 2020) for example applications of this implementation.

Comparisons within an individual

Voxel-wise D2 resolution

In the case of comparisons within a single subject, one of the possible applications is to compute D2 between specific ROIs. If the reference ROI is a set of NAWM voxels, the covariance matrix will be computed based on all voxels within that ROI in that subject. The path of the images (i.e., one image per measure) can be provided to the `feature_gen` function, along with the ROI mask, to create the reference feature matrix (`m_f_mat`) and mask vector (`mat_mask`). The `norm_covar_inv` function is then used to compute the covariance matrix (`s`) and its pseudoinverse (`pinv_s`) from the feature and mask matrices.

The `correlation_fig` function can again be used to visualize relationships between measures.

Voxel-voxel matrix D2 resolution

For this approach, the covariance matrix is computed from a feature matrix that includes all voxels in the mask of analysis. For instance, if we are interested in computing D2 between each voxel and all other voxels in the whole WM, the covariance matrix is based on all WM voxels. Therefore, the matrix provided to the `norm_covar_inv` function will be of shape n voxels in the mask \times n features.

3.3.4 Computing D2

Once the mean of the reference and the covariance matrix have been computed and the data for comparisons has been prepared, the D2 computation can be performed. Depending on the *resolution* of D2, this computation may be repeated several times (i.e., between every pair of voxels or once for each voxel or each ROI; **Figure 1a-c**), or it may only be done once if the user is interested in obtaining a single individualized score of deviation from a group (**Figure 1d**). The MVComp tool contains functions to easily compute D2 for each of these applications, according to this equation:

$$D^2 = (x - m)^T C^{-1} (x - m), \quad (\text{Eq. 13})$$

where x is the vector of data for one observation (e.g., one subject), m is the vector of averages of all observations for each independent variable (e.g., MRI measures), and C^{-1} is the inverse of the covariance matrix.

Comparisons between an individual and a group (reference)

Combining MRI measures

The `model_comp` function allows the calculation of voxel-wise D2 between each subject contained in the provided `subject_ids` list and the reference (group average) (**Figure 1** right panel; b). The user should specify the directories and suffix of the subjects' features and of the reference images (`feature_in_dir`, `model_dir`,

`suffix_name_comp` and `suffix_name_model`), the mask of analysis (`mask_f`) and a threshold if the mask is not binary (`mask_threshold`). If subjects or features are to be excluded at this point, they can be specified with the `exclude_subject_ids` and the `feat_sub` options, respectively. If the user wishes to use the leave-one-out approach, the `exclude_comp_from_mean_cov` option should be set to True. If this option is set to True, the mean (reference) and `pinv_s` are computed for each subject comparison, excluding the subject being compared before computing its D2. Therefore, it is not necessary to specify the directory of the reference (`model_dir`) in this application. The `model_comp` function yields a matrix containing the D2 data of all subjects (of size number of voxels x number of subjects). To obtain a D2 map (in nifti format) for each subject, the `dist_plot` function can then be used. The function also outputs a mean D2 map of all subjects and a histogram of all D2 values.

Combining spatial dimensions

The `spatial_mvcomp` function is used to compute a D2 score between each subject and the reference computed from all subjects (**Figure 1ii**). A matrix containing the data (e.g., mean FA in each WM tract) of all subjects (n subjects x n tracts) should be provided to the function. The `spatial_mvcomp` function returns a vector with a single D2 value per subject, reflecting the subject's individualized score of deviation from the group. As in `model_comp`, setting the `exclude_comp_from_mean_cov` to True leaves out the current subject when computing the mean and covariance.

Comparisons within an individual

Voxel-wise D2 resolution

The `mah_dist_mat_2_roi` function is used to compute voxel-wise D2 between all voxels within a mask and a specific ROI (**Figure 1** left panel; b). Here, in addition to the feature matrix containing the data for the voxels to be evaluated (n voxels in the mask x n features), the user will need to provide a vector of data for the reference ROI (i.e., mean across voxels in the ROI for each measure) and the inverse of the covariance matrix (`pinv_s`) calculated previously.

Voxel-voxel matrix D2 resolution

The `voxel2voxel_dist` function is used to compute D2 between each voxel and all other voxels in a mask (**Figure 1** left panel; a). This yields a symmetric 2-D matrix of size n voxels \times n voxels containing D2 values between each pair of voxels.

3.3.5 Statistical analysis

Once D2 values are computed, second-level statistical analyses can be used to assess group differences and longitudinal trajectories, to explore relationships between D2 and behavior. Machine learning techniques can also be used to reduce dimensionality and produce network maps based on (dis)similarity.

Comparisons between an individual and a group (reference)

For group comparisons, a two-samples t-test can be performed on D2 values (e.g., D2 values in patients vs D2 in controls), which would be equivalent to performing a Hotelling's T^2 test on raw measures (i.e., without computing D2). Alternatively, a statistical method such as the Bhattacharyya coefficient can be used to estimate the degree of overlap between the distribution of each group, where less overlap indicates a higher probability that the groups differ, as in (Dean et al., 2017). However, such group analyses are likely to average out interindividual variability and may be problematic when heterogeneity is high (Guberman et al., 2022). Wilk's criterion is another approach that can be used to define abnormality based on a calculated critical value that accounts for normative sample size, number of features, and multiple comparisons (Guerrero-Gonzalez et al., 2022; Gyebnár et al., 2019; Wilks, 1963).

Comparisons within an individual

In within-subject analyses, clustering approaches can be applied to the voxel-voxel matrix D2 to partition brain voxels into networks or other parcellations.

Changes in D2, either from the group or subject-level, can also be assessed through longitudinal analyses, to investigate WM damage progression or brain maturation for instance (Kulikova et al., 2015; Lindemer et al., 2015). D2, or changes in D2, can also be related to behavioral outcomes

(e.g., cognitive score, performance on a skill test, or symptom severity) in the same way one would with univariate measures of fractional anisotropy for instance (Dean et al., 2017; Owen et al., 2021; P. N. Taylor et al., 2020).

3.3.6 Determining feature importance

D2 summarizes the amount of deviation from a reference, based on several measures or brain regions, into a single score. This yields a useful metric to easily quantify *abnormalities*, whether due to pathology or to exceptional abilities such as musical skills. However, when summarizing several features into a single score, we lose specificity. To help address this limitation, it is possible to extract the contribution of each feature to the multivariate distances (D2) using functions of the MVComp tool to recover biological or spatial specificity.

Comparisons between an individual and a group (reference)

Combining MRI measures

If the user is interested in understanding the physiological mechanisms underlying microstructural deviations in a region of interest (e.g., voxels where D2 is high), the `return_raw` option of the `model_comp` function can be used. This allows the extraction of each measure's weight in D2. If `return_raw` is set to True, the function returns a 3D array of size (number of voxels) x (number of measures) x (number of subjects) that contains the voxel-wise distances for each feature and each subject. A flattened mask of the region of interest (e.g., a region of high D2) can then be applied to select voxels from the 3D array. The distances can be summarized across voxels and/or subjects to obtain a % contribution to D2 for each MRI measure within that region.

Combining spatial dimensions

The `return_raw` option is also available in the `spatial_mvcomp` function. If set to True, a 2D array of size (number of subjects) x (number of tracts) containing the distances between every subject's tract and the mean tract values is returned. These *raw* distances provide information regarding the contribution of each WM tract to D2, which gives insights on the localization of greatest deviation for each subject.

Comparisons within an individual

Voxel-wise D2 resolution

The `return_raw` option of the `mah_dist_mat_2_roi` function can be used to extract features' contributions. In this case, the distances between features in all voxels being compared and feature values in the ROI are returned. The output will be of shape (number of voxels) x (number of measures).

3.3.7 Experiments

Data Description

We computed 10 microstructural features for 1001 subjects from the Human Connectome Project S1200 data release (Van Essen et al., 2013) for these experiments. DWI, T1- and T2-weighted data were acquired using a custom-made Siemens Connectom Skyra 3 Tesla scanner with a 32-channel head coil. The DWI data (TE/TR=89.5/5520 ms, FOV=210×180 mm) were multi-shell with b-values of 1000, 2000 and 3000 s/mm² and a 1.25 mm isotropic resolution, 90 uniformly distributed directions, and 6 b=0 volumes. T1-w data was acquired with a 3D-MPRAGE sequence and T2w images with a 3D T2-SPACE sequence, both with a 0.7mm isotropic resolution (T1w: 0.7 mm iso, TI/TE/TR=1000/2.14/2400 ms, FOV=224×224 mm; T2w: 0.7 mm iso, TE/TR=565/3200 ms, FOV=224×224 mm). Anatomical scans were acquired during the first session, and DWI data were acquired during the fourth session. More details on the acquisitions can be found at: <https://www.humanconnectome.org/hcp-protocols-ya-3t-imaging>. The imaging data of 1065 young healthy adults, those who had undergone T1w, T2w and diffusion-weighted imaging, were preprocessed. The data of 64 participants were excluded due to poor cerebellar coverage.

Preprocessing

Diffusion Tensor Imaging

The minimally preprocessed HCP data was used (Glasser et al., 2013; Van Essen et al., 2013). The minimal preprocessing pipeline for DWI data includes intensity normalization of the b₀ images, eddy current and susceptibility-induced distortions correction, using DWI

volumes of opposite phase-encoding directions, motion correction and gradient nonlinearity correction. DWI data were registered to native structural space (T1w image), using a rigid transform computed from the mean b_0 image, and diffusion gradient vectors (bvecs) were rotated accordingly.

Most subsequent processing steps were performed using the MRtrix3 toolbox (Tournier et al., 2019). The minimally preprocessed DWI data was converted to the mif format, with the bvals and bvecs files embedded, after which a bias field correction was performed using the ANTs algorithm (N4) of the `dwibiascorrect` function of MRtrix3 (Tustison et al., 2010). The tensor was computed on the bias field-corrected DWI data (using `dwi2tensor`) and DTI measures were then calculated (FA, MD, AD and RD) using `tensor2metric` (Basser et al., 1994a, 1994b; Veraart et al., 2013).

Multi-tissue Multi-shell Constrained Spherical Deconvolution

The multi-tissue Constrained Spherical Deconvolution (CSD) was performed following the [fixel-based analysis \(FBA\) workflow](#) (Tournier et al., 2019). The T1-w images were segmented using the `5ttgen` FSL function of MRtrix3, which uses the FAST algorithm (Patenaude et al., 2011; R. E. Smith et al., 2012; S. M. Smith, 2002; S. M. Smith et al., 2004; Y. Zhang et al., 2001). Response functions for each tissue type were then computed from the minimally preprocessed DWI data (without bias field correction) and the five-tissue-type (5tt) image using the `dwi2response` function (`msmt_5tt` algorithm) (Jeurissen et al., 2014). The bias-uncorrected DWI data was used because bias field correction is performed at a later step in the FBA pipeline (Raffelt, Tournier, et al., 2017). The WM, GM and CSF response functions were then averaged across all participants, resulting in a single response function for each of the three tissue types. Multi-shell multi-tissue CSD was then performed based on the response functions to obtain an estimation of orientation distribution functions (ODFs) for each tissue type (Jeurissen et al., 2014). This step is performed using the `dwi2fod msmt_csd` function of MRtrix3 within a brain mask (i.e., `nodif_brain_mask.nii.gz`). Bias field correction and global intensity normalization, which normalizes signal amplitudes to make subjects comparable, were then

performed on the ODFs, using the `mtnormalise` function in MRtrix3 (Dhollander, Tabbara, et al., 2021; Raffelt, Dhollander, et al., 2017).

Registration

In order to optimize the alignment of WM as well as gray matter, multi-contrast registration was performed. Population templates were generated from the WM, GM and CSF FODs and the “nodif” brain masks of a subset of 200 participants using the `population_template` function of MRtrix3 (with regularization parameters: `nl_update_smooth= 1.0` and `nl_disp_smooth= 0.75`), resulting in a group template for each of the three tissue types (Tournier et al., 2019).

Subject-to-template warps were computed using `mrregister` in MRtrix3 with the same regularization parameters and warps were then applied to the brain masks, WM FODs, DTI metrics (i.e., FA, MD, AD and RD), T1w, and T2w images using `mrtransform` (Raffelt et al., 2011). T1w and T2w images were kept in native resolution (0.7mm) and the ratio of T1w/T2w was calculated to produce a myelin map (Glasser & Essen, 2011). WM FODs were transformed but not reoriented at this step, which aligns the voxels of the images but not the *fixels* (“fibre bundle elements”). A template mask was computed as the intersection of all warped brain masks (`mrmath min` function). This template mask includes only the voxels that contain data in all subjects. The WM volumes of the five-tissue-type (5tt) 4-D images were also warped to the group template space since these are then used to generate a WM mask for analyses.

Computing fixel measures

The WM FOD template was segmented to generate a fixel mask using the `fod2fixel` function (Raffelt et al., 2012; R. E. Smith et al., 2013). This mask determines the fiber bundle elements (i.e., fixels), within each voxel of the template mask, that will be considered for subsequent analyses. Fixel segmentation was then performed from the WM FODs of each subject using the `fod2fixel` function, which also yields the apparent fibre density (FD) metric. The `fixelreorient` and `fixelcorrespondence` functions were then used to ensure subjects’ fixels map onto the fixel mask (Tournier et al., 2019).

The fibre bundle cross-section (FC) metric was then computed from the warps generated during registration (using the `warp2metric` function) as FC is a measure of how much a fiber bundle has to be expanded/contracted for it to fit the fiber bundles of the fixel template. Lastly, a combined metric, fibre density and cross-section (FDC), representing a fibre bundle's total capacity to carry information, was computed as the product of FD and FC.

Transforming fixel measures into voxel space

In order to integrate all measures into the same multi-modal model, fixel metric maps were transformed into voxel-wise maps. As a voxel aggregate of fiber density, we chose to use the $l=0$ term of the WM FOD spherical harmonic expansion (i.e., 1st volume of the WM FOD, which is equal to the sum of FOD lobe integrals) to obtain a measure of the total fibre density (FD_{total}) per voxel. This was shown to result in more reproducible estimates than when deriving this measure from fiber specific FD (i.e., by summing the FD fixel metric) (Calamante et al., 2015). The FOD $l=0$ term was scaled by the spherical harmonic basis factor (by multiplying the intensity value at each voxel by the square root of 4π).

For the fiber cross-section voxel aggregate measure, we opted for computing the mean of FC, weighed by FD (using the mean option of the `fixel2voxel` function). We thus obtained the typical expansion/contraction necessary to align fiber bundles in a voxel to the fixels in the template.

Lastly, the voxel-wise sum of FDC, reflecting the total information-carrying capacity at each voxel, was computed using the `fixel2voxel sum` option.

NODDI measures

Bias field corrected DWI data was fitted to the neurite orientation dispersion and density imaging (NODDI) model using the python implementation of Accelerated Microstructure Imaging via Convex Optimization (AMICO) (Daducci et al., 2015; H. Zhang et al., 2012b). First, small variations in b values were removed by assigning the closest target bval (0, 1000, 2000 or 3000) to each value of the bvals file. This is to prevent the fitting algorithm from interpreting every slightly different bval as a different diffusion shell. A diffusion gradient scheme file is then created from the bvecs, and the new bvals file. The response

functions are computed for all compartments and fitting is then performed on the unbiased DWI volumes, within the non-diffusion weighted brain mask (nodif_brain_mask.nii.gz). The resulting parameters obtained are: the intracellular volume fraction (ICVF, also referred to as neurite density), the isotropic volume fraction (ISOVF), and the orientation dispersion index (OD). In this study, we will use ICVF and OD.

Generating masks for analyses

The maps of each of the 10 measures of interest (FA, AD, RD, MD, T1w/T2w, FDtotal, FCmean, FDCsum, ICVF and OD) were then averaged across all subjects. These average maps served as the reference. A WM mask was created by computing the group average of the corresponding volume of the T1 5tt image (volume 2). A threshold of 0.99 was applied within the MVComp toolbox's functions.

Experiment 1: Comparisons between an individual and a group (reference)

Here, we present an example case of using D2 in a large sample from the HCP dataset to quantify voxel-wise microstructural differences in WM according to several dMRI measures. Since the dataset used in this study contains the data of healthy young adults, a relatively homogeneous population, the entire sample was set as the reference and the leave-one-out approach was used to exclude the subject under evaluation. The analysis was restricted to the corpus callosum (CC). Voxel-wise D2 from 10 microstructural features was computed in the CC for each subject, yielding a D2 matrix of 1001 subjects X 2845 voxels. The D2 values represent voxel-wise microstructural differences in an individual's CC relative to the group average, while accounting for the covariance between features. Large D2 scores in a voxel indicate greater deviation from the group average, whereas scores closer to 0 indicate lower distance (i.e., more typical microstructure).

Past literature on CC neuroanatomy shows several segments that are distributed along the anterior to posterior axis, where each segment is defined by common microstructural properties and/or connectivity profiles (Aboitiz et al., 1992; Chao et al., 2009; Hofer & Frahm, 2006). We therefore hypothesized that these segments could be extracted via clustering, an unsupervised machine learning technique, of D2 values in the CC. We performed k-means clustering on the D2 matrix, setting the number of clusters to 9 based

on literature on CC topography (Aboitiz et al., 1992; Chao et al., 2009; Hofer & Frahm, 2006). Prior to clustering, we applied z-score and power transformation on the D2 matrix to achieve gaussian distributions of the standardized scores. Due to the large number of datapoints and potential effects of partial voluming, we observed several outliers in D2 maps of several subjects. We therefore excluded participants with at least 50 voxels that were deemed as outliers (i.e. exceeded a threshold of 5 standard deviations from the voxel mean D2). This yielded a final sample of 723 participants. Final visualization was done using BrainNet Viewer (<http://www.nitrc.org/projects/bnv/>).

Experiment 2: Comparisons within an individual

The within-subject approach allows the computation of voxel-voxel D2 in a single individual from multiple microstructural features. Here, D2 was calculated between each voxel and every other voxel in a subject's CC, while accounting for the covariance between the 10 microstructural features. All voxels within the CC of that subject were used to compute the covariance matrix and this same covariance matrix was used in the D2 calculation of every voxel. The resulting D2 matrix is a 2845 voxel X 2845 voxel dense matrix representing the distance between each voxel and every other voxel in the CC (**Figure 4a-b**). We standardized the matrix to z-scores and applied Principal component analysis (PCA) to reduce the matrix dimensionality (**Figure 4c**). Of note, eigendecomposition on the D2 matrix would be a valid alternative approach to reduce matrix dimensionality. In fact, because data was centered prior to applying PCA, the first eigenvector should be equivalent to the first principal component from PCA. We then extracted the contributions of each metric to D2 within the voxels with the largest and the lowest scores on the first principal component (**Figure 4d-f**).

3.4 Results

3.4.1 Experiment 1: Comparisons between an individual and a group

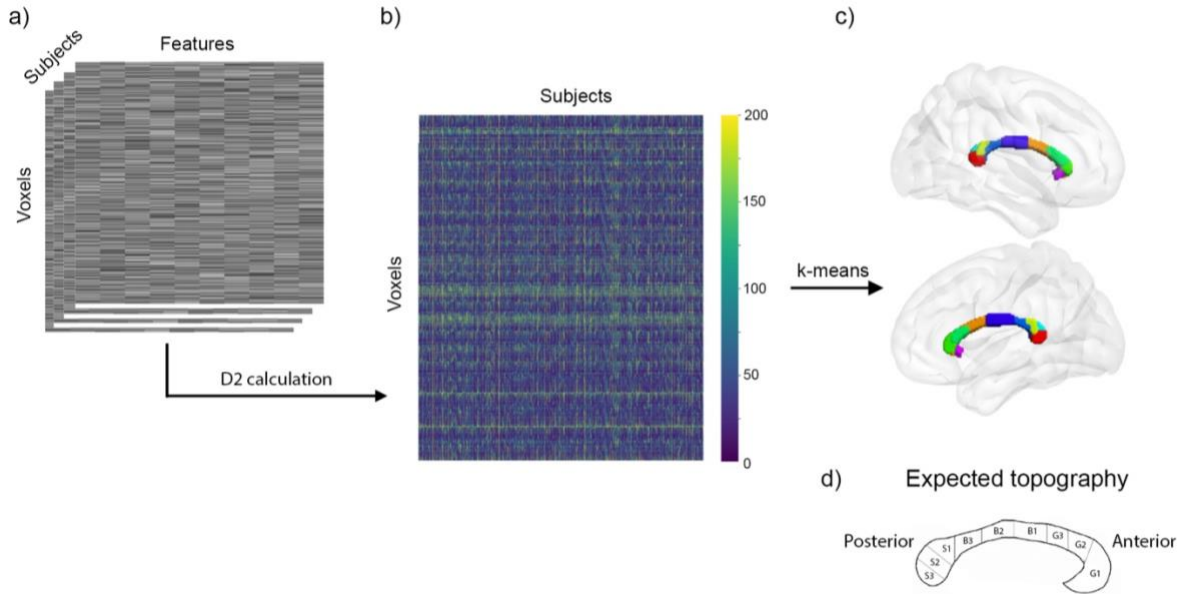


Figure 3. Voxel-wise comparisons between each subject and the reference. (a) Voxel-wise $D2$ is calculated between the reference (group average of the whole sample, except the subject under evaluation) and each subject's data (feature (10) \times voxel (2845) matrix), in voxels of the corpus callosum (CC). (b) This results in a $D2$ matrix of size subject (723 after exclusion of outliers) \times voxel (2845) containing the multivariate distance between a subject's data and the reference at each CC voxel. (c) Applying k -means clustering to the $D2$ matrix, voxels of the CC were partitioned into 9 clusters distributed along the anterior-posterior axis, in close accordance with known topography of the CC as seen in (d). (d) Schematic representation of CC topography based on literature (Aboitiz et al., 1992; Chao et al., 2009; Hofer & Frahm, 2006).

For this experiment, $D2$ was computed voxel-wise in the CC between each subject and a reference consisting in all other subjects (**Figure 3a-b**). K -means clustering was applied to the $D2$ matrix of size (subjects) \times (voxels). We observed that the 9 clusters were distributed along the anterior-posterior axis, in accordance with past evidence on CC microstructure and connectivity (Aboitiz et al., 1992; Chao et al., 2009; Hofer & Frahm, 2006). **Figure 3c** shows the clusters identified via k -means and **Figure 3d** shows the topography expected according to literature. The genu of the CC was clustered into 3 segments, while the midbody displays 2 segments. The splenium was divided into 4 segments (with one segment positioned on the isthmus). Segmentations from individual MRI measures are also presented in Supplementary material (Appendix II).

3.4.2 Experiment 2: Comparisons within an individual

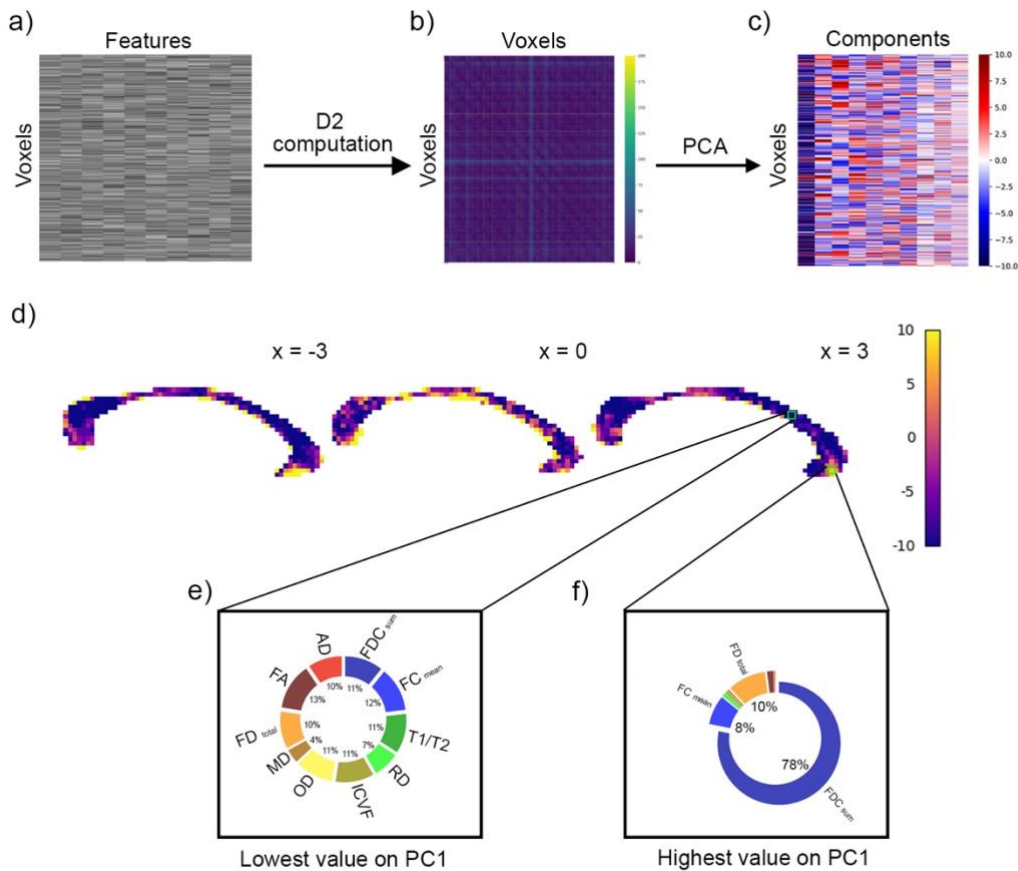


Figure 4. Within-subject voxel-voxel comparisons. D2 was computed between all voxel pairs from the (a) (features) x (voxels in the CC) matrix of a subject. (b) A voxel x voxel D2 matrix was generated. (c) PCA was then applied to the D2 matrix. The PCA matrix shows the first 10 principal components. (d) Voxels with the highest and lowest score on PC1 are shown. PC1 scores were scaled between -10 and 10 to facilitate visualization. (e) In the voxel with the lowest value on PC1, located in the midbody of the CC, all measures had approximately equal contribution to D2. (f) SumFDC contributed most to D2 in the voxel with the highest PC1 score, located in the genu of the CC.

For the within-subject experiment, D2 was computed between all voxel pairs in the CC of a single individual, yielding a voxel X voxel D2 matrix (**Figure 4a-b**). PCA was applied to the D2 matrix. **Figure 4c** shows the first 10 principal components (PCs). We then extracted the contributions (i.e., loadings) of each metric to D2 within the voxels with the largest and the lowest scores on the first principal component. The first PC explained 95% of the variance in the voxel X voxel dense D2 matrix. The highest and the lowest PC1 scores were in the genu and in the midbody of the CC, respectively (**Figure 4d**). In the voxel with the largest value on PC1, the fibre density and cross-section metric (sumFDC) contributed most

to D2, while mean diffusivity (MD) contributed the least (**Figure 4f**). On the other hand, in the voxel with the lowest score on PC1, all microstructural features had nearly equal contributions to D2, indicating minimal variability in this voxel (**Figure 4e**).

3.5 Discussion

In the present study, we introduced the MVComp tool (Tremblay, Alasmar, et al., 2024a), a set of python-based functions that can be used to compute the Mahalanobis distance (D2) for a wide range of neuroimaging applications. At the group-level, MVComp allows the calculation of a score that quantifies how different the brain structure of an individual is from a reference group. The MVComp tool provides a versatile framework that can be used to answer various research questions, from quantifying the degree of abnormality relative to a control group in individuals with a pathology, to exploring interindividual variability in healthy cohorts. At the subject level, D2 can be used to assess differences between regions of interest or to compute a measure of similarity that can then be used for subsequent analyses (e.g., graph theory/network analyses). Lastly, D2 can combine multiple MRI measures in the same spatial locations, or it can combine a single metric across several brain regions.

Our approach allows the integration of several variables while accounting for the relationships between these variables. Several biological properties influence the same neuroimaging metric and multiple neuroimaging measures indirectly reflect a similar underlying physiological property. This overlap means that accounting for covariance between measures is essential. It also means that using a single neuroimaging measure, or measures stemming from a single model, offers limited potential for interpretation and is biased by the set of assumptions of the chosen model (e.g., some models assume fixed compartment diffusivities while others attempt to estimate them) (Novikov et al., 2018). Similarly, integrating the assessment of multiple brain regions may map better onto behavior (e.g., cognition or disease severity) than assessing each region separately. Here, again the relationships between variables should be accounted for as observations are not completely independent from each other (i.e., in the same individual, there is likely a great amount of covariance between FA in different voxels or in different WM tracts). While some multivariate frameworks have been implemented in the neuroimaging field, several of them are either applicable at the group level or at the subject level (Alexander-Bloch et al., 2013; Hotelling, 1947; Marquand

et al., 2016; Seidlitz et al., 2018), and do not extend from one level to another. Frameworks using PCA can be implemented at both levels of analysis and recent studies have used PCA to combine dMRI measures, forming a reduced set of biologically interpretable variables (Chamberland et al., 2019; Guberman et al., 2022). While this method is interesting as it allows for dimensionality reduction and visualization of patterns between variables, it differs from D2 in several aspects. For instance, in PCA, the component loadings are usually calculated once on the whole sample and yield a set of new variables that will then be used for all subjects and in all brain regions. On the other hand, the features' loadings in D2 can be different for each subject and at each voxel. In this sense, D2 would provide a more individualized measure of deviation or dissimilarity relative to a reference, whereas PCA can be seen more as a dimensionality reduction method (Alexopoulos, 2010; Gyebnár et al., 2019; Hayasaka et al., 2006). Another advantage of the D2 framework is that it is highly versatile and relatively simple to implement. Moreover, the open-source MVComp toolbox we propose makes its implementation accessible for flexibly assessing a wide variety of research questions (see **Figure 1**).

One of the novelties of this work is that it provides the option to extract the contributions of all features within the D2 measure, similar to extracting loadings in PCA (Chamberland et al., 2019). This addresses one of the main limitations of some multivariate frameworks, allowing researchers to develop more mechanistic interpretations. In previous work using the D2 approach, the loadings (or weights) of the elements combined in the multivariate measure (i.e., either WM tracts or MRI measures) were not extracted, which has been a significant limitation (Dean et al., 2017). Characterizing the extent by which each feature contributes to D2 can provide important insights into the physiological underpinnings of the differences observed and/or their localization. To our knowledge, MVComp is the only available toolbox for computing D2 on imaging data. In this paper, we detailed the usage of MVComp through 4 example cases (see Supplementary material) covering a wide range of applications and presented the results of 2 experiments.

3.5.1 D2 reflects the underlying microstructure of WM

To provide specific examples of how MVComp can be used, the D2 framework was applied to the assessment of WM microstructure. We found the approach to be particularly suitable for the study of WM because of the number of modeling methods available for dMRI data. However, it is important to note that other types of tissues and imaging techniques can also be used within the

MVComp framework. By applying K-Means clustering to D2 in the corpus callosum, we observed a clear segmentation along the anterior-posterior axis (**Figure 3**), consistent with known topography from ex-vivo anatomical studies and tractography-based connectivity (Aboitiz et al., 1992; Chao et al., 2009; Hofer & Frahm, 2006). This high correspondence between clustered D2 and previously described CC topography suggests that the microstructural score obtained by combining several WM neuroimaging measures through D2 provides a useful index of microstructure.

At the individual level, D2 can capture the amount of (dis)similarity between voxels and, through the extraction of features' contributions (i.e., loadings), the specific microstructural properties underlying regional differences can be inferred. For example, in our within-subject experiment (**Figure 4**) we found high spatial heterogeneity in the relative contributions of different features to D2. The voxel with the highest loading on the first latent component (PC1) was primarily dominated by one metric (sumFDC) while the voxel with the lowest loading was characterized by similar weightings across all features. In the voxel with the highest PC1 score, sumFDC (combined metric of fiber cross-section and density, indicative of the amount of information-carrying capacity) contributed most to D2, meaning sumFDC had higher variability across CC voxels than other measures. This is consistent with the known microstructural properties of the CC, which shows regional variations in densities of fibers of different sizes along the CC (Aboitiz et al., 1992; Hofer & Frahm, 2006). Further, given that the CC is composed of tightly packed fiber tracts, MD would likely be very low in all those CC voxels (i.e., low variability), which would explain its low contribution. Overall, this supports the relevance of D2 in assessing variability in WM microstructure properties and showcases the use of the features contribution option (i.e., `return_raw`) included in MVComp.

3.5.2 D2 in the study of pathologies

Given the complexity of underlying pathological changes in various brain conditions, multiparametric approaches are a promising avenue to capture the combination of multiple changes in brain properties (Dean et al., 2017; Guberman et al., 2022; Guerrero-Gonzalez et al., 2022; Iturria-Medina et al., 2017; Owen et al., 2021; P. N. Taylor et al., 2020). For instance, D2 incorporating fractional anisotropy (FA) in multiple WM tracts in epileptic patients was found to show stronger associations with epilepsy duration than any univariate measure (e.g., mean FA in a

single WM tract) (Owen et al., 2021). Another study reported better performance using D2 encompassing FA in several WM tracts, vs using FA in a single tract, in discriminating between controls and individuals with TBI (P. N. Taylor et al., 2020). The multivariate D2 measure allowed for the discrimination of even mild TBI cases from controls and correlated significantly with cognitive scores. Similarly, using D2 combining both spatial (i.e., WM regions) and feature (i.e., different DTI measures) dimensions led to improved detection between autistic and typically developing individuals compared to univariate approaches or to D2 computed by combining brain regions only (Dean et al., 2017). Associations between D2 and autism symptom severity were also reported in this study, providing additional evidence that D2 can serve as a behaviorally relevant measure of WM abnormality.

Other interesting implementations have used D2 to detect and characterize lesions. Gyebnár et al. (2019) combined DTI eigenvalues into a voxel-wise D2 measure between epilepsy patients and controls to detect cortical malformations in patients. Voxels were identified as belonging to a lesion if their D2 value exceeded a critical value calculated using Wilks' criterion (Wilks, 1963), a criterion used for multivariate statistical outlier detection. In another implementation, D2 was employed to characterize the heterogeneity within WM lesions by computing the multivariate distance (combining T1-w, T2-w and PD-w signal intensities) between voxels in WM hyperintensities and those in normal appearing WM (NAWM) (Lindemer et al., 2015). D2 in WM hyperintensities progressed at a quicker rate in individuals who converted from mild cognitive impairment to Alzheimer's disease (AD) compared to those who did not convert. Interestingly, the rate of change of WM hyperintensities volume (i.e., lesion load), a metric more commonly used (Bilello et al., 2015; Schmidt et al., 2005), did not differentiate converters from non-converters cross-sectionally and longitudinally, suggesting that a characterization of WM lesion heterogeneity through a multivariate framework was more informative than the volume of WM lesions (Lindemer et al., 2015).

3.5.3 Limitations

There are some limitations of D2 computation as presented in MVComp. First, D2 itself is a squared measure, thus the directionality of the difference is non-specific. As it is currently implemented, it is not possible to determine whether a given subject's features are higher or lower than the average, although this information can be easily extracted by comparing the subject's

voxel values or ROI means to the mean of the group average on a per-metric basis. Future studies could potentially address this limitation indirectly by integrating with studies that model ground-truth biophysical properties to better interpret differences and/or splitting groups based on expected direction of change. Then, the directions of deviations from the average could be hypothesized a priori.

D2 is a sensitive multivariate distance measure that has since found applications in various fields, such as classification, cluster analysis, and outlier detection. Our implementation makes use of the sensitivity of D2 to detect multivariate deviations in WM microstructure. This high sensitivity also means the method can be affected by registration inaccuracies and partial voluming (PV). Therefore, special attention must be paid to ensure optimal alignment across subjects and modalities (e.g., using directional information from dMRI to align WM tracts). Strict tissue type masking (e.g., using a high threshold on probabilistic segmentation images) can also be used to limit the amount of PV. However, this may result in a large number of excluded voxels, especially for low resolution images. Alternatively, the PV effect can be quantified and accounted for (González Ballester et al., 2002; Gyebnár et al., 2019). The latter option would be preferable if the D2 framework was used to detect tumors and estimate their volume, for instance.

Another limitation of D2 as presented in MVComp is that its use is restricted to continuous variables. However, more recent formulations of D2 allow for nominal and ordinal variables to be incorporated in the model, in addition to continuous variables (Barhen & Daudin, 1995; de Leon & Carrière, 2005). Future developments of MVComp could thus allow generalization of D2 to include mixed data types (e.g. WM, sex, or other grouping variable).

3.6 Conclusion

We introduce a new open-source tool for the computation of the Mahalanobis distance (D2), the MVComp (MultiVariate Comparisons) toolbox (Tremblay, Alasmar, et al., 2024a). D2 is a multivariate distance measure relative to a reference that inherently accounts for covariance between features. MVComp can be used in a wide range of neuroimaging implementations, at both the group and subject levels. In line with the current shift towards precision medicine, MVComp

can be used to obtain personalized assessments of brain structure and function, which is essential in the study of brain conditions with high heterogeneity.

Data and Code Availability

The data is openly available from the Human Connectome Project

(<https://www.humanconnectome.org/study/hcp-young-adult/document/1200-subjects-data-release>) and the code of the MVComp toolbox is available at

<https://github.com/neuralabc/mvcomp> (Tremblay, Alasmar, et al., 2024a).

CHAPTER IV: Multivariate white matter in pre-clinical Alzheimer's disease

Preface

In study 2 (Chapter III), the usage of the MVComp toolbox was demonstrated in a large sample of healthy young adults. The toolbox allows the computation of the Mahalanobis distance (D2) from neuroimaging data, integrating information from several imaging metrics into a single score while considering the covariance between metrics. D2 provides a measure of deviation between a point and a reference distribution in a multi-dimensional space. Moreover, biological specificity can be recovered by extracting the contribution of each MRI metric to D2 in regions of interest. We showed in Chapter III that D2 is an integrative measure that meaningfully reflects the underlying microstructure, in line with known neuroanatomy. In addition, work by our group showed that D2 relates to cognitive and motor function in the same sample of healthy young adults (Alasmar et al., 2024). Together, these studies validate the D2 method, as implemented in MVComp, for the personalized assessment of alterations in WM microstructure.

For study 3, we applied the MVComp framework to the study of pathological alterations in a sample of older adults at risk of Alzheimer's disease (AD). Studying brain abnormalities in individuals with a familial history, and other AD risk factors, provides an opportunity to better understand the nature of the pathological changes occurring at the earliest disease stage. Changes in WM microstructure have been found to precede macrostructural atrophy and symptom onset in the prodromal stage of AD (Agosta et al., 2011; Araque Caballero et al., 2018; Maier-Hein et al., 2015). Alterations in WM microstructure have thus been suggested as early biomarkers for AD (G. Adluru et al., 2014; Bartzokis, 2004b; Maier-Hein et al., 2015). In study 3, we characterized WM microstructure comprehensively using 14 MRI metrics reflective of axonal density, fiber bundle cross-section, orientation dispersion, myelin and iron content, which were integrated within D2. Multivariate statistical analyses were then used to capture covariance patterns between multiple AD risk factors and WM microstructural deviations (D2) and links with cognition were explored.

Sex and APOE4-specific links between cardiometabolic risk factors and white matter alterations in individuals with a family history of Alzheimer's disease

Stefanie A. Tremblay, R. Nathan Spreng, Alfie Wearn, Zaki Alasmar, Amir Pirhadi, Christine L. Tardif, Mallar M. Chakravarty, Sylvia Villeneuve, Ilana R. Leppert, Felix Carbonell, Yasser Iturria Medina, Christopher J. Steele, Claudine J. Gauthier

For the PREVENT-AD Research Group

In revisions at Neurobiol aging (BioRxiv: <https://doi.org/10.1101/2024.08.21.608995>)

4.1 Abstract

Introduction: White matter (WM) alterations are among the earliest changes in Alzheimer's disease (AD), yet limited work has comprehensively characterized the effects of AD risk factors on WM.

Methods: In older adults with a family history of AD, we investigated the sex-specific and APOE genotype-related relationships between WM microstructure and risk factors. Multiple MRI-derived metrics were integrated using a multivariate approach based on the Mahalanobis distance (D2). The links between WM D2 and cognition were also explored.

Results: WM D2 in several regions was associated with high systolic blood pressure, BMI, and glycated hemoglobin, and low cholesterol, in both males and females. APOE4+ displayed a distinct risk pattern, with LDL-cholesterol having a detrimental effect only in carriers, and this pattern was linked to immediate memory performance. Myelination was the main mechanism underlying WM alterations.

Discussion: Our findings reveal that combined exposure to multiple cardiometabolic risk factors negatively impacts microstructural health, which may subsequently affect cognition. Notably, APOE4 carriers exhibited a different risk pattern, especially in the role of LDL, suggesting distinct underlying mechanisms in this group.

Keywords: White matter, cardiometabolic risk factors, LDL-cholesterol, sex differences, familial history, APOE4, myelin, memory

4.2 Introduction

Recent findings highlight widespread white matter (WM) alterations as a key mechanism in Alzheimer's disease (AD) development and progression (Agosta et al., 2011; Araque Caballero et al., 2018; Bartzokis, 2004b; Bartzokis et al., 2003; Tian et al., 2023; Wearn et al., 2024; R.-H. Yin et al., 2015). In fact, changes in WM microstructure were found to precede macrostructural atrophy and symptom onset in AD patients (Agosta et al., 2011; Araque Caballero et al., 2018; Maier-Hein et al., 2015), which suggests myelin breakdown is an important contributor to the pathophysiology of AD (Bartzokis, 2011). The particular vulnerability of oligodendrocytes to various insults (e.g., toxins, oxidative damage) is hypothesized to result in myelin and axonal degeneration over time, precipitating other pathological changes seen in AD such as increased iron (Bartzokis, 2004b, 2011). Alterations in WM microstructure have thus been suggested as early biomarkers for AD (N. Adluru et al., 2014; Bartzokis, 2004b; Maier-Hein et al., 2015).

Despite WM microstructure being affected early, WM measures are not frequently included in the study of prodromal AD, as more attention has been given to grey matter (GM) abnormalities, such as loss of cortical and hippocampal GM volume (Barnes et al., 2009; W.-Y. Wang et al., 2015). Characterizing WM microstructural alterations in individuals at high risk of developing AD is thus crucial in understanding this early stage. Having a familial history and the E4 genotype of the apolipoprotein E (APOE) gene increase the likelihood of developing AD, with a higher risk in females (Altmann et al., 2014). The APOE4 genotype impacts the brain's WM microstructure, likely due to its role in the transport of cholesterol, one of the main constituents of myelin (Bartzokis, 2004b). Modifiable risk factors such as physical inactivity, smoking, alcohol consumption, hypertension, diabetes, obesity, and low education also contribute to AD risk (Livingston et al., 2024). Understanding how these factors impact brain health may inform future interventions.

These modifiable risk factors exhibit complex relationships with WM. For instance, obesity and hypercholesterolemia, known risks for cardiovascular disease and AD (Alfaro et al., 2018; Lamar et al., 2020; Shobab et al., 2005), show mixed associations with WM integrity and cognition (Alfaro et al., 2018; Lamar et al., 2020; Warstadt et al., 2014). These inconsistencies may stem from the limited specificity of diffusion MRI measures, typically derived from diffusion tensor imaging

(DTI). For instance, reductions in fractional anisotropy (FA), often interpreted as a measure of WM integrity, can be due to axonal loss, but also to increased fiber orientation dispersion (Riffert et al., 2014). Advanced diffusion models such as NODDI (Dell'Acqua & Tournier, 2019; H. Zhang et al., 2012b) and myelin-sensitive techniques such as magnetization transfer imaging are thus needed to fully capture WM microstructural properties (Campbell et al., 2018; Helms, Dathe, Kallenberg, et al., 2008).

The multifaceted interplay between risk factors and WM health may also introduce complexity, leading to seemingly inconsistent results as some factors synergistically influence outcomes while others counteract each other (Alfaro et al., 2018; Foley et al., 2014; Mole et al., 2020; R. Wang et al., 2015; O. A. Williams et al., 2019). Importantly, genetic risk (i.e., APOE4) seems to exacerbate the impact of modifiable risk factors on WM (Foley et al., 2014; Mole et al., 2020; R. Wang et al., 2015; O. A. Williams et al., 2019). Together, this suggests that the combined effects of multiple risk factors contribute to alterations in WM microstructure. Therefore, integrative approaches, along with advanced WM imaging models, are needed to comprehensively assess the effects of AD risk factors on WM microstructure.

Multi-modal imaging and multivariate frameworks that combine several parameters are promising avenues to harness the complementarity of different neuroimaging-derived metrics (Tardif et al., 2016). One such approach, the Mahalanobis distance (D2) (Mahalanobis, 1936), provides an individual-level measure of deviation relative to a reference group, where voxels with greater D2 values in an individual represent WM areas that differ to a larger extent from the reference group. D2 is a squared distance measure between a point (i.e., measurements in an individual) and a distribution (i.e., reference data) in a multi-dimensional space, integrating several MRI metrics while accounting for covariance between metrics (**Figure 1**). We previously demonstrated that this method yields an integrative index that meaningfully reflects underlying microstructure in WM in line with known neuroanatomy (Tremblay, Alasmar, et al., 2024b), and that relates to cognitive and motor function in normal subjects (Alasmar et al., 2024).

In this study, we computed voxel-wise deviations in WM microstructure (WM D2) in a cohort of older adults with a family history of AD. We characterized the relationships between known risk factors for AD (education, BMI, blood pressure, cholesterol, and HbA1c) and WM D2 in each sex.

The effect of APOE4 genotype on the relationships between risk factors and WM microstructure was also assessed and links with cognition were explored in regions of interest.

4.3 Methods

4.3.1 Participants

The study population was taken from the PResymptomatic EValuation of Experimental or Novel Treatments for Alzheimer's Disease (PREVENT-AD) cohort which is composed of older adults (≥ 55 years old) with a familial history of Alzheimer's disease (parental or multiple-sibling) (Tremblay-Mercier et al., 2021). The participants, who were followed longitudinally starting in 2011 (some participants are still currently being followed), were all cognitively unimpaired (MoCA ≤ 25 , or considered normal after an exhaustive neuropsychological evaluation if < 25 , and CDR = 0) at the time of recruitment. Participants gave informed written consent before participating in the study. The procedures of the PREVENT-AD study were approved by the McGill institutional review board and/or Douglas Mental Health University Institute Research Ethics Board. The study was performed in accordance with the ethical standards of the 1964 Declaration of Helsinki.

In this study, we used the 'stage 2' MRI data acquired in 2019-2020 (data release 6.0) with a novel imaging protocol that includes multi-shell diffusion-weighted imaging (DWI) and multi-parametric mapping (MPM). Participants who had all DWI and MPM data were included in this cross-sectional study (N= 134). Of those, 97 were female (age = 67.7 ± 4.8 years, education years = 15.3 ± 3.5) and 37 were male (age = 68.6 ± 6.5 , education years = 15.7 ± 3.3). Previous time points were not used in this study since these advanced imaging protocols were not acquired in 'stage 1' (Tremblay-Mercier et al., 2021).

Table 1. Demographics data for each sex and for the sex-balanced reference group that was used for D2 calculation (mean \pm standard deviation). Missing data, if any, is indicated.

	Females	Missing	Males	Missing	Reference
N	97		37		74
Age (yrs)	67.7 \pm 4.8		68.6 \pm 6.5		68.1 \pm 5.9
Education (yrs)	15.3 \pm 3.5		15.7 \pm 3.3		15.5 \pm 3.2
APOE4 status	35 (36.1%)		18 (48.6%)		33 (44.6%)
SBP (mmHg)	124.0 \pm 13.9		127.4 \pm 11.7		124.2 \pm 12.3
BMI (kg/m ²)	26.9 \pm 4.9		27.3 \pm 4.1		27.2 \pm 4.8
Total cholesterol (mmol/L)	5.52 \pm 0.88	N = 1	4.80 \pm 0.90		5.19 \pm 0.90
HDL (mmol/L)	1.66 \pm 0.44	N = 1	1.35 \pm 0.33		1.52 \pm 0.44
LDL (mmol/L)	3.09 \pm 0.79	N = 1	2.71 \pm 0.88	N = 1	2.92 \pm 0.83
HbA1c (decimal percentage)	5.42 \pm 0.30		5.42 \pm 0.44		5.43 \pm 0.36
Hypertension treatment	22 [†]		10		14
Dyslipidemia treatment	15		12		19
Diabetes treatment	1		4		4
MoCA	28.35 \pm 1.38		27.78 \pm 1.83		28.0 \pm 1.59
RBANS - Immediate memory	106.5 \pm 13.1		102.1 \pm 12.8		105.0 \pm 13.1
RBANS - Delayed memory	104.9 \pm 11.4		103.6 \pm 9.9		105.6 \pm 9.6
RBANS - Total	101.1 \pm 11.1		101.9 \pm 11.7		102.6 \pm 10.7

SBP - systolic blood pressure, BMI - body mass index, HDL - high-density lipoprotein, LDL - low-density lipoprotein, HbA1c - glycated haemoglobin, MoCA - Montreal cognitive assessment, RBANS - Repeatable Battery for the Assessment of Neuropsychological Status.

*Normal ranges: SBP: < 120 mmHg, BMI: 18.5 to 24.9, total cholesterol: < 5.17 mmol/L, HDL: \geq 1.55 mmol/L, LDL: < 2.6 mmol/L, HbA1c: 4.0-5.2% (Cleeman, 2001; Karakaya et al., 2014).

†Current (at the time of the MRI) and past treatments were combined.

4.3.2 MRI Protocol

MRI data were acquired on a 3T Siemens PrismaFit scanner at the Douglas Research Centre. The multi-shell DWI sequence was a spin-echo EPI sequence (TR = 3000 ms, TE = 66 ms, phase-encoding direction = posterior-anterior (PA), resolution = 2 mm isotropic) with 100 measurements (isotropically spaced around a sphere) across 3 diffusion-weighted shells with gradient strengths of $b = 300$ s/mm² (7 volumes), $b = 1000$ s/mm² (29 volumes) and $b = 2000$ s/mm² (64 volumes) and 9 volumes acquired without diffusion weighting ($b = 0$). Five non-diffusion weighted volumes ($b = 0$) were also acquired in the opposite phase encoding direction (AP) for distortion correction.

An MPM acquisition was performed using three multi-echo gradient echo sequences (resolution = 1 mm isotropic) with different repetition times (TR) and flip angles (α) to obtain images with predominant T1- (TR = 18 ms, 6 echoes, TE = 2.16-14.81 ms, echo-spacing = 2.53 ms, $\alpha = 20^\circ$), PD- (TR = 27ms, 8 echoes, TE = 2.04-22.20 ms, echo-spacing = 2.57 ms, $\alpha = 6^\circ$), and MT-weighting (TR = 27 ms, 6 echoes, TE = 2.04-14.89 ms, echo-spacing = 2.57 ms, $\alpha = 6^\circ$). An off-resonance MT pulse (off-resonance frequency = 2.2 kHz, duration = 12.8 ms, flip angle = 540°) was applied prior to RF excitation to obtain MT-weighting (Helms, Dathe, Kallenberg, et al., 2008). The RF transmit field was measured using two Siemens turbo-flash sequences with flip angles of 8° and 80° (TR = 5000 ms, TE = 1.83 ms, resolution = 4 x 4 x 16 mm) preceded by a slice-selective preconditioning radiofrequency pulse, yielding anatomical and flip angle maps (Chung et al., 2010). RF receive field inhomogeneities were estimated using a pair of PD-weighted turbo-flash sequences acquired using either a body coil or a 32-channel head coil (TR = 344 ms, TE = 1.55 ms, $\alpha = 3^\circ$, resolution = 2 mm isotropic).

A T1-weighted anatomical scan was also acquired using a Magnetization-Prepared Rapid Acquisition Gradient Echo (MPRAGE) sequence (TR = 2300 ms, TE = 2.96 ms, TI = 900 ms, $\alpha = 9^\circ$, resolution = 1 mm isotropic) during the same session.

4.3.3 Preprocessing

We computed 14 microstructural metrics from the DWI and MPM data of the ‘stage 2’ time point in 134 participants of the PREVENT-AD cohort. These metrics were derived from the diffusion tensor imaging (DTI) model, the fixel-based analysis framework that derives fibre density and cross-section from fibre orientation distributions (FODs) computed using multi-tissue constrained spherical deconvolution (CSD) (Jeurissen et al., 2014), and the neurite orientation dispersion and density imaging (NODDI) model (H. Zhang et al., 2012b). MPM was used to compute quantitative maps of longitudinal relaxation rate (R1), effective transverse relaxation rate (R2*), effective proton density (PD*), and magnetization transfer saturation (MTsat) (Weiskopf et al., 2013).

Diffusion Tensor Imaging

Most processing steps were performed using the MRtrix3 toolbox (Tournier et al., 2019). DWI data were denoised and then preprocessed using the `dwifslpreproc` MRtrix3 function, which includes correction for motion and Eddy currents (Eddy tool in FSL 6.0.1), and correction for susceptibility-induced distortions (`topup` tool in FSL) using b0 volumes of opposite phase-encoding polarities (AP). Preprocessed DWI data were then upsampled to the MPRAGE T1w image resolution (1mm isotropic). Bias field correction was performed using the N4 algorithm of ANTs (3.0) within a mask computed using the brain extraction tool (`bet`) of FSL on the b = 0 preprocessed volume (Tustison et al., 2010). A brain extraction of all DWI volumes was then applied using the b = 0 mask to remove all non-brain voxels. The tensor was computed on the bias field-corrected DWI data (using `dwi2tensor`) and DTI metrics were then calculated (FA, MD, AD and RD) using `tensor2metric` (Basser et al., 1994b).

Fixel-based analysis

The fixel-based analysis (FBA) [pipeline](#) which allows the computation of fibre density and cross-section from FODs was followed (Tournier et al., 2019). The workflow is described in details in (Tremblay, Alasmar, et al., 2024b) and briefly summarized here. First, MPRAGE T1-w images were segmented using the `5ttgen` FSL function of MRtrix3, which relies on the FAST algorithm (R. E. Smith et al., 2012). Response functions for WM, GM, and CSF were computed from the uncorrected DWI data and the five-tissue-type (5tt) image via the `dwi2response` function (`msmt_5tt` algorithm) (Jeurissen et al., 2014). The response functions were then averaged across

participants to generate a single response function per tissue type. Multi-shell multi-tissue CSD was performed to estimate orientation distribution functions (ODFs) for each tissue type using the `dwi2fod msmt_csd` (Jeurissen et al., 2014). Finally, bias field correction and global intensity normalization were applied to the ODFs using `mtnormalise` (Raffelt, Dhollander, et al., 2017).

Registration

Multi-contrast registration was used to optimize the alignment of white and gray matter, as described previously (Tremblay, Alasmar, et al., 2024b). Population templates for WM, GM and CSF were created using the `population_template` function of `Mrtrix3` (with `nl_update_smooth= 1.0` and `nl_disp_smooth= 0.75`) from the FODs of all participants (Tournier et al., 2019). Subject-to-template warps were computed with `mrregister` and applied to brain masks, WM FODs, and DTI metrics (i.e., FA, MD, AD and RD) using `mrtransform` (Raffelt et al., 2011). A template mask, including only voxels present in all subjects, was derived from the intersection of all warped brain masks (`mrmath min` function). The WM volumes from the five-tissue-type images were also warped to the group template space and averaged across participants to be used as a WM mask for analyses (thresholded at a later step).

Computing fixel metrics

Fixel metrics were computed as described in (Tremblay, Alasmar, et al., 2024b). Briefly, a fixel mask, containing all fiber bundle elements (i.e., fixels) for each voxel, was created by segmenting the WM FOD template (Raffelt et al., 2012; R. E. Smith et al., 2013). The WM FOD of each subject was then segmented using the `fod2fixel` function, which also provided the apparent fibre density (FD) metric. The `fixelreorient` and `fixelcorrespondence` functions were then used to ensure correspondence between the subjects' fixels and the fixel mask (Tournier et al., 2019). The fibre bundle cross-section (FC) metric was derived from the warps created during registration using the `warp2metric` function. FC quantifies the extent of expansion or contraction required for a fibre bundle to align with those in the fixel template. Finally, a combined metric, fibre density and cross-section (FDC), representing the overall capacity of a fibre bundle to carry information, was calculated as the product of FD and FC.

Fixel metrics were then converted into voxel-wise maps to allow for integration with other voxel-wise metrics. For the voxel aggregate of fiber density, we used the $l=0$ term of the WM FOD

spherical harmonic expansion (i.e., 1st volume of the WM FOD, equivalent to the sum of FOD lobe integrals), which provides a voxel-wise measure of total fibre density (AFD_{total}). This approach yields more reproducible estimates than summing fiber-specific FD (Calamante et al., 2015). For the voxel aggregate of fiber cross-section, we calculated the mean of FC, weighted by FD, using the `mean` option of the `fixel2voxel` function. This metric represents the typical expansion/contraction required to align fiber bundles in a voxel to the template fixels. Finally, the voxel-wise sum of FDC, representing the total information-carrying capacity per voxel, was computed using the `fixel2voxel` `sum` option.

NODDI metrics

The python implementation of Accelerated Microstructure Imaging via Convex Optimization (AMICO) was used to fit the neurite orientation dispersion and density imaging (NODDI) model to bias field-corrected DWI data using default parameters (Daducci et al., 2015; H. Zhang et al., 2012b). Fitting was performed within the brain mask and yielded 3 parameters: the intracellular volume fraction (ICVF, also referred to as neurite density), the isotropic volume fraction (ISOVF), and the orientation dispersion index (OD). The NODDI metrics were then warped to group space using the transforms generated previously.

Multi-parametric mapping

Multi-echo T1-w, PD-w and MT-w images were processed using the hMRI toolbox (v 0.3.0) in Matlab (Tabelow et al., 2019; Weiskopf et al., 2013). First, all images including field maps were re-oriented using the “AutoReorient” module. This reorientation is based on rigid-body coregistration of a reference image to an MNI template. The first T1-w echo was coregistered to the avg152T1 SPM canonical template and all other images were reoriented. Quantitative R2*, R1, PD and MTsat maps were computed from the reoriented images and field maps using the “Create hMRI maps” module with default parameters. Corrections for RF sensitivity bias, using measured body and head coil sensitivity maps, and for B1 transmit bias field using the TFL B1 mapping method (requires an anatomical image and a flip angle map) were also performed within the “Create hMRI maps” module. MPM maps were warped to the group space.

4.3.4 Computing multivariate distance metric (D2)

The MVComp toolbox was used to compute D2 from the 14 WM features (FA, AD, RD, MD, AFDtotal, meanFC, sumFDC, ICVF, ISOVF, OD, R2*, R1, PD and MTsat) (Tremblay, Alasmar, et al., 2024b). The first step in computing D2 is to determine the reference from which the multivariate distance will be calculated. Here, because the sample is unbalanced in terms of sex, a sex-balanced reference was built from the 37 male participants and 37 randomly selected females. Demographic characteristics of the reference group, shown in **Table 1**, were representative of the full sample in terms of age (68.1 ± 5.9), education, cognitive status, and other risk variables. Group averages were then computed from the reference group ($N = 74$) for each of the 14 metrics using the `compute_average` function of MVComp. The `norm_covar_inv` function was then used to compute the covariance matrix (s) and its pseudoinverse (`pinv_s`) from the reference. A figure showing the correlations between MRI metrics was generated using the `correlation_fig` function which uses the covariance matrix (s) to calculate correlations (**Figure 1**). D2 was then computed within MVComp according to this equation:

$$D^2 = (x - m)^T C^{-1} (x - m),$$

where x is the vector of data for one observation (e.g., one subject), m is the vector of averages of all observations for each independent variable (i.e., MRI metrics), and C^{-1} is the inverse of the covariance matrix. The `model_comp` function allows the computation of voxel-wise D2 between each subject and the reference average within a specified mask of analysis. Here, a WM mask generated from the average of the WM volumes of the five-tissue-type images of all participants was provided and the threshold was set at 0.99 to limit partial volume effects. The `model_comp` function yields a matrix containing the D2 data of all subjects (of size: number of voxels x number of subjects). The `dist_plot` function was then used to obtain a D2 map (in nifti format) for each subject. The workflow for D2 calculation is illustrated in **Figure 1**.

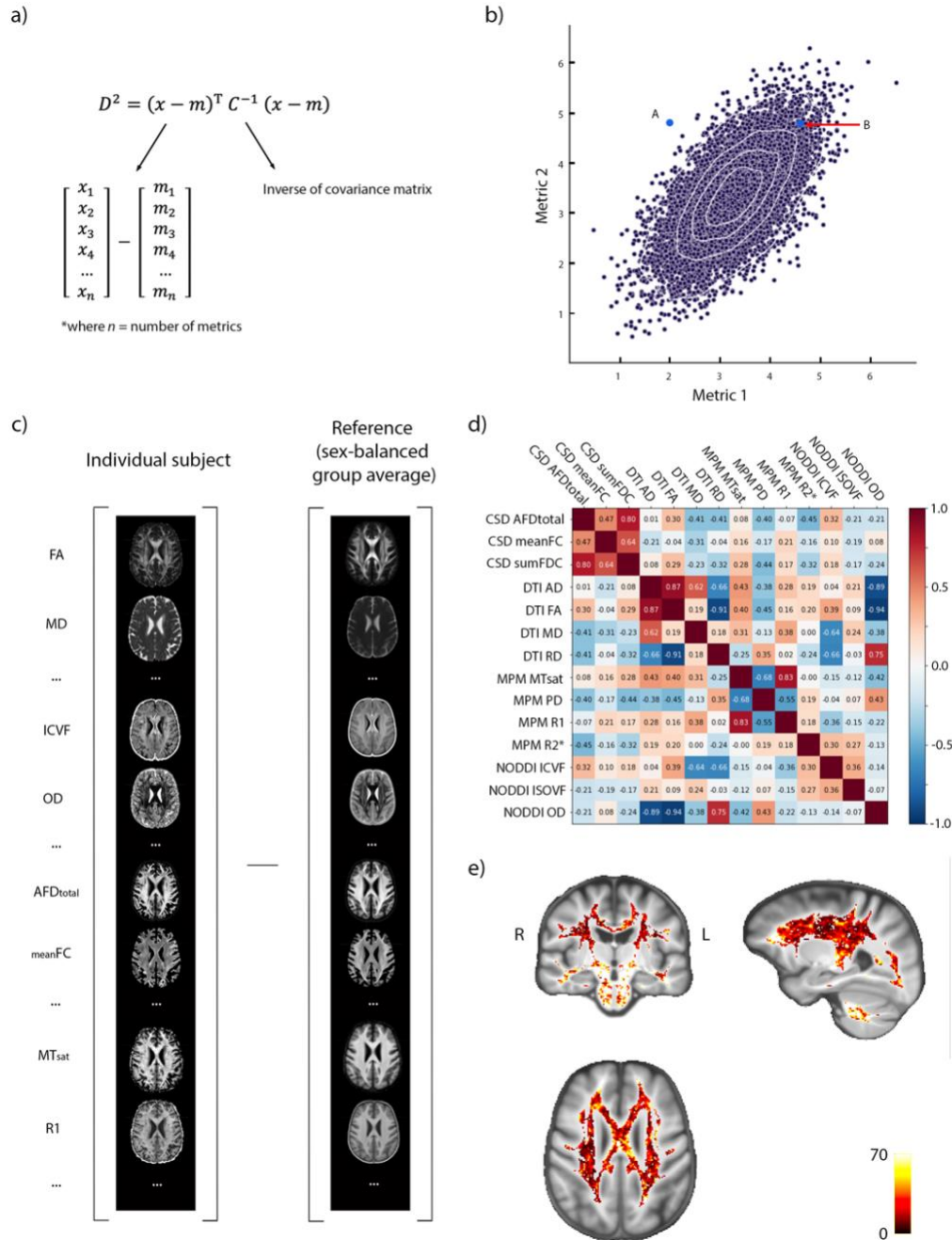


Figure 1. Methodological framework. a) Equation for computing D^2 . Two vectors, one containing the data of one observation (x) and the other containing the mean of all observations for each independent variable (m), are subtracted. The covariance between variables is accounted for by multiplying by the inverse of the covariance matrix (C^{-1}). b) Schematic illustration of the D^2 concept in a 2-dimensional space. The purple dots represent the reference distribution (each point represents a subject of the reference group). The probability distance (D^2) is the distance, in multivariate space, between each of the blue points (two different subjects; A and B) and the distribution that takes into account covariance in the data. In this example, because the two metrics are positively correlated, A will have a larger D^2 value than B. c) The vectors of data are illustrated: the first contains the data of one subject (x) and the second contains the reference group average (sex-balanced group) for each metric (m). d) The correlation matrix shows relationships between MRI metrics, highlighting the importance of accounting for covariance between variables in multivariate frameworks. e) Example D^2 map of a subject. The intensity indicates the amount of deviation in the WM microstructure of this subject compared to the reference, at each voxel.

The effect of age on D2 was removed by fitting a linear model predicting voxel-wise D2 from age using LinearRegression in sklearn.linear_model and computing the residuals. Residualized D2 data were then normalized using yeo-johnson power transformation voxel-wise in sklearn (version 0.23.2). The residualized and normalized D2 data were used as inputs for the partial least squares (PLS) analysis between WM D2 and risk factors.

Since D2 is a measure of deviation from the reference distribution, the interpretation of D2 depends on the characteristics of the reference sample. High D2 could indicate a region of abnormality if the reference is healthy or it could be indicative of WM microstructure that is healthier than that of the reference sample if the reference is generally unhealthy. Here, the mean risk variable values of the reference group were slightly higher than the normal healthy ranges for these variables (i.e., SBP, BMI, total cholesterol, LDL, HDL and HbA1c) (Cleeman, 2001; Karakaya et al., 2014), suggesting the latter case.

4.3.5 Blood samples

Blood samples were collected at every annual visit. Variables known to be associated with cardiometabolic risk were used in PLS analyses: total cholesterol, high density lipoprotein (HDL) cholesterol, low density lipoprotein (LDL) cholesterol, and glycated haemoglobin (HbA1c), a clinical index that reflects long-term glycemic control. We used the average of all measurements available in years prior to the MRI date (2011-2018) to reflect cardiometabolic risk history.

4.3.6 Body composition and physiological measures

Blood pressure (BP), heart rate, and body weight (in kg) were measured at every annual visit, while height (in cm) was measured at the eligibility visit. Here we used the average of all measurements available for BP and weight. BMI was calculated as: mean weight (kg) / height² (m). BMI and systolic BP (SBP) were used as ‘risk variables’ in PLS analyses.

4.3.7 APOE4 genotyping

Genotyping methods for this dataset have been described in (Tremblay-Mercier et al., 2021). Briefly, DNA was isolated from 200 µl whole blood using a QIASymphony apparatus and the DNABlood Mini QIA Kit (Qiagen, Valencia, CA, USA). Allelic variants of AD-related genes including APOE rs429358 and rs7412 were characterized using pyrosequencing (PyroMark24 or

PyroMark96) or DNA microarray (Illumina). Participants were classified as either APOE4+ (N= 35 females; N= 17 males) if they had one or more E4 alleles or as APOE4- (N= 61 females; N= 19 males) if they had none. The low number of participants with two E4 alleles (N= 3 females; N= 1 male) did not allow the exploration of a dose-dependent effect of APOE4.

4.3.8 Cognitive assessment

The Repeatable Battery for the Assessment of Neuropsychological Status (RBANS) (Randolph et al., 1998), a brief test (less than 30 minutes) that measures performance in five cognitive domains, was administered to participants at every annual visit. The test yields scaled scores (i.e., age-adjusted index scores with a mean of 100 and standard deviation of 15) for immediate memory, visuospatial/constructional, attention, language and delayed memory. For this study, the RBANS scores of the evaluation conducted on the same day as the MRI session were used and analyses focused on the immediate and delayed memory subscores, the components that were shown to be the best predictors of AD and mild cognitive impairment (Duff et al., 2010).

4.3.9 Statistical analyses

Relationships between WM microstructure and risk factors

Partial least squares (PLS) analyses were conducted between D2 in WM and risk factors of AD, separately in each sex. PLS is a multivariate statistical approach that can be used to describe spatial relationships between brain MRI data and multiple other variables, in our case risk factors (McIntosh & Lobaugh, 2004). PLS finds the weight vectors that maximize the covariance between brain data and risk variables, forming new variables called latent variables (LVs). Each WM voxel is assigned a weight, or salience, indicating how strongly it covaries with the pattern of the latent variable, which is a linear combination of the risk factors data.

PLS analyses were conducted in Matlab R2023b (Mathworks Inc.) using the [PLS toolbox](#) (McIntosh & Lobaugh, 2004). The “Regular Behav PLS” was selected as the type of analysis and risk factor data were loaded as the “behavioural data”. Risk factor variables included: education (total number of years of formal education), SBP, BMI, HDL, LDL, total cholesterol, and HbA1c. One participant in each group (males and females) were excluded from these analyses due to missing cholesterol data (see **Table 1**). The analyses were run with 1000 permutations to determine

the significance of each LV, and 1000 bootstraps to determine overall reliability of each voxel's association to each LV by calculating the standard error of each voxel's salience value. Only significant LVs ($p < 0.05$) and voxels with absolute bootstrap ratios (BSR) > 2 (equivalent to $p < 0.05$) were interpreted. ROIs were created using the `fsl-cluster` function. BSR values greater than the level of significance were used as thresholds for cluster creation to limit the spatial extent of ROIs (described in the Results section).

Similar analyses were conducted between D2 in WM and the same risk factors, this time disaggregating by APOE4 status (APOE4+ if one E4 allele or more; APOE4- if no E4 allele), irrespective of sex. ROIs were created following a similar process as described above.

Analyses were conducted separately in each group to assess patterns specific to each APOE4 group and to each sex. Patterns common to more than one group were then tested for statistical group differences using a 2x2 ANOVA with sex and APOE4 status as fixed factors and with the brain scores (usc) from a PLS analysis in the overall group as the dependent variable. This allowed us to determine whether the pattern was expressed more strongly in one group compared to the others and to test for interaction between APOE4 and sex.

Relationships between deviations in WM microstructure and cognition

Correlation analyses were conducted between mean D2 in ROIs (significant clusters from PLS analyses) and the immediate and delayed memory subscores of the RBANS. Analyses were targeted to these two subscores, known to be the most affected cognitive domains in AD (Duff et al., 2010), and to significant clusters identified in the PLS analysis, to limit the number of comparisons. Correction for multiple comparisons was performed using the false discovery rate (FDR) Benjamini-Hochberg method (FDR-corrected p -value < 0.05 was considered statistically significant).

Determining feature importance in regions of interest

The relative contributions of each feature (i.e., MRI metric) to D2 in significant ROIs (of size > 100 voxels) were then extracted using the `return_raw` option of the `model_comp` function in MVComp. The `return_raw` option yields a matrix of size (number of voxels) \times (number of metrics) \times (number of subjects). Contributions were then summarised by averaging distance values across voxels within the ROI and across subjects and dividing by the total distance (for all features),

resulting in one distance value per metric, expressed as a percentage, for each ROI. This analysis provides a measure of the importance of each metric in determining D2 in the ROI.

4.4 Results

4.4.1 Relationships between WM microstructure and risk factors in each sex

Significant patterns of covariance were found between risk factors for AD and WM D2 in both males and females. In males, only the first LV of the PLS analysis was significant ($p = 0.002$) and it explained 34.4% of total crossblock covariance (**Figure 2a-b**). Low SBP, low BMI, low HbA1c and high cholesterol (total chol, HDL and LDL) were associated with high D2 in several WM regions including the body of corpus callosum, superior corona radiata, superior thalamic radiation (bilaterally) and the right frontal aslant tract. In females, only the first LV was significant ($p < 0.001$) and explained 40.9% of total crossblock covariance (**Figure 2c-d**). Similar relationships were observed but in slightly different WM regions. D2 in the superior longitudinal fasciculus, corticospinal tract, cingulum, splenium of corpus callosum, posterior corona radiata, and arcuate fasciculus (bilaterally), as well as the right forceps major and body of corpus callosum was associated with these risk factors in females. Generally, associations were found in more frontal and parietal regions in males, while they were found in more posterior and temporal locations in females. There were also overlapping regions in both sexes, specifically in parietal regions and in WM tracts underlying the precentral gyrus. Education was the only non-significant factor in both groups. **Figure 2** shows the strength and direction of the relationships between D2 and each risk factor (left panel), as well as the WM regions in which those relationships are located (right panel). Only significant voxels ($|BSR| > 2.0$) and those belonging to clusters of size > 100 voxels are shown. Clusters were formed from significant voxels. Thresholds higher than the significance limit ($|BSR| = 2.0$, equivalent to $p = 0.05$) were used to limit the spatial extent of clusters and different cluster thresholds were used in each sex to result in similarly sized clusters, so that D2 was averaged across a similar number of voxels for analyses with cognition ($|BSR| > 2.5$ in females and > 3.0 in males). Further analyses were focused on clusters of size > 100 voxels. Cluster information, including the size, maximal $|BSR|$ and brain region, is displayed in **Table 2**.

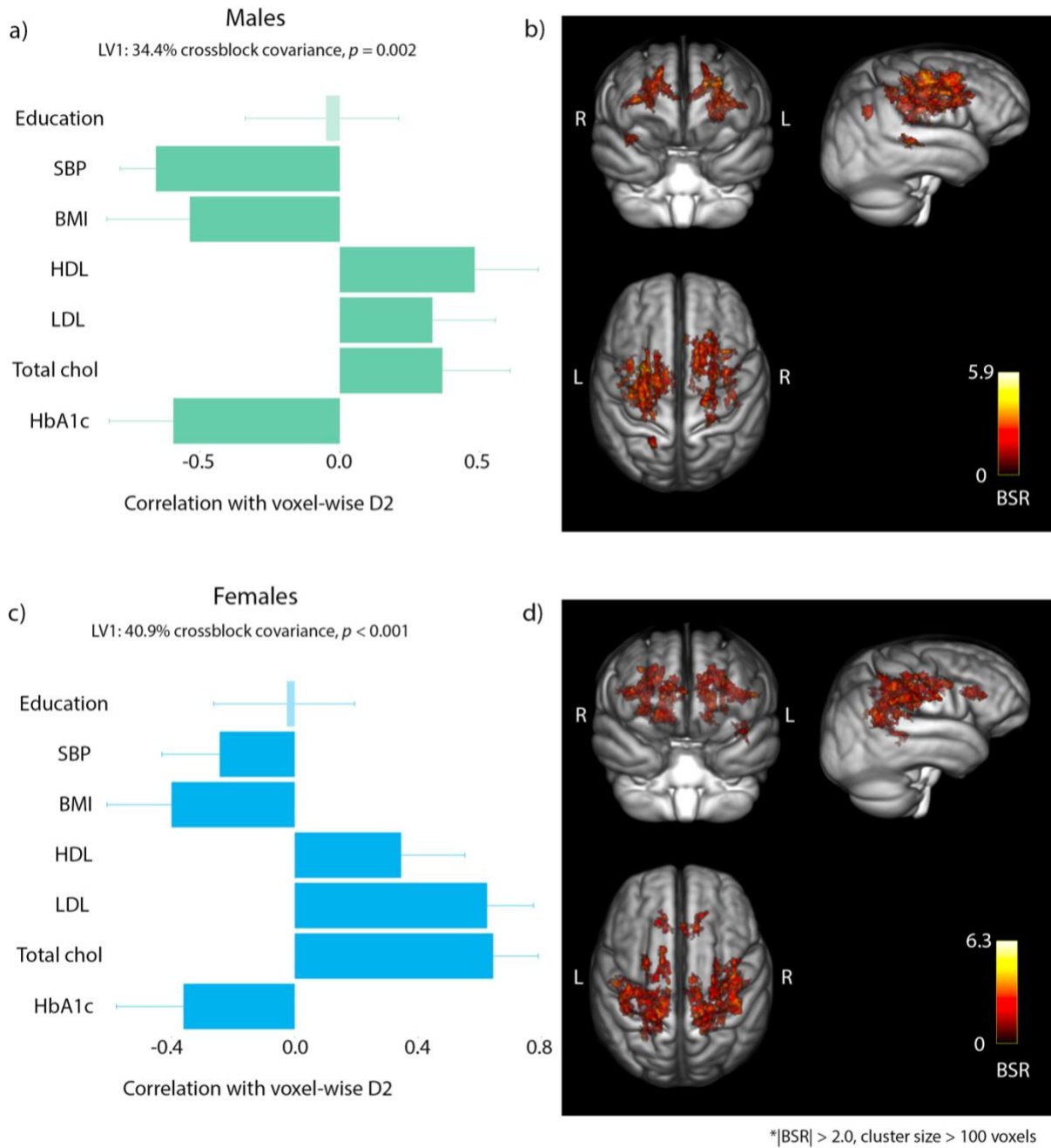


Figure 2. Relationships between D2 in WM and risk factors in each sex. Left panel (a & c): The strength and direction of the relationship that each risk factor has with D2 in the voxels shown on the brain images on the right. Error bars show 95% confidence intervals. Correlations are non-significant when confidence intervals overlap with zero (faded bar). Right panel (b & d): Colored voxels ($|BSR| > 2.0$) have a positive relationship with the patterns shown in the left panel. The BSR maps are overlaid on a MPRAGE T1w group average image. Males (a-b) Several risk factors were associated with D2 across broad WM regions. Higher D2 was associated with lower SBP, BMI and HbA1c and with higher HDL, LDL and total cholesterol. Females (c-d) Similar relationships were observed in females but across different WM regions.

Table 2. Cluster information (PLS analyses in each sex). Location identified according to the JHU ICBM-DTI-81 White-Matter and XTRACT HCP Probabilistic tract atlases and cortical region closest to the WM region identified using the Harvard-Oxford cortical structural atlas.

	Size (#voxels)	Max BSR 	WM region	Cortical region near
Males				
Cluster 1	346	5.63	Superior corona radiata & superior thalamic radiation L	Precentral & superior frontal gyri
Cluster 2	266	5.88	Body of corpus callosum, superior corona radiata & superior thalamic radiation L	Superior frontal & cingulate gyri, supplementary motor cortex
Cluster 3	140	4.93	Body of corpus callosum, frontal aslant tract & superior/ant corona radiata R	Superior frontal, cingulate & paracingulate gyri
Females				
Cluster 1	348	5.39	Superior longitudinal fasciculus (temporal part), arcuate fasciculus R	Supramarginal, precentral & postcentral gyri, opercular cortex
Cluster 2	252	5.2	Cingulum, splenium of corpus callosum, posterior corona radiata L	Cingulate gyrus (posterior division), precuneus cortex
Cluster 3	180	5.3	Splenium of corpus callosum, forceps major & cingulum R	Cingulate Gyrus (posterior division), precuneus cortex
Cluster 4	174	5.16	Superior longitudinal fasciculus, arcuate fasciculus & corticospinal tract L	Precentral & postcentral gyri, parietal operculum cortex

Cluster 5	157	5.76	Cingulum, splenium & body of corpus callosum, posterior corona radiata R	Cingulate gyrus
Cluster 6	151	5.08	Corticospinal tract & superior longitudinal fasciculus L	Precentral & postcentral gyri
Cluster 7	107	4.66	Superior longitudinal fasciculus & corticospinal tract R	Precentral & postcentral gyri

4.4.2 Relationships between WM microstructure and risk factors in each APOE4 group

Different patterns of covariance were found between risk factors for AD and WM D2 in the APOE4+ and APOE4- groups. In APOE4+, LV1 ($p = 0.013$, crossblock covariance = 34.9%) and LV2 ($p = 0.048$, crossblock covariance = 22.5%) were significant. The LV1 pattern revealed that low BMI and high cholesterol (total chol, HDL and LDL) were associated with high D2 in several WM regions including the left body of corpus callosum, frontal aslant tract, superior thalamic radiation, and arcuate fasciculus (**Figure 3a-b**). These risk factors and their directions of association to D2 represent a subset of the pattern seen in sex-specific analyses. On the other hand, LV2 revealed a different risk pattern: low SBP, low BMI, high HDL, low LDL, and low HbA1c were associated with high D2 in the right superior longitudinal fasciculus, superior corona radiata, superior thalamic radiation, and corticospinal tract (**Figure 3c-d**). Generally, associations of the first LV were found in the left hemisphere and included commissural fibers such as the corpus callosum, while LV2 associations were found mostly on the right and included projection fibers such as the superior corona radiata as well as association tracts.

In APOE4-, only the first LV of the PLS analysis was significant ($p < 0.001$) and it explained 46.5% of total crossblock covariance (**Figure 3e-f**). The risk factors pattern was very similar to that of previous analyses (sex-disaggregated PLS analyses). Low SBP, low BMI, low HbA1c and high cholesterol (total chol, HDL and LDL) were associated with high D2 in broad WM regions including the superior longitudinal fasciculus, arcuate fasciculus, superior corona radiata, and

corticospinal tract. Significant regions of the PLS analysis in APOE4- overlapped to a large extent with significant regions seen in sex analyses.

Education was non-significant in all LVs. **Figure 3** shows the strength and direction of the relationships between D2 and each risk factor (left panel), as well as the WM regions in which those relationships are located (right panel). Only significant voxels ($|BSR| > 2.0$) and those belonging to clusters of size > 100 voxels are shown. Clusters were formed from significant voxels. Thresholds of $|BSR| > 2.5$ in APOE4+ and > 3.0 in APOE4- were used for clustering to result in similar size clusters across groups and further analyses were focused on clusters of size > 100 voxels. Cluster information is displayed in **Table 3**.

Because a general common pattern was observed in both sexes and in the APOE4- group, we performed another PLS analysis in the whole sample to test for group differences and interactions between sex and APOE4. This analysis showed a very similar pattern as that observed in these groups (**Supplementary Figure 1**; Appendix III). The ANOVA on the brain scores (i.e., usc) from this analysis revealed a significant main effect of sex ($p < 0.001$), indicating that males expressed the pattern of the LV more strongly than females (**Supplementary Table 1** and **Supplementary Figure 2**). There were no significant APOE4 group differences and no significant sex x APOE4 interaction ($p > 0.05$) (**Supplementary Table 1**).

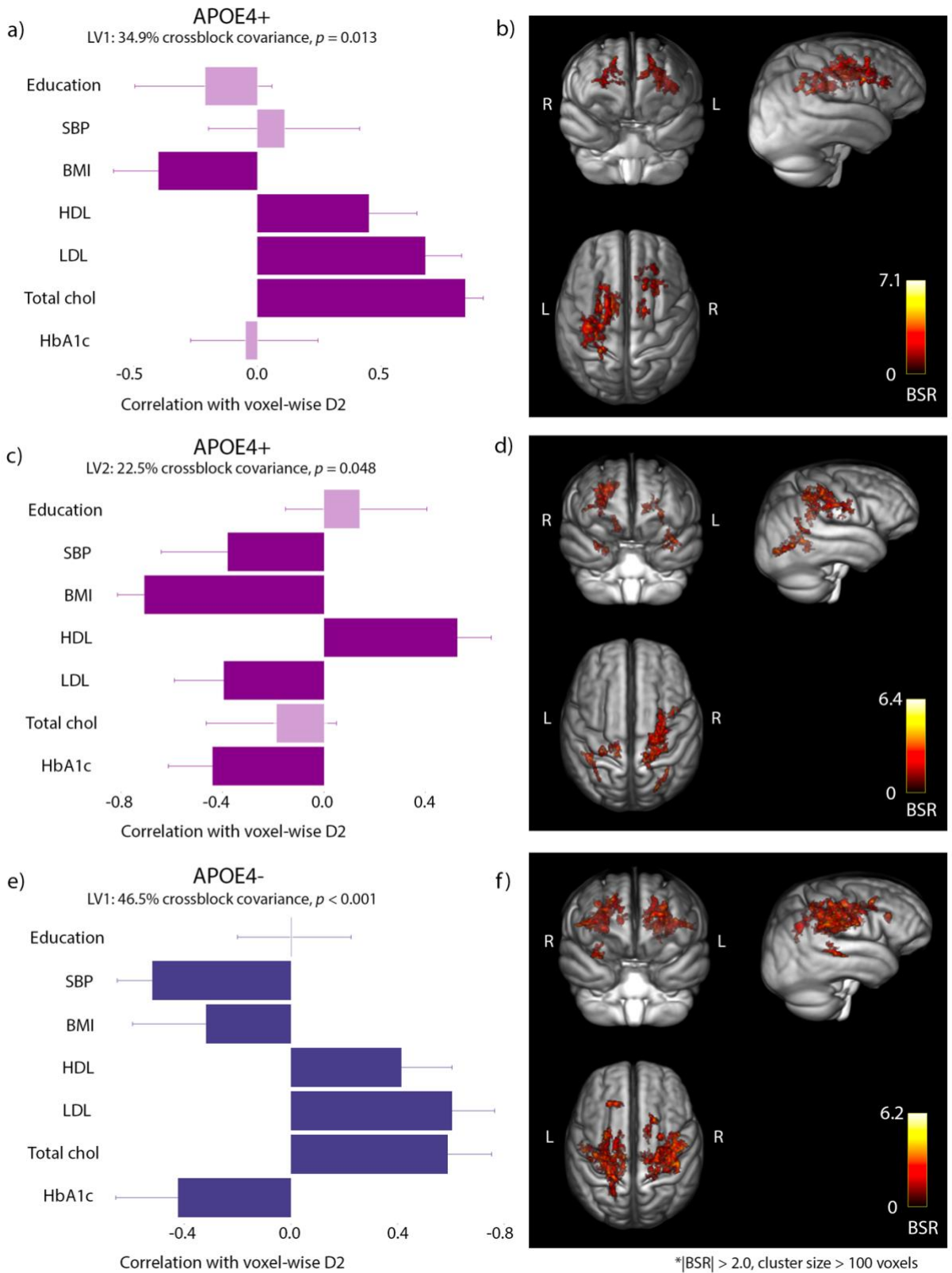


Figure 3. Relationships between D2 in WM and risk factors in each APOE4 group. Left panel: The strength and direction of the relationship that each risk factor has with D2 in the voxels shown on the brain images on the right. Error bars show 95% confidence intervals. Correlations are non-significant when confidence intervals overlap with zero (faded bar). Right panel: Colored voxels

($|BSR| > 2.0$) have a positive relationship with the patterns shown in the left panel. The BSR maps are overlaid on a MP-RAGE T1w group average image. APOE4+ (a-b) LV1: Higher D2 was associated with lower BMI and higher HDL, LDL and total cholesterol. (c-d) LV2: Higher D2 was associated with low SBP, low BMI, high HDL, low LDL, and low HbA1c. APOE4- (e-f) Higher D2 was associated with low SBP, BMI, HbA1c and with high HDL, LDL and total cholesterol.

Table 3. Cluster information (PLS analyses in each APOE4 group). Location identified according to the JHU ICBM-DTI-81 White-Matter and XTRACT HCP Probabilistic tract atlases and cortical region closest to the WM region identified using the Harvard-Oxford cortical structural atlas.

	Size (#voxels)	Max BSR	WM region	Cortical region near
<u>APOE4+</u>				
LV1				
Cluster 1	499	6.27	Body of corpus callosum, frontal aslant tract & superior thalamic radiation L	Superior frontal, precentral & anterior cingulate gyri
Cluster 2	326	7.12	Superior longitudinal fasciculus & arcuate fasciculus L	Precentral & postcentral gyri, insular cortex & operculum cortex
Cluster 3	106	6.63	Superior longitudinal fasciculus L	Postcentral gyrus & superior parietal lobule
Cluster 4	100	5.31	Superior corona radiata, frontal aslant tract & superior thalamic radiation L	Superior & middle frontal gyrus
LV2				
Cluster 1	391	5.48	Superior corona radiata, superior thalamic radiation & corticospinal tract R	Precentral gyrus
Cluster 2	190	6.37	Superior longitudinal fasciculus & corticospinal tract R	Precentral & postcentral gyri

APOE4-

Cluster 1	264	4.94	Superior longitudinal fasciculus & arcuate fasciculus R	Precentral & postcentral gyri & operculum cortex
Cluster 2	127	5.7	Superior corona radiata & corticospinal tract L	Precentral gyrus, insular cortex & operculum cortex

4.4.3 Determining feature importance in regions of interest

In females, features' contributions were extracted in the 7 clusters that were significant in the PLS analysis (**Figure 4a**). D2 in cluster 1 was driven mainly by MTsat (28.8%), R1 (23.4%), and RD (12.5%). In cluster 2, meanFC (29.9%), R1 (23.6%), and MTsat (11.9%) contributed the most to D2. Similarly, in cluster 3, meanFC (28.1%), R1 (18.3%), and MTsat (14.3%) were the top contributors. In cluster 4, R1 (28.7%), MTsat (25.5%), and ISOVF (15.6%) contributed most to D2. D2 in cluster 5 was driven mainly by R1 (44.5%) and meanFC (23.2%). In cluster 6, R1 (20.8%), ISOVF (18.1%), meanFC (16.0%), and MTsat (14.2%) were the metrics that contributed the most to D2. In cluster 7, D2 was mainly driven by R1 (25.3%), meanFC (19.5%), AD (13.5%), and MD (10.8%). Overall, R1, meanFC, and MTsat were the most important metrics in females. The isotropic volume fraction (ISOVF) metric from NODDI was also an important contributor in 2 clusters.

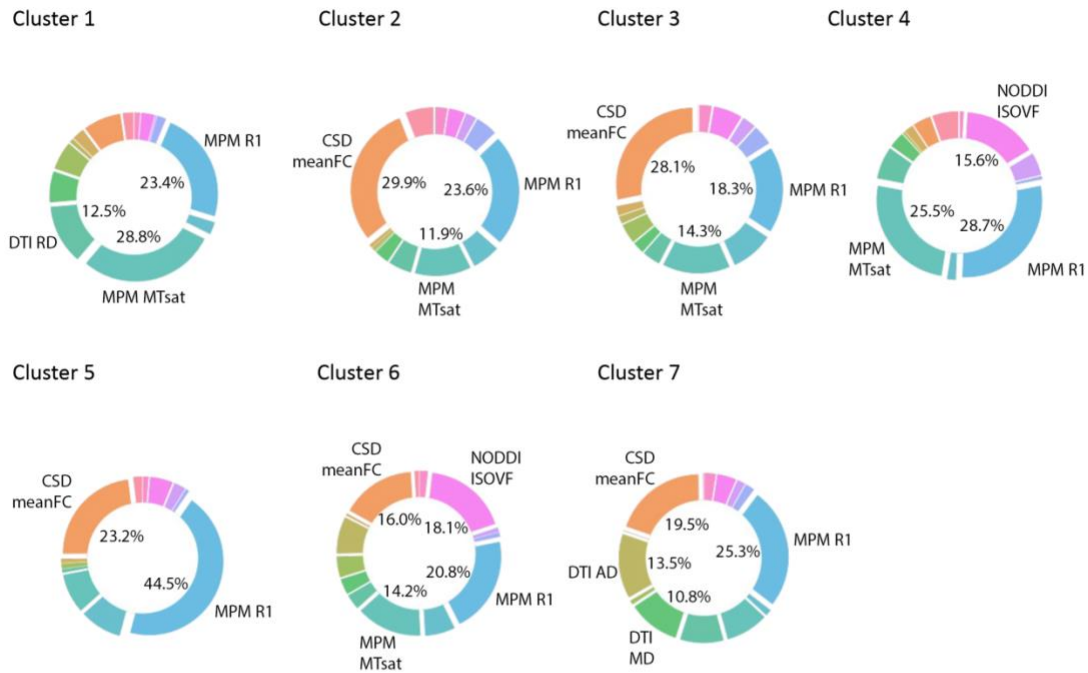
In males, features' contributions were extracted in the 3 significant clusters from PLS analysis (**Figure 4b**). D2 in cluster 1 was driven mainly by R1 (43.3%) and, to a lesser extent, by AD (10.9%). In cluster 2, R1 (17.8%), MTsat (15.5%), and PD (13.2%) contributed the most to D2. In cluster 3, R1 (33.7%) and MTsat (15.2%) were the top contributors. Like in females, R1 and MTsat emerged as top contributors to D2 in males. However, meanFC was not an important contributor to D2 (<10%) in any of the males' clusters.

In the APOE4+ group, there were 4 clusters from the first LV and 2 clusters from the second LV (**Figure 5a-b**). D2 in the first LV1 cluster was driven mainly by R1 (28.8%), MTsat (20.4%), and PD (12.6%). In cluster 2, R1 (28.4%), MTsat (28.1%), and meanFC (10.5%) were the top contributors. In cluster 3, R1 (26.1%), MTsat (17.1%), meanFC (12.5%), and ISOVF (12.4%) contributed most to D2. D2 in cluster 4 was driven mainly by R1 (36.6%) and meanFC (20.5%).

In cluster 1 of the second LV, R1 (26.0%), MTsat (23.3%), and meanFC (18.5%) contributed most to D2. In cluster 2, MTsat (25.7%), R1 (24.4%), and OD (11.2%) were the metrics that contributed most to D2.

In the APOE4- group, features' importance was extracted in the 2 significant clusters (Fig 5d). D2 in cluster 1 was driven mainly by R1 (27.1%), MTsat (23.5%), and RD (15.8%). In cluster 2, R1 (38.0%), MTsat (17.1%), and ICVF (12.4%) contributed the most to D2.

a) **Females**



b) **Males**

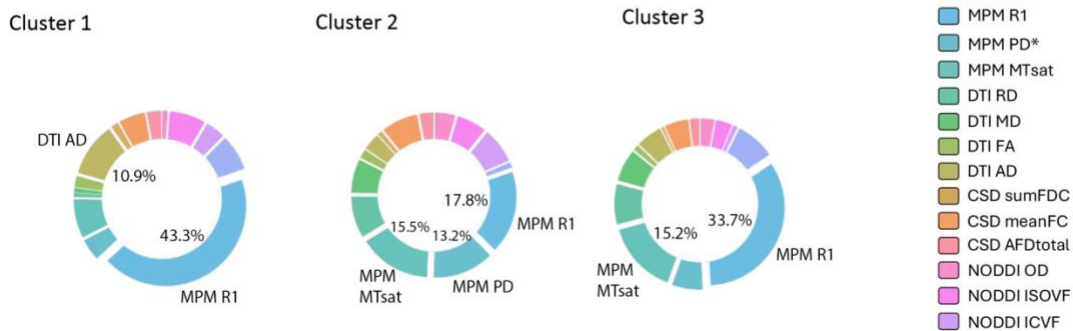


Figure 4. Features contribution to D2 in each significant cluster from PLS analyses in females (a) and males (b). For each significant cluster, the relative contribution (%) of each MRI metric is indicated by its size on the pie chart (see the legend for color of each MRI metric). The metric name and its contribution (in %) is indicated only for the most important contributors (those that account for >10%), for clarity. MPM R1 = macromolecular content (axons and myelin) (Callaghan et al., 2014); MPM MTsat = more specific to myelin content (Helms, Dathe, Kallenberg, et al., 2008); MPM PD = amount of water (if increased could reflect neurite atrophy); CSD meanFC = fiber bundle cross-section (Raffelt, Tournier, et al., 2017); NODDI ISOVF = amount of free water (if increased it could reflect neurite atrophy) (H. Zhang et al., 2012b); AD = axonal integrity; RD = myelin integrity (Winklewski et al., 2018); MD = overall diffusivity (typically increased with higher water content/cell atrophy).

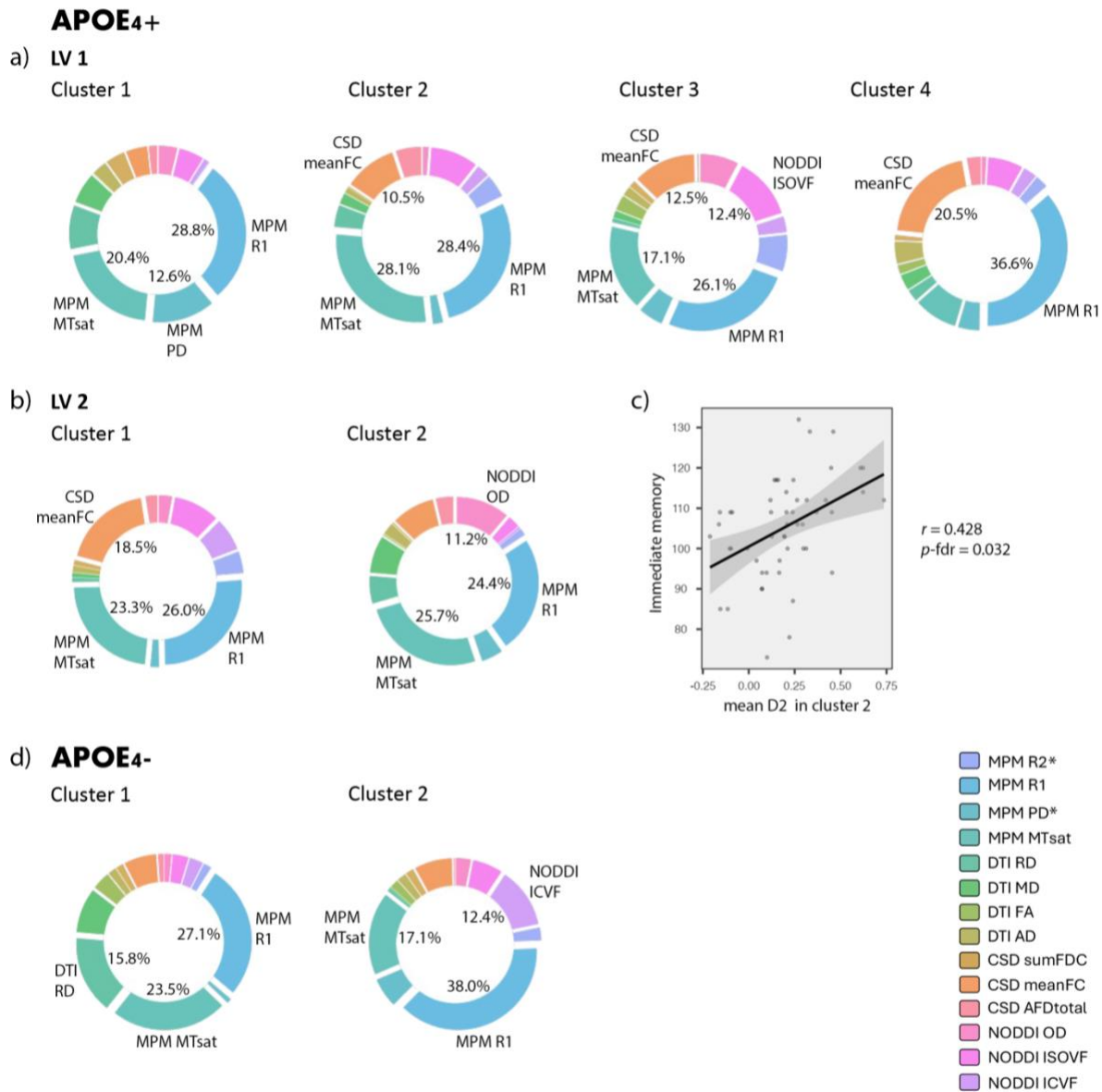


Figure 5. Features contribution to D2 in each significant cluster from PLS analyses in APOE4+ (a-b) and APOE4- (d). For each significant cluster, the relative contribution (%) of each MRI metric is indicated by its size on the pie chart (see the legend for color of each MRI metric). The metric name and its contribution (in %) is indicated only for the most important contributors (those that account for >10%), for clarity. c) Plots are shown for significant correlations between D2 and the RBANS memory items. Immediate memory was positively associated with D2 in cluster 2 of the APOE4+ analysis (LV2). MPM R1 = macromolecular content (axons and myelin) (Callaghan et al., 2014); MPM MTsat = more specific to myelin content (Helms, Dathe, Kallenberg, et al., 2008); MPM PD = amount of water (if increased could reflect neurite atrophy); CSD meanFC = fiber bundle cross-section (Raffelt, Tournier, et al., 2017); NODDI ISOVF = amount of free water (if increased it could reflect neurite atrophy); NODDI ICVF = neurite density; NODDI OD = orientation dispersion of fiber tracts (H. Zhang et al., 2012b); RD = myelin integrity (Winklewski et al., 2018).

4.4.4 Relationships between deviations in WM microstructure and cognition

To understand the associations between deviations in WM microstructure and cognition, correlation analyses were performed between D2 in significant clusters from the PLS analysis disaggregated by APOE4 status (8 clusters; **Table 3**) and scores in the immediate and delayed memory RBANS items. D2 in the two LV2 clusters was positively associated with immediate memory. The first cluster, located in a WM region corresponding to part of the right superior corona radiata, superior thalamic radiation and corticospinal tract, had a product-moment correlation (*Pearson's*) $r = 0.313$ and a p value = 0.024 (p -fdr corrected = 0.192). Cluster 2, located in a WM region corresponding to part of the right superior longitudinal fasciculus and corticospinal tract, had a product-moment correlation $r = 0.428$, $p = 0.002$ (p -fdr corrected = 0.032) (**Figure 5c**). Only the correlation in cluster 2 remained significant after FDR correction. All other correlations were non-significant ($p > 0.05$).

4.5 Discussion

In this study, we identified the presence of WM microstructural impairments linked to cardiometabolic risk factors in individuals with a family history of Alzheimer's disease (AD). These impairments were identified using a novel approach, whereby we investigated the sex-specific and APOE genotype-related relationships between WM microstructural deviations, quantified using a multivariate score derived from several MRI-derived features, and cardiometabolic risk factors.

4.5.1 Sex-related effects

In our sex-disaggregated analysis, we found that in both males and females, high systolic blood pressure, high BMI, high HbA1c (blood sugar levels), and low cholesterol (total, HDL, and LDL) were associated with low D2 (**Figure 2**, left panel). Due to the directions of relationships between risk factors and D2, we inferred that, in our analyses, greater D2 is likely to represent a healthier state. Since D2 represents the amount of deviation from the reference distribution (i.e., sex-balanced reference group), this would mean that higher D2 indicates WM microstructure that is healthier than the average of our reference group. Although the patterns of association were similar in males and females, the WM regions in which these relationships were observed differed between sexes (**Figure 2**, right panel), with partially overlapping significant clusters, but more frontal

regions in males and more posterior and temporal locations in females. There was also a significant sex difference, where males expressed this general risk–WM pattern more strongly than females. There are known sex differences in WM microstructure (Kanaan et al., 2012a; van Hemmen et al., 2017) and in the aging trajectory of myelin (Toschi et al., 2020). Age-related declines in WM health follow an anterior to posterior gradient and these changes start occurring later in life in females, likely owing to the pro-myelinating effects of female hormones (Bartzokis, 2004b; Toschi et al., 2020). In this study, we regressed out age to remove any age effects and the pattern of WM differences we observe does not fit this model. The sex differences observed may thus be due to factors more specifically related to sex differences in WM susceptibility to vascular risk factors. More research is needed to understand the sex-specific relationships between risk factors, early pathological changes and AD, as well as to disentangle the contributions of gender (Dhamala et al., 2024), which may confound these relationships.

The directions of several of the associations we found between WM D2 and risk factors are in line with the literature. Several studies report WM alterations in hypertensive individuals and the effects of high blood pressure may start accumulating as early as the fourth decade of life (Maillard et al., 2012). Obesity has also been associated with changes in WM microstructure such as decreased FA and myelin content (R1) in several WM tracts (Kullmann et al., 2015, 2016). In line with the extant literature on subclinical hyperglycemia (Garfield et al., 2021; Repple et al., 2021), we also identified WM differences associated with HbA1c levels, even though the vast majority of participants did not have diabetes (99% of females and 92% of males). Moreover, HDL cholesterol was positively associated with WM D2, in line with the well-established protective role of HDL on cognition and brain structure (Vitali et al., 2014).

4.5.2 APOE4-dependent effects of LDL

We found complex relationships between WM microstructure and LDL. Peripheral LDL and total cholesterol were positively associated with better WM health (high D2) in all but one latent variable. While LDL and total cholesterol are typically thought of as being detrimental, evidence on their impact on the brain’s WM and on cognition is unclear (Alfaro et al., 2018; Lamar et al., 2020; Lv et al., 2016; Silverman & Schmeidler, 2018; van Vliet, 2012; Warstadt et al., 2014). These discrepancies may be due to the unknown contribution of oxidized LDL to total LDL. Oxidation of LDL, which is enhanced in inflammatory states when oxidative stress is high, has been shown

to be a better predictor of atherosclerosis and cardiovascular disease than LDL itself (Hecht & Harman, 2003; Holvoet et al., 2003, 2004; Nishi et al., 2002) and is also associated with deleterious effects on brain health (Dias et al., 2014; Draczynska-Lusiak et al., 1998). It is thus likely that the relationship we observed between LDL and WM was due to predominantly non-oxidized LDL. The fact that LDL and HDL cholesterol were related to WM D2 in the same direction also supports this hypothesis as the antioxidant property of HDL would contribute to preventing LDL oxidation (Holvoet et al., 2004; Sigurdardottir et al., 2002; Vitali et al., 2014). Furthermore, as ~80% of participants in this study were taking lipid-lowering medications, LDL oxidation may be reduced in the participants taking statins (Ndrepepa et al., 2005).

In contrast, we found that high LDL was associated with poorer WM health in APOE4 carriers (LV2). This is consistent with a study reporting a detrimental effect of elevated LDL on WM microstructure in APOE4 carriers, but a beneficial effect in non-carriers (Ye et al., 2024). As a cholesterol-transporter, APOE4 may modulate the impact of LDL on WM microstructure through increased LDL circulation time, increased free radical formation and decreased plasma antioxidant concentrations, increasing LDL oxidation (Dias et al., 2014). Overall, our study supports the idea of differential effects of LDL-cholesterol on the brain's WM depending on APOE genotype. However, future studies that include measurements of oxidized LDL and a larger sample size (especially of APOE4 homozygotes) are needed to confirm these findings.

The distinct pattern observed in APOE4 carriers (LV2), where low D2 was associated with high LDL, low HDL-cholesterol, high HbA1c, high BMI and high SBP, was found to be linked with cognition. D2 in a cluster of LV2 was positively associated with immediate memory performance, indicating that this pattern of risk factors likely had a negative impact on cognition in APOE4 carriers. The direction of the relationship with cognition also supports our interpretation of low D2 reflecting poor WM health. On the other hand, in non-carriers, WM D2 in regions associated with risk factors did not relate with cognition. Together, this suggests that WM health is differentially affected by cardiometabolic risk factors in APOE4 carriers and that the pattern uncovered by LV2 may be more detrimental to cognitive health.

4.5.3 Role of myelin and other components

Several WM regions were associated with the patterns of risk factors discussed above and extracting the contribution of each MRI feature to D2 in these regions revealed that inter-individual variations in myelin content (as measured by R1 and MTsat) was a major contributor in most significant clusters. Our results are partially in line with the myelin breakdown theory stating that late-myelinating WM tracts would be especially vulnerable to aging and adverse risk factors such as those investigated in this study (Bartzokis, 2004b, 2011; Bartzokis et al., 2003, 2004). For instance, decreased FA in late-myelinating tracts has been reported in individuals with elevated glycated hemoglobin (HbA1c) (Foley et al., 2014). Most of our significant clusters were located in late-myelinating regions (i.e., supramarginal, superior frontal, superior parietal, superior temporal, and precuneus WM), but we also found significant associations in the splenium of the corpus callosum, a region that develops at an intermediate stage (Bartzokis, 2004b, 2011; Bartzokis et al., 2003, 2004; Foley et al., 2014).

4.5.4 Strengths and limitations

In this study, we assessed relationships between risk factors and WM microstructure separately in each sex and APOE4 group, which allowed the identification of patterns specific to APOE4 carriers. Importantly, this pattern would not have been detected in a whole sample analysis (see **Supplementary Table 1**; Appendix III). Another strength of our study is the use of a multivariate approach to integrate several MRI measures of WM, allowing for a comprehensive assessment of the biological mechanisms underlying WM differences (Tremblay, Alasmar, et al., 2024b). This is of interest because multiple pathological mechanisms (e.g., demyelination, axonal changes, iron accumulation) are likely involved concurrently in AD and in its prodromal stage (Iturria-Medina et al., 2017). However, the D2 method has some inherent limitations. Because D2 is a squared measure, the directionality of differences is non-specific (Tremblay, Alasmar, et al., 2024b). Future studies could address this limitation by integrating models of ground-truth biophysical properties to better interpret these differences, or by stratifying groups based on the expected direction of change to have a strong prior on the directions of deviations. Further, the high sensitivity of D2 makes it susceptible to registration inaccuracies and partial voluming. Special attention must thus be paid to optimize alignment and minimize partial voluming. In this study, strict masking (i.e., 0.99 of group average tissue segmentation) was applied to restrict the analyses to voxels containing

only WM. Another limitation of this study is that the sample size did not allow the investigation of a dose-dependent effect of the number of APOE ϵ 4 alleles. Future studies, in larger samples, and with measurements of oxidized LDL could help clarify the effects of the APOE genotype on cholesterol metabolism and the downstream impact on WM microstructure.

4.6 Conclusion

Our findings support the myelin breakdown hypothesis of AD, suggesting that oligodendrocytes' vulnerability to aging and stressors makes myelin an early target in AD's pathology (Bartzokis, 2004b, 2011). Modifiable risk factors for AD (e.g., hypertension, diabetes, dyslipidemia) act as stressors that negatively impact WM health and cognition, especially when combined with familial history and APOE4. We found that WM microstructural changes, especially myelination, were associated with cardiometabolic risk factors in older adults with a family history of AD. Notably, LDL-cholesterol adversely affected WM microstructure only in APOE4 carriers. Our results also suggest that these WM alterations lead to impaired cognition, particularly short-term memory, in APOE4 carriers. This aligns with the theory that genetic and environmental risk factors exacerbate myelin breakdown and accelerate cognitive decline (Bartzokis, 2004b, 2011; Burzynska et al., 2023).

CHAPTER V: White matter microstructure in older adults with cardiovascular disease

Preface

In Study 3 (Chapter IV), we showed that WM microstructural alterations in older adults with a familial history of Alzheimer's disease (AD) can be detected using the MVComp toolbox. These alterations, which were linked to the presence of cardiometabolic risk factors, likely represent an early disease stage. We also investigated how genetic risk (i.e., familial history of AD and APOE4 genotype) and cardiometabolic factors interact to impact WM microstructure. Cardiovascular disease alone, even in the absence of genetic predisposition, can also increase the risk of both vascular and AD dementia (Kovacic et al., 2012; Olesen et al., 2024; Polidori et al., 2012; Zheng et al., 2012).

In Study 4, we investigated cardiovascular risk more deeply by assessing the impact of coronary artery disease (CAD), the most common form of cardiovascular disease, on WM microstructure. CAD has been associated with WM damage (Johansen et al., 2021; Vidal et al., 2010; Vuorinen et al., 2014) and this damage is thought to contribute to cognitive impairments (Filley & Fields, 2016; O'Brien, 2014). However, most studies have focused on characterizing lesions (WM hyperintensities), while very few have investigated more subtle alterations in WM microstructure. Quantifying alterations to microstructural health in addition to WM hyperintensities is necessary to capture the full range of pathological alterations occurring in CAD and how they impact cognition.

In this study, we used the MVComp framework to quantify WM alterations relative to a healthy sample. The inclusion of a healthy control group in this study (which was a limitation in Study 3) provided a robust reference sample, facilitating the interpretation of D2 scores, where a high D2 value (indicating high deviation from the healthy reference) would suggest an area of abnormality. We also explored the impact of fitness (VO₂max) on WM alterations in this population as fitness may provide a protective effect on WM health.

Multivariate white matter microstructure alterations link to fitness and cognition in older adults with coronary artery disease

Stefanie A. Tremblay, Zacharie Potvin-Jutras, Dalia Sabra, Ali Rezaei, Safa Sanami, Christine Gagnon, Brittany Intzandt, Amélie Mainville-Berthiaume, Lindsay Wright, Ilana R. Leppert, Christine L. Tardif, Mathieu Gayda, Christopher J. Steele, Josep Iglesias-Grau, Anil Nigam, Louis Bherer, Claudine J. Gauthier

In preparation.

5.1 Abstract

Introduction: Patients with coronary artery disease (CAD) are at an increased risk of cognitive impairment, dementia and stroke. Although white matter (WM) lesions are frequently reported in CAD patients, evidence regarding pathological alterations in WM microstructure is lacking. This study aimed to assess WM abnormalities in CAD patients, as well as the links with fitness (VO₂max) and cognition.

Methods: A novel multivariate approach - the Mahalanobis distance (D₂) - was used to quantify WM abnormalities as the amount of deviation from a healthy reference group. D₂ integrates the information from multiple MRI-derived metrics (here 12 metrics from diffusion-weighted imaging [DWI] and magnetization transfer imaging [MTI]), while accounting for the covariance between metrics. 46 CAD patients and 41 healthy controls (HC) aged 50 and older completed the study. An arterial territories atlas was applied to the WM D₂ maps to conduct region of interest analyses.

Results: CAD patients had higher D₂ values compared to HC in the whole WM, right anterior cerebral artery (ACA) and left and right posterior cerebral artery (PCA). Higher cardiorespiratory fitness (VO₂max) was associated with lower D₂ values in the whole WM and in the PCA. Furthermore, higher processing speed was linked with lower D₂ values in the left middle cerebral artery (MCA).

Discussion: These findings suggest that higher WM abnormalities observed in CAD patients may contribute to a heightened risk of cognitive impairment and that cardiorespiratory fitness may provide a protective effect on WM health, potentially aiding in the management of the disease.

5.2 Introduction

Patients with coronary artery disease (CAD) face a heightened risk of cognitive decline, dementia, and stroke (Kovacic et al., 2012; Olesen et al., 2017, 2024; Polidori et al., 2012; Zheng et al., 2012). Vascular risk factors such as hypertension impact several components of brain health, including cerebral vessels, grey matter and white matter (WM) (Barekatain et al., 2014; Haight et al., 2018; Launer et al., 2015; Vuorinen et al., 2014). Major cardiac events, such as myocardial infarction, are likely to accelerate brain damage and the ensuing cognitive decline (Schievink et al., 2022; Xie et al., 2019). For instance, WM lesions, appearing as WM hyperintensities (WMHs) in magnetic resonance imaging (MRI), are commonly reported in CAD patients (Johansen et al., 2021; Vidal et al., 2010; Vuorinen et al., 2014). Because it is not as well perfused as grey matter, WM is more vulnerable to changes in perfusion, and it is thus more prone to hypoxic injuries as a result of cerebrovascular dysfunction (Inoue et al., 2023). WMHs are known to contribute to the cognitive impairments seen in CAD patients (Filley & Fields, 2016; O'Brien, 2014). However, macrostructural measures do not suffice to fully explain the impact of CAD on cognition as shown in Zheng and colleagues (2012), where CAD remained significantly associated with cognition after adjusting for WMH, and hippocampal and cortical GM volumes (Santiago et al., 2015). This suggests that more sensitive neuroimaging metrics are needed to detect subtle changes in brain health, such as changes in the so-called “normal-appearing” WM. Diffusion-weighted imaging (DWI) and magnetization transfer imaging (MTI) allow to capture such changes in WM microstructure.

Changes in diffusion tensor (DTI) metrics in several major WM tracts, including the fornix, body of the corpus callosum, superior corona radiata and superior fronto-occipital fasciculus, have been reported in CAD patients (Poirier et al., 2024). Importantly, WM microstructural integrity, quantified using fractional anisotropy (FA), has been linked with cognitive performance, especially executive function, in cognitively intact CAD patients (Santiago et al., 2015). This suggests that alterations in WM microstructure may be an important factor contributing to subtle changes in cognition in CAD patients. While there is evidence for an association between CAD and WM changes, the mechanisms through which WM damage occurs and causes cognitive decline are poorly understood, as the few studies that have looked at this used techniques that are physiologically unspecific (i.e., DTI) (Poirier et al., 2024; Riffert et al., 2014; Santiago et al., 2015).

Metrics derived from more advanced multi-compartment DWI models, complemented with quantitative measures of myelin (MTsat and R1), can provide greater insights into the pathophysiological mechanisms underlying WM microstructural alterations in CAD patients. This has important implications as WM microstructural impairments may be reversed through interventions such as exercise-based cardiac rehabilitation (Poirier et al., 2024).

Fitness is an important contributor to both cardiovascular and cerebral health (España-Irla et al., 2021). In patients with CAD, higher cardiorespiratory fitness has been associated with preserved cognitive performance, including executive function (Swardfager et al., 2010). Furthermore, the relationship between fitness and cognition in CAD is believed to be mediated by enhanced cerebral health (Swardfager et al., 2010, 2011). For instance, greater cardiorespiratory fitness has been associated with higher cerebral gray matter density and perfusion in men with CAD (MacIntosh et al., 2014). The beneficial effect of exercise on WM integrity may thus be an important mechanism through which cognition can be preserved in CAD (Poirier et al., 2024; Roig-Coll et al., 2024; Stephen et al., 2020).

In this cross-sectional study, we used a multivariate approach to comprehensively assess WM microstructural health. The MultiVariate Comparison (MVComp) toolbox was used to compute the Mahalanobis distance (D2), a measure of deviation between an observation (e.g., a patient) and a reference distribution (e.g., a control group) (Tremblay, Alasmar, et al., 2024b). D2 integrates several MRI measures into a single score, while accounting for the covariance between these metrics, yielding a measure of deviation, or abnormality at each WM voxel. The relationships between WM D2, fitness (VO₂peak), and cognition were also assessed.

5.3 Methods

5.3.1 Participants

One hundred and nine (109) participants of 50 years and above were recruited, from which 87 completed the study (46 CAD patients and 41 healthy controls; HC). The study was approved by the Comité d'éthique de la recherche et du développement des nouvelles technologies (CÉRDNT) de l'Institut de Cardiologie de Montréal, in accordance with the Declaration of Helsinki. Written informed consent was obtained at the first visit. A medical questionnaire, which had been previously filled out on the phone, was also reviewed at this visit and the mini-mental state

examination (MMSE) was administered to ensure eligibility. Participants with a MMSE < 25 were excluded as it could indicate the presence of mild cognitive impairment.

Inclusion criteria for patients included documented coronary artery disease (prior acute coronary syndrome, prior coronary angiography or revascularization, or myocardial ischemia documented on myocardial scintigraphy). Healthy controls (HCs) had to be free of any cardiac and neurological issues, diabetes, hypertension, and current use of medications known to be vasoactive (such as statins or beta-blockers). All participants had to be fluent in either English or French (for informed consent and cognitive assessment).

Exclusion criteria for all participants included history of stroke, neurological, psychiatric or respiratory disorders, thyroid disease, cognitive impairment, tobacco use, high alcohol consumption (more than 2 drinks per day), contraindications to MRI (e.g., ferromagnetic implant, claustrophobia), and use of oral or patch hormone therapy. Participants were also excluded if they had surgery under general anesthesia within the last 6 months, a recent acute coronary event (< 3 months), chronic systolic heart failure, resting left ventricular ejection fraction < 40%, symptomatic aortic stenosis, severe nonrevascularizable coronary artery disease, including left main coronary stenosis, awaiting coronary artery bypass surgery, implanted automatic defibrillator or permanent pacemaker. Limitations to exercise such as malignant arrhythmias during exercise, arthritis or claudication, severe exercise intolerance, as well as excessive discomfort due to hypercapnia (> 5 on the dyspnea scale of [Banzett et al., 1996](#)) also constituted exclusion criteria.

All participants completed a neuropsychological battery, a maximal cardiopulmonary exercise test (CPET), and an MRI session. Participants who had all DWI and MTI data were included in this study (N= 84). However, 5 participants were excluded due to the presence of artefacts in their DWI data (N=4) or of an incidental finding in their MRI data (N=1), resulting in a sample size of 79. Of those, 43 were CAD patients (age = 68.2 ± 8.7 years, 8 females) and 36 were HCs (age = 64.1 ± 7.8 , 10 females).

Table 1. Demographic data of the cohort.

Descriptives							
	Group	N	Missing	Mean	SD	Minimum	Maximum
Age	control	36	0	64.0556	7.79357	52	81
	patient	43	0	68.2326	8.70095	51	84
Education	control	36	0	16.0278	2.43177	11.0000	20.0000
	patient	43	0	16.1628	4.53521	9.0000	27.0000
SYNTAX score	control	0	36	NaN	NaN	NaN	NaN
	patient	26	17	13.4231	9.44743	0.0000	34.5000
VO2max	control	36	0	28.8806	6.51354	14.7000	39.9000
	patient	43	0	21.0884	5.38610	10.4000	32.2000
MoCA	control	35	1	26.5714	2.15960	22.0000	30.0000
	patient	43	0	25.4419	2.95443	17.0000	30.0000
Working memory	control	34	2	-0.0393	0.86347	-1.5519	1.6974
	patient	42	1	0.0318	0.81779	-1.5519	2.3245
Processing Speed	control	34	2	0.2496	0.70300	-2.2221	1.3117
	patient	42	1	-0.2149	0.81540	-2.0740	1.7707
Executive Function	control	35	1	0.2937	0.62587	-1.5330	1.3504
	patient	42	1	-0.2448	0.95137	-2.9248	1.1953
Verbal/Episodic Memory	control	35	1	0.1630	0.94458	-1.4776	1.7258
	patient	43	0	-0.1327	0.94304	-2.5765	1.6949
WMH	control	36	0	4.1051	4.56826	0.5870	19.8270
	patient	43	0	9.5770	19.45160	0.6050	117.1410
GM_Volume	control	36	0	0.1205	0.01650	0.0750	0.1543
	patient	43	0	0.1115	0.01669	0.0687	0.1474
WM_Volume	control	36	0	0.0619	0.00818	0.0442	0.0771
	patient	43	0	0.0582	0.00923	0.0415	0.0853
SBP	control	33	3	127.7273	14.22206	105.0000	160.0000
	patient	41	2	127.1707	14.56177	100.0000	160.0000
BMI	control	36	0	26.0333	3.91816	19.3000	36.4000
	patient	42	1	28.0857	4.53278	20.4000	42.8000

SYNTAX score = complexity of coronary artery disease, WMH = white matter hyperintensity (volume), GM = gray matter, WM = white matter, SBP = systolic blood pressure, BMI = body mass index.

5.3.2 MRI Protocol

MRI data were acquired on a 3T Siemens Magnetom Skyra scanner at the Montreal Heart Institute. The multi-shell DWI acquisition was a spin-echo sequence with echo planar imaging (EPI) readout (TR= 6000 ms, TE= 106 ms, phase-encoding direction = posterior-anterior (PA), resolution = 2 mm isotropic) across 3 diffusion-weighted shells with gradient strengths of $b= 300$ (10 directions), 700 (30 directions), and 2500 s/mm^2 (64 directions), and 3 volumes acquired without diffusion weighting ($b = 0$). Six non-diffusion weighted volumes ($b = 0$) were also acquired in the opposite phase encoding direction (AP) for distortion correction.

Two gradient echo sequences (TR= 33 ms, TE= 3.81 ms, flip angle= 10° , resolution= 2 mm isotropic), one with (MT-w) and one without a preparatory MT pulse (MT-off), and a T1w image (TR= 15 ms, TE= 3.81 ms, flip angle= 25° , resolution= 2 mm isotropic) were acquired for MTsat computation. An off-resonance MT pulse (off-resonance frequency = 2.2 kHz, duration = 12.8 ms, flip angle = 540°) was applied prior to RF excitation to obtain MT-weighting (Helms, Dathe, & Dechent, 2008). A B1 map (an anatomical image and a flip angle map) was also acquired to correct B1 field inhomogeneities.

High-resolution T1-weighted structural images were acquired with a Magnetization Prepared RAPid Gradient Echo (MPRAGE) sequence (TR= 2300 ms, TE= 2.32 ms, flip angle= 8° , resolution= 0.9 mm isotropic). These images were used for segmentation by tissue type. Axial fluid attenuated inversion recovery (FLAIR) images (TR= 9000 ms, TE= 91 ms, TI= 2500 ms, flip angle= 150° , resolution= 0.9 x 0.9 x 5.0 mm) were acquired for WMH segmentation.

5.3.3 Preprocessing

We computed 12 microstructural metrics from the DWI and MTI data of 83 participants. These metrics were derived from the diffusion tensor imaging (DTI) model, the fixel-based analysis framework that derives fibre density and cross-section from fibre orientation distributions (FODs) computed using multi-tissue constrained spherical deconvolution (CSD) (Jeurissen et al., 2014), and the neurite orientation dispersion and density imaging (NODDI) model (H. Zhang et al., 2012a). The MT saturation index was computed from the MT-w and MT-off images, using the T1w images to reduce T1 dependence (Helms, Dathe, & Dechent, 2008) and R1 maps were also generated.

Diffusion Tensor Imaging

DWI data were denoised and preprocessed with the MRtrix3 (v3.0.2) function `dwifslpreproc`, which corrects for motion and Eddy current (using the Eddy tool in FSL 6.0.1) and susceptibility-induced distortion (using the `topup` tool in FSL) (Andersson et al., 2003; Andersson & Sotiropoulos, 2016; S. M. Smith et al., 2004). `Topup` uses pairs of `b0` volumes with opposite phase-encoding polarities (AP) and with the same phase encoding as the input DWI series to correct for susceptibility-induced distortion. Preprocessed DWI data were then upsampled to match the MPRAGE T1w image resolution (0.9 mm isotropic) as recommended. A brain mask was created using FSL's brain extraction tool (`bet`) and applied to the DWI volumes to eliminate non-brain voxels (Jenkinson, 2005). Bias field correction was performed using the N4 algorithm of ANTs (3.0) (Tustison et al., 2010), and the tensor was computed on the bias field-corrected DWI data (using `dwi2tensor`). Finally, DTI metrics (FA, MD, AD, and RD) were calculated using `tensor2metric` (Basser et al., 1994a).

Fixel-based analysis

The fixel-based analysis (FBA) framework was used to compute fibre density and cross-section from FODs (Tournier et al., 2019) as in (Tremblay, Alasmar, et al., 2024b). MPRAGE T1-w images were registered and warped (rigid, linear) to the non-diffusion weighted (`b=0`) preprocessed DWI volume using `antsRegistration` (v2.4.2) before being segmented using the `5ttgen` FSL function of Mrtrix3, which uses the FAST algorithm (Avants et al., 2009; R. E. Smith et al., 2012). Response functions for each tissue type were then computed from the preprocessed DWI data and the five-tissue-type (5tt) image using the `dwi2response` function (`msmt_5tt` algorithm) (Jeurissen et al., 2014). The WM, GM and CSF response functions were then averaged across all participants, resulting in a single response function for each of the three tissue types. Multi-shell multi-tissue CSD was then performed based on the average response functions to obtain an estimation of orientation distribution functions (ODFs) for each tissue type (Jeurissen et al., 2014). This step is performed using the `dwi2fod msmt_csd` function of Mrtrix3 within the previously generated brain mask. Bias field correction and global intensity normalization, which normalizes signal amplitudes to make subjects comparable, were then performed on the ODFs, using the `mtnormalise` function in Mrtrix3 (Raffelt, Tournier, et al., 2017).

Registration

Multi-contrast registration was performed based on the WM, GM and CSF FODs using the `population_template` function of Mrtrix3 (Tremblay, Alasmar, et al., 2024b). This generates a group template for each of the three tissue types (Tournier et al., 2019). The WM FODs and DTI metrics (i.e., FA, MD, AD and RD) were then warped to the population templates using `mrtransform` (Raffelt et al., 2011). A template mask was computed as the intersection of all warped brain masks (`mrmath min` function). This template mask includes only the voxels that contain data in all subjects. The WM volumes of the five-tissue-type (5tt) 4-D images were also warped to the group template space and averaged across participants to be used as a WM mask for analyses.

Computing fixel metrics

Fixel metrics were computed as outlined in Tremblay et al. (2024). In summary, a fixel mask, which contains all fiber bundle elements (fixels) per voxel, was created by segmenting the WM FOD template (Raffelt et al., 2011; R. E. Smith et al., 2013). The WM FOD of each subject was then segmented using the `fod2fixel` function, which also provided the apparent fibre density (FD) metric. The `fixelreorient` and `fixelcorrespondence` functions were applied to ensure consistent fixel correspondence between subjects and the fixel mask (Tournier et al., 2019). The fibre bundle cross-section (FC) metric, which quantifies the degree of expansion or contraction needed to align a fibre bundle with the template fixels, was derived from the registration warps using the `warp2metric` function. A combined fibre density and cross-section (FDC) metric, representing the overall information-carrying capacity of a fibre bundle, was then calculated as the product of FD and FC.

Next, the fixel metrics were converted into voxel-wise maps for integration with other voxel-wise metrics. For the aggregate fibre density per voxel (FD total), we used the $l = 0$ term of the WM FOD spherical harmonic expansion (i.e., the first volume of the WM FOD, equivalent to the sum of FOD lobe integrals). This approach yields more reproducible estimates than summing fibre-specific FD (Calamante et al., 2015). For the aggregate fibre cross-section per voxel, the mean FC was calculated, weighted by FD, using the `fixel2voxel mean` function. This metric reflects the typical expansion or contraction required to align fibre bundles within a voxel to the template

fixels. Finally, the voxel-wise sum of FDC, representing the total information-carrying capacity per voxel, was calculated using the `fixel2voxel sum` option.

NODDI metrics

DWI data was fitted to the neurite orientation dispersion and density imaging (NODDI) model using the python implementation of Accelerated Microstructure Imaging via Convex Optimization (AMICO) (Daducci et al., 2015; H. Zhang et al., 2012a). Response functions were computed for all compartments and fitting was then performed on the bias-corrected DWI volumes using default parameters. The NODDI metric maps, including intracellular volume fraction (ICVF, or neurite density), isotropic volume fraction (ISOVF), and orientation dispersion index (OD), were subsequently warped into group space.

MTsat and R1 maps

The MTsat and R1 maps were calculated using the hMRI-toolbox (v 0.3.0) in Statistical Parametric Mapping (Tabelow et al., 2019). The anterior and posterior commissure of the MT-w, MT-off and T1w images were reoriented to MNI space. The reorientation process was performed before processing the MTsat and R1 maps to enhance the alignment of the images' WM. The B1 transmit bias correction field was computed using an anatomical map and a scaled flip angle map from a turbo flash sequence using the "Create hMRI maps" module of the hMRI-toolbox. Then, the B1 correction field, MT-w, MT-off and T1w images were included in the "Create hMRI maps" module to measure MTsat and R1 maps with default parameters. Finally, non-brain voxels were removed from the T1w maps using FSL's brain extraction tool (bet) (Jenkinson, 2005). The T1w brain masks were then applied to the MTsat and R1 maps. The MTsat and R1 maps were registered and warped (rigid, linear) using the MPRAGE image that was previously warped to the DWI space (within-subject) as a target, with `antsRegistration` (Avants et al., 2009). The MTsat and R1 maps were then warped to the population template using the previously generated transforms.

White matter hyperintensities

White matter hyperintensities (WMH) were segmented using the Brain TISsue segmentatiON (BISON) classifier (Dadar & Collins, 2021). Prior to BISON segmentation, the T1w and FLAIR images were preprocessed with the minc-toolkit and ANTs packages. Initially, the images were

denoised using the `mincnlm` tool. Then, the FLAIR maps were co-registered to the T1w images using the `minc-toolkit` function `bestlinreg_s2`. Temporary masks were generated via `minresample` to facilitate non-uniformity correction with `nu_correct`. Intensity normalisation was conducted with the `volume_pol` tool. The FLAIR images were then registered to stereotaxic space using `bestlin_reg` and resampled with `itk_resample` (McCormick et al., 2014). Brain voxels were extracted using `mincbeast`, followed by nonlinear registration of the FLAIR images to the T1w maps using `antsRegistration` (Avants et al., 2009). Finally, the BISON classifier was applied to the preprocessed FLAIR and T1w images to segment WMH. Further details on the performance and methods of the BISON classifier can be found in (Dadar & Collins, 2021).

5.3.4 Computing multivariate distance metric (D2)

The MVComp toolbox was used to compute D2 from the 12 WM features (FA, AD, RD, MD, ICVF, ISOVF, OD, AFDtotal, meanFC, sumFDC, MTsat and R1) (Tremblay, Alasmar, et al., 2024b). Prior to D2 calculation, the effect of age was removed from feature maps by fitting a linear model predicting voxel-wise metric values from age using `LinearRegression` in `sklearn.linear_model` and computing the residuals. Residualized maps were then used for D2 calculation.

D2 was computed voxel-wise between each subject of the CAD group and the reference, consisting of the group average of the HCs. The D2 scores obtained thus indicate the extent of deviation in WM microstructure from a healthy reference. Group averages were computed from the reference group (N = 36) for each of the 12 metrics using the `compute_average` function of MVComp. The `norm_covar_inv` function was then used to compute the covariance matrix (`s`) and its pseudoinverse (`pinv_s`) from the reference. A figure showing the correlations between MRI metrics was generated using the `correlation_fig` function which uses the covariance matrix (`s`) to calculate correlations (**Figure 1**). D2 was then computed within MVComp according to this equation:

$$D^2 = (x - m)^T C^{-1}(x - m),$$

where x is the vector of data for one observation (e.g., one subject), m is the vector of averages of all observations for each independent variable (i.e., MRI metrics), and C^{-1} is the inverse of the covariance matrix. The `model_comp` function allows the computation of voxel-wise D2 between each subject and the reference average within a specified mask of analysis. Here, a WM mask generated from the average of the WM volumes of the five-tissue-type images of all participants was provided and the threshold was set at 0.97 to limit partial volume effects. The `model_comp` function yields a matrix containing the D2 data of all subjects (of size: number of voxels x number of subjects). The `dist_plot` function was then used to obtain a D2 map (in nifti format) for each subject. The workflow for D2 calculation is illustrated in **Figure 1**.

D2 maps were also computed for subjects of the HC group using a leave-one-out approach to exclude the subject under evaluation (i.e., comparing each subject of the HC group to all other HCs). This is done within MVComp using the `exclude_comp_from_mean_cov` option of the `model_comp` function.

Because we wanted the reference to represent a healthy state, subjects of the HC group that were identified as outliers in D2 (i.e., mean D2 in whole WM > 2 SD) were excluded from the reference and from further analyses (N= 2). D2 was re-computed with this new reference (N= 34) for both the CAD and HC groups (using the leave-one-out approach).

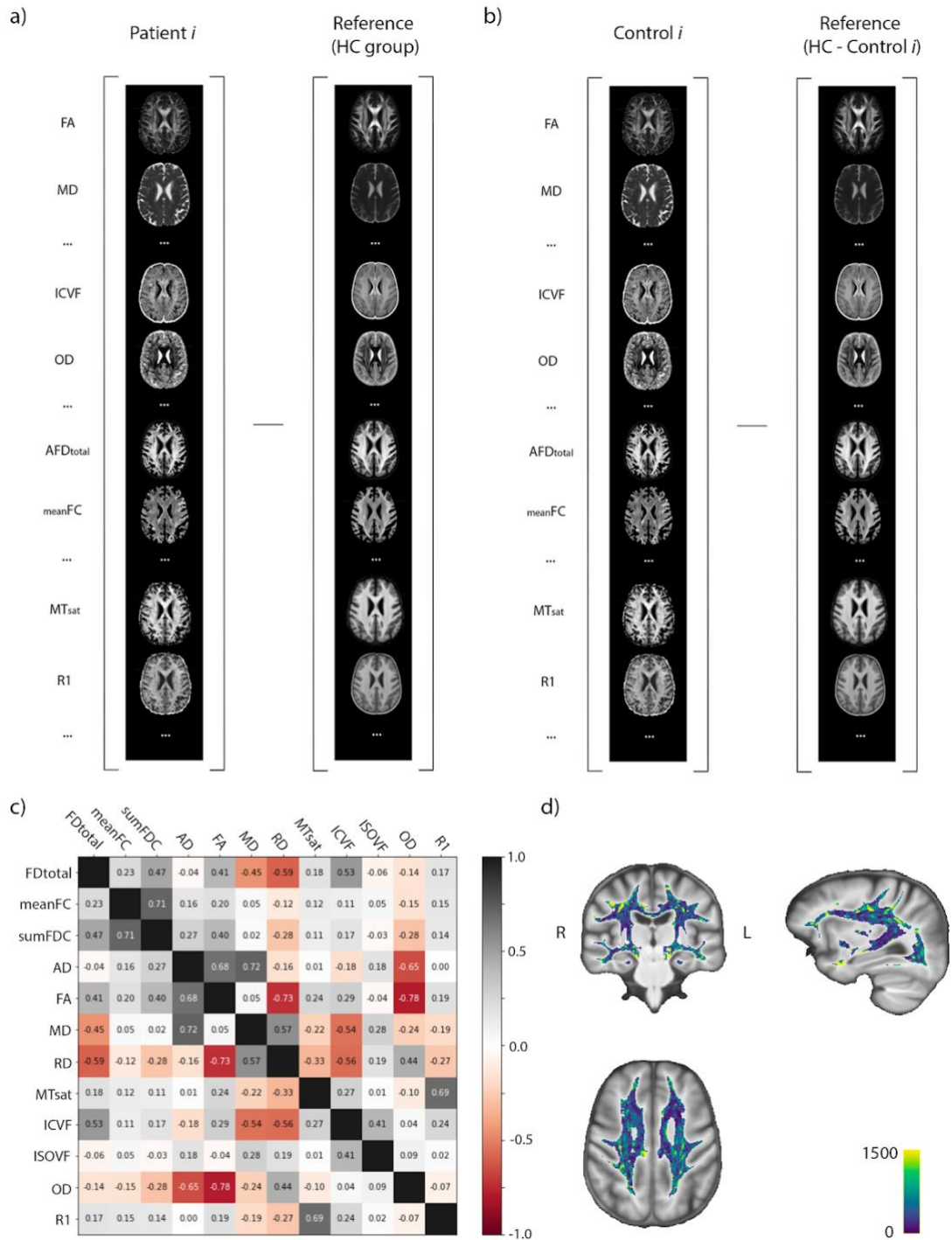


Figure 1. Workflow for computing $D2$. a) For subjects of the CAD group, $D2$ is computed by subtracting the data of each patient i and the reference sample, here the average of the HC group ($N=34$). b) For subjects of the HC group, $D2$ is computed by subtracting the data of each control i and the reference sample, here the average of the HC group excluding the subject under evaluation (HC group - control i). c) The correlation matrix shows relationships between MRI metrics (residualized for age), highlighting the importance of accounting for covariance between variables in multivariate frameworks. d) Example $D2$ map of a patient. The intensity indicates the amount of deviation in the WM microstructure of this subject relative to the reference, at each voxel.

5.3.5 Extracting D2 in arterial territories

A cerebral arterial territories atlas (C.-F. Liu et al., 2023) was used to define regions of interests (ROIs) in WM (**Figure 2**). The 3D MR-based cerebral arterial atlas was registered and warped to the D2 maps space using `antsRegistration` (Avants et al., 2009). Average D2 values were then calculated across WM voxels in the left and right anterior cerebral artery (ACA), middle cerebral artery (MCA) and posterior cerebral artery (PCA).

5.3.6 Cardiorespiratory fitness assessment

Participants completed a maximal cardiopulmonary exercise test (CPET) on an electromagnetic braking ergometer bicycle (Ergoline 800s, Blitz, Germany) to measure peak oxygen uptake ($\text{VO}_{2\text{peak}}$). The CPET protocol was individualised according to each subject's level of physical activity. An electrocardiogram (ECG) (GE Healthcare, Case ® Marquette, Missouri, USA) was monitored by a nurse and reviewed by a cardiologist. Blood pressure and a Borg perception scale (ranging from 6 to 20) were assessed every 2 to 3 minutes. The CPET began with a 3-minute warm-up at 10-20 watts, maintaining a cadence of 60 to 80 revolutions per minute. After the warm-up, the power was increased by 10 to 15 watt every minute until the subject could no longer maintain the cadence or met any of the following stopping criteria: 1) ECG abnormality or angina, 2) oxygen desaturation, 3) a reduced systolic blood pressure despite increase in workload or hypertensive response, 4) a rate of perceived exhaustion > 17 , or 5) the subject's desire to stop. A 5-minute recovery period was performed including 2 minutes of active recovery (10-20 watts) and 3 minutes of passive recovery. Oxygen uptake was continuously measured using a gas analyser (Quark CPET, COSMED, Rome, Italy) connected to a leak-free face mask. Participants' relative $\text{VO}_{2\text{peak}}$ (ml/kg/min) was determined by measuring the highest oxygen consumption over a 10-second interval.

5.3.7 Cognitive assessment

A comprehensive neuropsychological assessment was administered in the following order. The Montreal Cognitive Assessment (MoCA) was first conducted to assess global cognition. The Rey auditory verbal learning test (RAVLT) was conducted through 5 learning trials of a 15-word list to assess verbal and auditory episodic memory. Participants attempt to recall as many words from this list as possible for each of the 5 trials, after an interfering list (immediate recall), and after a 30-

min delay (delayed recall). The Digit Span forward and backward tests were then administered by asking participants to recall series of digits, starting with short sequences and then progressively increasing their length. Participants must repeat the series in the same order for the forward test and in the inverse order for the backward part. Both scores were used as proxies of working memory. In the Digit Symbol Substitution Test (DSST), measuring processing speed, participants have to draw the appropriate symbol corresponding to a number between 1-9, using a response key with 9 digit-symbol pairs. The score is the number of symbols drawn in 120 seconds. The Delis-Kaplan Executive Function System (D-KEFS) Color Word Interference Test (CWIT) test consists of 4 conditions: color naming, reading, inhibition, and switching (Delis et al., 2001). In the color naming condition, participants have to name the color of colored squares presented to them as quickly as possible. In the reading condition, a page containing the words “red,” “green,” and “blue” printed in black ink is presented to participants who have to read the words. In the inhibition condition, participants have to inhibit reading and instead name the color of the ink as a page with the words “red,” “green,” and “blue” printed in incongruent colors is presented to them (Stroop, 1935). Lastly, the switching trial requires participants to alternate between reading and color naming (inhibiting reading) as they are presented with a page similar to the preceding condition but with half the words enclosed in boxes. When enclosed within a box, the words should be read and when they are not enclosed, the color of the ink should be said instead. For each condition, participants should read all words, or name all colors, as quickly as possible without making mistakes. The first two conditions assess processing speed and the last two measure different aspects of executive function (inhibition, flexibility and switching) (Lezak, 2004). The Trail Making Test (TMT) part A, which measures processing speed, and part B, a measure of executive function, was administered last. In part A of this test, participants have to link numbers from 1-25 in the ascending order as quickly as possible. For part B, participants must link numbers and letters, alternating between a number and a letter in ascending and alphabetical order.

All scores were transformed into standardized z-scores and 4 composite scores, representing different cognitive domains, were then created using those z-scores: (1) working memory = $((DS \text{ forward} + DS \text{ backward scores})/2)$; (2) processing speed = $((DSST + TMT \text{ A} + CWIT \text{ 1} + CWIT \text{ 2 scores})/4)$; (3) executive functioning = $((TMT \text{ B} + CWIT \text{ 3} + CWIT \text{ 4 scores})/3)$; and (4) verbal memory/episodic memory $((\text{immediate recall} + \text{delayed recall} + \text{total words scores recalled during the 5 learning trials from the RAVLT test})/3)$ (Desjardins-Crépeau et al., 2014).

5.3.8 Statistical analyses

As a sanity check, we performed independent sample t-tests to compare D2 in each arterial territory and in the whole WM between CAD and HCs. Given the unequal variances of the data (assessed by Levene's test $p < 0.05$), *Welch's* t-test was employed to compare the means between groups and one-tailed t-tests were used because patients were expected to have higher D2 values than HCs.

Because there was an age difference between groups ($p < 0.05$), special attention was given to account for age in analyses. D2 maps were created from age residualized feature maps, and should thus be free of any age effects. Age was also regressed out from composite scores of cognition and from VO2max scores and the residuals were used in all subsequent analyses. Group differences in residuals of cognitive composite scores and of VO2max scores were tested using independent sample t-tests (*Student's t*).

Linear regression models were then used to assess the relationships between fitness (VO2max), cognition, and D2 in each arterial territory and in the whole WM, using age residualized scores and with sex and education as covariates. Analyses with cognition were focused on composite scores reflecting cognitive domains of interest (e.g., significant group difference). Linear regression models were also used to evaluate the relationship between fitness, cognition and WMH volume. Regression analyses were performed on the whole sample.

To evaluate whether fitness had a differential effect on WM health in CAD patients, we added the interaction of Group * VO2 residuals to the regression model. Similarly, we evaluated whether D2 had a differential effect on cognition by adding a group interaction term to significant models.

5.3.9 Determining features contribution to D2

The relative contributions of each feature (i.e., MRI metric) to D2 in the whole WM, as well as in each arterial territory, were extracted using the `return_raw` option of the `model_comp` function in MVComp (Tremblay, Alasmar, et al., 2024b). The `return_raw` option yields a matrix of size (number of voxels) x (number of metrics) x (number of subjects). Contributions were then summarised by averaging distance values across voxels within the mask and across subjects and dividing by the total distance (for all features), resulting in one distance value per metric, expressed

as a percentage, for each region. This analysis provides a measure of the importance of each metric in determining D2.

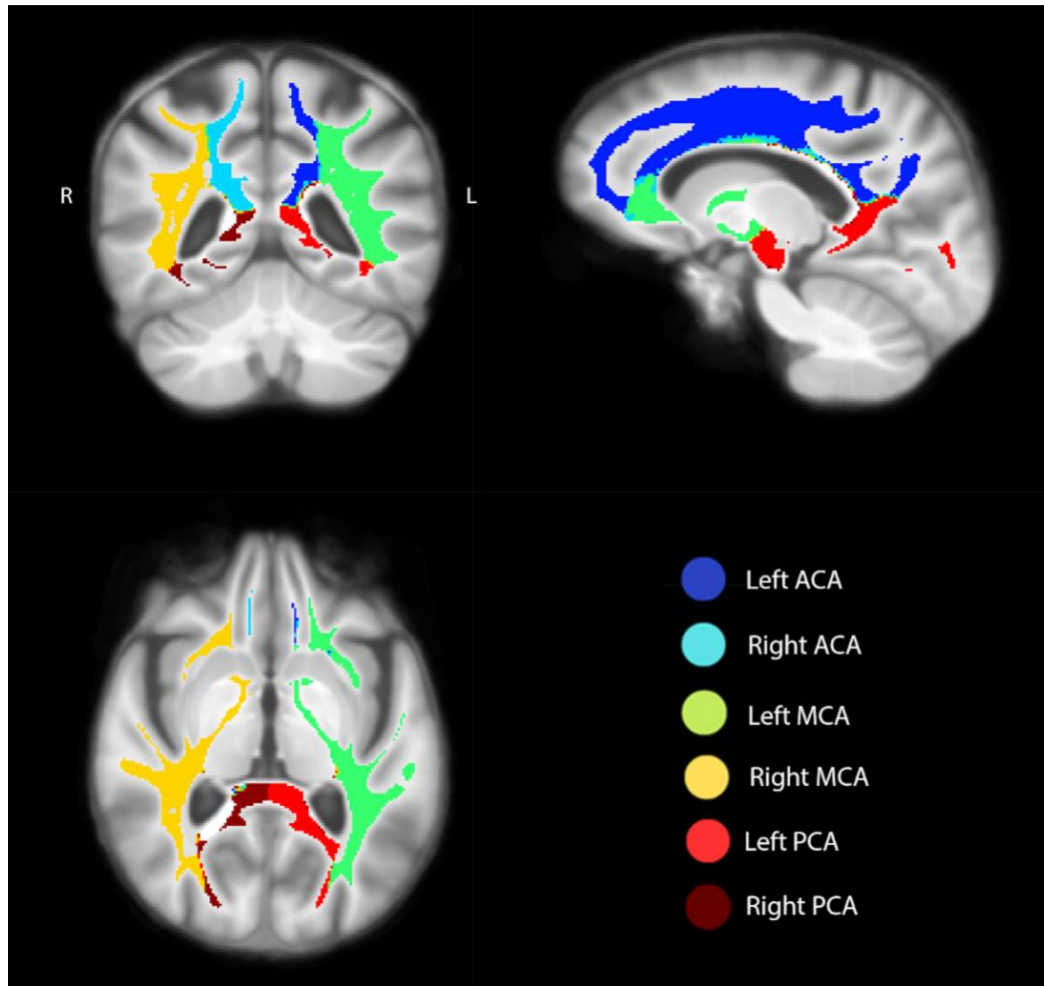


Figure 2. Arterial territories within the WM mask, overlaid on the group average MPRAGE T1w image.

5.4 Results

5.4.1 Group differences

There were significant group differences in WM microstructural deviations (WM D2) in the whole WM (*Welch's t* (47.3) = -1.83, $p = 0.037$) and in several arterial territories, indicating that CAD patients had higher D2 values than HCs (**Figure 3**). D2 was significantly different between groups in the right ACA (*Welch's t* (58.3) = -2.46, $p = 0.008$) and near significant on the left (*Welch's t* (74.5) = -1.62, $p = 0.055$). The same trend was observed in the MCA, with patients having higher D2 values, but it did not reach statistical significance (left: *Welch's t* (44.5) = -1.41, $p = 0.082$;

right: *Welch's t* (46.9) = -1.59, $p = 0.059$). D2 was statistically different in both the left and the right PCA (left: *Welch's t* (58.8) = -1.95, $p = 0.028$; right: *Welch's t* (58.1) = -2.70, $p = 0.005$).

In terms of fitness and cognitive measures, HCs had significantly higher fitness (VO2 residuals) than CAD patients (*Student's t* (76.0) = 5.269, $p < 0.001$). Executive function (residuals) was also greater in HCs (*Student's t* (75.0) = 2.006, $p = 0.048$) and there was a trend for processing speed (*Student's t* (74.0) = 1.740, $p = 0.086$) in the same direction. There were no group differences in working memory and in episodic memory ($p = 0.499$ and $p = 0.536$, respectively). Further analyses were focused on executive function and processing speed.

5.4.2 Features contribution to D2

In the whole WM, D2 was driven mainly by R1 (14.6%), MTsat (11.2%), and RD (10.4%). In the left ACA, R1 (13.4%), ICVF (12.3%), and FA (10.7%) contributed the most to D2. D2 in the right ACA was driven mainly by R1 (18.0%) and MTsat (10.3%). In the left MCA, R1 (14.1%), RD (12.0%), and MTsat (10.7%) were the metrics that contributed the most to D2. In the right MCA, R1 (15.0%), MTsat (14.5%), and RD (10.7%) contributed most to D2. D2 in the left PCA was mainly driven by R1 (21.7%) and MTsat (10.5%), while it was driven by R1 (23%) and FA (10.4%) in the right PCA. Overall, R1 was an important contributor in all regions and MTsat was also an important metric for several arterial territories (4 out of 6) in addition to the whole WM.

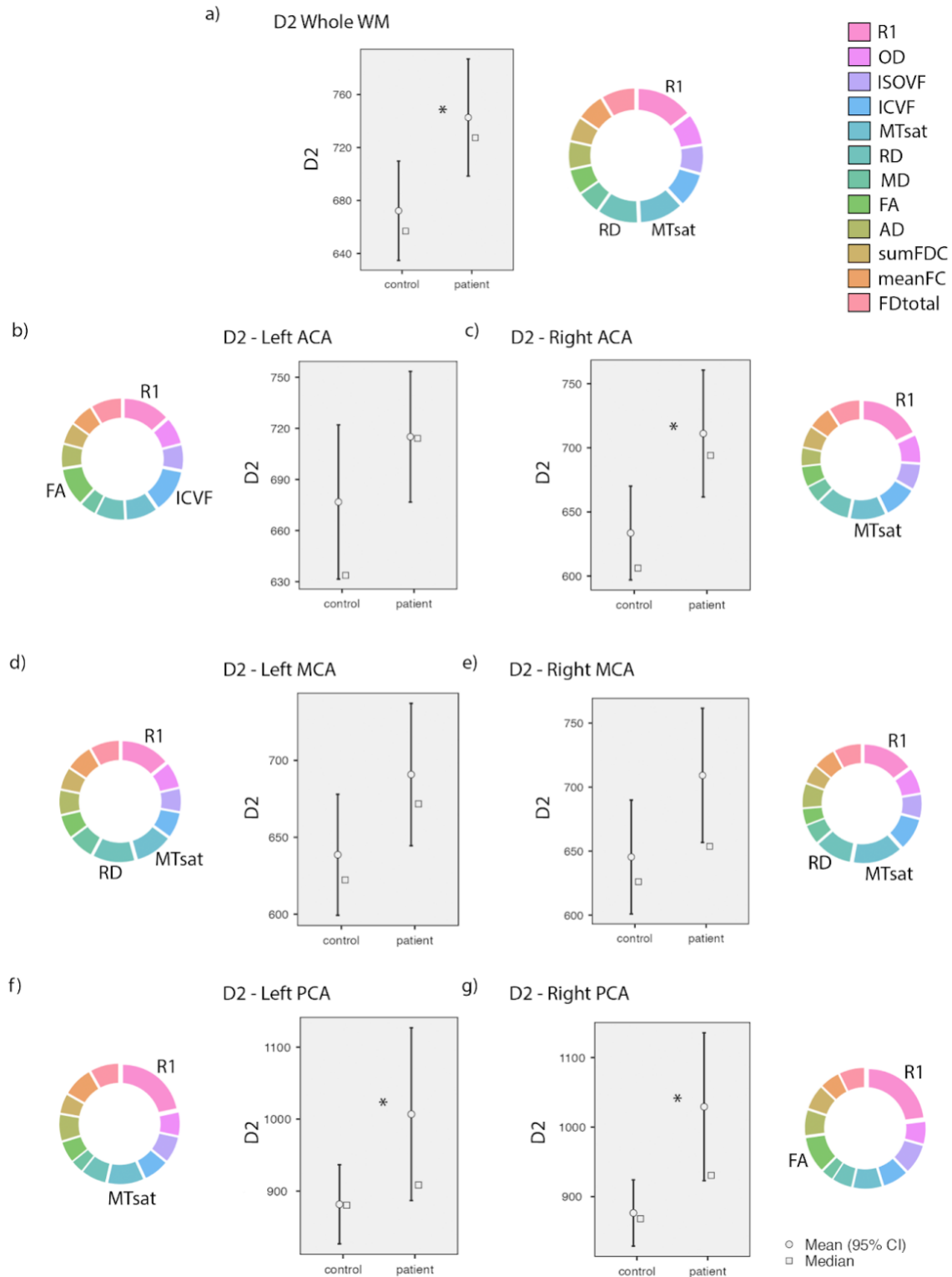


Figure 3. Mean and median D2 in whole WM (a) and in each arterial territory (b-g) for each group. Significant group differences where CAD > HC are indicated with an asterisk. Pie charts show the relative contribution (%) of each MRI metric to D2 in each region. The metric name is indicated only for the most important contributors (those that account for >10%), for clarity.

5.4.3 Links between WM D2, fitness, and cognition

Fitness was negatively associated with D2 in the whole WM ($t = -2.206$, $p_{uncorr.} = 0.031$) and in the left PCA ($t = -2.41$, $p = 0.019$), suggesting that participants with higher fitness had lower WM D2 (i.e., less WM alterations) (**Figure 4a,c**). The association between fitness and D2 in the right MCA was also nearly significant ($t = -1.924$, $p = 0.058$). Sex and education were not significant in these analyses ($p > 0.05$).

D2 in the left MCA was negatively associated with processing speed ($t = -2.255$, $p = 0.027$), indicating that participants with better performance in this cognitive domain had lower WM D2 (**Figure 5a**). Sex was also significant ($t = -2.143$, $p = 0.036$) and education approached significance ($t = -1.943$, $p = 0.056$).

There were no significant associations between D2 and executive function ($p > 0.05$). A subject of the CAD group who was identified as an outlier (whole WM D2 > 2 SD from the mean) was excluded from those analyses.

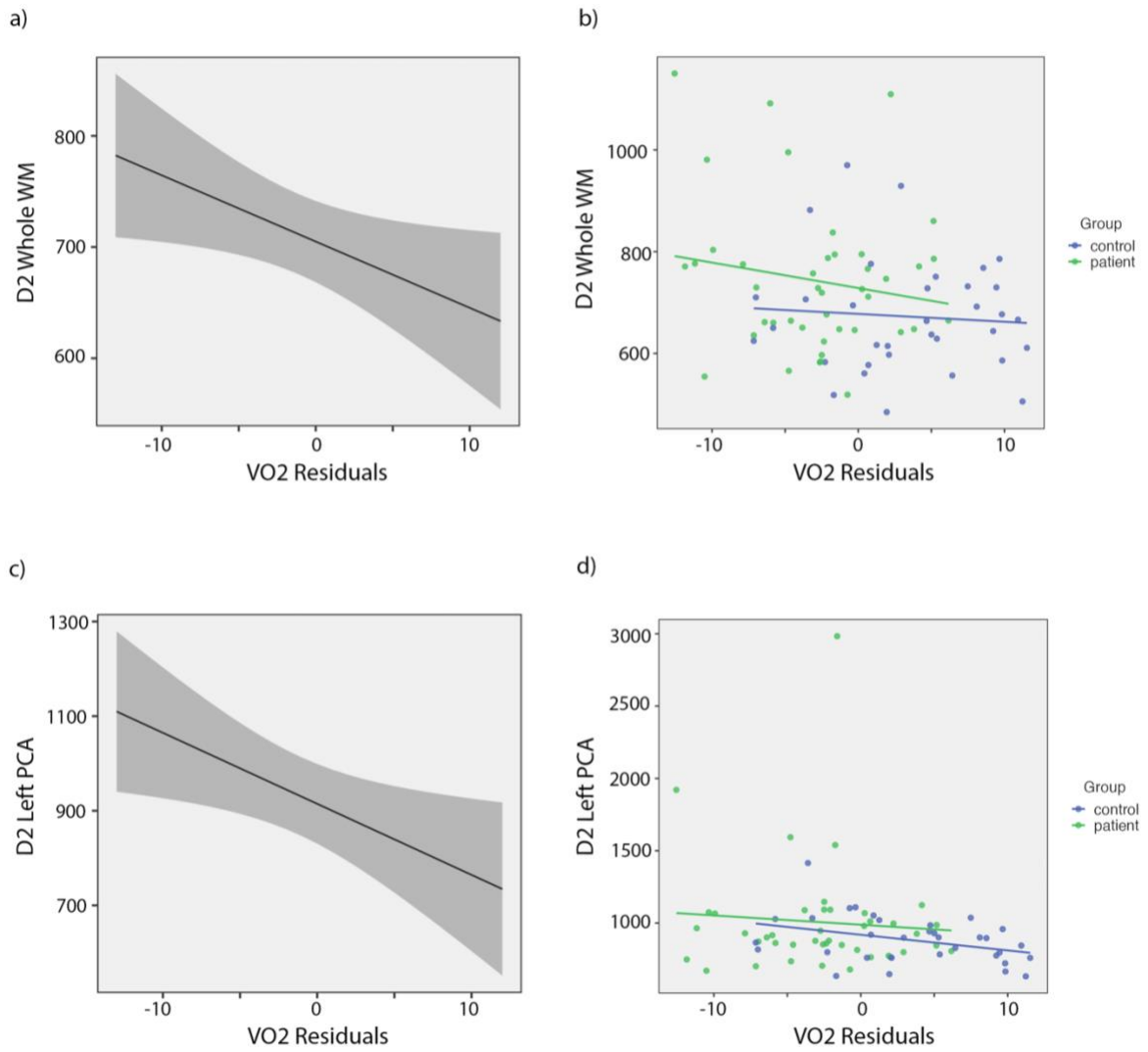


Figure 4. Associations between VO2max and D2 in whole WM (a-b) and in the left PCA (c-d) in the whole sample. Plots in the right panel (c, d) show the distribution of the data and the regression line for each group.

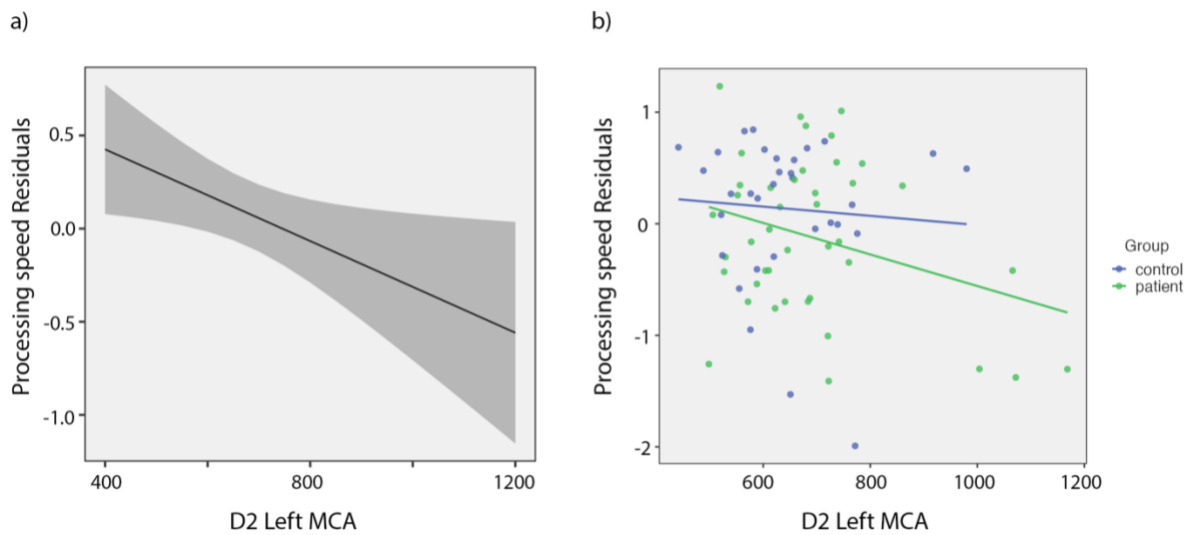


Figure 5. Associations between D2 in the left MCA and processing speed in the whole sample.

5.4.4 Differential effects in patients vs controls

Visual inspection of the scatterplot between VO2 residuals and D2 in the whole WM suggests the relationship was stronger in CAD than in HC (**Figure 4b**). However, the interaction was non-significant ($p > 0.05$), and all main effects became non-significant when adding Group and Group*VO2 interaction terms to the regression model.

Similarly, the relationship between D2 in the left MCA and processing speed appeared stronger in CAD patients (**Figure 5b**). However, the interaction was non-significant ($p > 0.05$), and all main effects, except sex ($p = 0.046$), became non-significant when adding Group and Group*D2 in left MCA interaction terms to the regression model.

5.4.5 Links between WMH, fitness and cognition

Total WMH volumes were correlated with MoCA scores ($t = -2.517, p_{uncorr.} = 0.014$), indicating that participants with lower cognitive performance had more WM lesions (**Figure 6**). Education was also significant ($t = 2.893, p = 0.005$), where greater MoCA scores were associated with higher education. The associations between cognitive composite scores and WMH volumes, as well as between fitness and WMH were non-significant ($p > 0.05$).

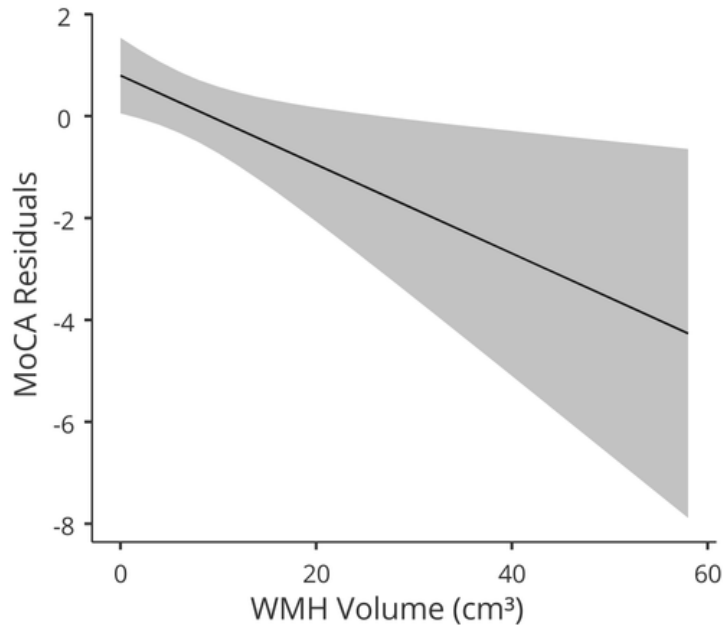


Figure 6. Associations between WMH volumes and MoCA in the whole sample.

5.5 Discussion

In this study, we demonstrated links between fitness, cognition and WM microstructural deviations from a group of healthy older adults in a population of CAD patients. Deviations in WM microstructure were quantified using a novel multivariate approach that allows the integration of several MRI measures of WM into a single score indicative of the extent of *abnormality*.

5.5.1 WM microstructural alterations in CAD patients

Cardiovascular disease is known to impact several aspects of brain health, including WM (Barekattain et al., 2014; Haight et al., 2018; Launer et al., 2015; Vuorinen et al., 2014). Here, we found that CAD patients had a significantly greater extent of WM alterations relative to healthy subjects in several arterial territories (right ACA, bilateral PCA), as well as in the whole WM (**Figure 3**). Very few studies have investigated WM microstructure in CAD patients (Poirier et al., 2024; Santiago et al., 2015) as most have been focused on macrostructural changes in WM such as the volume of WM lesions (WMH) (Johansen et al., 2021; Vidal et al., 2010; Vuorinen et al., 2014). In the study by Poirier and colleagues (2024), impairments in WM microstructure were observed in several major WM tracts, including the fornix, body of the corpus callosum, superior corona radiata and superior fronto-occipital fasciculus, in CAD patients. Also of interest, loss in WM

integrity (i.e., decreased FA and increased MD) in widespread WM areas (corpus callosum, bilateral internal capsule/corona radiata/posterior thalamic radiation/inferior fronto-occipital fasciculus and right inferior/superior longitudinal fasciculus) have been reported in subjects with vascular cognitive impairment (H.-J. Chen et al., 2018). However, since our study is the first to characterize WM integrity in arterial territories in the context of vascular disease, we cannot directly compare our findings with others. Characterizing white matter (WM) changes in specific arterial territories is crucial, as WM damage in vascular disease often stems from episodes of misery perfusion and transient hypoxia. These events are likely to occur in distinct arterial regions, particularly where small vessels at the end of the vascular tree experience insufficient perfusion (Inoue et al., 2023; O'Rourke & Hashimoto, 2007). The dearth of evidence in this field calls for further research effort focused on comprehensively evaluating the impact of CAD on brain WM health.

5.5.2 Links with fitness

Cardiorespiratory fitness (VO₂max) was negatively associated with WM alterations (D2) in the whole WM, as well as in the left posterior cerebral artery (PCA) territory in the whole sample comprising CAD patients and HCs (**Figure 4**). This indicates that individuals with greater WM deviations from a healthy reference had lower levels of fitness. In line with the association we found between fitness and lower whole WM D2, several studies have reported a positive effect of cardiorespiratory fitness on global WM integrity (Maleki et al., 2022; Sexton et al., 2016; Zhu et al., 2015). Although no other studies have focused on arterial territories, it is interesting to note that a study found positive associations between fitness and WM health (quantified using FA) in multiple WM posterior regions such as the splenium, sagittal stratum, posterior corona radiata, and superior parietal white matter in normal aging (Hayes et al., 2015), which is consistent with our findings in the PCA territory.

Exercise-based interventions are promising tools in the prevention of cognitive decline and dementia and may be particularly beneficial for CAD patients. In this study, we observed a steeper association slope between VO₂max and whole WM D2 in CAD patients, indicating that fitness may have a greater impact on WM health in patients than in healthy controls. The Group*VO₂ interaction was however not statistically non-significant, perhaps due to the small sample size. Moreover, in a study using an exercise intervention for cardiac rehabilitation in ischemic heart

disease patients, improvements in WM integrity were observed following intervention (Poirier et al., 2024). Our findings and that of others (Poirier et al., 2024) thus suggest that cardiorespiratory fitness and physical activity may act as protective mechanisms for WM health.

5.5.3 Links with cognition

WM abnormalities have been suggested to underlie cognitive impairments in aging and in vascular diseases (H.-J. Chen et al., 2018; Filley & Fields, 2016; Santiago et al., 2015; Vernooij et al., 2009). Santiago and colleagues (2015) found that FA in the left parahippocampal cingulum and inferior fronto-occipital fasciculus was positively associated with executive function and processing speed in CAD patients. Although we did find a significant group difference in executive function, WM D2 was not significantly associated with executive function in any of the arterial territories. We however found an association between WM D2 in the left MCA and processing speed, where participants with a greater amount of microstructural alterations had poorer performance in this cognitive domain (**Figure 5**). Other studies have reported associations between processing speed (e.g., reaction time) and WM microstructure in cognitively unimpaired older adults, where decreased FA was found to mediate the relationship between age and processing speed (Kerchner et al., 2012). Together, our findings support the idea that WM alterations are an important part of the pathophysiology behind vascular cognitive impairment.

5.5.4 Biological mechanisms underlying WM alterations

We found that WM alterations were greater in CAD patients than in HC in all regions, reaching statistical significance in the whole WM as well as in 3 arterial territories (right ACA, left and right PCA). The MCA territory is known to be most commonly affected in ischemic stroke and in CAD, likely due to its direct connection to the internal carotid artery, which is a common site of atherosclerosis (Mathur et al., 1963; Vigen et al., 2020). Although group differences in the MCA were non-significant, we found a significant association between D2 in the left MCA and processing speed, which suggests that perhaps subtle impairments in this region may be detrimental to cognition.

Extracting the contribution of each MRI feature to D2 in each of these regions revealed that differences in myelin content (as measured by R1 and MTsat) was likely a primary mechanism driving microstructural alterations in CAD patients (**Figure 3**). Axonal degeneration may also have

been an important mechanism in the left ACA where ICVF was also a strong contributor. To our knowledge, no other studies have examined changes in myelination specifically in CAD patients. However, lower myelin content has been reported in older adults with cardiovascular risk factors such as hypertension and obesity (Trofimova et al., 2023). On the other hand, a study examining the impact of arterial stiffness found an association with axonal degeneration rather than demyelination (Badji et al., 2019). Overall, our findings suggest that axonal and myelin loss may occur concurrently in CAD. More studies are however needed to characterize WM health in this specific population.

5.5.5 Limitations & Future directions

A strength of our study is the use of advanced models of WM microstructure that yield several measures of WM health, including measures of axonal density, neurite dispersion and myelin content. These measures were integrated using a multivariate approach developed by our group that yields a single score of deviation (Tremblay, Alasmar, et al., 2024b). The interpretation of this score as a measure of the extent of WM abnormality was facilitated by the presence of a well-defined control group, composed of healthy individuals. We were also the first to investigate WM microstructural health in arterial territories using a novel 3D MR-based atlas (C.-F. Liu et al., 2023).

However, our study also suffered from some limitations. The small sample size gave us limited statistical power, which may have impaired our ability to detect associations between fitness, cognition, and WM alterations. The sample size also did not allow the investigation of more complex interactions between variables. For example, there are known sex effects in the relationships between fitness, cognition, and WM that could be explored in a larger sample (Intzandt et al., 2023). In future analyses, participants from another study (ActionCardioRisk) will be added. These participants are at an intermediate disease stage between the HCs and CAD patients as they do not have overt disease, but they have a certain number of cardiovascular risk factors and are physically inactive. Their addition would thus allow for the characterization of a broader spectrum of the health - disease continuum in addition to increasing statistical power. Here we included subjects of the control group in the regression analyses as those that display higher than average (i.e., the average of all other subjects of the control group) WM D2 would represent individuals that have an intermediate level of microstructural health. As such, by including the

whole sample we were able to model both ends of the health - disease spectrum, as well as identify individuals of the HC group that are deviating from the healthy state, indicating potential subclinical vascular brain disease.

5.6 Conclusion

In summary, this study implemented a novel multivariate approach to assess WM health in both HCs and CAD patients. Our findings revealed that CAD patients had higher D2 values, indicative of greater WM deviation from a healthy reference group, compared to HC in the whole WM, right ACA and both left and right PCA. Additionally, fitness and cognition were linked to D2 values in specific arterial territories across all participants. Together, these results suggest that heightened WM abnormalities observed in CAD patients may elevate the risk of cognitive impairment. Thus, improving fitness could play an important role in managing CAD by promoting better WM health. Future research should investigate the effects of exercise interventions on WM integrity in individuals at risk or diagnosed with CAD. Research in this field is paramount as the progression from subclinical vascular disease to vascular cognitive impairment and dementia may be avoided through proper intervention (Inoue et al., 2023; Middleton et al., 2008; Moorhouse & Rockwood, 2008; Poirier et al., 2024).

CHAPTER VI: General discussion

The overarching goal of this thesis was to understand how the brain's white matter (WM) microstructural health is altered in older adults at risk of dementia and how this impacts cognition. This is of particular importance as WM, which supports cognitive functioning and virtually all behaviors through efficient neural transmission, remains plastic throughout life (Sampaio-Baptista & Johansen-Berg, 2017) and can be remodeled by various interventions such as cognitive training and exercise (Konwar et al., 2023; McPhee et al., 2019; Mendez Colmenares et al., 2021; Poirier et al., 2024; Roig-Coll et al., 2024; Stephen et al., 2020). Interestingly, interventions that promote neuroplasticity are also known to be beneficial in slowing cognitive decline and reducing dementia risk (McPhee et al., 2019; Mendez Colmenares et al., 2021; Poirier et al., 2024; Roig-Coll et al., 2024; Stephen et al., 2020). Measuring WM microstructural properties may thus offer a promising avenue for the early detection of abnormalities, which would allow interventions to be initiated earlier, as well as to monitor progression and assess improvements in response to treatment. Despite the importance of WM in supporting normal behavioral function and the promises WM plasticity holds as a target in interventions, the evidence on WM plasticity is rather scarce. For instance, while there is evidence for WM changes with learning, we have limited knowledge regarding the time scales at which plastic changes in WM can occur, and the specific alterations that occur at different stages of learning, even in healthy adults.

Manuscript one thus aimed at characterizing the temporal dynamics of changes in WM microstructure across the learning stages of a motor sequence learning task, a common paradigm used to study neuroplasticity due to its straightforward implementation. Multiple MRI scans at 7 Tesla were used to assess longitudinal changes in WM during a 5-days learning period and following a retention period. Our findings provided evidence for highly dynamic WM plasticity in the sensorimotor network, where most changes occurred between the two first days of training. The high-resolution 7T acquisition and longitudinal study design allowed for a temporally- and spatially-specific characterization of learning-induced WM changes. However, the single-shell DWI acquisition did not allow for advanced modeling, and we were thus limited to the use of DTI, a simplistic model yielding metrics that do not allow specific physiological interpretations (Riffert

et al., 2014). Therefore, in this study, we were unable to assign the changes observed in imaging metrics to a specific biological mechanism (i.e., myelination, neurite density, or dispersion).

The ambiguity intrinsic to the DTI model can be partly addressed using more comprehensive diffusion methods. As most modern DWI acquisitions are multi-shell, it is now often possible to fit advanced models, which yield more readily interpretable metrics. However, with the rapid growth in the number of available modeling approaches, we were faced with a plethora of different methods to choose from (Novikov et al., 2018). Knowing each method comprises its own set of assumptions and biases, but also provides some insight into the underlying microstructure, the use of a single model is often limiting (Tardif et al., 2016; Uddin et al., 2019). We thus set out to develop a tool that would allow the integration of multiple MRI measures, leveraging the strengths of each method, while mitigating their weaknesses. The Mahalanobis distance (D2), a multivariate measure of deviation relative to a reference distribution, appeared as an ideal candidate as it is highly versatile, making it applicable for a wide array of research questions, and because it inherently accounts for covariance between measures. This makes it ideal for combining measures which are likely to be highly correlated, such as multiple metrics derived from the same DWI data. We created an open-source toolbox to facilitate the computation of D2 in neuroimaging: the MultiVariate Comparison (MVComp) toolbox (<https://github.com/neuralabc/mvcomp>). The second manuscript presents the toolbox, using example cases to demonstrate its usage and to validate the approach in a large sample of young healthy adults. Namely, we showed that D2 meaningfully reflects the underlying WM microstructure, in line with known neuroanatomy (Aboitiz et al., 1992; Chao et al., 2009; Hofer & Frahm, 2006). Work by our group also demonstrated the use of D2 in the study of brain-behaviour associations in normal subjects (Alasmar et al., 2024).

The subsequent manuscripts leveraged the MVComp toolbox to comprehensively assess WM alterations in two different populations of older adults at risk of dementia: individuals with a familial history of AD and patients with coronary artery disease. Manuscript 3 sought to characterize the associations between risk factors of AD, mostly cardiometabolic factors, and WM alterations, using D2 as a measure of deviation, in each sex and each genetic risk group (APOE4+ and APOE4-). Evaluating these associations through separate analyses allowed us to identify sex-specific and APOE genotype-related patterns. Contrary to our hypothesis, similar risk – WM

associations were observed in males and females, but the association pattern was stronger in males. Considering the well-documented sex differences in WM microstructure (Kanaan et al., 2012b; van Hemmen et al., 2017), and in the aging trajectory of myelin (Toschi et al., 2020), we were expecting different risk factors to impact WM in each sex. However, our male sample size may have been too small to observe such differences. In our sample, the APOE genotype had a stronger effect on the risk – WM relationships. We found a pattern unique to APOE4 carriers, where LDL-cholesterol seemed to have a detrimental effect only in carriers. Although the literature on the effects of LDL on WM health is inconsistent, the fact that APOE is a cholesterol transporter supports these differential effects depending on APOE genotype found by us and others (Ye et al., 2024). Further analysis of metric contributions to D2 indicated that myelination was likely the primary mechanism driving microstructural alterations (D2). Additionally, exploratory analyses revealed that cognition was related to D2 only in subjects with high genetic risk (APOE4+). Together, our findings support the theory that the combined effects of genetic and cardiometabolic risk factors exacerbate age-related myelin breakdown and accelerate cognitive decline (Bartzokis, 2004b, 2011; Burzynska et al., 2023). However, the absence of a control group without familial history to use as a reference complicated the interpretation of results in this study. This limitation was addressed in the fourth study.

Lastly, in the fourth manuscript, we further investigated how cardiovascular risk impacts WM microstructural health and cognition, this time in individuals with coronary artery disease (CAD). Since cardiovascular diseases such as CAD are known to increase the risk of dementia (Kovacic et al., 2012; Polidori et al., 2012), studying this population may provide another window into the early disease stage. WM microstructure deviations from a healthy state were quantified using D2, with subjects of a healthy control group as the reference. The presence of a well-defined control group in this study facilitated the interpretation of results which had been a limitation in Study 3. As expected, we found that the extent of WM alterations was greater in CAD patients than in healthy controls in the whole WM, as well as in defined arterial territories. We also found that fitness and cognition were linked to WM D2 in specific arterial territories. To our knowledge, this study is the first to investigate WM health using regions defined by an arterial territories atlas (C.-F. Liu et al., 2023). Since vascular impairment likely progresses from large arteries entering the brain that then propagates through cerebral arteries (Inoue et al., 2023; O'Rourke & Hashimoto, 2007), we believe

this approach can offer valuable insights into the pathophysiological mechanisms underlying WM changes in this population.

6.1 Contributions of this thesis

6.1.1 Studying white matter with a multivariate approach

In manuscript one, we have shown that the use of a single MRI technique (i.e., DWI) and model (i.e., DTI) makes interpretation of underlying biological mechanisms very challenging. Although still the most commonly used model, DTI yields metrics that are particularly ambiguous (Curran et al., 2016; Riffert et al., 2014). For instance, we found both increases and decreases in FA following training on a motor sequence learning task. FA is often interpreted as a measure of WM integrity. However, FA is a summary measure, and several different fibers configurations can lead to the same FA value (Curran et al., 2016). Similarly, the same change in FA, say a decrease, can either be due to a loss in neurite density or to the development of a secondary fiber population in a direction perpendicular to the main orientation. FA, and other DTI metrics, are thus highly unspecific and their interpretation will often be guided by other factors, such as behavioral data. For instance, decreased FA associated with improved performance will likely be interpreted as an increased orientation dispersion rather than neurite loss.

More advanced models can improve specificity in the characterization of microstructural properties. For example, with the NODDI model, changes in density can be disentangled from changes in orientation dispersion, two factors that impact FA (H. Zhang et al., 2012a). However, NODDI also has some limitations and relies on a specific set of assumptions, and this is the case for every model of microstructure (Novikov et al., 2018). Realizing no single model would give us a perfect, unbiased, measure of the underlying microstructure, led us to reflect on how to best integrate information from different methods, while considering the redundancy between metrics. By combining several MRI metrics, from different DWI models and different modalities, we were able to leverage the information given by each metric, capturing a more holistic view of the microstructure, while remaining agnostic to the model. Another advantage of multivariate approaches is their higher sensitivity compared to univariate approaches (Avants, Duda, et al., 2008; Naylor et al., 2014; Owen et al., 2021). Because we were interested in detecting early,

potentially subtle, changes in WM microstructure in at-risk individuals, this high sensitivity was key. We opted for the Mahalanobis distance (D2), because of its flexibility and because it inherently accounts for covariance between metrics. We made its use more widely accessible through the creation of an open-source toolbox: MVComp (Tremblay, Alasmar, et al., 2024a). Study 2 details the comprehensive ways in which the D2 framework can be applied in neuroimaging studies. Importantly, using an unsupervised machine learning clustering technique, we showed that D2 meaningfully reflects the underlying microstructure as clusters obtained were in close accordance with known topography of the corpus callosum (Aboitiz et al., 1992; Chao et al., 2009; Hofer & Frahm, 2006). To assess whether D2 performed better than single metrics, we applied the same clustering technique to individual MRI measures. The segmentations we obtained appeared noisier (i.e., individual clusters not located in contiguous regions) than those obtained from D2 (Appendix II). This suggests that the integration of information from several WM microstructure MRI measures better reflects the underlying neuroanatomy than any of those measures alone and that D2 constitutes a practical mean of combining this information.

In study 3, we used the D2 framework to obtain a comprehensive characterization of WM microstructural health, combining DWI and MPM metrics, and conducted a multivariate statistical analysis (i.e., PLS) to investigate the links between WM D2 and several risk factors of AD. Through this double multivariate approach, we were able to explore how the combined effects of multiple risk factors contribute to alterations in WM microstructure. Using the metrics contribution extraction feature of the MVComp toolbox, we were also able to show that myelination was likely the primary mechanism driving WM alterations, as MTsat and R1 were the most frequent high contributors in significant clusters. Univariate, or single model, approaches often don't allow such detailed interpretations as researchers are typically limited to a few select MRI measures to avoid multiple comparisons issues. Lastly, in study 4, another application of MVComp was demonstrated in a two-samples study, where the healthy control group was used as the reference. In this case, D2 can be interpreted in a more straight-forward manner, with high values reflecting a greater degree of abnormality.

6.1.2 Dynamic white matter changes in health and disease

The microstructure of WM changes highly dynamically in response to both enriching (e.g., learning a new task) and damaging (e.g., myocardial infarction) exposures. In Study 1, we demonstrated

how quickly microstructure can be remodeled following learning of a motor sequence task – as fast as within days – indicating cellular changes may start occurring immediately after, perhaps even during, training (Fields, 2015; Hofstetter et al., 2013; Wake et al., 2011). We also showed that the time course of WM changes differed in different WM regions, which may reflect the involvement of specific networks in distinct aspects of learning. Interestingly, we found that structural changes in WM preceded changes in resting-state functional connectivity in a region involved in the task (Jäger et al., 2021). This suggests that modulation of the supporting connections may be necessary to allow for greater communication as WM tracts form the structural basis of connectivity, linking regions within resting-state networks (Fields, 2015). Overall, our study adds to the literature on short-term WM plasticity and highlights specific spatial and temporal patterns over the course of motor learning.

Knowing that WM microstructure can be altered in such a dynamic manner, it becomes evident that the use of a single scan in cross-sectional studies, such as Study 3 and 4, provides only a limited snapshot of microstructural health along an individual's lifespan. Nevertheless, a cross-sectional design appeared appropriate as a first step in understanding the complex relationships between WM health and several risk factors of AD, as well as to disentangle the effects of sex and APOE4 genetic risk on these relationships, using a novel multivariate score (D2). Moreover, since multivariate methods are dependent on several types of data, obtaining a complete dataset can be challenging, even in cross-sectional studies. This can result in the exclusion of several participants due to missing or poor-quality data. This issue would likely be exacerbated in longitudinal studies although data imputation methods could be used to replace missing data.

The dynamic nature of WM changes in response to adverse factors could thus not be assessed in Study 3 and 4, due to the cross-sectional design employed. However, we demonstrated that WM microstructure is altered not only following major events such as myocardial infarction (Study 4), but also as a result of subclinical conditions such as hypertension, dyslipidemia, and hyperglycemia (Study 3). This underscores the vulnerability of WM microstructure to even subtle alterations in biomarkers such as blood glucose and cholesterol.

6.1.3 Comparing AD- and vascular-related impairments in white matter

Alzheimer's disease and cerebral small vessel disease are the two most common causes of dementia (Cao et al., 2020; Ritchie & Lovestone, 2002). WM alterations have been reported in both dementia types (i.e., AD and vascular dementia), as well as their prodromal stage, albeit in different WM regions (Tranfa et al., 2024). Limbic tracts disruptions have been associated with AD pathology and APOE4, while damage to commissural, associative, and projection tracts has been related to cardiovascular risk and cerebral small vessel disease (Tranfa et al., 2024). This thesis examined WM microstructural health in individuals genetically predisposed to AD because of a familial history (Study 3) and in those perhaps more at risk of vascular cognitive impairment and dementia because of coronary artery disease (Study 4). While we did not tailor our study designs and analyses methods to explicitly compare findings between the two studies, some tendencies can be noted in the spatial localization of our findings. In Study 3 (AD-related), some of the significant clusters we found included parts of the cingulum, which is considered a limbic tract, but there were also several clusters in regions that are thought to be more vascular-related. The WM microstructural impairments observed in Study 3 may thus reflect mixed pathology. This is consistent with the fact that we focused on assessing the impact of cardiometabolic risk factors in this cohort with a genetic predisposition for AD. It is increasingly acknowledged that there is a great amount of overlap in the neuropathology and predisposing factors between different dementia types (Fierini, 2020; Korczyn, 2002; Ritchie & Lovestone, 2002) and that cases of pure AD are in fact rather rare. Evidence of a vascular contribution in the pathogenesis of AD supports this view (Fierini, 2020; Iturria-Medina et al., 2016). The observation of differential effects of cardiometabolic risk factors on WM microstructure depending on APOE genotype further highlights the complex interactions between genetic and lifestyle factors and the need to use integrative approaches to better understand these interactions. Another possibility for the lack of significant results in limbic tracts could be that these tracts, because of their complex architecture (Pascalau et al., 2018), would be harder to capture with MRI resolution.

In Study 4, we used arterial territories as regions of interest for analysis which makes comparison with Study 3 difficult. However, the global effects we observed is consistent with the study by Tranfa and colleagues (2024) in which integrity in widespread WM regions, including commissural, associative, and projection tract, was associated with cardiovascular risk and cerebral

small vessel disease. Future analyses could employ a tract-based approach or smaller arterial ROIs to assess WM damage with greater spatial specificity.

6.2 Future directions

6.2.1 Studying white matter longitudinally

Throughout this thesis, the important role of WM microstructure in supporting motor and cognitive function, as well as its vulnerability to several adverse factors (e.g., high blood pressure, blood sugar, CAD), were highlighted. We also touched on the potential role of fitness as a protective factor to maintain WM health. Few studies have assessed WM alterations in early disease stages using advanced imaging techniques, and even fewer have done so comprehensively, using multi-modal imaging and multivariate frameworks to combine parameters. The work presented in this thesis thus aimed to address this gap and provide a foundation from which future studies should expand upon. For instance, using the D2 framework to characterize WM microstructure in longitudinal studies could provide a deeper understanding of healthy aging trajectories across the lifespan and of the factors that cause departures from this trajectory (Tucker-Drob, 2019). Because the work presented in Study 3 and 4 employed cross-sectional designs, causal inferences cannot be drawn from our findings. Longitudinal designs could also be used to test interventions that aim to promote neuroplasticity and rescue cognitive function. This would allow to gain further insight into the types of intervention that are most effective and the time scales at which neuroplastic changes occur in these populations, which would inform on the necessary duration. The use of a comprehensive assessment method such as the D2 framework would provide improved sensitivity, ensuring even minor improvements in microstructural health can be detected, in addition to providing specificity through extraction of metrics contributions. This could contribute to furthering our understanding of the biological mechanisms that underlie pathological changes in WM and of the repair mechanisms initiated by interventions.

6.2.2 Expanding beyond white matter

The D2 method can also be expanded beyond WM and into other imaging techniques and tissue types. For instance, brain vascular and metabolic measures (e.g., cerebral blood flow, cerebrovascular reactivity, oxygen extraction fraction) could be integrated through D2 and the links

between metabolic and structural changes could be examined using multivariate statistical analysis methods such as PLS (as in [Wearn et al., 2024](#)). Obtaining these measurements (e.g., functional, metabolic, structural) at several time points in individuals at risk of dementia could then provide insight into the spatiotemporal characteristics of different pathological alterations. For instance, in a large cohort from the Alzheimer's Disease Neuroimaging Initiative (ADNI), multifactorial data-driven analysis revealed vascular dysregulation as the earliest change in the pathological course of AD, preceding A β pathology, functional and structural changes (Iturria-Medina et al., 2016). However, WM impairment was not included in this study. Considering the vulnerability of oligodendrocytes and myelin to damage, WM measures should be included to these data-driven models to understand when WM alterations occur in relation to other factors and how these factors interact with each other (Iturria-Medina et al., 2016, 2017). This could help elucidate whether WM truly is the weakest link.

6.2.3 Assessing the entire health-disease continuum

*“There is no such thing as a single-issue struggle because we do not live single-issue lives”—
Audre Lorde*

Group analyses entail some limitations as humans tend not to fit into perfectly neat categories, or as stated by Audre Lorde: “we do not live single-issue lives” (Bertram & Pai, 2023). In case-control studies, researchers typically try to minimize heterogeneity within groups using strict criteria that effectively result in the exclusion of patients with comorbidities from patients' groups and of subjects with common health conditions (e.g., hypertension) from HC groups. This approach simplifies the problem by reducing the number of potential confounding factors. Although non-ideal, this approach is often necessary when resources don't allow for data collection in large sample sizes, which is often the case for imaging studies. Because patients (e.g., CAD patients) rarely present with a single issue and older adults without any health conditions or history of trauma (e.g., head trauma) are rare, this approach however limits the generalizability of findings.

Strict inclusion criteria can also pose challenge for recruitment as we have experienced in trying to recruit healthy older adults. We found that older adults with no health conditions were extremely difficult to find (especially in the 68 years and above range) and this resulted in our patients and control groups being unbalanced for age despite our attempt to age-match participants.

When resources permit, larger sample sizes are preferable as the higher statistical power allows for consideration of potential confounding effects (e.g., as covariates) in analyses and their interacting effects can also be explored. Further, by moving away from the case-control approach, we can begin to obtain a more representative picture of the individual, which could enable precision medicine in the future (Chamberland et al., 2021; Marquand et al., 2016). In study 4, the small sample size did not allow the exploration of interaction effects. For instance, it was not possible to investigate whether sex influenced the relationships between WM, fitness, and cognition. In the future, the data of participants from another study (ActionCardioRisk) will be added to our analyses. These participants are at an intermediate disease stage between the HCs and CAD patients as they do not have overt disease, but they have a certain number of cardiovascular risk factors and are physically inactive. Their addition would thus allow for the characterization of a broader spectrum of the health - disease continuum in addition to increasing statistical power. The effects of sex and of other variables of interest (e.g., physical activity) could then be assessed.

6.2.4 Expanding beyond biology

In the second half of this thesis, the impact of risk factors on WM microstructural health was assessed. Factors such as education level, hypertension, obesity, physical inactivity, diabetes and dyslipidemia are referred to as *modifiable* factors in the field (Livingston et al., 2024). However, it is evident that an individual's ability to address these factors largely depends on their context – the environment in which they live and work and the resources available to them (Alzheimer Society of Canada, 2024; Tremblay, 2024). The upstream factors that influence lifestyle behaviors, called structural and social determinants of health, are thought to be the main drivers of disparities in the prevalence of dementia and of its risk factors (Adkins-Jackson et al., 2023). For instance, there is a higher prevalence of dementia in ethnic and cultural minority groups, such as Black people and Indigenous people in Canada (Iroanyah et al., 2021). Risk factors for dementia such as diabetes, physical inactivity, and obesity are also more prevalent in Latin American and Black individuals (M. Lee et al., 2022). Despite this, structural and social determinants of health remain understudied in the context of aging and dementia. The potential impact of addressing these factors through systemic changes in policy is enormous. Before these policies can be put into place, researchers must however address the glaring gaps in our knowledge through the recruitment of more culturally, ethnically and socioeconomically diverse cohorts and through the integration of

structural and social determinants of health as variables of interest in their analyses. If conscious efforts are not made to reduce inequities, people of ethnic, cultural, and sexual minorities will continue to be disproportionately impacted by dementia (Alzheimer Society of Canada, 2024). In addition to be fairer, a population-based approach that aims to reduce the risk of everyone across society has the potential of having a more far-reaching impact on dementia prevalence in Canada (Tremblay, 2024; Walsh et al., 2022).

CHAPTER VII: Conclusion

In this thesis, we demonstrated that WM microstructure changes occur highly dynamically in response to both enriching (e.g., learning a new task) and damaging (e.g., cardiovascular risk factors) experiences and that these alterations underlie changes in behaviour. A wide array of adverse factors can impact WM health and there are complex interactions between non-modifiable and modifiable risk factors. Notably, in study 3, we were able to confirm the theory that the impact of modifiable risk factors on WM is exacerbated by genetic factors such as APOE4 and our findings provide a potential mechanism by which this may occur. A distinct risk pattern was observed in APOE4 carriers, where LDL-cholesterol appeared detrimental to WM microstructure, especially myelin, only in carriers. Since APOE4 is a cholesterol transporter and given that cholesterol is a main constituent of myelin, impaired cholesterol metabolism in carriers may lead to these differential effects of LDL on microstructure. We also highlighted the pertinence of using multivariate approaches in the study of early WM pathological changes as it allows for a more comprehensive characterization of the multiple factors contributing to impairments and of the biological mechanisms driving these changes.

Our last manuscript provided evidence for the role of fitness in preserving WM microstructural health in a cohort of coronary artery disease patients and healthy subjects. Improving fitness through exercise-based interventions may thus constitute a promising strategy for promoting microstructural repair and preserving cognitive function, especially in individuals with cardiovascular risk factors. WM microstructural properties may thus constitute useful biomarkers to monitor improvements in response to interventions as plastic changes in WM can occur on short timescales as shown by us (study one) and others (Hofstetter et al., 2013; Scholz et al., 2009).

Overall, this thesis made significant contributions to the field through the creation of an open-source toolbox for the computation of a multivariate distance measure from neuroimaging data. Our hope is that this tool will make such approaches more accessible, thus promoting their wider use in the neuroimaging community. This thesis also provides a foundation for the use of integrative multivariate models in the study of early pathological alterations in older adults at risk of dementia. This foundation is essential in expanding our understanding of the complex brain-behavior relationships and the multiple factors underlying disease development and progression.

Such a deeper understanding is crucial in designing therapeutic interventions that address the multifactorial causes of dementia.

Bibliography

- Abdul-Kareem, I. A., Stancak, A., Parkes, L. M., Al-Ameen, M., AlGhamdi, J., Aldhafeeri, F. M., Embleton, K., Morris, D., & Sluming, V. (2011). Plasticity of the Superior and Middle Cerebellar Peduncles in Musicians Revealed by Quantitative Analysis of Volume and Number of Streamlines Based on Diffusion Tensor Tractography. *The Cerebellum*, *10*(3), 611–623. <https://doi.org/10.1007/s12311-011-0274-1>
- Aboitiz, F., Scheibel, A. B., Fisher, R. S., & Zaidel, E. (1992). Fiber composition of the human corpus callosum. *Brain Research*, *598*(1), 143–153. [https://doi.org/10.1016/0006-8993\(92\)90178-C](https://doi.org/10.1016/0006-8993(92)90178-C)
- Ades, P. A., & Savage, P. D. (2010). The Obesity Paradox: Perception vs Knowledge. *Mayo Clinic Proceedings*, *85*(2), 112–114. <https://doi.org/10.4065/mcp.2009.0777>
- Adkins-Jackson, P. B., George, K. M., Besser, L. M., Hyun, J., Lamar, M., Hill-Jarrett, T. G., Bubu, O. M., Flatt, J. D., Heyn, P. C., Cicero, E. C., Zarina Kraal, A., Pushpalata Zanwar, P., Peterson, R., Kim, B., Turner II, R. W., Viswanathan, J., Kulick, E. R., Zuelsdorff, M., Stites, S. D., ... Babulal, G. (2023). The structural and social determinants of Alzheimer's disease related dementias. *Alzheimer's & Dementia*, *19*(7), 3171–3185. <https://doi.org/10.1002/alz.13027>
- Adluru, G., Gur, Y., Anderson, J. S., Richards, L. G., Adluru, N., & DiBella, E. V. R. (2014). Assessment of white matter microstructure in stroke patients using NODDI. *2014 36th Annual International Conference of the IEEE Engineering in Medicine and Biology Society*, 742–745. <https://doi.org/10.1109/EMBC.2014.6943697>
- Adluru, N., Destiche, D. J., Lu, S. Y.-F., Doran, S. T., Birdsill, A. C., Melah, K. E., Okonkwo, O. C., Alexander, A. L., Dowling, N. M., Johnson, S. C., Sager, M. A., & Bendlin, B. B. (2014). White matter microstructure in late middle-age: Effects of apolipoprotein E4 and parental family history of Alzheimer's disease. *NeuroImage: Clinical*, *4*, 730–742. <https://doi.org/10.1016/j.nicl.2014.04.008>
- Agosta, F., Pievani, M., Sala, S., Geroldi, C., Galluzzi, S., Frisoni, G. B., & Filippi, M. (2011). White Matter Damage in Alzheimer Disease and Its Relationship to Gray Matter Atrophy. *Radiology*, *258*(3), 853–863. <https://doi.org/10.1148/radiol.10101284>

- Alasmar, Z., Tremblay, S. A., Baumeister, T. R., Carbonell, F., Iturria-Medina, Y., Gauthier, C. J., & Steele, C. J. (2024). *White Matter Microstructural Correlates of Cognitive and Motor Functioning Revealed via Multimodal Multivariate Analysis* (p. 2024.06.05.597645). bioRxiv. <https://doi.org/10.1101/2024.06.05.597645>
- Albert, N. B., Robertson, E. M., & Miall, R. C. (2009). The Resting Human Brain and Motor Learning. *Current Biology*, *19*(12), 1023–1027. <https://doi.org/10.1016/j.cub.2009.04.028>
- Alexander, A. L., Hasan, K., Kindlmann, G., Parker, D. L., & Tsuruda, J. S. (2000). A geometric analysis of diffusion tensor measurements of the human brain. *Magnetic Resonance in Medicine*, *44*(2), 283–291. [https://doi.org/10.1002/1522-2594\(200008\)44:2<283::AID-MRM16>3.0.CO;2-V](https://doi.org/10.1002/1522-2594(200008)44:2<283::AID-MRM16>3.0.CO;2-V)
- Alexander, A. L., Tsuruda, J. S., & Parker, D. L. (1997). Elimination of eddy current artifacts in diffusion-weighted echo-planar images: The use of bipolar gradients. *Magnetic Resonance in Medicine*, *38*(6), 1016–1021. <https://doi.org/10.1002/mrm.1910380623>
- Alexander, D. C., Dyrby, T. B., Nilsson, M., & Zhang, H. (2019). Imaging brain microstructure with diffusion MRI: Practicality and applications. *NMR in Biomedicine*, *32*(4), e3841. <https://doi.org/10.1002/nbm.3841>
- Alexander-Bloch, A., Giedd, J. N., & Bullmore, E. (2013). Imaging structural co-variance between human brain regions. *Nature Reviews Neuroscience*, *14*(5), Article 5. <https://doi.org/10.1038/nrn3465>
- Alexopoulos, E. C. (2010). Introduction to Multivariate Regression Analysis. *Hippokratia*, *14*(Suppl 1), 23–28.
- Alfaro, F. J., Gavrieli, A., Saade-Lemus, P., Lioutas, V.-A., Upadhyay, J., & Novak, V. (2018). White matter microstructure and cognitive decline in metabolic syndrome: A review of diffusion tensor imaging. *Metabolism*, *78*, 52–68. <https://doi.org/10.1016/j.metabol.2017.08.009>
- Alotaibi, A., Tench, C., Stevenson, R., Felmban, G., Altokhis, A., Aldhebaib, A., Dineen, R. A., & Constantinescu, C. S. (2021). Investigating Brain Microstructural Alterations in Type 1 and Type 2 Diabetes Using Diffusion Tensor Imaging: A Systematic Review. *Brain Sciences*, *11*(2), Article 2. <https://doi.org/10.3390/brainsci11020140>

- Altmann, A., Tian, L., Henderson, V. W., Greicius, M. D., & Investigators, A. D. N. I. (2014). Sex modifies the APOE-related risk of developing Alzheimer disease. *Annals of Neurology*, *75*(4), 563–573. <https://doi.org/10.1002/ana.24135>
- Alzheimer Society of Canada. (2024). *The Many Faces of Dementia in Canada: The Landmark Study Report #2*. <https://alzheimer.ca/en/the-many-faces-of-dementia-in-canada-landmark-study-volume-2>
- Anderson, T. J., Meredith, I. T., Charbonneau, F., Yeung, A. C., Frei, B., Selwyn, A. P., & Ganz, P. (1996). Endothelium-Dependent Coronary Vasomotion Relates to the Susceptibility of LDL to Oxidation in Humans. *Circulation*, *93*(9), 1647–1650. <https://doi.org/10.1161/01.CIR.93.9.1647>
- Andersson, J. L., Skare, S., & Ashburner, J. (2003). How to correct susceptibility distortions in spin-echo echo-planar images: Application to diffusion tensor imaging. *Neuroimage*, *20*(2), 870–888.
- Andersson, J. L., & Sotiropoulos, S. N. (2016). An integrated approach to correction for off-resonance effects and subject movement in diffusion MR imaging. *Neuroimage*, *125*, 1063–1078.
- Andrieu, S., Coley, N., Lovestone, S., Aisen, P. S., & Vellas, B. (2015). Prevention of sporadic Alzheimer’s disease: Lessons learned from clinical trials and future directions. *The Lancet Neurology*, *14*(9), 926–944. [https://doi.org/10.1016/S1474-4422\(15\)00153-2](https://doi.org/10.1016/S1474-4422(15)00153-2)
- Araque Caballero, M. Á., Suárez-Calvet, M., Duering, M., Franzmeier, N., Benzinger, T., Fagan, A. M., Bateman, R. J., Jack, C. R., Levin, J., Dichgans, M., Jucker, M., Karch, C., Masters, C. L., Morris, J. C., Weiner, M., Rossor, M., Fox, N. C., Lee, J.-H., Salloway, S., ... Ewers, M. (2018). White matter diffusion alterations precede symptom onset in autosomal dominant Alzheimer’s disease. *Brain*, *141*(10), 3065–3080. <https://doi.org/10.1093/brain/awy229>
- Area-Gomez, E., & Schon, E. A. (2024). Towards a Unitary Hypothesis of Alzheimer’s Disease Pathogenesis. *Journal of Alzheimer’s Disease*, *98*(4), 1243–1275. <https://doi.org/10.3233/JAD-231318>
- Arenaza-Urquijo, E. M., Landeau, B., La Joie, R., Mevel, K., Mézenge, F., Perrotin, A., Desgranges, B., Bartrés-Faz, D., Eustache, F., & Chételat, G. (2013). Relationships between years of education and gray matter volume, metabolism and functional

- connectivity in healthy elders. *NeuroImage*, 83, 450–457.
<https://doi.org/10.1016/j.neuroimage.2013.06.053>
- Arsigny, V., Fillard, P., Pennec, X., & Ayache, N. (2006). Log-Euclidean metrics for fast and simple calculus on diffusion tensors. *Magnetic Resonance in Medicine*, 56(2), 411–421.
<https://doi.org/10.1002/mrm.20965>
- Avants, B., Duda, J. T., Kim, J., Zhang, H., Pluta, J., Gee, J. C., & Whyte, J. (2008). Multivariate Analysis of Structural and Diffusion Imaging in Traumatic Brain Injury. *Academic Radiology*, 15(11), 1360–1375. <https://doi.org/10.1016/j.acra.2008.07.007>
- Avants, Epstein, C. L., Grossman, M., & Gee, J. C. (2008). Symmetric diffeomorphic image registration with cross-correlation: Evaluating automated labeling of elderly and neurodegenerative brain. *Medical Image Analysis*, 12(1), 26–41.
<https://doi.org/10.1016/j.media.2007.06.004>
- Avants, Tustison, N., & Johnson, H. (2009). *Advanced Normalization Tools (ANTs)*. 41.
- Azzarito, M., Emmenegger, T. M., Ziegler, G., Huber, E., Grabher, P., Callaghan, M. F., Thompson, A., Friston, K., Weiskopf, N., Killeen, T., & Freund, P. (2023). Coherent, time-shifted patterns of microstructural plasticity during motor-skill learning. *NeuroImage*, 274, 120128. <https://doi.org/10.1016/j.neuroimage.2023.120128>
- Badji, A., Sabra, D., Bherer, L., Cohen-Adad, J., Girouard, H., & Gauthier, C. J. (2019). Arterial stiffness and brain integrity: A review of MRI findings. *Ageing Research Reviews*, 53, 100907. <https://doi.org/10.1016/j.arr.2019.05.001>
- Bae, H.-G., Kim, T. K., Suk, H. Y., Jung, S., & Jo, D.-G. (2020). White matter and neurological disorders. *Archives of Pharmacal Research*, 43(9), 920–931.
<https://doi.org/10.1007/s12272-020-01270-x>
- Banack, H. R., & Stokes, A. (2017). The ‘obesity paradox’ may not be a paradox at all. *International Journal of Obesity*, 41(8), 1162–1163. <https://doi.org/10.1038/ijo.2017.99>
- Banzett, R. B., Lansing, R. W., Evans, K. C., & Shea, S. A. (1996). Stimulus-response characteristics of CO₂-induced air hunger in normal subjects. *Respiration Physiology*, 103(1), 19–31.
- Barbiellini Amidei, C., Fayosse, A., Dumurgier, J., Machado-Fragua, M. D., Tabak, A. G., van Sloten, T., Kivimäki, M., Dugravot, A., Sabia, S., & Singh-Manoux, A. (2021).

- Association Between Age at Diabetes Onset and Subsequent Risk of Dementia. *JAMA*, 325(16), 1640–1649. <https://doi.org/10.1001/jama.2021.4001>
- Barekattain, M., Askarpour, H., Zahedian, F., Walterfang, M., Velakoulis, D., Maracy, M. R., & Jazi, M. H. (2014). The relationship between regional brain volumes and the extent of coronary artery disease in mild cognitive impairment. *Journal of Research in Medical Sciences : The Official Journal of Isfahan University of Medical Sciences*, 19(8), 739–745.
- Barhen, A., & Daudin, J. J. (1995). Generalization of the Mahalanobis Distance in the Mixed Case. *Journal of Multivariate Analysis*, 53(2), 332–342. <https://doi.org/10.1006/jmva.1995.1040>
- Barnes, J., Bartlett, J. W., van de Pol, L. A., Loy, C. T., Scahill, R. I., Frost, C., Thompson, P., & Fox, N. C. (2009). A meta-analysis of hippocampal atrophy rates in Alzheimer’s disease. *Neurobiology of Aging*, 30(11), 1711–1723. <https://doi.org/10.1016/j.neurobiolaging.2008.01.010>
- Bartrés-Faz, D., & Arenaza-Urquijo, E. M. (2011). Structural and Functional Imaging Correlates of Cognitive and Brain Reserve Hypotheses in Healthy and Pathological Aging. *Brain Topography*, 24(3), 340–357. <https://doi.org/10.1007/s10548-011-0195-9>
- Bartzokis, G. (2004a). Age-related myelin breakdown: A developmental model of cognitive decline and Alzheimer’s disease. *Neurobiology of Aging*, 25(1), 5–18. <https://doi.org/10.1016/j.neurobiolaging.2003.03.001>
- Bartzokis, G. (2004b). Age-related myelin breakdown: A developmental model of cognitive decline and Alzheimer’s disease. *Neurobiology of Aging*, 25(1), 5–18. <https://doi.org/10.1016/j.neurobiolaging.2003.03.001>
- Bartzokis, G. (2011). Alzheimer’s disease as homeostatic responses to age-related myelin breakdown. *Neurobiology of Aging*, 32(8), 1341–1371. <https://doi.org/10.1016/j.neurobiolaging.2009.08.007>
- Bartzokis, G., Cummings, J. L., Sultzer, D., Henderson, V. W., Nuechterlein, K. H., & Mintz, J. (2003). White Matter Structural Integrity in Healthy Aging Adults and Patients With Alzheimer Disease: A Magnetic Resonance Imaging Study. *Archives of Neurology*, 60(3), 393–398. <https://doi.org/10.1001/archneur.60.3.393>

- Bartzokis, G., Lu, P. H., Geschwind, D. H., Edwards, N., Mintz, J., & Cummings, J. L. (2006). Apolipoprotein E Genotype and Age-Related Myelin Breakdown in Healthy Individuals: Implications for Cognitive Decline and Dementia. *Archives of General Psychiatry*, *63*(1), 63–72. <https://doi.org/10.1001/archpsyc.63.1.63>
- Bartzokis, G., Lu, P. H., Geschwind, D. H., Tingus, K., Huang, D., Mendez, M. F., Edwards, N., & Mintz, J. (2007). Apolipoprotein E Affects Both Myelin Breakdown and Cognition: Implications for Age-Related Trajectories of Decline Into Dementia. *Biological Psychiatry*, *62*(12), 1380–1387. <https://doi.org/10.1016/j.biopsych.2007.03.024>
- Bartzokis, G., Sultzer, D., Lu, P. H., Nuechterlein, K. H., Mintz, J., & Cummings, J. L. (2004). Heterogeneous age-related breakdown of white matter structural integrity: Implications for cortical “disconnection” in aging and Alzheimer’s disease. *Neurobiology of Aging*, *25*(7), 843–851. <https://doi.org/10.1016/j.neurobiolaging.2003.09.005>
- Basser, P. J., Mattiello, J., & LeBihan, D. (1994a). Estimation of the effective self-diffusion tensor from the NMR spin echo. *Journal of Magnetic Resonance, Series B*, *103*(3), 247–254.
- Basser, P. J., Mattiello, J., & LeBihan, D. (1994b). MR diffusion tensor spectroscopy and imaging. *Biophysical Journal*, *66*(1), 259–267. [https://doi.org/10.1016/S0006-3495\(94\)80775-1](https://doi.org/10.1016/S0006-3495(94)80775-1)
- Bassett, D. S., Yang, M., Wymbs, N. F., & Grafton, S. T. (2015). Learning-induced autonomy of sensorimotor systems. *Nature Neuroscience*, *18*(5), Article 5. <https://doi.org/10.1038/nn.3993>
- Baumann, N., & Pham-Dinh, D. (2001). Biology of oligodendrocyte and myelin in the mammalian central nervous system. *Physiological Reviews*, *81*(2), 871–927.
- Beason-Held, L. L., Goh, J. O., An, Y., Kraut, M. A., O’Brien, R. J., Ferrucci, L., & Resnick, S. M. (2013). Changes in Brain Function Occur Years before the Onset of Cognitive Impairment. *The Journal of Neuroscience*, *33*(46), 18008–18014. <https://doi.org/10.1523/JNEUROSCI.1402-13.2013>
- Beaulieu, C. (2002). The basis of anisotropic water diffusion in the nervous system—a technical review. *NMR in Biomedicine: An International Journal Devoted to the Development and Application of Magnetic Resonance In Vivo*, *15*(7–8), 435–455.

- Bell, R. D., & Zlokovic, B. V. (2009). Neurovascular mechanisms and blood–brain barrier disorder in Alzheimer’s disease. *Acta Neuropathologica*, *118*(1), 103–113.
<https://doi.org/10.1007/s00401-009-0522-3>
- Bells, S., Cercignani, M., Deoni, S., Assaf, Y., Pasternak, O., Evans, C. J., Leemans, A., & Jones, D. K. (2011). Tractometry—comprehensive multi-modal quantitative assessment of white matter along specific tracts. *Proc. ISMRM*, *678*(1).
- Bengtsson, S. L., Nagy, Z., Skare, S., Forsman, L., Forssberg, H., & Ullén, F. (2005). Extensive piano practicing has regionally specific effects on white matter development. *Nature Neuroscience*, *8*(9), Article 9. <https://doi.org/10.1038/nn1516>
- Bertram, K., & Pai, M. (2023). Single-issue advocacy in global health: Possibilities and perils. *PLOS Global Public Health*, *3*(9), e0002368.
<https://doi.org/10.1371/journal.pgph.0002368>
- Biessels, G. J., Strachan, M. W. J., Visseren, F. L. J., Kappelle, L. J., & Whitmer, R. A. (2014). Dementia and cognitive decline in type 2 diabetes and prediabetic stages: Towards targeted interventions. *The Lancet Diabetes & Endocrinology*, *2*(3), 246–255.
[https://doi.org/10.1016/S2213-8587\(13\)70088-3](https://doi.org/10.1016/S2213-8587(13)70088-3)
- Bilello, M., Doshi, J., Nabavizadeh, S. A., Toledo, J. B., Erus, G., Xie, S. X., Trojanowski, J. Q., Han, X., & Davatzikos, C. (2015). Correlating Cognitive Decline with White Matter Lesion and Brain Atrophy Magnetic Resonance Imaging Measurements in Alzheimer’s Disease. *Journal of Alzheimer’s Disease*, *48*(4), 987–994.
<https://doi.org/10.3233/JAD-150400>
- Birdsill, A. C., Oleson, S., Kaur, S., Pasha, E., Ireton, A., Tanaka, H., & Haley, A. (2017). Abdominal obesity and white matter microstructure in midlife. *Human Brain Mapping*, *38*(7), 3337–3344. <https://doi.org/10.1002/hbm.23576>
- Bloechle, J., Huber, S., Bahnmüller, J., Rennig, J., Willmes, K., Cavdaroglu, S., Moeller, K., & Klein, E. (2016). Fact learning in complex arithmetic—The role of the angular gyrus revisited. *Human Brain Mapping*, *37*(9), 3061–3079. <https://doi.org/10.1002/hbm.23226>
- Bozzali, M., Falini, A., Franceschi, M., Cercignani, M., Zuffi, M., Scotti, G., Comi, G., & Filippi, M. (2002). White matter damage in Alzheimer’s disease assessed in vivo using diffusion tensor magnetic resonance imaging. *Journal of Neurology, Neurosurgery, and Psychiatry*, *72*(6), 742–746. <https://doi.org/10.1136/jnnp.72.6.742>

- Braak, H., & Braak, E. (1996). Development of Alzheimer-related neurofibrillary changes in the neocortex inversely recapitulates cortical myelogenesis. *Acta Neuropathologica*, *92*(2), 197–201. <https://doi.org/10.1007/s004010050508>
- Braun, C., Schweizer, R., Elbert, T., Birbaumer, N., & Taub, E. (2000). Differential Activation in Somatosensory Cortex for Different Discrimination Tasks. *Journal of Neuroscience*, *20*(1), 446–450. <https://doi.org/10.1523/JNEUROSCI.20-01-00446.2000>
- Briggs, R. G., Chakraborty, A. R., Anderson, C. D., Abraham, C. J., Palejwala, A. H., Conner, A. K., Pelargos, P. E., O'Donoghue, D. L., Glenn, C. A., & Sughrue, M. E. (2019). Anatomy and white matter connections of the inferior frontal gyrus. *Clinical Anatomy*, *32*(4), 546–556. <https://doi.org/10.1002/ca.23349>
- Briggs, R. G., Conner, A. K., Rahimi, M., Sali, G., Baker, C. M., Burks, J. D., Glenn, C. A., Battiste, J. D., & Sughrue, M. E. (2018). A Connectomic Atlas of the Human Cerebrum—Chapter 14: Tractographic Description of the Frontal Aslant Tract. *Operative Neurosurgery*, *15*(suppl_1), S444–S449. <https://doi.org/10.1093/ons/opy268>
- Bronge, L., Bogdanovic, N., & Wahlund, L.-O. (2002). Postmortem MRI and Histopathology of White Matter Changes in Alzheimer Brains: A Quantitative, Comparative Study. *Dementia and Geriatric Cognitive Disorders*, *13*(4), 205–212. <https://doi.org/10.1159/000057698>
- Brown, R. (1828). XXVII. A brief account of microscopical observations made in the months of June, July and August 1827, on the particles contained in the pollen of plants; and on the general existence of active molecules in organic and inorganic bodies. *The Philosophical Magazine*, *4*(21), 161–173.
- Burzynska, A. Z., Anderson, C., Arciniegas, D. B., Calhoun, V., Choi, I.-Y., Colmenares, A. M., Hiner, G., Kramer, A. F., Li, K., Lee, J., Lee, P., Oh, S.-H., Umland, S., & Thomas, M. L. (2023). Metabolic syndrome and adiposity: Risk factors for decreased myelin in cognitively healthy adults. *Cerebral Circulation - Cognition and Behavior*, *5*, 100180. <https://doi.org/10.1016/j.cccb.2023.100180>
- Caeyenberghs, K., Metzler-Baddeley, C., Foley, S., & Jones, D. K. (2016). Dynamics of the Human Structural Connectome Underlying Working Memory Training. *Journal of Neuroscience*, *36*(14), 4056–4066. <https://doi.org/10.1523/JNEUROSCI.1973-15.2016>

- Calamante, F., Smith, R. E., Tournier, J.-D., Raffelt, D., & Connelly, A. (2015). Quantification of voxel-wise total fibre density: Investigating the problems associated with track-count mapping. *NeuroImage*, *117*, 284–293. <https://doi.org/10.1016/j.neuroimage.2015.05.070>
- Calhoun, V. d., Adali, T., Pearlson, G. d., & Pekar, J. j. (2001). A method for making group inferences from functional MRI data using independent component analysis. *Human Brain Mapping*, *14*(3), 140–151. <https://doi.org/10.1002/hbm.1048>
- Callaghan, M. F., Freund, P., Draganski, B., Anderson, E., Cappelletti, M., Chowdhury, R., Diedrichsen, J., FitzGerald, T. H. B., Smittenaar, P., Helms, G., Lutti, A., & Weiskopf, N. (2014). Widespread age-related differences in the human brain microstructure revealed by quantitative magnetic resonance imaging. *Neurobiology of Aging*, *35*(8), 1862–1872. <https://doi.org/10.1016/j.neurobiolaging.2014.02.008>
- Campbell, J. S., Leppert, I. R., Narayanan, S., Boudreau, M., Duval, T., Cohen-Adad, J., Pike, G. B., & Stikov, N. (2018). Promise and pitfalls of g-ratio estimation with MRI. *Neuroimage*, *182*, 80–96.
- Camus, M., Ragert, P., Vandermeeren, Y., & Cohen, L. G. (2009). Mechanisms controlling motor output to a transfer hand after learning a sequential pinch force skill with the opposite hand. *Clinical Neurophysiology*, *120*(10), 1859–1865. <https://doi.org/10.1016/j.clinph.2009.08.013>
- Cao, Q., Tan, C.-C., Xu, W., Hu, H., Cao, X.-P., Dong, Q., Tan, L., & Yu, J.-T. (2020). The Prevalence of Dementia: A Systematic Review and Meta-Analysis. *Journal of Alzheimer's Disease*, *73*(3), 1157–1166. <https://doi.org/10.3233/JAD-191092>
- Carbonell, F., Zijdenbos, A. P., & Bedell, B. J. (2020). Spatially Distributed Amyloid- β Reduces Glucose Metabolism in Mild Cognitive Impairment. *Journal of Alzheimer's Disease*, *73*(2), 543–557. <https://doi.org/10.3233/JAD-190560>
- Carter, F., Anwander, A., Goucha, T., Adamson, H., Friederici, A. D., Lutti, A., Gauthier, C. J., Weiskopf, N., Bazin, P.-L., & Steele, C. J. (2022). *Assessing Quantitative MRI Techniques using Multimodal Comparisons* (p. 2022.02.10.479780). bioRxiv. <https://doi.org/10.1101/2022.02.10.479780>
- Catani, M., Dell'Acqua, F., Vergani, F., Malik, F., Hodge, H., Roy, P., Valabregue, R., & Thiebaut de Schotten, M. (2012). Short frontal lobe connections of the human brain. *Cortex*, *48*(2), 273–291. <https://doi.org/10.1016/j.cortex.2011.12.001>

- Catani, M., Robertsson, N., Beyh, A., Huynh, V., de Santiago Requejo, F., Howells, H., Barrett, R. L., Aiello, M., Cavaliere, C., & Dyrby, T. B. (2017). Short parietal lobe connections of the human and monkey brain. *Cortex*, *97*, 339–357.
- Chaim, T. M., Duran, F. L. S., Uchida, R. R., Périco, C. A. M., de Castro, C. C., & Busatto, G. F. (2007). Volumetric reduction of the corpus callosum in Alzheimer's disease in vivo as assessed with voxel-based morphometry. *Psychiatry Research*, *154*(1), 59–68.
<https://doi.org/10.1016/j.psychresns.2006.04.003>
- Chamberland, M., Genc, S., Tax, C. M. W., Shastin, D., Koller, K., Raven, E. P., Cunningham, A., Doherty, J., van den Bree, M. B. M., Parker, G. D., Hamandi, K., Gray, W. P., & Jones, D. K. (2021). Detecting microstructural deviations in individuals with deep diffusion MRI tractometry. *Nature Computational Science*, *1*(9), Article 9.
<https://doi.org/10.1038/s43588-021-00126-8>
- Chamberland, M., Raven, E. P., Genc, S., Duffy, K., Descoteaux, M., Parker, G. D., Tax, C. M. W., & Jones, D. K. (2019). Dimensionality reduction of diffusion MRI measures for improved tractometry of the human brain. *NeuroImage*, *200*, 89–100.
<https://doi.org/10.1016/j.neuroimage.2019.06.020>
- Chanes, L., Chica, A. B., Quentin, R., & Valero-Cabré, A. (2012). Manipulation of Pre-Target Activity on the Right Frontal Eye Field Enhances Conscious Visual Perception in Humans. *PLOS ONE*, *7*(5), e36232. <https://doi.org/10.1371/journal.pone.0036232>
- Chao, Y., Cho, K., Yeh, C., Chou, K., Chen, J., & Lin, C. (2009). Probabilistic topography of human corpus callosum using cytoarchitectural parcellation and high angular resolution diffusion imaging tractography. *Human Brain Mapping*, *30*(10), 3172–3187.
<https://doi.org/10.1002/hbm.20739>
- Chen, C., Cao, X., & Tian, L. (2019). Partial least squares regression performs well in MRI-based individualized estimations. *Frontiers in Neuroscience*, *13*, 1282.
- Chen, H.-J., Gao, Y.-Q., Che, C.-H., Lin, H., & Ruan, X.-L. (2018). Diffusion Tensor Imaging With Tract-Based Spatial Statistics Reveals White Matter Abnormalities in Patients With Vascular Cognitive Impairment. *Frontiers in Neuroanatomy*, *12*.
<https://doi.org/10.3389/fnana.2018.00053>

- Chen, Z.-C., Gan, J., Yang, Y., Meng, Q., Han, J., & Ji, Y. (2022). The vascular risk factors and vascular neuropathology in subjects with autopsy-confirmed dementia with Lewy bodies. *International Journal of Geriatric Psychiatry*, 37(3). <https://doi.org/10.1002/gps.5683>
- Cheng, G. W.-Y., Mok, K. K.-S., Yeung, S. H.-S., Kofler, J., Herrup, K., & Tse, K.-H. (2022). Apolipoprotein E ϵ 4 Mediates Myelin Breakdown by Targeting Oligodendrocytes in Sporadic Alzheimer Disease. *Journal of Neuropathology & Experimental Neurology*, 81(9), 717–730. <https://doi.org/10.1093/jnen/nlac054>
- Chéreau, R., Saraceno, G. E., Angibaud, J., Cattaert, D., & Nägerl, U. V. (2017). Superresolution imaging reveals activity-dependent plasticity of axon morphology linked to changes in action potential conduction velocity. *Proceedings of the National Academy of Sciences*, 114(6), 1401–1406. <https://doi.org/10.1073/pnas.1607541114>
- Chojdak-Łukasiewicz, J., Dziadkowiak, E., Zimny, A., & Paradowski, B. (2021). Cerebral small vessel disease: A review. *Advances in Clinical and Experimental Medicine: Official Organ Wroclaw Medical University*, 30(3), 349–356. <https://doi.org/10.17219/acem/131216>
- Chorghay, Z., Káradóttir, R. T., & Ruthazer, E. S. (2018). White matter plasticity keeps the brain in tune: Axons conduct while glia wrap. *Frontiers in Cellular Neuroscience*, 12, 428.
- Chuang, Y.-F., An, Y., Bilgel, M., Wong, D. F., Troncoso, J. C., O'Brien, R. J., Breitner, J. C., Ferrucci, L., Resnick, S. M., & Thambisetty, M. (2016). Midlife adiposity predicts earlier onset of Alzheimer's dementia, neuropathology and presymptomatic cerebral amyloid accumulation. *Molecular Psychiatry*, 21(7), 910–915. <https://doi.org/10.1038/mp.2015.129>
- Chung, S., Kim, D., Breton, E., & Axel, L. (2010). Rapid B1+ mapping using a preconditioning RF pulse with TurboFLASH readout. *Magnetic Resonance in Medicine*, 64(2), 439–446. <https://doi.org/10.1002/mrm.22423>
- Clark, K. L., Noudoost, B., & Moore, T. (2012). Persistent Spatial Information in the Frontal Eye Field during Object-Based Short-Term Memory. *Journal of Neuroscience*, 32(32), 10907–10914. <https://doi.org/10.1523/JNEUROSCI.1450-12.2012>
- Cleeman, J. (2001). *ATP III Guidelines At-A-Glance Quick Desk Reference*.
- Cohen, J. I., Cazettes, F., & Convit, A. (2011). Abnormal Cholesterol is Associated with Prefrontal White Matter Abnormalities among Obese Adults: A Diffusion Tensor Imaging

- Study. *The Neuroradiology Journal*, 24(6), 854–861.
<https://doi.org/10.1177/197140091102400604>
- Cona, G., & Semenza, C. (2017). Supplementary motor area as key structure for domain-general sequence processing: A unified account. *Neuroscience & Biobehavioral Reviews*, 72, 28–42. <https://doi.org/10.1016/j.neubiorev.2016.10.033>
- Concha, L. (2014). A macroscopic view of microstructure: Using diffusion-weighted images to infer damage, repair, and plasticity of white matter. *Neuroscience*, 276, 14–28.
<https://doi.org/10.1016/j.neuroscience.2013.09.004>
- Connor, J. R., & Menzies, S. L. (1996). Relationship of iron to oligodendrocytes and myelination. *Glia*, 17(2), 83–93. [https://doi.org/10.1002/\(SICI\)1098-1136\(199606\)17:2<83::AID-GLIA1>3.0.CO;2-7](https://doi.org/10.1002/(SICI)1098-1136(199606)17:2<83::AID-GLIA1>3.0.CO;2-7)
- Corbetta, M., & Shulman, G. L. (2002). Control of goal-directed and stimulus-driven attention in the brain. *Nature Reviews Neuroscience*, 3(3), Article 3. <https://doi.org/10.1038/nrn755>
- Costa, R. M., Cohen, D., & Nicolelis, M. A. L. (2004). Differential Corticostriatal Plasticity during Fast and Slow Motor Skill Learning in Mice. *Current Biology*, 14(13), 1124–1134.
<https://doi.org/10.1016/j.cub.2004.06.053>
- Curran, K. M., Emsell, L., & Leemans, A. (2016). Quantitative DTI Measures. In W. Van Hecke, L. Emsell, & S. Sunaert (Eds.), *Diffusion Tensor Imaging: A Practical Handbook* (pp. 65–87). Springer. https://doi.org/10.1007/978-1-4939-3118-7_5
- Dadar, M., & Collins, D. L. (2021). BISON: Brain tissue segmentation pipeline using T1 - weighted magnetic resonance images and a random forest classifier. *Magnetic Resonance in Medicine*, 85(4), 1881–1894. <https://doi.org/10.1002/mrm.28547>
- Daducci, A., Canales-Rodríguez, E. J., Zhang, H., Dyrby, T. B., Alexander, D. C., & Thiran, J.-P. (2015). Accelerated Microstructure Imaging via Convex Optimization (AMICO) from diffusion MRI data. *NeuroImage*, 105, 32–44.
<https://doi.org/10.1016/j.neuroimage.2014.10.026>
- Daducci, A., Canales-Rodríguez, E. J., Descoteaux, M., Garyfallidis, E., Gur, Y., Lin, Y., Mani, M., Merlet, S., Paquette, M., Ramirez-Manzanares, A., Reisert, M., Rodrigues, P. R., Seppehrband, F., Caruyer, E., Choupan, J., Deriche, R., Jacob, M., Menegaz, G., Překovska, V., ... Thiran, J. (2014). Quantitative Comparison of Reconstruction Methods for Intra-Voxel Fiber Recovery From Diffusion MRI. *IEEE Transactions on Medical*

- Imaging*, 33(2), 384–399. IEEE Transactions on Medical Imaging.
<https://doi.org/10.1109/TMI.2013.2285500>
- Daoust, J., Schaffer, J., Zeighami, Y., Dagher, A., García-García, I., & Michaud, A. (2021). White matter integrity differences in obesity: A meta-analysis of diffusion tensor imaging studies. *Neuroscience & Biobehavioral Reviews*, 129, 133–141.
<https://doi.org/10.1016/j.neubiorev.2021.07.020>
- Day, J. J., & Sweatt, J. D. (2011). Epigenetic Mechanisms in Cognition. *Neuron*, 70(5), 813–829.
<https://doi.org/10.1016/j.neuron.2011.05.019>
- Dayan, E., & Cohen, L. G. (2011). Neuroplasticity subserving motor skill learning. *Neuron*, 72(3), 443–454. <https://doi.org/10.1016/j.neuron.2011.10.008>
- De Boer, R. W. (1995). Magnetization transfer contrast Part 1: MR physics. *Medicamundi*, 40, 64–73.
- de la Monte, S. M. (1989). Quantitation of cerebral atrophy in preclinical and end-stage alzheimer's disease. *Annals of Neurology*, 25(5), 450–459.
<https://doi.org/10.1002/ana.410250506>
- de Leon, A. R., & Carrière, K. C. (2005). A generalized Mahalanobis distance for mixed data. *Journal of Multivariate Analysis*, 92(1), 174–185.
<https://doi.org/10.1016/j.jmva.2003.08.006>
- Dean, D. C., Lange, N., Travers, B. G., Prigge, M. B., Matsunami, N., Kellett, K. A., Freeman, A., Kane, K. L., Adluru, N., Tromp, D. P. M., Destiche, D. J., Samsin, D., Zielinski, B. A., Fletcher, P. T., Anderson, J. S., Froehlich, A. L., Leppert, M. F., Bigler, E. D., Lainhart, J. E., & Alexander, A. L. (2017). Multivariate characterization of white matter heterogeneity in autism spectrum disorder. *NeuroImage: Clinical*, 14, 54–66.
<https://doi.org/10.1016/j.nicl.2017.01.002>
- Deckers, K., Schievink, S. H. J., Rodriguez, M. M. F., Oostenbrugge, R. J. van, Boxtel, M. P. J. van, Verhey, F. R. J., & Köhler, S. (2017). Coronary heart disease and risk for cognitive impairment or dementia: Systematic review and meta-analysis. *PLOS ONE*, 12(9), e0184244. <https://doi.org/10.1371/journal.pone.0184244>
- Delis, D. C., Kaplan, E., & Kramer, J. H. (2001). *Delis-Kaplan executive function system*.
- Dell'Acqua, F., & Tournier, J.-D. (2019). Modelling white matter with spherical deconvolution: How and why? *NMR in Biomedicine*, 32(4), e3945. <https://doi.org/10.1002/nbm.3945>

- Deng, F., Zhao, L., Liu, C., Lu, M., Zhang, S., Huang, H., Chen, L., Wu, X., Niu, C., He, Y., Wang, J., & Huang, R. (2018). Plasticity in deep and superficial white matter: A DTI study in world class gymnasts. *Brain Structure and Function*, *223*(4), 1849–1862. <https://doi.org/10.1007/s00429-017-1594-9>
- Deoni, S. C. L., Rutt, B. K., Arun, T., Pierpaoli, C., & Jones, D. K. (2008). Gleaning multicomponent T1 and T2 information from steady-state imaging data. *Magnetic Resonance in Medicine*, *60*(6), 1372–1387. <https://doi.org/10.1002/mrm.21704>
- Descoteaux, M. (2015). High Angular Resolution Diffusion Imaging (HARDI). In *Wiley Encyclopedia of Electrical and Electronics Engineering* (pp. 1–25). American Cancer Society. <https://doi.org/10.1002/047134608X.W8258>
- Desjardins-Crépeau, L., Berryman, N., Vu, T. T. M., Villalpando, J. M., Kergoat, M.-J., Li, K. Z., Bosquet, L., & Bherer, L. (2014). Physical Functioning Is Associated With Processing Speed and Executive Functions in Community-Dwelling Older Adults. *The Journals of Gerontology: Series B*, *69*(6), 837–844. <https://doi.org/10.1093/geronb/gbu036>
- Dhamala, E., Bassett, D. S., Yeo, B. T., & Holmes, A. J. (2024). Functional brain networks are associated with both sex and gender in children. *Science Advances*, *10*(28), eadn4202. <https://doi.org/10.1126/sciadv.adn4202>
- Dhollander, T., Clemente, A., Singh, M., Boonstra, F., Civier, O., Duque, J. D., Egorova, N., Enticott, P., Fuelscher, I., Gajamange, S., Genc, S., Gottlieb, E., Hyde, C., Imms, P., Kelly, C., Kirkovski, M., Kolbe, S., Liang, X., Malhotra, A., ... Caeyenberghs, K. (2021). Fixel-based Analysis of Diffusion MRI: Methods, Applications, Challenges and Opportunities. *NeuroImage*, *241*, 118417. <https://doi.org/10.1016/j.neuroimage.2021.118417>
- Dhollander, T., Tabbara, R., Rosnarho-Tornstrand, J., Tournier, J.-D., Raffelt, D., & Connelly, A. (2021). Multi-tissue log-domain intensity and inhomogeneity normalisation for quantitative apparent fibre density. *In Proc. ISMRM*.
- Di Paolo, G., & Kim, T.-W. (2011). Linking lipids to Alzheimer’s disease: Cholesterol and beyond. *Nature Reviews Neuroscience*, *12*(5), 284–296. <https://doi.org/10.1038/nrn3012>
- Dias, I. H. K., Polidori, M. C., & Griffiths, H. R. (2014). Hypercholesterolaemia-induced oxidative stress at the blood–brain barrier. *Biochemical Society Transactions*, *42*(4), 1001–1005. <https://doi.org/10.1042/BST20140164>

- Dick, A. S., Garic, D., Graziano, P., & Tremblay, P. (2019). The frontal aslant tract (FAT) and its role in speech, language and executive function. *Cortex*, *111*, 148–163.
<https://doi.org/10.1016/j.cortex.2018.10.015>
- Ding, Z., Gore, J. C., & Anderson, A. W. (2005). Reduction of noise in diffusion tensor images using anisotropic smoothing. *Magnetic Resonance in Medicine*, *53*(2), 485–490.
<https://doi.org/10.1002/mrm.20339>
- Donini, L. M., Pinto, A., Giusti, A. M., Lenzi, A., & Poggiogalle, E. (2020). Obesity or BMI Paradox? Beneath the Tip of the Iceberg. *Frontiers in Nutrition*, *7*.
<https://doi.org/10.3389/fnut.2020.00053>
- Donner, T., Kettermann, A., Diesch, E., Ostendorf, F., Villringer, A., & Brandt, S. A. (2000). Involvement of the human frontal eye field and multiple parietal areas in covert visual selection during conjunction search. *European Journal of Neuroscience*, *12*(9), 3407–3414. <https://doi.org/10.1046/j.1460-9568.2000.00223.x>
- Doyon, J., Bellec, P., Amsel, R., Penhune, V., Monchi, O., Carrier, J., Lehericy, S., & Benali, H. (2009). Contributions of the basal ganglia and functionally related brain structures to motor learning. *Behavioural Brain Research*, *199*(1), 61–75.
<https://doi.org/10.1016/j.bbr.2008.11.012>
- Doyon, J., & Benali, H. (2005). Reorganization and plasticity in the adult brain during learning of motor skills. *Current Opinion in Neurobiology*, *15*(2), 161–167.
- Doyon, J., Ungerleider, L. G., Squire, L., & Schacter, D. (2002). Functional anatomy of motor skill learning. *Neuropsychology of Memory*, *3*, 225–238.
- Draczynska-Lusiak, B., Doung, A., & Sun, A. Y. (1998). Oxidized lipoproteins may play a role in neuronal cell death in Alzheimer disease. *Molecular and Chemical Neuropathology*, *33*(2), 139–148. <https://doi.org/10.1007/BF02870187>
- Drevets, W. C., Burton, H., Videen, T. O., Snyder, A. Z., Simpson, J. R., & Raichle, M. E. (1995). Blood flow changes in human somatosensory cortex during anticipated stimulation. *Nature*, *373*(6511), Article 6511. <https://doi.org/10.1038/373249a0>
- Duchesne, S., Rousseau, L.-S., Belzile-Marsolais, F., Welch, L.-A., Cournoyer, B., Arseneau, M., Lapierre, V., Poulin, S.-M., Potvin, O., & Hudon, C. (2024). A Scoping Review of Alzheimers Disease Hypotheses: An Array of Uni- and Multi-Factorial Theories. *Journal of Alzheimer's Disease*, *99*(3), 843–856. <https://doi.org/10.3233/JAD-230772>

- Duff, K., Hobson, V. L., Beglinger, L. J., & O'Bryant, S. E. (2010). Diagnostic Accuracy of the RBANS in Mild Cognitive Impairment: Limitations on Assessing Milder Impairments. *Archives of Clinical Neuropsychology*, *25*(5), 429–441.
<https://doi.org/10.1093/arclin/acq045>
- Dufouil, C., Alperovitch, A., & Tzourio, C. (2003). Influence of education on the relationship between white matter lesions and cognition. *Neurology*, *60*(5), 831–836.
<https://doi.org/10.1212/01.WNL.0000049456.33231.96>
- Dumoulin, S. O., Fracasso, A., van der Zwaag, W., Siero, J. C. W., & Petridou, N. (2018). Ultra-high field MRI: Advancing systems neuroscience towards mesoscopic human brain function. *NeuroImage*, *168*, 345–357. <https://doi.org/10.1016/j.neuroimage.2017.01.028>
- Einstein, A. (1905). Über die von der molekularkinetischen Theorie der Wärme geforderte Bewegung von in ruhenden Flüssigkeiten suspendierten Teilchen. *Annalen Der Physik*, *322*(8), 549–560. <https://doi.org/10.1002/andp.19053220806>
- Elias, P. K., Elias, M. F., D'Agostino, R. B., Sullivan, L. M., & Wolf, P. A. (2005). Serum Cholesterol and Cognitive Performance in the Framingham Heart Study. *Psychosomatic Medicine*, *67*(1), 24. <https://doi.org/10.1097/01.psy.0000151745.67285.c2>
- España-Irla, G., Gomes-Osman, J., Cattaneo, G., Albu, S., Cabello-Toscano, M., Solana-Sánchez, J., Redondo-Camós, M., Delgado-Gallén, S., Alviarez-Schulze, V., Pachón-García, C., Tormos, J. M., Bartrés-Faz, D., Morris, T. P., & Pascual-Leone, Á. (2021). Associations Between Cardiorespiratory Fitness, Cardiovascular Risk, and Cognition Are Mediated by Structural Brain Health in Midlife. *Journal of the American Heart Association: Cardiovascular and Cerebrovascular Disease*, *10*(18), e020688.
<https://doi.org/10.1161/JAHA.120.020688>
- Farrer, L. A., Cupples, L. A., Haines, J. L., Hyman, B., Kukull, W. A., Mayeux, R., Myers, R. H., Pericak-Vance, M. A., Risch, N., & van Duijn, C. M. (1997). Effects of Age, Sex, and Ethnicity on the Association Between Apolipoprotein E Genotype and Alzheimer Disease: A Meta-analysis. *JAMA*, *278*(16), 1349–1356.
<https://doi.org/10.1001/jama.1997.03550160069041>
- Fields, R. D. (2008a). White matter in learning, cognition and psychiatric disorders. *Trends in Neurosciences*, *31*(7), 361–370. <https://doi.org/10.1016/j.tins.2008.04.001>

- Fields, R. D. (2008b). *White Matter Matters*. Scientific American.
<https://doi.org/10.1038/scientificamerican0308-54>
- Fields, R. D. (2015). A new mechanism of nervous system plasticity: Activity-dependent myelination. *Nature Reviews Neuroscience*, *16*(12), Article 12.
<https://doi.org/10.1038/nrn4023>
- Fierini, F. (2020). Mixed dementia: Neglected clinical entity or nosographic artifice? *Journal of the Neurological Sciences*, *410*, 116662. <https://doi.org/10.1016/j.jns.2019.116662>
- Filippi, M., Campi, A., Dousset, V., Baratti, C., Martinelli, V., Canal, N., Scotti, G., & Comi, G. (1995). A magnetization transfer imaging study of normal-appearing white matter in multiple sclerosis. *Neurology*, *45*(3), 478–482.
- Filley, C. M., & Fields, R. D. (2016). White matter and cognition: Making the connection. *Journal of Neurophysiology*, *116*(5), 2093–2104. <https://doi.org/10.1152/jn.00221.2016>
- Finc, K., Bonna, K., He, X., Lydon-Staley, D. M., Kühn, S., Duch, W., & Bassett, D. S. (2020). Dynamic reconfiguration of functional brain networks during working memory training. *Nature Communications*, *11*(1), Article 1. <https://doi.org/10.1038/s41467-020-15631-z>
- Fissler, P., Müller, H.-P., Küster, O. C., Laptinskaya, D., Thurm, F., Woll, A., Elbert, T., Kassubek, J., von Arnim, C. A. F., & Kolassa, I.-T. (2017). No Evidence That Short-Term Cognitive or Physical Training Programs or Lifestyles Are Related to Changes in White Matter Integrity in Older Adults at Risk of Dementia. *Frontiers in Human Neuroscience*, *11*. <https://doi.org/10.3389/fnhum.2017.00110>
- Foley, J. M., Salat, D. H., Stricker, N. H., Zink, T. A., Grande, L. J., McGlinchey, R. E., Milberg, W. P., & Leritz, E. C. (2014). Interactive Effects of Apolipoprotein E4 and Diabetes Risk on Later Myelinating White Matter Regions in Neurologically Healthy Older Aged Adults. *American Journal of Alzheimer's Disease & Other Dementias*®, *29*(3), 222–235. <https://doi.org/10.1177/1533317513517045>
- Foong, J., Symms, M. R., Barker, G. J., Maier, M., Woermann, F. G., Miller, D. H., & Ron, M. A. (2001). Neuropathological abnormalities in schizophrenia: Evidence from magnetization transfer imaging. *Brain*, *124*(5), 882–892.
- Forbes, T. A., & Gallo, V. (2017). All Wrapped Up: Environmental Effects on Myelination. *Trends in Neurosciences*, *40*(9), 572–587. <https://doi.org/10.1016/j.tins.2017.06.009>

- Frangou, S., Doucet, G., & Lee, W.-H. (2020). Myelination Abnormalities in Schizophrenia Using Ultra-High Field MR Brain Imaging. *Biological Psychiatry*, *87*(9), S100–S101. <https://doi.org/10.1016/j.biopsych.2020.02.276>
- García-García, I., Michaud, A., Jurado, M. Á., Dagher, A., & Morys, F. (2022). Mechanisms linking obesity and its metabolic comorbidities with cerebral grey and white matter changes. *Reviews in Endocrine and Metabolic Disorders*, *23*(4), 833–843. <https://doi.org/10.1007/s11154-021-09706-5>
- Garfield, V., Farmaki, A.-E., Eastwood, S. V., Mathur, R., Rentsch, C. T., Bhaskaran, K., Smeeth, L., & Chaturvedi, N. (2021). HbA1c and brain health across the entire glycaemic spectrum. *Diabetes, Obesity and Metabolism*, *23*(5), 1140–1149. <https://doi.org/10.1111/dom.14321>
- Gaymard, B., Ploner, C. J., Rivaud-Péchoix, S., & Pierrot-Deseilligny, C. (1999). The frontal eye field is involved in spatial short-term memory but not in reflexive saccade inhibition. *Experimental Brain Research*, *129*(2), 288–301. <https://doi.org/10.1007/s002210050899>
- Genin, E., Hannequin, D., Wallon, D., Slegers, K., Hiltunen, M., Combarros, O., Bullido, M. J., Engelborghs, S., De Deyn, P., Berr, C., Pasquier, F., Dubois, B., Tognoni, G., Fiévet, N., Brouwers, N., Bettens, K., Arosio, B., Coto, E., Del Zompo, M., ... Campion, D. (2011). APOE and Alzheimer disease: A major gene with semi-dominant inheritance | Molecular Psychiatry. *Molecular Psychiatry*, *16*(9), 903–907. <https://doi.org/10.1038/mp.2011.52>
- Geraets, A. F. J., & Leist, A. K. (2023). Sex/gender and socioeconomic differences in modifiable risk factors for dementia. *Scientific Reports*, *13*(1), 80. <https://doi.org/10.1038/s41598-022-27368-4>
- Ghorbani, H. (2019). MAHALANOBIS DISTANCE AND ITS APPLICATION FOR DETECTING MULTIVARIATE OUTLIERS. *Facta Universitatis, Series: Mathematics and Informatics*, *0*, Article 0. <https://doi.org/10.22190/FUMI1903583G>
- Giacosa, C., Karpati, F. J., Foster, N. E. V., Hyde, K. L., & Penhune, V. B. (2019). The descending motor tracts are different in dancers and musicians. *Brain Structure & Function*, *224*(9), 3229–3246. <https://doi.org/10.1007/s00429-019-01963-0>
- Giacosa, C., Karpati, F. J., Foster, N. E. V., Penhune, V. B., & Hyde, K. L. (2016). Dance and music training have different effects on white matter diffusivity in sensorimotor pathways. *NeuroImage*, *135*, 273–286. <https://doi.org/10.1016/j.neuroimage.2016.04.048>

- Glasser, M. F., & Essen, D. C. V. (2011). Mapping Human Cortical Areas In Vivo Based on Myelin Content as Revealed by T1- and T2-Weighted MRI. *Journal of Neuroscience*, *31*(32), 11597–11616. <https://doi.org/10.1523/JNEUROSCI.2180-11.2011>
- Glasser, M. F., Sotiropoulos, S. N., Wilson, J. A., Coalson, T. S., Fischl, B., Andersson, J. L., Xu, J., Jbabdi, S., Webster, M., Polimeni, J. R., Van Essen, D. C., & Jenkinson, M. (2013). The minimal preprocessing pipelines for the Human Connectome Project. *NeuroImage*, *80*, 105–124. <https://doi.org/10.1016/j.neuroimage.2013.04.127>
- Gons, R. A. R., van Oudheusden, L. J. B., de Laat, K. F., van Norden, A. G. W., van Uden, I. W. M., Norris, D. G., Zwiers, M. P., van Dijk, E., & de Leeuw, F.-E. (2012). Hypertension is Related to the Microstructure of the Corpus Callosum: The RUN DMC Study. *Journal of Alzheimer's Disease*, *32*(3), 623–631. <https://doi.org/10.3233/JAD-2012-121006>
- González Ballester, M. Á., Zisserman, A. P., & Brady, M. (2002). Estimation of the partial volume effect in MRI. *Medical Image Analysis*, *6*(4), 389–405. [https://doi.org/10.1016/S1361-8415\(02\)00061-0](https://doi.org/10.1016/S1361-8415(02)00061-0)
- Grosbras, M.-H., & Paus, T. (2002). Transcranial Magnetic Stimulation of the Human Frontal Eye Field: Effects on Visual Perception and Attention. *Journal of Cognitive Neuroscience*, *14*(7), 1109–1120. <https://doi.org/10.1162/089892902320474553>
- Gryga, M., Taubert, M., Dukart, J., Vollmann, H., Conde, V., Sehm, B., Villringer, A., & Ragert, P. (2012). Bidirectional gray matter changes after complex motor skill learning. *Frontiers in Systems Neuroscience*, *6*, 37.
- Guberman, G. I., Stojanovski, S., Nishat, E., Ptito, A., Bzdok, D., Wheeler, A. L., & Descoteaux, M. (2022). Multi-tract multi-symptom relationships in pediatric concussion. *eLife*, *11*, e70450. <https://doi.org/10.7554/eLife.70450>
- Guerrero-Gonzalez, J. M., Yeske, B., Kirk, G. R., Bell, M. J., Ferrazzano, P. A., & Alexander, A. L. (2022). Mahalanobis distance tractometry (MaD-Tract) – a framework for personalized white matter anomaly detection applied to TBI. *NeuroImage*, *260*, 119475. <https://doi.org/10.1016/j.neuroimage.2022.119475>
- Guye, M., Bettus, G., Bartolomei, F., & Cozzone, P. J. (2010). Graph theoretical analysis of structural and functional connectivity MRI in normal and pathological brain networks. *Magnetic Resonance Materials in Physics, Biology and Medicine*, *23*(5–6), 409–421. <https://doi.org/10.1007/s10334-010-0205-z>

- Gyebnár, G., Klimaj, Z., Entz, L., Fabó, D., Rudas, G., Barsi, P., & Kozák, L. R. (2019). Personalized microstructural evaluation using a Mahalanobis-distance based outlier detection strategy on epilepsy patients' DTI data – Theory, simulations and example cases. *PLOS ONE*, *14*(9), e0222720. <https://doi.org/10.1371/journal.pone.0222720>
- Haight, T., Nick Bryan, R., Erus, G., Hsieh, M.-K., Davatzikos, C., Nasrallah, I., D'Esposito, M., Jacobs, D. R., Lewis, C., Schreiner, P., Sidney, S., Meirelles, O., & Launer, L. J. (2018). White matter microstructure, white matter lesions, and hypertension: An examination of early surrogate markers of vascular-related brain change in midlife. *NeuroImage: Clinical*, *18*, 753–761. <https://doi.org/10.1016/j.nicl.2018.02.032>
- Halsband, U., & Lange, R. K. (2006). Motor learning in man: A review of functional and clinical studies. *Journal of Physiology-Paris*, *99*(4–6), 414–424.
- Hänggi, J., Koeneke, S., Bezzola, L., & Jäncke, L. (2010). Structural neuroplasticity in the sensorimotor network of professional female ballet dancers. *Human Brain Mapping*, *31*(8), 1196–1206. <https://doi.org/10.1002/hbm.20928>
- Hardwick, R. M., Rottschy, C., Miall, R. C., & Eickhoff, S. B. (2013). A quantitative meta-analysis and review of motor learning in the human brain. *NeuroImage*, *67*, 283–297. <https://doi.org/10.1016/j.neuroimage.2012.11.020>
- Hayasaka, S., Du, A.-T., Duarte, A., Kornak, J., Jahng, G.-H., Weiner, M. W., & Schuff, N. (2006). A non-parametric approach for co-analysis of multi-modal brain imaging data: Application to Alzheimer's disease. *NeuroImage*, *30*(3), 768–779. <https://doi.org/10.1016/j.neuroimage.2005.10.052>
- Hayes, S. M., Salat, D. H., Forman, D. E., Sperling, R. A., & Verfaellie, M. (2015). Cardiorespiratory fitness is associated with white matter integrity in aging. *Annals of Clinical and Translational Neurology*, *2*(6), 688–698. <https://doi.org/10.1002/acn3.204>
- Head, D., Bugg, J. M., Goate, A. M., Fagan, A. M., Mintun, M. A., Benzinger, T., Holtzman, D. M., & Morris, J. C. (2012). Exercise Engagement as a Moderator of the Effects of APOE Genotype on Amyloid Deposition. *Archives of Neurology*, *69*(5), 636–643. <https://doi.org/10.1001/archneurol.2011.845>
- Hecht, H. S., & Harman, S. M. (2003). Relation of aggressiveness of lipid-lowering treatment to changes in calcified plaque burden by electron beam tomography. *The American Journal of Cardiology*, *92*(3), 334–336. [https://doi.org/10.1016/S0002-9149\(03\)00642-8](https://doi.org/10.1016/S0002-9149(03)00642-8)

- Heidemann, R. M., Anwander, A., Feiweier, T., Knösche, T. R., & Turner, R. (2012). k-space and q-space: Combining ultra-high spatial and angular resolution in diffusion imaging using ZOOPPA at 7T. *NeuroImage*, *60*(2), 967–978.
<https://doi.org/10.1016/j.neuroimage.2011.12.081>
- Heise, V., Filippini, N., Ebmeier, K. P., & Mackay, C. E. (2011). The APOE $\epsilon 4$ allele modulates brain white matter integrity in healthy adults. *Molecular Psychiatry*, *16*(9), 908–916.
<https://doi.org/10.1038/mp.2010.90>
- Helms, G., Dathe, H., & Dechent, P. (2008). Quantitative FLASH MRI at 3T using a rational approximation of the Ernst equation. *Magnetic Resonance in Medicine*, *59*(3), 667–672.
<https://doi.org/10.1002/mrm.21542>
- Helms, G., Dathe, H., Kallenberg, K., & Dechent, P. (2008). High-resolution maps of magnetization transfer with inherent correction for RF inhomogeneity and T1 relaxation obtained from 3D FLASH MRI. *Magnetic Resonance in Medicine: An Official Journal of the International Society for Magnetic Resonance in Medicine*, *60*(6), 1396–1407.
- Hikosaka, O., Nakamura, K., Sakai, K., & Nakahara, H. (2002). Central mechanisms of motor skill learning. *Current Opinion in Neurobiology*, *12*(2), 217–222.
[https://doi.org/10.1016/S0959-4388\(02\)00307-0](https://doi.org/10.1016/S0959-4388(02)00307-0)
- Hikosaka, O., Rand, M. K., Miyachi, S., & Miyashita, K. (1995). Learning of sequential movements in the monkey: Process of learning and retention of memory. *Journal of Neurophysiology*, *74*(4), 1652–1661.
- Hikosaka, O., Sakai, K., Miyauchi, S., Takino, R., Sasaki, Y., & Putz, B. (1996). Activation of human presupplementary motor area in learning of sequential procedures: A functional MRI study. *Journal of Neurophysiology*, *76*(1), 617–621.
<https://doi.org/10.1152/jn.1996.76.1.617>
- Hofer, S., & Frahm, J. (2006). Topography of the human corpus callosum revisited—Comprehensive fiber tractography using diffusion tensor magnetic resonance imaging. *NeuroImage*, *32*(3), 989–994. <https://doi.org/10.1016/j.neuroimage.2006.05.044>
- Hofstetter, S., Tavor, I., Moryosef, S. T., & Assaf, Y. (2013). Short-Term Learning Induces White Matter Plasticity in the Fornix. *Journal of Neuroscience*, *33*(31), 12844–12850.
<https://doi.org/10.1523/JNEUROSCI.4520-12.2013>

- Holvoet, P., Harris, T. B., Tracy, R. P., Verhamme, P., Newman, A. B., Rubin, S. M., Simonsick, E. M., Colbert, L. H., & Kritchevsky, S. B. (2003). Association of High Coronary Heart Disease Risk Status With Circulating Oxidized LDL in the Well-Functioning Elderly. *Arteriosclerosis, Thrombosis, and Vascular Biology*, 23(8), 1444–1448. <https://doi.org/10.1161/01.ATV.0000080379.05071.22>
- Holvoet, P., Kritchevsky, S. B., Tracy, R. P., Mertens, A., Rubin, S. M., Butler, J., Goodpaster, B., & Harris, T. B. (2004). The Metabolic Syndrome, Circulating Oxidized LDL, and Risk of Myocardial Infarction in Well-Functioning Elderly People in the Health, Aging, and Body Composition Cohort. *Diabetes*, 53(4), 1068–1073. <https://doi.org/10.2337/diabetes.53.4.1068>
- Honea, R. A., Vidoni, E., Harsha, A., & Burns, J. M. (2009). Impact of APOE on the Healthy Aging Brain: A Voxel-Based MRI and DTI Study. *Journal of Alzheimer's Disease*, 18(3), 553–564. <https://doi.org/10.3233/JAD-2009-1163>
- Hotelling, H. (1947). Multivariate quality control. *Techniques of Statistical Analysis*.
- Hua, X., Hibar, D. P., Lee, S., Toga, A. W., Jack, C. R., Weiner, M. W., & Thompson, P. M. (2010). Sex and age differences in atrophic rates: An ADNI study with N=1368 MRI scans. *Neurobiology of Aging*, 31(8), 1463–1480. <https://doi.org/10.1016/j.neurobiolaging.2010.04.033>
- Huang, H., Fan, X., Weiner, M., Martin-Cook, K., Xiao, G., Davis, J., Devous, M., Rosenberg, R., & Diaz-Arrastia, R. (2012). Distinctive disruption patterns of white matter tracts in Alzheimer's disease with full diffusion tensor characterization. *Neurobiology of Aging*, 33(9), 2029–2045. <https://doi.org/10.1016/j.neurobiolaging.2011.06.027>
- Hyde, K. L., Lerch, J., Norton, A., Forgeard, M., Winner, E., Evans, A. C., & Schlaug, G. (2009). Musical Training Shapes Structural Brain Development. *Journal of Neuroscience*, 29(10), 3019–3025. <https://doi.org/10.1523/JNEUROSCI.5118-08.2009>
- Im, K., Lee, J.-M., Seo, S. W., Hyung Kim, S., Kim, S. I., & Na, D. L. (2008). Sulcal morphology changes and their relationship with cortical thickness and gyral white matter volume in mild cognitive impairment and Alzheimer's disease. *NeuroImage*, 43(1), 103–113. <https://doi.org/10.1016/j.neuroimage.2008.07.016>

- Imfeld, A., Oechslin, M. S., Meyer, M., Loenneker, T., & Jancke, L. (2009). White matter plasticity in the corticospinal tract of musicians: A diffusion tensor imaging study. *NeuroImage*, *46*(3), 600–607. <https://doi.org/10.1016/j.neuroimage.2009.02.025>
- Inoue, Y., Shue, F., Bu, G., & Kanekiyo, T. (2023). Pathophysiology and probable etiology of cerebral small vessel disease in vascular dementia and Alzheimer’s disease. *Molecular Neurodegeneration*, *18*(1), 46. <https://doi.org/10.1186/s13024-023-00640-5>
- Intzandt, B., Sanami, S., Huck, J., Labonté, A., Binette, A. P., Mathieu, A., Picard, C., Dea, D., Cuello, C., Evans, A., Tardif, C., Mulhaup, G., Near, J., Leoutsakos, J.-M., Bretiner, J. C. S., Poirier, J., Münterm, L.-M., Collins, L., Chakravarty, M., ... PREVENT-AD Research group. (2023). Sex-specific relationships between obesity, physical activity, and gray and white matter volume in cognitively unimpaired older adults. *GeroScience*, *45*(3), 1869–1888. <https://doi.org/10.1007/s11357-023-00734-4>
- Irie, F., Fitzpatrick, A. L., Lopez, O. L., Kuller, L. H., Peila, R., Newman, A. B., & Launer, L. J. (2008). Enhanced Risk for Alzheimer Disease in Persons With Type 2 Diabetes and APOE ε4: The Cardiovascular Health Study Cognition Study. *Archives of Neurology*, *65*(1), 89–93. <https://doi.org/10.1001/archneurol.2007.29>
- Iriondo, A., García-Sebastian, M., Arrospide, A., Arriba, M., Aurtenetxe, S., Barandiaran, M., Clerigue, M., Ecay-Torres, M., Estanga, A., Gabilondo, A., Izagirre, A., Saldias, J., Tainta, M., Villanua, J., Mar, J., Goñi, F. M., & Martínez-Lage, P. (2021). Plasma lipids are associated with white matter microstructural changes and axonal degeneration. *Brain Imaging and Behavior*, *15*(2), 1043–1057. <https://doi.org/10.1007/s11682-020-00311-9>
- Iroanyah, N., Savundranayagam, M. Y., Mundadan, R. G., & Sivananthan, S. (2021). Equity, diversity and inclusion in dementia diagnosis: A Canadian perspective. *World Alzheimer Report 2021: Journey through the Diagnosis of Dementia*, 235–237.
- Iturria-Medina, Y., Carbonell, F. M., Sotero, R. C., Chouinard-Decorte, F., & Evans, A. C. (2017). Multifactorial causal model of brain (dis)organization and therapeutic intervention: Application to Alzheimer’s disease. *NeuroImage*, *152*, 60–77. <https://doi.org/10.1016/j.neuroimage.2017.02.058>
- Iturria-Medina, Y., Sotero, R. C., Toussaint, P. J., Mateos-Pérez, J. M., & Evans, A. C. (2016). Early role of vascular dysregulation on late-onset Alzheimer’s disease based on

- multifactorial data-driven analysis. *Nature Communications*, 7(1), 11934.
<https://doi.org/10.1038/ncomms11934>
- Jäger, A.-T. P., Huntenburg, J. M., Tremblay, S. A., Schneider, U., Grahl, S., Huck, J., Tardif, C. L., Villringer, A., Gauthier, C. J., Bazin, P.-L., & Steele, C. J. (2021). Motor sequences; separating the sequence from the motor. A longitudinal rsfMRI study. *Brain Structure and Function*. <https://doi.org/10.1007/s00429-021-02412-7>
- Jenkins, I. H., Brooks, D. J., Nixon, P. D., Frackowiak, R. S., & Passingham, R. E. (1994). Motor sequence learning: A study with positron emission tomography. *Journal of Neuroscience*, 14(6), 3775–3790. <https://doi.org/10.1523/JNEUROSCI.14-06-03775.1994>
- Jenkinson, M. (2005). BET2: MR-Based Estimation of Brain, Skull and Scalp Surfaces. *Eleventh Annual Meeting of the Organization for Human Brain Mapping, 2005*, 17, 167.
- Jespersen, S. N., Bjarkam, C. R., Nyengaard, J. R., Chakravarty, M. M., Hansen, B., Vosegaard, T., Østergaard, L., Yablonskiy, D., Nielsen, N. C., & Vestergaard-Poulsen, P. (2010). Neurite density from magnetic resonance diffusion measurements at ultrahigh field: Comparison with light microscopy and electron microscopy. *NeuroImage*, 49(1), 205–216. <https://doi.org/10.1016/j.neuroimage.2009.08.053>
- Jespersen, S. N., Leigland, L. A., Cornea, A., & Kroenke, C. D. (2012). Determination of Axonal and Dendritic Orientation Distributions Within the Developing Cerebral Cortex by Diffusion Tensor Imaging. *IEEE Transactions on Medical Imaging*, 31(1), 16–32. *IEEE Transactions on Medical Imaging*. <https://doi.org/10.1109/TMI.2011.2162099>
- Jeurissen, B., Leemans, A., Tournier, J.-D., Jones, D. K., & Sijbers, J. (2013). Investigating the prevalence of complex fiber configurations in white matter tissue with diffusion magnetic resonance imaging. *Human Brain Mapping*, 34(11), 2747–2766.
<https://doi.org/10.1002/hbm.22099>
- Jeurissen, B., Tournier, J.-D., Dhollander, T., Connelly, A., & Sijbers, J. (2014). Multi-tissue constrained spherical deconvolution for improved analysis of multi-shell diffusion MRI data. *NeuroImage*, 103, 411–426. <https://doi.org/10.1016/j.neuroimage.2014.07.061>
- Johansen, M. C., Gottesman, R. F., Kral, B. G., Vaidya, D., Yanek, L. R., Becker, L. C., Becker, D. M., & Nyquist, P. (2021). Association of Coronary Artery Atherosclerosis With Brain White Matter Hyperintensity. *Stroke*, 52(8), 2594–2600.
<https://doi.org/10.1161/STROKEAHA.120.032674>

- Jones, D. K., Symms, M. R., Cercignani, M., & Howard, R. J. (2005). The effect of filter size on VBM analyses of DT-MRI data. *NeuroImage*, *26*(2), 546–554.
<https://doi.org/10.1016/j.neuroimage.2005.02.013>
- Justin, B. N., Turek, M., & Hakim, A. M. (2013). Heart disease as a risk factor for dementia. *Clinical Epidemiology*, *5*, 135–145. <https://doi.org/10.2147/CLEP.S30621>
- Kado, H., Kimura, H., Tsuchida, T., Yonekura, Y., Tokime, T., Tokuriki, Y., & Itoh, H. (2001). Abnormal Magnetization Transfer Ratios in Normal-appearing White Matter on Conventional MR Images of Patients with Occlusive Cerebrovascular Disease. *American Journal of Neuroradiology*, *22*(5), 922–927.
- Kanaan, R. A., Allin, M., Picchioni, M., Barker, G. J., Daly, E., Shergill, S. S., Woolley, J., & McGuire, P. K. (2012a). Gender Differences in White Matter Microstructure. *PLoS ONE*, *7*(6), e38272. <https://doi.org/10.1371/journal.pone.0038272>
- Kanaan, R. A., Allin, M., Picchioni, M., Barker, G. J., Daly, E., Shergill, S. S., Woolley, J., & McGuire, P. K. (2012b). Gender Differences in White Matter Microstructure. *PLoS ONE*, *7*(6), e38272. <https://doi.org/10.1371/journal.pone.0038272>
- Karakaya, J., Akin, S., Karagaoglu, E., & Gurlek, A. (2014). The performance of hemoglobin A1c against fasting plasma glucose and oral glucose tolerance test in detecting prediabetes and diabetes. *Journal of Research in Medical Sciences : The Official Journal of Isfahan University of Medical Sciences*, *19*(11), 1051–1057.
- Karni, A., Meyer, G., Jezard, P., Adams, M. M., Turner, R., & Ungerleider, L. G. (1995). Functional MRI evidence for adult motor cortex plasticity during motor skill learning. *Nature*, *377*(6545), 155–158. <https://doi.org/10.1038/377155a0>
- Karni, A., & Sagi, D. (1993). The time course of learning a visual skill. *Nature*, *365*(6443), Article 6443. <https://doi.org/10.1038/365250a0>
- Kastrup, A., Baudewig, J., Schnaudigel, S., Huonker, R., Becker, L., Sohns, J. M., Dechent, P., Klingner, C., & Witte, O. W. (2008). Behavioral correlates of negative BOLD signal changes in the primary somatosensory cortex. *NeuroImage*, *41*(4), 1364–1371.
<https://doi.org/10.1016/j.neuroimage.2008.03.049>
- Keller, J. N., Hanni, K. B., & Markesbery, W. R. (2002). Oxidized Low-Density Lipoprotein Induces Neuronal Death. *Journal of Neurochemistry*, *72*(6), 2601–2609.
<https://doi.org/10.1046/j.1471-4159.1999.0722601.x>

- Kerchner, G. A., Racine, C. A., Hale, S., Wilhelm, R., Laluz, V., Miller, B. L., & Kramer, J. H. (2012). Cognitive Processing Speed in Older Adults: Relationship with White Matter Integrity. *PLOS ONE*, 7(11), e50425. <https://doi.org/10.1371/journal.pone.0050425>
- Khedher, L., Ramírez, J., Górriz, J. M., Brahim, A., & Segovia, F. (2015). Early diagnosis of Alzheimer's disease based on partial least squares, principal component analysis and support vector machine using segmented MRI images. *Neurocomputing*, 151, 139–150. <https://doi.org/10.1016/j.neucom.2014.09.072>
- Kivipelto, M., Mangialasche, F., Snyder, H. M., Allegri, R., Andrieu, S., Arai, H., Baker, L., Belleville, S., Brodaty, H., Brucki, S. M., Calandri, I., Caramelli, P., Chen, C., Chertkow, H., Chew, E., Choi, S. H., Chowdhary, N., Crivelli, L., Torre, R. D. L., ... Carrillo, M. C. (2020). World-Wide FINGERS Network: A global approach to risk reduction and prevention of dementia. *Alzheimer's & Dementia*, 16(7), 1078–1094. <https://doi.org/10.1002/alz.12123>
- Klein, E., Willmes, K., Bieck, S. M., Bloechle, J., & Moeller, K. (2019). White matter neuroplasticity in mental arithmetic: Changes in hippocampal connectivity following arithmetic drill training. *Cortex*, 114, 115–123. <https://doi.org/10.1016/j.cortex.2018.05.017>
- Knight, R. T., Staines, W. R., Swick, D., & Chao, L. L. (1999). Prefrontal cortex regulates inhibition and excitation in distributed neural networks. *Acta Psychologica*, 101(2–3), 159–178.
- Kodiweera, C., Alexander, A. L., Harezlak, J., McAllister, T. W., & Wu, Y.-C. (2016). Age effects and sex differences in human brain white matter of young to middle-aged adults: A DTI, NODDI, and q-space study. *Neuroimage*, 128, 180–192.
- Kohn, K. P., Underwood, S. M., & Cooper, M. M. (2018). Connecting Structure–Property and Structure–Function Relationships across the Disciplines of Chemistry and Biology: Exploring Student Perceptions. *CBE Life Sciences Education*, 17(2). <https://doi.org/10.1187/cbe.18-01-0004>
- Konwar, S., Manca, R., De Marco, M., Soininen, H., & Venneri, A. (2023). The effect of physical activity on white matter integrity in aging and prodromal to mild Alzheimer's disease with vascular comorbidity. *Frontiers in Aging Neuroscience*, 15. <https://www.frontiersin.org/articles/10.3389/fnagi.2023.1096798>

- Korczyn, A. D. (2002). Mixed Dementia—The Most Common Cause of Dementia. *Annals of the New York Academy of Sciences*, 977(1), 129–134. <https://doi.org/10.1111/j.1749-6632.2002.tb04807.x>
- Korman, M., Raz, N., Flash, T., & Karni, A. (2003). Multiple shifts in the representation of a motor sequence during the acquisition of skilled performance. *Proceedings of the National Academy of Sciences*, 100(21), 12492–12497. <https://doi.org/10.1073/pnas.2035019100>
- Kovacic, J. C., Castellano, J. M., & Fuster, V. (2012). The links between complex coronary disease, cerebrovascular disease, and degenerative brain disease. *Annals of the New York Academy of Sciences*, 1254(1), 99–105. <https://doi.org/10.1111/j.1749-6632.2012.06482.x>
- Krakauer, J. W., Hadjiosif, A. M., Xu, J., Wong, A. L., & Haith, A. M. (2019). Motor Learning. *Comprehensive Physiology*, 9(2), 613–663. <https://doi.org/10.1002/cphy.c170043>
- Kritzman, M., & Li, Y. (2010). Skulls, Financial Turbulence, and Risk Management. *Financial Analysts Journal*, 66(5), 30–41. <https://doi.org/10.2469/faj.v66.n5.3>
- Kucharczyk, W., Macdonald, P. M., Stanis, G. J., & Henkelman, R. (1994). Relaxivity and magnetization transfer of white matter lipids at MR imaging: Importance of cerebroside and pH. *Radiology*, 192(2), 521–529.
- Kulikova, S., Hertz-Pannier, L., Dehaene-Lambertz, G., Buzmakov, A., Poupon, C., & Dubois, J. (2015). Multi-parametric evaluation of the white matter maturation. *Brain Structure and Function*, 220(6), 3657–3672. <https://doi.org/10.1007/s00429-014-0881-y>
- Kullmann, S., Callaghan, M. F., Heni, M., Weiskopf, N., Scheffler, K., Häring, H.-U., Fritsche, A., Veit, R., & Preissl, H. (2016). Specific white matter tissue microstructure changes associated with obesity. *NeuroImage*, 125, 36–44. Scopus. <https://doi.org/10.1016/j.neuroimage.2015.10.006>
- Kullmann, S., Schweizer, F., Veit, R., Fritsche, A., & Preissl, H. (2015). Compromised white matter integrity in obesity. *Obesity Reviews*, 16(4), 273–281. <https://doi.org/10.1111/obr.12248>
- Kung, H. F. (2012). The β -Amyloid Hypothesis in Alzheimer's Disease: Seeing Is Believing. *ACS Medicinal Chemistry Letters*, 3(4), 265–267. <https://doi.org/10.1021/ml300058m>
- L Woodard, J., A Sugarman, M., A Nielson, K., Carson Smith, J., Seidenberg, M., Durgerian, S., Butts, A., Hantke, N., Lancaster, M., & A Matthews, M. (2012). Lifestyle and genetic

- contributions to cognitive decline and hippocampal structure and function in healthy aging. *Current Alzheimer Research*, 9(4), 436–446.
- Lakhani, B., Borich, M. R., Jackson, J. N., Wadden, K. P., Peters, S., Villamayor, A., MacKay, A. L., Vavasour, I. M., Rauscher, A., & Boyd, L. A. (2016, May 16). *Motor Skill Acquisition Promotes Human Brain Myelin Plasticity* [Research Article]. *Neural Plasticity*; Hindawi. <https://doi.org/10.1155/2016/7526135>
- Lamar, M., Durazo-Arvizu, R. A., Rodriguez, C. J., Kaplan, R. C., Perera, M. J., Cai, J., Giacinto, R. A. E., González, H. M., & Daviglius, M. L. (2020). Associations of Lipid Levels and Cognition: Findings from the Hispanic Community Health Study/Study of Latinos. *Journal of the International Neuropsychological Society*, 26(3), 251–262. <https://doi.org/10.1017/S1355617719001000>
- Laule, C., Vavasour, I. M., Kolind, S. H., Li, D. K., Traboulsee, T. L., Moore, G. W., & MacKay, A. L. (2007). Magnetic resonance imaging of myelin. *Neurotherapeutics*, 4(3), 460–484.
- Launer, L. J., Lewis, C. E., Schreiner, P. J., Sidney, S., Battapady, H., Jacobs, D. R., Lim, K. O., D’Esposito, M., Zhang, Q., Reis, J., Davatzikos, C., & Bryan, R. N. (2015). Vascular Factors and Multiple Measures of Early Brain Health: CARDIA Brain MRI Study. *PLOS ONE*, 10(3), e0122138. <https://doi.org/10.1371/journal.pone.0122138>
- Lazari, A., Koudelka, S., & Sampaio-Baptista, C. (2018). Experience-related reductions of myelin and axon diameter in adulthood. *Journal of Neurophysiology*, 120(4), 1772–1775. <https://doi.org/10.1152/jn.00070.2018>
- Le Bihan, D., Breton, E., Lallemand, D., Aubin, M. L., Vignaud, J., & Laval-Jeantet, M. (1988). Separation of diffusion and perfusion in intravoxel incoherent motion MR imaging. *Radiology*, 168(2), 497–505.
- Le Bihan, D., Breton, E., Lallemand, D., Grenier, P., Cabanis, E., & Laval-Jeantet, M. (1986). MR imaging of intravoxel incoherent motions: Application to diffusion and perfusion in neurologic disorders. *Radiology*, 161(2), 401–407. <https://doi.org/10.1148/radiology.161.2.3763909>
- Le Bihan, D., & Iima, M. (2015). Diffusion magnetic resonance imaging: What water tells us about biological tissues. *PLoS Biology*, 13(7).

- Le Bihan, D., Mangin, J. F., Poupon, C., Clark, C. A., Pappata, S., Molko, N., & Chabriat, H. (2001). Diffusion tensor imaging: Concepts and applications. *Journal of Magnetic Resonance Imaging: JMRI*, *13*(4), 534–546. <https://doi.org/10.1002/jmri.1076>
- Lee, C. M., Woodward, M., Batty, G. D., Beiser, A. S., Bell, S., Berr, C., Bjertness, E., Chalmers, J., Clarke, R., Dartigues, J.-F., Davis-Plourde, K., Debette, S., Di Angelantonio, E., Feart, C., Frikke-Schmidt, R., Gregson, J., Haan, M. N., Hassing, L. B., Hayden, K. M., ... Huxley, R. R. (2020). Association of anthropometry and weight change with risk of dementia and its major subtypes: A meta-analysis consisting 2.8 million adults with 57 294 cases of dementia. *Obesity Reviews*, *21*(4), e12989. <https://doi.org/10.1111/obr.12989>
- Lee, M., Whitsel, E., Avery, C., Hughes, T. M., Griswold, M. E., Sedaghat, S., Gottesman, R. F., Mosley, T. H., Heiss, G., & Lutsey, P. L. (2022). Variation in Population Attributable Fraction of Dementia Associated With Potentially Modifiable Risk Factors by Race and Ethnicity in the US. *JAMA Network Open*, *5*(7), e2219672. <https://doi.org/10.1001/jamanetworkopen.2022.19672>
- Lee, S., Leach, M. K., Redmond, S. A., Chong, S. Y. C., Mellon, S. H., Tuck, S. J., Feng, Z.-Q., Corey, J. M., & Chan, J. R. (2012). A culture system to study oligodendrocyte myelination processes using engineered nanofibers. *Nature Methods*, *9*(9), Article 9. <https://doi.org/10.1038/nmeth.2105>
- Lei, Y., & Perez, M. A. (2017). Cortical contributions to sensory gating in the ipsilateral somatosensory cortex during voluntary activity. *The Journal of Physiology*, *595*(18), 6203–6217. <https://doi.org/10.1113/JP274504>
- Lema, A., Bishop, C., Malik, O., Mattoscio, M., Ali, R., Nicholas, R., Muraro, P. A., Matthews, P. M., Waldman, A. D., & Newbould, R. D. (2017). A comparison of magnetization transfer methods to assess brain and cervical cord microstructure in multiple sclerosis. *Journal of Neuroimaging*, *27*(2), 221–226.
- Lenth, R., Singmann, H., Love, J., Buerkner, P., & Herve, M. (2018). Emmeans: Estimated marginal means, aka least-squares means. *R Package Version*, *1*(1), 3.
- Levesque, I., Sled, J. G., Narayanan, S., Santos, A. C., Brass, S. D., Francis, S. J., Arnold, D. L., & Pike, G. B. (2005). The role of edema and demyelination in chronic T1 black holes: A quantitative magnetization transfer study. *Journal of Magnetic Resonance Imaging: An*

- Official Journal of the International Society for Magnetic Resonance in Medicine*, 21(2), 103–110.
- Lewis, C. M., Baldassarre, A., Committeri, G., Romani, G. L., & Corbetta, M. (2009). Learning sculpts the spontaneous activity of the resting human brain. *Proceedings of the National Academy of Sciences*, 106(41), 17558–17563. <https://doi.org/10.1073/pnas.0902455106>
- Lezak, M. D. (2004). *Neuropsychological Assessment*.
- Li, X., Liang, Y., Chen, Y., Zhang, J., Wei, D., Chen, K., Shu, N., Reiman, E. M., & Zhang, Z. (2015). Disrupted Frontoparietal Network Mediates White Matter Structure Dysfunction Associated with Cognitive Decline in Hypertension Patients. *Journal of Neuroscience*, 35(27), 10015–10024. <https://doi.org/10.1523/JNEUROSCI.5113-14.2015>
- Li, Z., Wang, W., Sang, F., Zhang, Z., & Li, X. (2023). White matter changes underlie hypertension-related cognitive decline in older adults. *NeuroImage: Clinical*, 38, 103389. <https://doi.org/10.1016/j.nicl.2023.103389>
- Liakakis, G., Nickel, J., & Seitz, R. J. (2011). Diversity of the inferior frontal gyrus—A meta-analysis of neuroimaging studies. *Behavioural Brain Research*, 225(1), 341–347. <https://doi.org/10.1016/j.bbr.2011.06.022>
- Libby, P., & Theroux, P. (2005). Pathophysiology of Coronary Artery Disease. *Circulation*, 111(25), 3481–3488. <https://doi.org/10.1161/CIRCULATIONAHA.105.537878>
- Lindemer, E. R., Salat, D. H., Smith, E. E., Nguyen, K., Fischl, B., & Greve, D. N. (2015). White matter signal abnormality quality differentiates mild cognitive impairment that converts to Alzheimer’s disease from nonconverters. *Neurobiology of Aging*, 36(9), 2447–2457. <https://doi.org/10.1016/j.neurobiolaging.2015.05.011>
- Liu, C.-F., Hsu, J., Xu, X., Kim, G., Sheppard, S. M., Meier, E. L., Miller, M. I., Hillis, A. E., & Faria, A. V. (2023). Digital 3D Brain MRI Arterial Territories Atlas. *Scientific Data*, 10(1), 74. <https://doi.org/10.1038/s41597-022-01923-0>
- Liu, Y., Julkunen, V., Paajanen, T., Westman, E., Wahlund, L.-O., Aitken, A., Sobow, T., Mecocci, P., Tsolaki, M., Vellas, B., Muehlboeck, S., Spenger, C., Lovestone, S., Simmons, A., Soininen, H., & AddNeuroMed Consortium. (2012). Education increases reserve against Alzheimer’s disease—Evidence from structural MRI analysis. *Neuroradiology*, 54(9), 929–938. <https://doi.org/10.1007/s00234-012-1005-0>

- Livingston, G., Huntley, J., Liu, K. Y., Costafreda, S. G., Selbæk, G., Alladi, S., Ames, D., Banerjee, S., Burns, A., Brayne, C., Fox, N. C., Ferri, C. P., Gitlin, L. N., Howard, R., Kales, H. C., Kivimäki, M., Larson, E. B., Nakasujja, N., Rockwood, K., ... Mukadam, N. (2024). Dementia prevention, intervention, and care: 2024 report of the Lancet standing Commission. *The Lancet*, *0*(0). [https://doi.org/10.1016/S0140-6736\(24\)01296-0](https://doi.org/10.1016/S0140-6736(24)01296-0)
- Livingston, G., Huntley, J., Sommerlad, A., Ames, D., Ballard, C., Banerjee, S., Brayne, C., Burns, A., Cohen-Mansfield, J., Cooper, C., Costafreda, S. G., Dias, A., Fox, N., Gitlin, L. N., Howard, R., Kales, H. C., Kivimäki, M., Larson, E. B., Ogunniyi, A., ... Mukadam, N. (2020). Dementia prevention, intervention, and care: 2020 report of the Lancet Commission. *The Lancet*, *396*(10248), 413–446. [https://doi.org/10.1016/S0140-6736\(20\)30367-6](https://doi.org/10.1016/S0140-6736(20)30367-6)
- Lotze, M., Scheler, G., Tan, H.-R., Braun, C., & Birbaumer, N. (2003). The musician's brain: Functional imaging of amateurs and professionals during performance and imagery. *Neuroimage*, *20*(3), 1817–1829.
- Luck, T., Riedel-Heller, S. G., Luppä, M., Wiese, B., Köhler, M., Jessen, F., Bickel, H., Weyerer, S., Pentzek, M., König, H.-H., Prokein, J., Ernst, A., Wagner, M., Mösch, E., Werle, J., Fuchs, A., Brettschneider, C., Scherer, M., & Maier, W. (2014). Apolipoprotein E epsilon 4 genotype and a physically active lifestyle in late life: Analysis of gene–environment interaction for the risk of dementia and Alzheimer's disease dementia. *Psychological Medicine*, *44*(6), 1319–1329. <https://doi.org/10.1017/S0033291713001918>
- Luft, A. R., & Buitrago, M. M. (2005). Stages of motor skill learning. *Molecular Neurobiology*, *32*(3), 205–216. <https://doi.org/10.1385/MN:32:3:205>
- Lv, Y.-B., Yin, Z. X., Chei, C.-L., Brasher, M. S., Zhang, J., Kraus, V. B., Qian, F., Shi, X., Matchar, D. B., & Zeng, Y. (2016). Serum cholesterol levels within the high normal range are associated with better cognitive performance among Chinese elderly. *The Journal of Nutrition, Health and Aging*, *20*(3), 280–287. <https://doi.org/10.1007/s12603-016-0701-6>
- Lynch, T., Cherny, R. A., & Bush, A. I. (2000). Oxidative processes in Alzheimer's disease: The role of A β -metal interactions. *Experimental Gerontology*, *35*(4), 445–451. [https://doi.org/10.1016/S0531-5565\(00\)00112-1](https://doi.org/10.1016/S0531-5565(00)00112-1)

- Ma, C., Yin, Z., Zhu, P., Luo, J., Shi, X., & Gao, X. (2017). Blood cholesterol in late-life and cognitive decline: A longitudinal study of the Chinese elderly. *Molecular Neurodegeneration*, *12*(1), 24. <https://doi.org/10.1186/s13024-017-0167-y>
- MacIntosh, B. J., Swardfager, W., Crane, D. E., Ranepura, N., Saleem, M., Oh, P. I., Stefanovic, B., Herrmann, N., & Lanctôt, K. L. (2014). Cardiopulmonary Fitness Correlates with Regional Cerebral Grey Matter Perfusion and Density in Men with Coronary Artery Disease. *PLOS ONE*, *9*(3), e91251. <https://doi.org/10.1371/journal.pone.0091251>
- Mahalanobis, P. C. (1936). *On the generalized distance in statistics*.
- Mahley, R. W. (2016). Central Nervous System Lipoproteins. *Arteriosclerosis, Thrombosis, and Vascular Biology*, *36*(7), 1305–1315. <https://doi.org/10.1161/ATVBAHA.116.307023>
- Maier-Hein, K. H., Westin, C.-F., Shenton, M. E., Weiner, M. W., Raj, A., Thomann, P., Kikinis, R., Stieltjes, B., & Pasternak, O. (2015). Widespread white matter degeneration preceding the onset of dementia. *Alzheimer's & Dementia*, *11*(5), 485-493.e2. <https://doi.org/10.1016/j.jalz.2014.04.518>
- Maillard, P., Seshadri, S., Beiser, A., Himali, J. J., Au, R., Fletcher, E., Carmichael, O., Wolf, P. A., & DeCarli, C. (2012). Effects of systolic blood pressure on white-matter integrity in young adults in the Framingham Heart Study: A cross-sectional study. *The Lancet Neurology*, *11*(12), 1039–1047. [https://doi.org/10.1016/S1474-4422\(12\)70241-7](https://doi.org/10.1016/S1474-4422(12)70241-7)
- Maleki, S., Hendrikse, J., Chye, Y., Caeyenberghs, K., Coxon, J. P., Oldham, S., Suo, C., & Yücel, M. (2022). Associations of cardiorespiratory fitness and exercise with brain white matter in healthy adults: A systematic review and meta-analysis. *Brain Imaging and Behavior*, *16*(5), 2402–2425. <https://doi.org/10.1007/s11682-022-00693-y>
- Manolio, T. A., Ettinger, W. H., Tracy, R. P., Kuller, L. H., Borhani, N. O., Lynch, J. C., & Fried, L. P. (1993). Epidemiology of low cholesterol levels in older adults. The Cardiovascular Health Study. *Circulation*, *87*(3), 728–737. <https://doi.org/10.1161/01.CIR.87.3.728>
- Marquand, A. F., Rezek, I., Buitelaar, J., & Beckmann, C. F. (2016). Understanding Heterogeneity in Clinical Cohorts Using Normative Models: Beyond Case-Control Studies. *Biological Psychiatry*, *80*(7), 552–561. <https://doi.org/10.1016/j.biopsych.2015.12.023>

- Marques, J. P., Kober, T., Krueger, G., van der Zwaag, W., Van de Moortele, P.-F., & Gruetter, R. (2010). MP2RAGE, a self bias-field corrected sequence for improved segmentation and T1-mapping at high field. *Neuroimage*, *49*(2), 1271–1281.
- Mathur, K. S., Kashyap, S. K., & Kumar, V. (1963). Correlation of the Extent and Severity of Atherosclerosis in the Coronary and Cerebral Arteries. *Circulation*, *27*(5), 929–934.
<https://doi.org/10.1161/01.CIR.27.5.929>
- Mayo, C. D., Mazerolle, E. L., Ritchie, L., Fisk, J. D., & Gawryluk, J. R. (2017). Longitudinal changes in microstructural white matter metrics in Alzheimer’s disease. *NeuroImage: Clinical*, *13*, 330–338. <https://doi.org/10.1016/j.nicl.2016.12.012>
- McCormick, M. M., Liu, X., Ibanez, L., Jomier, J., & Marion, C. (2014). ITK: Enabling reproducible research and open science. *Frontiers in Neuroinformatics*, *8*.
<https://doi.org/10.3389/fninf.2014.00013>
- McIntosh, A. R., & Lobaugh, N. J. (2004). Partial least squares analysis of neuroimaging data: Applications and advances. *NeuroImage*, *23 Suppl 1*, S250-263.
<https://doi.org/10.1016/j.neuroimage.2004.07.020>
- McPhee, G. M., Downey, L. A., & Stough, C. (2019). Effects of sustained cognitive activity on white matter microstructure and cognitive outcomes in healthy middle-aged adults: A systematic review. *Ageing Research Reviews*, *51*, 35–47.
<https://doi.org/10.1016/j.arr.2019.02.004>
- Melki, P. S., & Mulkern, R. V. (1992). Magnetization transfer effects in multislice RARE sequences. *Magnetic Resonance in Medicine*, *24*(1), 189–195.
<https://doi.org/10.1002/mrm.1910240122>
- Mendez Colmenares, A., Voss, M. W., Fanning, J., Salerno, E. A., Gothe, N. P., Thomas, M. L., McAuley, E., Kramer, A. F., & Burzynska, A. Z. (2021). White matter plasticity in healthy older adults: The effects of aerobic exercise. *NeuroImage*, *239*, 118305.
<https://doi.org/10.1016/j.neuroimage.2021.118305>
- Middleton, L., Kirkland, S., & Rockwood, K. (2008). Prevention of CIND by physical activity: Different impact on VCI-ND compared with MCI. *Journal of the Neurological Sciences*, *269*(1), 80–84. <https://doi.org/10.1016/j.jns.2007.04.054>

- Miller, E. K., & Cohen, J. D. (2001). An Integrative Theory of Prefrontal Cortex Function. *Annual Review of Neuroscience*, 24(1), 167–202.
<https://doi.org/10.1146/annurev.neuro.24.1.167>
- Minagawa, Y., & Saito, Y. (2021). The Role of Underweight in Active Life Expectancy Among Older Adults in Japan. *The Journals of Gerontology: Series B*, 76(4), 756–765.
<https://doi.org/10.1093/geronb/gbaa013>
- Mohr, H., Wolfensteller, U., Betzel, R. F., Mišić, B., Sporns, O., Richiardi, J., & Ruge, H. (2016). Integration and segregation of large-scale brain networks during short-term task automatization. *Nature Communications*, 7(1), Article 1.
<https://doi.org/10.1038/ncomms13217>
- Mole, J. P., Fasano, F., Evans, J., Sims, R., Hamilton, D. A., Kidd, E., & Metzler-Baddeley, C. (2020). Genetic risk of dementia modifies obesity effects on white matter myelin in cognitively healthy adults. *Neurobiology of Aging*, 94, 298–310.
<https://doi.org/10.1016/j.neurobiolaging.2020.06.014>
- Monfils, M.-H., Plautz, E. J., & Kleim, J. A. (2005). In Search of the Motor Engram: Motor Map Plasticity as a Mechanism for Encoding Motor Experience. *The Neuroscientist*, 11(5), 471–483. <https://doi.org/10.1177/1073858405278015>
- Moorhouse, P., & Rockwood, K. (2008). Vascular cognitive impairment: Current concepts and clinical developments. *The Lancet Neurology*, 7(3), 246–255.
[https://doi.org/10.1016/S1474-4422\(08\)70040-1](https://doi.org/10.1016/S1474-4422(08)70040-1)
- Moran, C., Beare, R., Phan, T., Starkstein, S., Bruce, D., Romina, M., & Srikanth, V. (2017). Neuroimaging and its Relevance to Understanding Pathways Linking Diabetes and Cognitive Dysfunction. *Journal of Alzheimer's Disease*, 59(2), 405–419.
<https://doi.org/10.3233/JAD-161166>
- Moraschi, M., Hagberg, G. E., Paola, M. D., Spalletta, G., Maraviglia, B., & Giove, F. (2010). Smoothing that does not blur: Effects of the anisotropic approach for evaluating diffusion tensor imaging data in the clinic. *Journal of Magnetic Resonance Imaging*, 31(3), 690–697. <https://doi.org/10.1002/jmri.22040>
- Mortamais, M., Portet, F., Brickman, A. M., Provenzano, F. A., Muraskin, J., Akbaraly, T. N., Berr, C., Touchon, J., Bonafé, A., le Bars, E., Menjot de Champfleury, N., Maller, J. J., Meslin, C., Sabatier, R., Ritchie, K., & Artero, S. (2014). Education Modulates the Impact

- of White Matter Lesions on the Risk of Mild Cognitive Impairment and Dementia. *The American Journal of Geriatric Psychiatry*, 22(11), 1336–1345.
<https://doi.org/10.1016/j.jagp.2013.06.002>
- Mukherjee, P., Chung, S. W., Berman, J. I., Hess, C. P., & Henry, R. G. (2008). Diffusion Tensor MR Imaging and Fiber Tractography: Technical Considerations. *American Journal of Neuroradiology*, 29(5), 843–852. <https://doi.org/10.3174/ajnr.A1052>
- Naylor, M. G., Cardenas, V. A., Tosun, D., Schuff, N., Weiner, M., & Schwartzman, A. (2014). Voxelwise multivariate analysis of multimodality magnetic resonance imaging. *Human Brain Mapping*, 35(3), 831–846. <https://doi.org/10.1002/hbm.22217>
- Ndrepepa, G., Braun, S., von Beckerath, N., Mehilli, J., Gorchakova, O., Vogt, W., Schömig, A., & Kastrati, A. (2005). Oxidized low density lipoproteins, statin therapy and severity of coronary artery disease. *Clinica Chimica Acta*, 360(1), 178–186.
<https://doi.org/10.1016/j.cccn.2005.04.032>
- Nestor, P. G., O'Donnell, B. F., McCarley, R. W., Niznikiewicz, M., Barnard, J., Jen Shen, Z., Bookstein, F. L., & Shenton, M. E. (2002). A new statistical method for testing hypotheses of neuropsychological/MRI relationships in schizophrenia: Partial least squares analysis. *Schizophrenia Research*, 53(1), 57–66. [https://doi.org/10.1016/S0920-9964\(00\)00171-7](https://doi.org/10.1016/S0920-9964(00)00171-7)
- Ngandu, T., Lehtisalo, J., Solomon, A., Levälähti, E., Ahtiluoto, S., Antikainen, R., Bäckman, L., Hänninen, T., Jula, A., Laatikainen, T., Lindström, J., Mangialasche, F., Pajananen, T., Pajala, S., Peltonen, M., Rauramaa, R., Stigsdotter-Neely, A., Strandberg, T., Tuomilehto, J., ... Kivipelto, M. (2015). A 2 year multidomain intervention of diet, exercise, cognitive training, and vascular risk monitoring versus control to prevent cognitive decline in at-risk elderly people (FINGER): A randomised controlled trial. *Lancet (London, England)*, 385(9984), 2255–2263. [https://doi.org/10.1016/S0140-6736\(15\)60461-5](https://doi.org/10.1016/S0140-6736(15)60461-5)
- Nirkko, A. C., Ozdoba, C., Redmond, S. M., Bürki, M., Schroth, G., Hess, C. W., & Wiesendanger, M. (2001). Different Ipsilateral Representations for Distal and Proximal Movements in the Sensorimotor Cortex: Activation and Deactivation Patterns. *NeuroImage*, 13(5), 825–835. <https://doi.org/10.1006/nimg.2000.0739>
- Nishi, K., Itabe, H., Uno, M., Kitazato, K. T., Horiguchi, H., Shinno, K., & Nagahiro, S. (2002). Oxidized LDL in Carotid Plaques and Plasma Associates With Plaque Instability.

- Arteriosclerosis, Thrombosis, and Vascular Biology*, 22(10), 1649–1654.
<https://doi.org/10.1161/01.ATV.0000033829.14012.18>
- Nissen, M. J., & Bullemer, P. (1987). Attentional requirements of learning: Evidence from performance measures. *Cognitive Psychology*, 19(1), 1–32. [https://doi.org/10.1016/0010-0285\(87\)90002-8](https://doi.org/10.1016/0010-0285(87)90002-8)
- Novikov, D. S., Kiselev, V. G., & Jespersen, S. N. (2018). On modeling. *Magnetic Resonance in Medicine*, 79(6), 3172–3193. <https://doi.org/10.1002/mrm.27101>
- O'Brien, J. T. (2014). Clinical Significance of White Matter Changes. *The American Journal of Geriatric Psychiatry*, 22(2), 133–137. <https://doi.org/10.1016/j.jagp.2013.07.006>
- Olesen, K. K. W., Madsen, M., Lip, G. Y. H., Egholm, G., Thim, T., Jensen, L. O., Raungaard, B., Nielsen, J. C., Bøtker, H. E., Sørensen, H. T., & Maeng, M. (2017). Coronary artery disease and risk of adverse cardiac events and stroke. *European Journal of Clinical Investigation*, 47(11), 819–828. <https://doi.org/10.1111/eci.12804>
- Olesen, K. K. W., Thrane, P. G., Gyldenkerne, C., Thomsen, R. W., Mortensen, J. K., Kristensen, S. D., & Maeng, M. (2024). Diabetes and coronary artery disease as risk factors for dementia. *European Journal of Preventive Cardiology*, zwae153.
<https://doi.org/10.1093/eurjpc/zwae153>
- O'Rourke, M. F., & Hashimoto, J. (2007). Mechanical Factors in Arterial Aging. *Journal of the American College of Cardiology*, 50(1), 1–13. <https://doi.org/10.1016/j.jacc.2006.12.050>
- Owen, T. W., de Tisi, J., Vos, S. B., Winston, G. P., Duncan, J. S., Wang, Y., & Taylor, P. N. (2021). Multivariate white matter alterations are associated with epilepsy duration. *The European Journal of Neuroscience*, 53(8), 2788–2803. <https://doi.org/10.1111/ejn.15055>
- Pascalau, R., Popa Stănilă, R., Sfrângeu, S., & Szabo, B. (2018). Anatomy of the Limbic White Matter Tracts as Revealed by Fiber Dissection and Tractography. *World Neurosurgery*, 113, e672–e689. <https://doi.org/10.1016/j.wneu.2018.02.121>
- Pascual-Leone, A., Amedi, A., Fregni, F., & Merabet, L. B. (2005). The Plastic Human Brain Cortex. *Annual Review of Neuroscience*, 28(1), 377–401.
<https://doi.org/10.1146/annurev.neuro.27.070203.144216>
- Patenaude, B., Smith, S. M., Kennedy, D. N., & Jenkinson, M. (2011). A Bayesian model of shape and appearance for subcortical brain segmentation. *NeuroImage*, 56(3), 907–922.
<https://doi.org/10.1016/j.neuroimage.2011.02.046>

- Paus, T. (2010). Growth of white matter in the adolescent brain: Myelin or axon? *Brain and Cognition*, 72(1), 26–35. <https://doi.org/10.1016/j.bandc.2009.06.002>
- Peila, R., Rodriguez, B. L., & Launer, L. J. (2002). Type 2 Diabetes, APOE Gene, and the Risk for Dementia and Related Pathologies: The Honolulu-Asia Aging Study. *Diabetes*, 51(4), 1256–1262. <https://doi.org/10.2337/diabetes.51.4.1256>
- Penhune, V. B., & Steele, C. J. (2012). Parallel contributions of cerebellar, striatal and M1 mechanisms to motor sequence learning. *Behavioural Brain Research*, 226(2), 579–591.
- Penninkilampi, R., Casey, A.-N., Singh, M. F., & Brodaty, H. (2018). The Association between Social Engagement, Loneliness, and Risk of Dementia: A Systematic Review and Meta-Analysis. *Journal of Alzheimer's Disease*, 66(4), 1619–1633. <https://doi.org/10.3233/JAD-180439>
- Perl, D. P. (2010). Neuropathology of Alzheimer's Disease. *Mount Sinai Journal of Medicine: A Journal of Translational and Personalized Medicine*, 77(1), 32–42. <https://doi.org/10.1002/msj.20157>
- Pike, G. B. (1996). Pulsed magnetization transfer contrast in gradient echo imaging: A two-pool analytic description of signal response. *Magnetic Resonance in Medicine*, 36(1), 95–103. <https://doi.org/10.1002/mrm.1910360117>
- Pike, G. B., Glover, G. H., Hu, B. S., & Enzmann, D. R. (1993). Pulsed magnetization transfer spin-echo MR imaging. *Journal of Magnetic Resonance Imaging*, 3(3), 531–539. <https://doi.org/10.1002/jmri.1880030316>
- Pines, A. R., Cieslak, M., Larsen, B., Baum, G. L., Cook, P. A., Adebimpe, A., Dávila, D. G., Elliott, M. A., Jirsaraie, R., Murtha, K., Oathes, D. J., Piiwaa, K., Rosen, A. F. G., Rush, S., Shinohara, R. T., Bassett, D. S., Roalf, D. R., & Satterthwaite, T. D. (2020). Leveraging multi-shell diffusion for studies of brain development in youth and young adulthood. *Developmental Cognitive Neuroscience*, 43, 100788. <https://doi.org/10.1016/j.dcn.2020.100788>
- Plitman, E., Ochi, R., Patel, R., Tsugawa, S., Tarumi, R., Honda, S., Matsushita, K., Fujii, S., Uchida, H., & Mimura, M. (2020). Using Non-Negative Matrix Factorization to Examine Treatment Resistance and Response in Patients With Schizophrenia: A Multimodal Imaging Study. *Biological Psychiatry*, 87(9), S350.

- Poirier, S. E., Suskin, N. G., Khaw, A. V., Thiessen, J. D., Shoemaker, J. K., & Anazodo, U. C. (2024). Probing Evidence of Cerebral White Matter Microstructural Disruptions in Ischemic Heart Disease Before and Following Cardiac Rehabilitation: A Diffusion Tensor MR Imaging Study. *Journal of Magnetic Resonance Imaging*, *59*(6), 2137–2149. <https://doi.org/10.1002/jmri.28964>
- Poldrack, R. A. (2000). Imaging brain plasticity: Conceptual and methodological issues—a theoretical review. *Neuroimage*, *12*(1), 1–13.
- Polidori, M. C., Pientka, L., & Mecocci, P. (2012). A Review of the Major Vascular Risk Factors Related to Alzheimer’s Disease. *Journal of Alzheimer’s Disease*, *32*(3), 521–530. <https://doi.org/10.3233/JAD-2012-120871>
- Posner, M. I. (1980). Orienting of Attention. *Quarterly Journal of Experimental Psychology*, *32*(1), 3–25. <https://doi.org/10.1080/00335558008248231>
- Qizilbash, N., Gregson, J., Johnson, M. E., Pearce, N., Douglas, I., Wing, K., Evans, S. J. W., & Pocock, S. J. (2015). BMI and risk of dementia in two million people over two decades: A retrospective cohort study. *The Lancet Diabetes & Endocrinology*, *3*(6), 431–436. [https://doi.org/10.1016/S2213-8587\(15\)00033-9](https://doi.org/10.1016/S2213-8587(15)00033-9)
- Qu, Y., Hu, H.-Y., Ou, Y.-N., Shen, X.-N., Xu, W., Wang, Z.-T., Dong, Q., Tan, L., & Yu, J.-T. (2020). Association of body mass index with risk of cognitive impairment and dementia: A systematic review and meta-analysis of prospective studies. *Neuroscience & Biobehavioral Reviews*, *115*, 189–198. <https://doi.org/10.1016/j.neubiorev.2020.05.012>
- Rademacher, J., Engelbrecht, V., Bürgel, U., Freund, H.-J., & Zilles, K. (1999). Measuring in Vivo Myelination of Human White Matter Fiber Tracts with Magnetization Transfer MR. *NeuroImage*, *9*(4), 393–406. <https://doi.org/10.1006/nimg.1998.0416>
- Raffelt, D., Dhollander, T., Tournier, J.-D., Tabbara, R., Smith, R. E., Pierre, E., & Connelly, A. (2017). Bias Field Correction and Intensity Normalisation for Quantitative Analysis of Apparent Fibre Density. *In Proc. ISMRM*.
- Raffelt, D., Tournier, J.-D., Fripp, J., Crozier, S., Connelly, A., & Salvado, O. (2011). Symmetric diffeomorphic registration of fibre orientation distributions. *NeuroImage*, *56*(3), 1171–1180. <https://doi.org/10.1016/j.neuroimage.2011.02.014>
- Raffelt, D., Tournier, J.-D., Rose, S., Ridgway, G. R., Henderson, R., Crozier, S., Salvado, O., & Connelly, A. (2012). Apparent Fibre Density: A novel measure for the analysis of

- diffusion-weighted magnetic resonance images. *NeuroImage*, *59*(4), 3976–3994.
<https://doi.org/10.1016/j.neuroimage.2011.10.045>
- Raffelt, D., Tournier, J.-D., Smith, R. E., Vaughan, D. N., Jackson, G., Ridgway, G. R., & Connelly, A. (2017). Investigating white matter fibre density and morphology using fixel-based analysis. *NeuroImage*, *144*, 58–73.
<https://doi.org/10.1016/j.neuroimage.2016.09.029>
- Raffin, J., Rolland, Y., He, L., Perus, L., Mangin, J.-F., Gabelle, A., Virecoulon Giudici, K., Vellas, B., & de Souto Barreto, P. (2021). Cross-sectional and longitudinal interaction effects of physical activity and *APOE-ε4* on white matter integrity in older adults: The MAPT study. *Maturitas*, *152*, 10–19. <https://doi.org/10.1016/j.maturitas.2021.06.010>
- Randolph, C., Tierney, M. C., Mohr, E., & Chase, T. N. (1998). The Repeatable Battery for the Assessment of Neuropsychological Status (RBANS): Preliminary Clinical Validity. *Journal of Clinical and Experimental Neuropsychology*, *20*(3), 310–319.
<https://doi.org/10.1076/jcen.20.3.310.823>
- Reese, T. G., Heid, O., Weisskoff, R. M., & Wedeen, V. J. (2003). Reduction of eddy-current-induced distortion in diffusion MRI using a twice-refocused spin echo. *Magnetic Resonance in Medicine*, *49*(1), 177–182. <https://doi.org/10.1002/mrm.10308>
- Reitz, C., Tang, M.-X., Schupf, N., Manly, J. J., Mayeux, R., & Luchsinger, J. A. (2010). Association of Higher Levels of High-Density Lipoprotein Cholesterol in Elderly Individuals and Lower Risk of Late-Onset Alzheimer Disease. *Archives of Neurology*, *67*(12), 1491–1497. <https://doi.org/10.1001/archneurol.2010.297>
- Repple, J., Karliczek, G., Meinert, S., Förster, K., Grotegerd, D., Goltermann, J., Redlich, R., Arolt, V., Baune, B. T., Dannlowski, U., & Opel, N. (2021). Variation of HbA1c affects cognition and white matter microstructure in healthy, young adults. *Molecular Psychiatry*, *26*(4), 1399–1408. <https://doi.org/10.1038/s41380-019-0504-3>
- Richie-Halford, A., Yeatman, J. D., Simon, N., & Rokem, A. (2021). Multidimensional analysis and detection of informative features in human brain white matter. *PLOS Computational Biology*, *17*(6), e1009136. <https://doi.org/10.1371/journal.pcbi.1009136>
- Riffert, T. W., Schreiber, J., Anwander, A., & Knösche, T. R. (2014). Beyond fractional anisotropy: Extraction of bundle-specific structural metrics from crossing fiber models. *NeuroImage*, *100*, 176–191. <https://doi.org/10.1016/j.neuroimage.2014.06.015>

- Rioult-Pedotti, M.-S., Friedman, D., & Donoghue, J. P. (2000). Learning-Induced LTP in Neocortex. *Science*, *290*(5491), 533–536. <https://doi.org/10.1126/science.290.5491.533>
- Ritchie, K., & Lovestone, S. (2002). The dementias. *The Lancet*, *360*(9347), 1759–1766. [https://doi.org/10.1016/S0140-6736\(02\)11667-9](https://doi.org/10.1016/S0140-6736(02)11667-9)
- Rodrigue, K. M., Daugherty, A. M., Haacke, E. M., & Raz, N. (2013). The Role of Hippocampal Iron Concentration and Hippocampal Volume in Age-Related Differences in Memory. *Cerebral Cortex*, *23*(7), 1533–1541. <https://doi.org/10.1093/cercor/bhs139>
- Roe, C. M., Xiong, C., Miller, J. P., & Morris, J. C. (2007). Education and Alzheimer disease without dementia. *Neurology*, *68*(3), 223–228. <https://doi.org/10.1212/01.wnl.0000251303.50459.8a>
- Roher, A. E., Weiss, N., Kokjohn, T. A., Kuo, Y.-M., Kalback, W., Anthony, J., Watson, D., Luehrs, D. C., Sue, L., Walker, D., Emmerling, M., Goux, W., & Beach, T. (2002). Increased A β Peptides and Reduced Cholesterol and Myelin Proteins Characterize White Matter Degeneration in Alzheimer’s Disease. *Biochemistry*, *41*(37), 11080–11090. <https://doi.org/10.1021/bi026173d>
- Roig-Coll, F., Castells-Sánchez, A., Monté-Rubio, G., Dacosta-Aguayo, R., Lamonja-Vicente, N., Torán-Monserrat, P., Pere, G., García-Molina, A., Tormos, J. M., Alzamora, M. T., Stavros, D., Sánchez-Ceron, M., Via, M., Erickson, K. I., & Mataró, M. (2024). Changes in cardiovascular health and white matter integrity with aerobic exercise, cognitive and combined training in physically inactive healthy late-middle-aged adults: The “Projecte Moviment” randomized controlled trial. *European Journal of Applied Physiology*, *124*(3), 909–924. <https://doi.org/10.1007/s00421-023-05319-9>
- Rosano, C., Abebe, K. Z., Aizenstein, H. J., Boudreau, R., Jennings, J. R., Venkatraman, V., Harris, T. B., Yaffe, K., Satterfield, S., Newman, A. B., & for the Health ABC Study. (2015). Longitudinal Systolic Blood Pressure Characteristics and Integrity of White Matter Tracts in a Cohort of Very Old Black and White Adults. *American Journal of Hypertension*, *28*(3), 326–334. <https://doi.org/10.1093/ajh/hpu134>
- Rosenbloom, M., Sullivan, E. V., & Pfefferbaum, A. (2003). Using magnetic resonance imaging and diffusion tensor imaging to assess brain damage in alcoholics. *Alcohol Research & Health*, *27*(2), 146.

- Roy, M., Edde, M., Fortier, M., Croteau, E., Castellano, C.-A., St-Pierre, V., Vandenberghe, C., Rheault, F., Dadar, M., Duchesne, S., Bocti, C., Fulop, T., Cunnane, S. C., & Descoteaux, M. (2022). A ketogenic intervention improves dorsal attention network functional and structural connectivity in mild cognitive impairment. *Neurobiology of Aging, 115*, 77–87. <https://doi.org/10.1016/j.neurobiolaging.2022.04.005>
- Salsone, M., Caligiuri, M. E., Castronovo, V., Canessa, N., Marelli, S., Quattrone, A., Quattrone, A., & Ferini-Strambi, L. (2021). Microstructural changes in normal-appearing white matter in male sleep apnea patients are reversible after treatment: A pilot study. *Journal of Neuroscience Research, 99*(10), 2646–2656. <https://doi.org/10.1002/jnr.24858>
- Sampaio-Baptista, C., & Johansen-Berg, H. (2017). White matter plasticity in the adult brain. *Neuron, 96*(6), 1239–1251.
- Sampaio-Baptista, C., Vallès, A., Khrapitchev, A. A., Akkermans, G., Winkler, A. M., Foxley, S., Sibson, N. R., Roberts, M., Miller, K., Diamond, M. E., Martens, G. J. M., De Weerd, P., & Johansen-Berg, H. (2020). White matter structure and myelin-related gene expression alterations with experience in adult rats. *Progress in Neurobiology, 187*, 101770. <https://doi.org/10.1016/j.pneurobio.2020.101770>
- Sanjari Moghaddam, H., Ghazi Sherbaf, F., & Aarabi, M. H. (2019). Brain microstructural abnormalities in type 2 diabetes mellitus: A systematic review of diffusion tensor imaging studies. *Frontiers in Neuroendocrinology, 55*, 100782. <https://doi.org/10.1016/j.yfrne.2019.100782>
- Santiago, C., Herrmann, N., Swardfager, W., Saleem, M., Oh, P. I., Black, S. E., & Lanctôt, K. L. (2015). White Matter Microstructural Integrity Is Associated with Executive Function and Processing Speed in Older Adults with Coronary Artery Disease. *The American Journal of Geriatric Psychiatry, 23*(7), 754–763. <https://doi.org/10.1016/j.jagp.2014.09.008>
- Sasaki, S., Kuwahara, N., Kunitomo, K., Harada, S., Yamada, T., Azuma, A., Takeda, K., & Nakagawa, M. (2002). Effects of *atorvastatin* on oxidized low-density lipoprotein, low-density lipoprotein subfraction distribution, and remnant lipoprotein in patients with mixed hyperlipoproteinemia. *The American Journal of Cardiology, 89*(4), 386–389. [https://doi.org/10.1016/S0002-9149\(01\)02257-3](https://doi.org/10.1016/S0002-9149(01)02257-3)
- Savion-Lemieux, T., & Penhune, V. B. (2005). The effects of practice and delay on motor skill learning and retention. *Experimental Brain Research, 161*(4), 423–431.

- Schall, J. D. (2004). On the role of frontal eye field in guiding attention and saccades. *Vision Research*, 44(12), 1453–1467. <https://doi.org/10.1016/j.visres.2003.10.025>
- Schall, J. D., & Bichot, N. P. (1998). Neural correlates of visual and motor decision processes. *Current Opinion in Neurobiology*, 8(2), 211–217. [https://doi.org/10.1016/S0959-4388\(98\)80142-6](https://doi.org/10.1016/S0959-4388(98)80142-6)
- Schievink, S. H. J., van Boxtel, M. P. J., Deckers, K., van Oostenbrugge, R. J., Verhey, F. R. J., & Köhler, S. (2022). Cognitive changes in prevalent and incident cardiovascular disease: A 12-year follow-up in the Maastricht Aging Study (MAAS). *European Heart Journal*, 43(7), e2–e9. <https://doi.org/10.1093/eurheartj/ehx365>
- Schmidt, R., Ropele, S., Enzinger, C., Petrovic, K., Smith, S., Schmidt, H., Matthews, P. M., & Fazekas, F. (2005). White matter lesion progression, brain atrophy, and cognitive decline: The Austrian stroke prevention study. *Annals of Neurology*, 58(4), 610–616. <https://doi.org/10.1002/ana.20630>
- Schmithorst, V. J., & Wilke, M. (2002). Differences in white matter architecture between musicians and non-musicians: A diffusion tensor imaging study. *Neuroscience Letters*, 321(1), 57–60. [https://doi.org/10.1016/S0304-3940\(02\)00054-X](https://doi.org/10.1016/S0304-3940(02)00054-X)
- Schneider, T., Brownlee, W., Zhang, H., Ciccarelli, O., Miller, D. H., & Wheeler-Kingshott, C. G. (2017). Sensitivity of multi-shell NODDI to multiple sclerosis white matter changes: A pilot study. *Functional Neurology*, 32(2), 97–101. <https://doi.org/10.11138/FNeur/2017.32.2.097>
- Scholz, J., Klein, M. C., Behrens, T. E., & Johansen-Berg, H. (2009). Training induces changes in white-matter architecture. *Nature Neuroscience*, 12(11), 1370–1371.
- Seeger, U., Klose, U., Mader, I., Grodd, W., & Nägele, T. (2003). Parameterized evaluation of macromolecules and lipids in proton MR spectroscopy of brain diseases. *Magnetic Resonance in Medicine*, 49(1), 19–28. <https://doi.org/10.1002/mrm.10332>
- Segura, B., Jurado, M. A., Freixenet, N., Falcón, C., Junqué, C., & Arboix, A. (2009). Microstructural white matter changes in metabolic syndrome. *Neurology*, 73(6), 438–444. <https://doi.org/10.1212/WNL.0b013e3181b163cd>
- Seidler, R. D., Purushotham, A., Kim, S.-G., Ugurbil, K., Willingham, D., & Ashe, J. (2005). Neural correlates of encoding and expression in implicit sequence learning. *Experimental Brain Research*, 165(1), 114–124. <https://doi.org/10.1007/s00221-005-2284-z>

- Seidlitz, J., Váša, F., Shinn, M., Romero-Garcia, R., Whitaker, K. J., Vértes, P. E., Wagstyl, K., Kirkpatrick Reardon, P., Clasen, L., Liu, S., Messinger, A., Leopold, D. A., Fonagy, P., Dolan, R. J., Jones, P. B., Goodyer, I. M., NSPN Consortium, Raznahan, A., & Bullmore, E. T. (2018). Morphometric Similarity Networks Detect Microscale Cortical Organization and Predict Inter-Individual Cognitive Variation. *Neuron*, *97*(1), 231-247.e7. <https://doi.org/10.1016/j.neuron.2017.11.039>
- Sepehrband, F., Clark, K. A., Ullmann, J. F. P., Kurniawan, N. D., Leanage, G., Reutens, D. C., & Yang, Z. (2015). Brain tissue compartment density estimated using diffusion-weighted MRI yields tissue parameters consistent with histology. *Human Brain Mapping*, *36*(9), 3687–3702. <https://doi.org/10.1002/hbm.22872>
- Sexton, C. E., Betts, J. F., Demnitz, N., Dawes, H., Ebmeier, K. P., & Johansen-Berg, H. (2016). A systematic review of MRI studies examining the relationship between physical fitness and activity and the white matter of the ageing brain. *NeuroImage*, *131*, 81–90. <https://doi.org/10.1016/j.neuroimage.2015.09.071>
- Seyedsalehi, A., Warriar, V., Bethlehem, R. A. I., Perry, B. I., Burgess, S., & Murray, G. K. (2023). Educational attainment, structural brain reserve and Alzheimer’s disease: A Mendelian randomization analysis. *Brain*, *146*(5), 2059–2074. <https://doi.org/10.1093/brain/awac392>
- Sheikh, S., Safia, Haque, E., & Mir, S. S. (2013). Neurodegenerative Diseases: Multifactorial Conformational Diseases and Their Therapeutic Interventions. *Journal of Neurodegenerative Diseases*, *2013*(1), 563481. <https://doi.org/10.1155/2013/563481>
- Shima, K., & Tanji, J. (2000). Neuronal Activity in the Supplementary and Presupplementary Motor Areas for Temporal Organization of Multiple Movements. *Journal of Neurophysiology*, *84*(4), 2148–2160. <https://doi.org/10.1152/jn.2000.84.4.2148>
- Shobab, L. A., Hsiung, G.-Y. R., & Feldman, H. H. (2005). Cholesterol in Alzheimer’s disease. *Lancet Neurology*, *4*(12), 841–852. Scopus. [https://doi.org/10.1016/S1474-4422\(05\)70248-9](https://doi.org/10.1016/S1474-4422(05)70248-9)
- Sidaros, A., Engberg, A. W., Sidaros, K., Liptrot, M. G., Herning, M., Petersen, P., Paulson, O. B., Jernigan, T. L., & Rostrup, E. (2008). Diffusion tensor imaging during recovery from severe traumatic brain injury and relation to clinical outcome: A longitudinal study. *Brain*, *131*(2), 559–572. <https://doi.org/10.1093/brain/awm294>

- Sigurdardottir, V., Fagerberg, B., & Hulthe, J. (2002). Circulating oxidized low-density lipoprotein (LDL) is associated with risk factors of the metabolic syndrome and LDL size in clinically healthy 58-year-old men (AIR study). *Journal of Internal Medicine*, *252*(5), 440–447. <https://doi.org/10.1046/j.1365-2796.2002.01054.x>
- Silverman, J. M., & Schmeidler, J. (2018). Outcome age-based prediction of successful cognitive aging by total cholesterol. *Alzheimer's & Dementia*, *14*(7), 952–960. <https://doi.org/10.1016/j.jalz.2018.01.009>
- Singh-Manoux, A., Gimeno, D., Kivimaki, M., Brunner, E., & Marmot, M. G. (2008). Low HDL Cholesterol Is a Risk Factor for Deficit and Decline in Memory in Midlife. *Arteriosclerosis, Thrombosis, and Vascular Biology*, *28*(8), 1556–1562. <https://doi.org/10.1161/ATVBAHA.108.163998>
- Singmann, H., Bolker, B., Westfall, J., & Aust, F. (2018). *afex: Analysis of Factorial Experiments. R package version 0.20-2*.
- Skare, S., & Bammer, R. (2010). Jacobian weighting of distortion corrected EPI data. *Positions*, *500*(1), 1.
- Sled, J. G., & Pike, G. B. (2001). Quantitative imaging of magnetization transfer exchange and relaxation properties in vivo using MRI. *Magnetic Resonance in Medicine: An Official Journal of the International Society for Magnetic Resonance in Medicine*, *46*(5), 923–931.
- Smith, J. C., Lancaster, M. A., Nielson, K. A., Woodard, J. L., Seidenberg, M., Durgerian, S., Sakaie, K., & Rao, S. M. (2016). Interactive effects of physical activity and *APOE-ε4* on white matter tract diffusivity in healthy elders. *NeuroImage*, *131*, 102–112. <https://doi.org/10.1016/j.neuroimage.2015.08.007>
- Smith, J. C., Nielson, K. A., Woodard, J. L., Seidenberg, M., & Rao, S. M. (2013). Physical Activity and Brain Function in Older Adults at Increased Risk for Alzheimer's Disease. *Brain Sciences*, *3*(1), Article 1. <https://doi.org/10.3390/brainsci3010054>
- Smith, R. E., Tournier, J.-D., Calamante, F., & Connelly, A. (2012). Anatomically-constrained tractography: Improved diffusion MRI streamlines tractography through effective use of anatomical information. *NeuroImage*, *62*(3), 1924–1938. <https://doi.org/10.1016/j.neuroimage.2012.06.005>

- Smith, R. E., Tournier, J.-D., Calamante, F., & Connelly, A. (2013). SIFT: Spherical-deconvolution informed filtering of tractograms. *NeuroImage*, *67*, 298–312. <https://doi.org/10.1016/j.neuroimage.2012.11.049>
- Smith, S. M. (2002). Fast robust automated brain extraction. *Human Brain Mapping*, *17*(3), 143–155. <https://doi.org/10.1002/hbm.10062>
- Smith, S. M., Jenkinson, M., Woolrich, M. W., Beckmann, C. F., Behrens, T. E., Johansen-Berg, H., Bannister, P. R., De Luca, M., Drobnjak, I., & Flitney, D. E. (2004). Advances in functional and structural MR image analysis and implementation as FSL. *Neuroimage*, *23*, S208–S219.
- Sow, A., Lamant, M., Bonny, J.-M., Larvaron, P., Piaud, O., Lécureuil, C., Fontaine, I., Saleh, M.-C., Garcia Otin, A. L., Renou, J.-P., Baron, B., Zakin, M., & Guillou, F. (2006). Oligodendrocyte differentiation is increased in transferrin transgenic mice. *Journal of Neuroscience Research*, *83*(3), 403–414. <https://doi.org/10.1002/jnr.20741>
- Sowell, E. R., Peterson, B. S., Thompson, P. M., Welcome, S. E., Henkenius, A. L., & Toga, A. W. (2003). Mapping cortical change across the human life span. *Nature Neuroscience*, *6*(3), 309–315. <https://doi.org/10.1038/nn1008>
- Staines, W. R., Graham, S. J., Black, S. E., & McIlroy, W. E. (2002). Task-Relevant Modulation of Contralateral and Ipsilateral Primary Somatosensory Cortex and the Role of a Prefrontal-Cortical Sensory Gating System. *NeuroImage*, *15*(1), 190–199. <https://doi.org/10.1006/nimg.2001.0953>
- Stanek, K. M., Grieve, S. M., Brickman, A. M., Korgaonkar, M. S., Paul, R. H., Cohen, R. A., & Gunstad, J. J. (2011). Obesity Is Associated With Reduced White Matter Integrity in Otherwise Healthy Adults*. *Obesity*, *19*(3), 500–504. <https://doi.org/10.1038/oby.2010.312>
- Steele, C. J., Scholz, J., Douaud, G., Johansen-berg, H., & Penhune, V. B. (2012). Structural correlates of skilled performance on a motor sequence task. *Frontiers in Human Neuroscience*, *6*. <https://doi.org/10.3389/fnhum.2012.00289>
- Steele, C. J., & Zatorre, R. J. (2018). Practice makes plasticity. *Nature Neuroscience*, *21*(12), Article 12. <https://doi.org/10.1038/s41593-018-0280-4>
- Stejskal, E. O., & Tanner, J. E. (1965). Spin diffusion measurements: Spin echoes in the presence of a time-dependent field gradient. *The Journal of Chemical Physics*, *42*(1), 288–292.

- Stephen, R., Solomon, A., Ngandu, T., Levälähti, E., Rinne, J. O., Kemppainen, N., Parkkola, R., Antikainen, R., Strandberg, T., Kivipelto, M., Soininen, H., Liu, Y., & Group, for the F. study. (2020). White Matter Changes on Diffusion Tensor Imaging in the FINGER Randomized Controlled Trial. *Journal of Alzheimer's Disease*, 78(1), 75–86. <https://doi.org/10.3233/JAD-200423>
- Stern, Y. (2006). Cognitive Reserve and Alzheimer Disease. *Alzheimer Disease & Associated Disorders*, 20(2), 112. <https://doi.org/10.1097/01.wad.0000213815.20177.19>
- Stern, Y., Arenaza-Urquijo, E. M., Bartrés-Faz, D., Belleville, S., Cantilon, M., Chetelat, G., Ewers, M., Franzmeier, N., Kempermann, G., Kremen, W. S., Okonkwo, O., Scarmeas, N., Soldan, A., Udeh-Momoh, C., Valenzuela, M., Vemuri, P., Vuoksimaa, E., & and the Reserve, Resilience and Protective Factors PIA Empirical Definitions and Conceptual Frameworks Workgroup. (2020). Whitepaper: Defining and investigating cognitive reserve, brain reserve, and brain maintenance. *Alzheimer's & Dementia*, 16(9), 1305–1311. <https://doi.org/10.1016/j.jalz.2018.07.219>
- Stroop, J. R. (1935). Studies of interference in serial verbal reactions. *Journal of Experimental Psychology*, 18(6), 643–662. <https://doi.org/10.1037/h0054651>
- Susuki, K. (2010). *Myelin: A specialized membrane for cell communication*.
- Swardfager, W., Herrmann, N., Marzolini, S., Saleem, M., Kiss, A., Shammi, P., Oh, P. I., & Lanctôt, K. L. (2010). Cardiopulmonary fitness is associated with cognitive performance in patients with coronary artery disease. *Journal of the American Geriatrics Society*, 58(8), 1519–1525. <https://doi.org/10.1111/j.1532-5415.2010.02966.x>
- Swardfager, W., Herrmann, N., Marzolini, S., Saleem, M., Shammi, P., Oh, P. I., Albert, P. R., Daigle, M., Kiss, A., & Lanctôt, K. L. (2011). Brain derived neurotrophic factor, cardiopulmonary fitness and cognition in patients with coronary artery disease. *Brain, Behavior, and Immunity*, 25(6), 1264–1271. <https://doi.org/10.1016/j.bbi.2011.04.017>
- Tabelow, K., Balteau, E., Ashburner, J., Callaghan, M. F., Draganski, B., Helms, G., Kherif, F., Leutritz, T., Lutti, A., Phillips, C., Reimer, E., Ruthotto, L., Seif, M., Weiskopf, N., Ziegler, G., & Mohammadi, S. (2019). hMRI - A toolbox for quantitative MRI in neuroscience and clinical research. *NeuroImage*, 194, 191–210. <https://doi.org/10.1016/j.neuroimage.2019.01.029>

- Takeuchi, H., Sekiguchi, A., Taki, Y., Yokoyama, S., Yomogida, Y., Komuro, N., Yamanouchi, T., Suzuki, S., & Kawashima, R. (2010). Training of Working Memory Impacts Structural Connectivity. *Journal of Neuroscience*, *30*(9), 3297–3303.
<https://doi.org/10.1523/JNEUROSCI.4611-09.2010>
- Tanji, J. (1996). New concepts of the supplementary motor area. *Current Opinion in Neurobiology*, *6*(6), 782–787. [https://doi.org/10.1016/S0959-4388\(96\)80028-6](https://doi.org/10.1016/S0959-4388(96)80028-6)
- Tardif, C. L., Gauthier, C. J., Steele, C. J., Bazin, P.-L., Schäfer, A., Schaefer, A., Turner, R., & Villringer, A. (2016). Advanced MRI techniques to improve our understanding of experience-induced neuroplasticity. *Neuroimage*, *131*, 55–72.
- Taubert, M., Villringer, A., & Ragert, P. (2012). Learning-Related Gray and White Matter Changes in Humans: An Update. *The Neuroscientist*, *18*(4), 320–325.
<https://doi.org/10.1177/1073858411419048>
- Tavor, I., Hofstetter, S., & Assaf, Y. (2013). Micro-structural assessment of short term plasticity dynamics. *NeuroImage*, *81*, 1–7. <https://doi.org/10.1016/j.neuroimage.2013.05.050>
- Taylor, P. A., & Saad, Z. S. (2013). FATCAT: (An efficient) Functional and Tractographic Connectivity Analysis Toolbox. *Brain Connectivity*, *3*(5), 523–535.
<https://doi.org/10.1089/brain.2013.0154>
- Taylor, P. N., Silva, N. M. da, Blamire, A., Wang, Y., & Forsyth, R. (2020). Early deviation from normal structural connectivity: A novel intrinsic severity score for mild TBI. *Neurology*, *94*(10), e1021–e1026. <https://doi.org/10.1212/WNL.00000000000008902>
- Teipel, S. J., Meindl, T., Wagner, M., Kohl, T., Bürger, K., Reiser, M. F., Herpertz, S., Möller, H.-J., & Hampel, H. (2009). White Matter Microstructure in Relation to Education in Aging and Alzheimer's Disease. *Journal of Alzheimer's Disease*, *17*(3), 571–583.
<https://doi.org/10.3233/JAD-2009-1077>
- ten Brinke, L. F., Davis, J. C., Barha, C. K., & Liu-Ambrose, T. (2017). Effects of computerized cognitive training on neuroimaging outcomes in older adults: A systematic review. *BMC Geriatrics*, *17*(1), 139. <https://doi.org/10.1186/s12877-017-0529-x>
- Thambisetty, M., Beason-Held, L., An, Y., Kraut, M. A., & Resnick, S. M. (2010). APOE ϵ 4 Genotype and Longitudinal Changes in Cerebral Blood Flow in Normal Aging. *Archives of Neurology*, *67*(1), 93–98. <https://doi.org/10.1001/archneurol.2009.913>

- Thiebaut de Schotten, M., & Forkel, S. J. (2022). The emergent properties of the connected brain. *Science*, 378(6619), 505–510. <https://doi.org/10.1126/science.abq2591>
- Tian, J., Raghavan, S., Reid, R. I., Przybelski, S. A., Lesnick, T. G., Gebre, R. K., Graff-Radford, J., Schwarz, C. G., Lowe, V. J., Kantarci, K., Knopman, D. S., Petersen, R. C., Jack, C. R., & Vemuri, P. (2023). White Matter Degeneration Pathways Associated With Tau Deposition in Alzheimer Disease. *Neurology*, 100(22), e2269–e2278. <https://doi.org/10.1212/WNL.0000000000207250>
- Toschi, N., Gisbert, R. A., Passamonti, L., Canals, S., & De Santis, S. (2020). Multishell diffusion imaging reveals sex-specific trajectories of early white matter degeneration in normal aging. *Neurobiology of Aging*, 86, 191–200. <https://doi.org/10.1016/j.neurobiolaging.2019.11.014>
- Tournier, J.-D., Smith, R., Raffelt, D., Tabbara, R., Dhollander, T., Pietsch, M., Christiaens, D., Jeurissen, B., Yeh, C.-H., & Connelly, A. (2019). MRtrix3: A fast, flexible and open software framework for medical image processing and visualisation. *NeuroImage*, 116137.
- Tranfa, M., Lorenzini, L., Collij, L. E., Vázquez García, D., Ingala, S., Pontillo, G., Pieperhoff, L., Maranzano, A., Wolz, R., Haller, S., Blennow, K., Frisoni, G., Sudre, C. H., Chételat, G., Ewers, M., Payoux, P., Waldman, A., Martinez-Lage, P., Schwarz, A. J., ... Barkhof, F. (2024). Alzheimer's Disease and Small Vessel Disease Differentially Affect White Matter Microstructure. *Annals of Clinical and Translational Neurology*, 11(6), 1541–1556. <https://doi.org/10.1002/acn3.52071>
- Tremblay, S. A. (2024). *The Social Determinants of Dementia: Canada Needs Collective Action to Prevent a Public Health Crisis - Policy Magazine*. <https://www.policymagazine.ca/the-social-determinants-of-dementia-canada-needs-collective-action-to-prevent-a-public-health-crisis/>
- Tremblay, S. A., Alasmar, Z., Pirhadi, A., Carbonell, F., Iturria-Medina, Y., Gauthier, C. J., & Steele, C. J. (2024a). *mvcomp: Multivariate Comparisons using Whole-brain and ROI-derived Metrics from MRI* (Version 0.9.2) [Computer software]. [doi:10.5281/zenodo.10713027](https://doi.org/10.5281/zenodo.10713027)
- Tremblay, S. A., Alasmar, Z., Pirhadi, A., Carbonell, F., Iturria-Medina, Y., Gauthier, C. J., & Steele, C. J. (2024b). MVComp toolbox: MultiVariate Comparisons of brain MRI

- features accounting for common information across measures. *Aperture Neuro*, 4. <https://doi.org/10.52294/001c.118427>
- Tremblay, S. A., Jäger, A.-T., Huck, J., Giacosa, C., Beram, S., Schneider, U., Grahl, S., Villringer, A., Tardif, C. L., Bazin, P.-L., Steele, C. J., & Gauthier, C. J. (2021). White matter microstructural changes in short-term learning of a continuous visuomotor sequence. *Brain Structure and Function*, 226(6), 1677–1698. <https://doi.org/10.1007/s00429-021-02267-y>
- Tremblay, S. A., Spreng, R. N., Wearn, A., Alasmar, Z., Pirhadi, A., Tardif, C. L., Chakravarty, M., Villeneuve, S., Leppert, I. R., Carbonell, F., Iturria-Medina, Y., Steele, C. J., Gauthier, C. J., & Group, the P.-A. R. (2024). *Sex and APOE4-specific links between cardiometabolic risk factors and white matter alterations in individuals with a family history of Alzheimer’s disease* (p. 2024.08.21.608995). bioRxiv. <https://doi.org/10.1101/2024.08.21.608995>
- Tremblay-Mercier, J., Madjar, C., Das, S., Pichet Binette, A., Dyke, S. O. M., Étienne, P., Lafaille-Magnan, M.-E., Remz, J., Bellec, P., Louis Collins, D., Natasha Rajah, M., Bohbot, V., Leoutsakos, J.-M., Iturria-Medina, Y., Kat, J., Hoge, R. D., Gauthier, S., Tardif, C. L., Mallar Chakravarty, M., ... Breitner, J. C. S. (2021). Open science datasets from PREVENT-AD, a longitudinal cohort of pre-symptomatic Alzheimer’s disease. *NeuroImage: Clinical*, 31, 102733. <https://doi.org/10.1016/j.nicl.2021.102733>
- Triebswetter, C., Kiely, M., Khatrar, N., Ferrucci, L., Resnick, S. M., Spencer, R. G., & Bouhrara, M. (2022). Differential associations between apolipoprotein E alleles and cerebral myelin content in normative aging. *NeuroImage*, 251, 118988. <https://doi.org/10.1016/j.neuroimage.2022.118988>
- Trofimova, O., Latypova, A., DiDomenicantonio, G., Lutti, A., de Lange, A.-M. G., Kliegel, M., Stringhini, S., Marques-Vidal, P., Vaucher, J., Vollenweider, P., Strippoli, M.-P. F., Preisig, M., Kherif, F., & Draganski, B. (2023). Topography of associations between cardiovascular risk factors and myelin loss in the ageing human brain. *Communications Biology*, 6(1), 1–14. <https://doi.org/10.1038/s42003-023-04741-1>
- Tucker-Drob, E. M. (2019). Cognitive Aging and Dementia: A Life-Span Perspective. *Annual Review of Developmental Psychology*, 1(Volume 1, 2019), 177–196. <https://doi.org/10.1146/annurev-devpsych-121318-085204>

- Tustison, N. J., Avants, B. B., Cook, P. A., Yuanjie Zheng, Egan, A., Yushkevich, P. A., & Gee, J. C. (2010). N4ITK: Improved N3 Bias Correction. *IEEE Transactions on Medical Imaging*, *29*(6), 1310–1320. <https://doi.org/10.1109/TMI.2010.2046908>
- Uddin, M. N., Figley, T. D., Solar, K. G., Shatil, A. S., & Figley, C. R. (2019). Comparisons between multi-component myelin water fraction, T1w/T2w ratio, and diffusion tensor imaging measures in healthy human brain structures. *Scientific Reports*, *9*(1), Article 1. <https://doi.org/10.1038/s41598-019-39199-x>
- Uno, M., Harada, M., Takimoto, O., Kitazato, K. T., Suzue, A., Yoneda, K., Morita, N., Itabe, H., & Nagahiro, S. (2005). Elevation of plasma oxidized LDL in acute stroke patients is associated with ischemic lesions depicted by DWI and predictive of infarct enlargement. *Neurological Research*, *27*(1), 94–102. <https://doi.org/10.1179/016164105X18395>
- Van Essen, D. C., Smith, S. M., Barch, D. M., Behrens, T. E. J., Yacoub, E., Ugurbil, K., & WU-Minn HCP Consortium. (2013). The WU-Minn Human Connectome Project: An overview. *NeuroImage*, *80*, 62–79. <https://doi.org/10.1016/j.neuroimage.2013.05.041>
- Van Exel, E., de Craen, A. J. M., Gussekloo, J., Houx, P., Bootsma-van der Wiel, A., Macfarlane, P. W., Blauw, G. J., & Westendorp, R. G. J. (2002). Association between high-density lipoprotein and cognitive impairment in the oldest old. *Annals of Neurology*, *51*(6), 716–721. <https://doi.org/10.1002/ana.10220>
- Van Hecke, W., Leemans, A., De Backer, S., Jeurissen, B., Parizel, P. M., & Sijbers, J. (2010). Comparing isotropic and anisotropic smoothing for voxel-based DTI analyses: A simulation study. *Human Brain Mapping*, *31*(1), 98–114.
- van Hemmen, J., Saris, I. M. J., Cohen-Kettenis, P. T., Veltman, D. J., Pouwels, P. J. W., & Bakker, J. (2017). Sex Differences in White Matter Microstructure in the Human Brain Predominantly Reflect Differences in Sex Hormone Exposure. *Cerebral Cortex*, *27*(5), 2994–3001. <https://doi.org/10.1093/cercor/bhw156>
- van Mier, H., Tempel, L. W., Perlmutter, J. S., Raichle, M. E., & Petersen, S. E. (1998). Changes in Brain Activity During Motor Learning Measured With PET: Effects of Hand of Performance and Practice. *Journal of Neurophysiology*, *80*(4), 2177–2199. <https://doi.org/10.1152/jn.1998.80.4.2177>
- van Vliet, P. (2012). Cholesterol and late-life cognitive decline. *Journal of Alzheimer's Disease: JAD*, *30 Suppl 2*, S147-162. <https://doi.org/10.3233/JAD-2011-111028>

- Vandekar, S. N., Shinohara, R. T., Raznahan, A., Hopson, R. D., Roalf, D. R., Ruparel, K., Gur, R. C., Gur, R. E., & Satterthwaite, T. D. (2016). Subject-level measurement of local cortical coupling. *NeuroImage*, *133*, 88–97.
<https://doi.org/10.1016/j.neuroimage.2016.03.002>
- Varma, V. R., Chuang, Y.-F., Harris, G. C., Tan, E. J., & Carlson, M. C. (2015). Low-intensity daily walking activity is associated with hippocampal volume in older adults. *Hippocampus*, *25*(5), 605–615. <https://doi.org/10.1002/hipo.22397>
- Varriano, F., Pascual-Diaz, S., & Prats-Galino, A. (2020). Distinct Components in the Right Extended Frontal Aslant Tract Mediate Language and Working Memory Performance: A Tractography-Informed VBM Study. *Frontiers in Neuroanatomy*, *14*.
<https://doi.org/10.3389/fnana.2020.00021>
- Vasankari, T., Ahotupa, M., Toikka, J., Mikkola, J., Irjala, K., Pasanen, P., Neuvonen, K., Raitakari, O., & Viikari, J. (2001). Oxidized LDL and thickness of carotid intima-media are associated with coronary atherosclerosis in middle-aged men: Lower levels of oxidized LDL with statin therapy. *Atherosclerosis*, *155*(2), 403–412.
[https://doi.org/10.1016/S0021-9150\(00\)00573-6](https://doi.org/10.1016/S0021-9150(00)00573-6)
- Veraart, J., Sijbers, J., Sunaert, S., Leemans, A., & Jeurissen, B. (2013). Weighted linear least squares estimation of diffusion MRI parameters: Strengths, limitations, and pitfalls. *NeuroImage*, *81*, 335–346. <https://doi.org/10.1016/j.neuroimage.2013.05.028>
- Vernet, M., Quentin, R., Chanes, L., Mitsumasu, A., & Valero-Cabré, A. (2014). Frontal eye field, where art thou? Anatomy, function, and non-invasive manipulation of frontal regions involved in eye movements and associated cognitive operations. *Frontiers in Integrative Neuroscience*, *8*. <https://doi.org/10.3389/fnint.2014.00066>
- Vernooij, M. W., Ikram, M. A., Vrooman, H. A., Wielopolski, P. A., Krestin, G. P., Hofman, A., Niessen, W. J., Lugt, A. V. der, & Breteler, M. M. B. (2009). White Matter Microstructural Integrity and Cognitive Function in a General Elderly Population. *Archives of General Psychiatry*, *66*(5), 545–553.
<https://doi.org/10.1001/archgenpsychiatry.2009.5>
- Vidal, J.-S., Sigurdsson, S., Jonsdottir, M. K., Eiriksdottir, G., Thorgeirsson, G., Kjartansson, O., Garcia, M. E., van Buchem, M. A., Harris, T. B., Gudnason, V., & Launer, L. J. (2010).

- Coronary Artery Calcium, Brain Function and Structure. *Stroke*, *41*(5), 891–897.
<https://doi.org/10.1161/STROKEAHA.110.579581>
- Vidoni, E. D., Acerra, N. E., Dao, E., Meehan, S. K., & Boyd, L. A. (2010). Role of the primary somatosensory cortex in motor learning: An rTMS study. *Neurobiology of Learning and Memory*, *93*(4), 532–539. <https://doi.org/10.1016/j.nlm.2010.01.011>
- Vigen, T., Ihle-Hansen, H., Lyngbakken, M. N., Berge, T., Thommessen, B., Ihle-Hansen, H., Orstad, E. B., Enger, S., Røsjø, H., Tveit, A., & Rønning, O. M. (2020). Carotid Atherosclerosis is Associated with Middle Cerebral Artery Pulsatility Index. *Journal of Neuroimaging*, *30*(2), 233–239. <https://doi.org/10.1111/jon.12684>
- Vitali, C., Wellington, C. L., & Calabresi, L. (2014). HDL and cholesterol handling in the brain. *Cardiovascular Research*, *103*(3), 405–413. <https://doi.org/10.1093/cvr/cvu148>
- Voldsbekk, I., Maximov, I. I., Zak, N., Roelfs, D., Geier, O., Due-Tønnessen, P., Elvsåshagen, T., Strømstad, M., Bjørnerud, A., & Groote, I. (2020). Evidence for wakefulness-related changes to extracellular space in human brain white matter from diffusion-weighted MRI. *NeuroImage*, *212*, 116682. <https://doi.org/10.1016/j.neuroimage.2020.116682>
- Vollmann, H., Conde, V., Sewerin, S., Taubert, M., Sehm, B., Witte, O. W., Villringer, A., & Ragert, P. (2013). Anodal transcranial direct current stimulation (tDCS) over supplementary motor area (SMA) but not pre-SMA promotes short-term visuomotor learning. *Brain Stimulation*, *6*(2), 101–107. <https://doi.org/10.1016/j.brs.2012.03.018>
- Vuorinen, M., Damangir, S., Niskanen, E., Miralbell, J., Rusanen, M., Spulber, G., Soininen, H., Kivipelto, M., & Solomon, A. (2014). Coronary Heart Disease and Cortical Thickness, Gray Matter and White Matter Lesion Volumes on MRI. *PLOS ONE*, *9*(10), e109250. <https://doi.org/10.1371/journal.pone.0109250>
- Wakana, S., Caprihan, A., Panzenboeck, M. M., Fallon, J. H., Perry, M., Gollub, R. L., Hua, K., Zhang, J., Jiang, H., Dubey, P., Blitz, A., van Zijl, P., & Mori, S. (2007). Reproducibility of quantitative tractography methods applied to cerebral white matter. *NeuroImage*, *36*(3), 630–644. <https://doi.org/10.1016/j.neuroimage.2007.02.049>
- Wake, H., Lee, P. R., & Fields, R. D. (2011). Control of Local Protein Synthesis and Initial Events in Myelination by Action Potentials. *Science*, *333*(6049), 1647–1651. <https://doi.org/10.1126/science.1206998>

- Walsh, S., Govia, I., Wallace, L., Richard, E., Peters, R., Anstey, K. J., & Brayne, C. (2022). A whole-population approach is required for dementia risk reduction. *The Lancet Healthy Longevity*, 3(1), e6–e8. [https://doi.org/10.1016/S2666-7568\(21\)00301-9](https://doi.org/10.1016/S2666-7568(21)00301-9)
- Wang, A., Liu, J., Meng, X., Li, J., Wang, H., Wang, Y., Su, Z., Zhang, N., Dai, L., Wang, Y., & Wang, Y. (2018). Association between oxidized low-density lipoprotein and cognitive impairment in patients with ischemic stroke. *European Journal of Neurology*, 25(1), 185–191. <https://doi.org/10.1111/ene.13497>
- Wang, P.-N., Chou, K.-H., Lirng, J.-F., Lin, K.-N., Chen, W.-T., & Lin, C.-P. (2012). Multiple diffusivities define white matter degeneration in amnesic mild cognitive impairment and Alzheimer's disease. *Journal of Alzheimer's Disease: JAD*, 30(2), 423–437. <https://doi.org/10.3233/JAD-2012-111304>
- Wang, R., Fratiglioni, L., Laukka, E. J., Lövdén, M., Kalpouzos, G., Keller, L., Graff, C., Salami, A., Bäckman, L., & Qiu, C. (2015). Effects of vascular risk factors and APOE ϵ 4 on white matter integrity and cognitive decline. *Neurology*, 84(11), 1128–1135. <https://doi.org/10.1212/WNL.0000000000001379>
- Wang, W.-Y., Yu, J.-T., Liu, Y., Yin, R.-H., Wang, H.-F., Wang, J., Tan, L., Radua, J., & Tan, L. (2015). Voxel-based meta-analysis of grey matter changes in Alzheimer's disease. *Translational Neurodegeneration*, 4(1), 6. <https://doi.org/10.1186/s40035-015-0027-z>
- Warstadt, N. M., Dennis, E. L., Jahanshad, N., Kohannim, O., Nir, T. M., McMahon, K. L., de Zubicaray, G. I., Montgomery, G. W., Henders, A. K., Martin, N. G., Whitfield, J. B., Jack, C. R., Bernstein, M. A., Weiner, M. W., Toga, A. W., Wright, M. J., & Thompson, P. M. (2014). Serum cholesterol and variant in cholesterol-related gene *CETP* predict white matter microstructure. *Neurobiology of Aging*, 35(11), 2504–2513. <https://doi.org/10.1016/j.neurobiolaging.2014.05.024>
- Waxman, S. G. (1975). Integrative properties and design principles of axons. *Int Rev Neurobiol*, 18, 1–40.
- Wearn, A., Tremblay, S. A., Tardif, C. L., Leppert, I. R., Gauthier, C. J., Baracchini, G., Hughes, C., Hewan, P., Tremblay-Mercier, J., Rosa-Neto, P., Poirier, J., Villeneuve, S., Schmitz, T. W., Turner, G. R., & Spreng, R. N. (2024). Neuromodulatory subcortical nucleus integrity is associated with white matter microstructure, tauopathy and APOE status. *Nature Communications*, 15(1), 4706. <https://doi.org/10.1038/s41467-024-48490-z>

- Wei, P., Bao, R., Lv, Z., & Jing, B. (2018). Weak but Critical Links between Primary Somatosensory Centers and Motor Cortex during Movement. *Frontiers in Human Neuroscience*, *12*. <https://doi.org/10.3389/fnhum.2018.00001>
- Weiskopf, N., Lutti, A., Helms, G., Novak, M., Ashburner, J., & Hutton, C. (2011). Unified segmentation based correction of R1 brain maps for RF transmit field inhomogeneities (UNICORT). *NeuroImage*, *54*(3), 2116–2124. <https://doi.org/10.1016/j.neuroimage.2010.10.023>
- Weiskopf, N., Mohammadi, S., Lutti, A., & Callaghan, M. F. (2015). Advances in MRI-based computational neuroanatomy: From morphometry to in-vivo histology. *Current Opinion in Neurology*, *28*(4), 313–322. <https://doi.org/10.1097/WCO.0000000000000222>
- Weiskopf, N., Suckling, J., Williams, G., Correia, M. M., Inkster, B., Tait, R., Ooi, C., Bullmore, E. T., & Lutti, A. (2013). Quantitative multi-parameter mapping of R1, PD*, MT, and R2* at 3T: A multi-center validation. *Frontiers in Neuroscience*, *7*, 95. <https://doi.org/10.3389/fnins.2013.00095>
- Westbrook, C., & Talbot, J. (2018). *MRI in Practice*. John Wiley & Sons.
- Whitaker, K. J., Vértes, P. E., Romero-Garcia, R., Váša, F., Moutoussis, M., Prabhu, G., Weiskopf, N., Callaghan, M. F., Wagstyl, K., Rittman, T., Tait, R., Ooi, C., Suckling, J., Inkster, B., Fonagy, P., Dolan, R. J., Jones, P. B., Goodyer, I. M., the NSPN Consortium, & Bullmore, E. T. (2016). Adolescence is associated with genomically patterned consolidation of the hubs of the human brain connectome. *Proceedings of the National Academy of Sciences*, *113*(32), 9105–9110. <https://doi.org/10.1073/pnas.1601745113>
- Wiggins, R. C. (1982). Myelin development and nutritional insufficiency. *Brain Research Reviews*, *4*(2), 151–175. [https://doi.org/10.1016/0165-0173\(82\)90016-9](https://doi.org/10.1016/0165-0173(82)90016-9)
- Wilks, S. S. (1963). Multivariate Statistical Outliers. *Sankhyā: The Indian Journal of Statistics, Series A (1961-2002)*, *25*(4), 407–426.
- Williams, O. A., An, Y., Beason-Held, L., Huo, Y., Ferrucci, L., Landman, B. A., & Resnick, S. M. (2019). Vascular burden and APOE ε4 are associated with white matter microstructural decline in cognitively normal older adults. *NeuroImage*, *188*, 572–583. <https://doi.org/10.1016/j.neuroimage.2018.12.009>
- Williams, V. J., Leritz, E. C., Shepel, J., McGlinchey, R. E., Milberg, W. P., Rudolph, J. L., Lipsitz, L. A., & Salat, D. H. (2013). Interindividual variation in serum cholesterol is

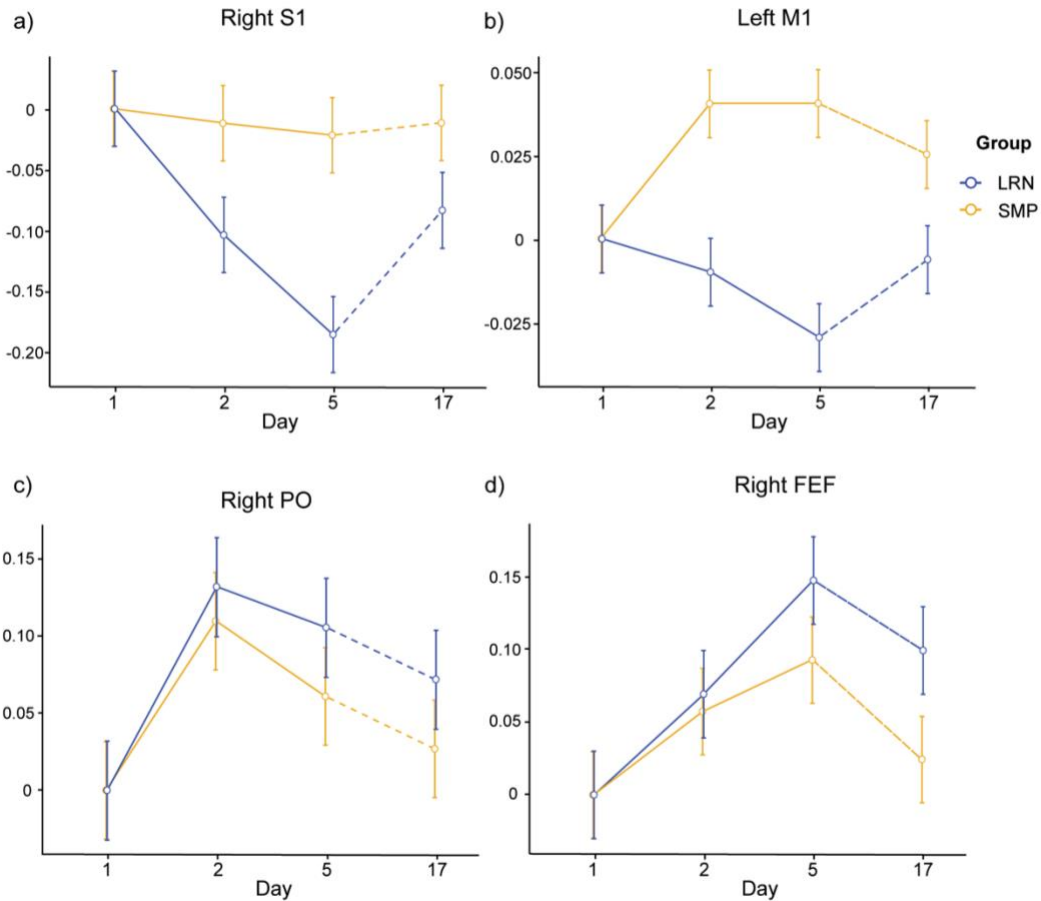
- associated with regional white matter tissue integrity in older adults. *Human Brain Mapping*, 34(8), 1826–1841. <https://doi.org/10.1002/hbm.22030>
- Wink, A. M., de Munck, J. C., van der Werf, Y. D., van den Heuvel, O. A., & Barkhof, F. (2012). Fast Eigenvector Centrality Mapping of Voxel-Wise Connectivity in Functional Magnetic Resonance Imaging: Implementation, Validation, and Interpretation. *Brain Connectivity*, 2(5), 265–274. <https://doi.org/10.1089/brain.2012.0087>
- Winklewski, P. J., Sabisz, A., Naumczyk, P., Jodzio, K., Szurawska, E., & Szarmach, A. (2018). Understanding the Physiopathology Behind Axial and Radial Diffusivity Changes—What Do We Know? *Frontiers in Neurology*, 9. <https://doi.org/10.3389/fneur.2018.00092>
- Wolfers, T., Doan, N. T., Kaufmann, T., Alnæs, D., Moberget, T., Agartz, I., Buitelaar, J. K., Ueland, T., Melle, I., Franke, B., Andreassen, O. A., Beckmann, C. F., Westlye, L. T., & Marquand, A. F. (2018). Mapping the Heterogeneous Phenotype of Schizophrenia and Bipolar Disorder Using Normative Models. *JAMA Psychiatry*, 75(11), 1146–1155. <https://doi.org/10.1001/jamapsychiatry.2018.2467>
- Wolff, S. D., Eng, J., & Balaban, R. S. (1991). Magnetization transfer contrast: Method for improving contrast in gradient-recalled-echo images. *Radiology*, 179(1), 133–137.
- Wolters, F. J., Chibnik, L. B., Waziry, R., Anderson, R., Berr, C., Beiser, A., Bis, J. C., Blacker, D., Bos, D., Brayne, C., Dartigues, J.-F., Darweesh, S. K. L., Davis-Plourde, K. L., de Wolf, F., Debette, S., Dufouil, C., Fornage, M., Goudsmit, J., Grasset, L., ... Hofman, A. (2020). Twenty-seven-year time trends in dementia incidence in Europe and the United States. *Neurology*, 95(5), e519–e531. <https://doi.org/10.1212/WNL.0000000000010022>
- Xiang, S., Nie, F., & Zhang, C. (2008). Learning a Mahalanobis distance metric for data clustering and classification. *Pattern Recognition*, 41(12), 3600–3612. <https://doi.org/10.1016/j.patcog.2008.05.018>
- Xie, W., Zheng, F., Yan, L., & Zhong, B. (2019). Cognitive Decline Before and After Incident Coronary Events. *Journal of the American College of Cardiology*, 73(24), 3041–3050. <https://doi.org/10.1016/j.jacc.2019.04.019>
- Xu, T., Yu, X., Perlik, A. J., Tobin, W. F., Zweig, J. A., Tennant, K., Jones, T., & Zuo, Y. (2009). Rapid formation and selective stabilization of synapses for enduring motor memories. *Nature*, 462(7275), 915–919.

- Xu, W., Wang, H. F., Wan, Y., Tan, C.-C., Yu, J.-T., & Tan, L. (2017). Leisure time physical activity and dementia risk: A dose-response meta-analysis of prospective studies. *BMJ Open*, 7(10), e014706. <https://doi.org/10.1136/bmjopen-2016-014706>
- Yaffe, K., Barrett-Connor, E., Lin, F., & Grady, D. (2002). Serum Lipoprotein Levels, Statin Use, and Cognitive Function in Older Women. *Archives of Neurology*, 59(3), 378–384. <https://doi.org/10.1001/archneur.59.3.378>
- Yamaguchi, S., & Knight, R. T. (1990). Gating of somatosensory input by human prefrontal cortex. *Brain Research*, 521(1), 281–288. [https://doi.org/10.1016/0006-8993\(90\)91553-S](https://doi.org/10.1016/0006-8993(90)91553-S)
- Yamazaki, Y., Zhao, N., Caulfield, T. R., Liu, C.-C., & Bu, G. (2019). Apolipoprotein E and Alzheimer disease: Pathobiology and targeting strategies. *Nature Reviews Neurology*, 15(9), 501–518. <https://doi.org/10.1038/s41582-019-0228-7>
- Yang, H. D., Kim, D. H., Lee, S. B., & Young, L. D. (2016). History of Alzheimer’s Disease. *Dementia and Neurocognitive Disorders*, 15(4), 115–121. <https://doi.org/10.12779/dnd.2016.15.4.115>
- Yang, W., Lui, R. L. M., Gao, J.-H., Chan, T. F., Yau, S.-T., Sperling, R. A., & Huang, X. (2011). Independent Component Analysis-Based Classification of Alzheimer’s Disease MRI Data. *Journal of Alzheimer’s Disease*, 24(4), 775–783. <https://doi.org/10.3233/JAD-2011-101371>
- Yarnykh, V. L., & Yuan, C. (2004). Cross-relaxation imaging reveals detailed anatomy of white matter fiber tracts in the human brain. *Neuroimage*, 23(1), 409–424.
- Ye, Z., Pan, Y., McCoy, R. G., Bi, C., Mo, C., Feng, L., Yu, J., Lu, T., Liu, S., Carson Smith, J., Duan, M., Gao, S., Ma, Y., Chen, C., Mitchell, B. D., Thompson, P. M., Elliot Hong, L., Kochunov, P., Ma, T., & Chen, S. (2024). Contrasting association pattern of plasma low-density lipoprotein with white matter integrity in *APOE4* carriers versus non-carriers. *Neurobiology of Aging*, 143, 41–52. <https://doi.org/10.1016/j.neurobiolaging.2024.08.005>
- Yeatman, J. D., Dougherty, R. F., Myall, N. J., Wandell, B. A., & Feldman, H. M. (2012). Tract Profiles of White Matter Properties: Automating Fiber-Tract Quantification. *PLOS ONE*, 7(11), e49790. <https://doi.org/10.1371/journal.pone.0049790>
- Yin, R.-H., Tan, L., Liu, Y., Wang, W.-Y., Wang, H.-F., Jiang, T., Joaquim Radua, Zhang, Y., Gao, J., Canu, E., Migliaccio, R., Filippi, M., Gorno-Tempini, M. L., & Yu, J.-T. (2015). Multimodal Voxel-Based Meta-Analysis of White Matter Abnormalities in Alzheimer’s

- Disease. *Journal of Alzheimer's Disease*, 47(2), 495–507. <https://doi.org/10.3233/JAD-150139>
- Yin, Z.-X., Shi, X.-M., Kraus, V. B., Fitzgerald, S. M., Qian, H., Xu, J., Zhai, Y., Sereny, M. D., & Zeng, Y. (2012). High normal plasma triglycerides are associated with preserved cognitive function in Chinese oldest-old. *Age and Ageing*, 41(5), 600–606. <https://doi.org/10.1093/ageing/afs033>
- Yokoi, A., Arbuckle, S. A., & Diedrichsen, J. (2018). The role of human primary motor cortex in the production of skilled finger sequences. *Journal of Neuroscience*, 38(6), 1430–1442.
- Young, K., Govind, V., Sharma, K., Studholme, C., Maudsley, A. A., & Schuff, N. (2010). Multivariate statistical mapping of spectroscopic imaging data. *Magnetic Resonance in Medicine*, 63(1), 20–24. <https://doi.org/10.1002/mrm.22190>
- Zatorre, R. J., Fields, R. D., & Johansen-Berg, H. (2012). Plasticity in gray and white: Neuroimaging changes in brain structure during learning. *Nature Neuroscience*, 15(4), 528–536.
- Zhang, H., Avants, B. B., Yushkevich, P. A., Woo, J. H., Wang, S., McCluskey, L. F., Elman, L. B., Melhem, E. R., & Gee, J. C. (2007). High-Dimensional Spatial Normalization of Diffusion Tensor Images Improves the Detection of White Matter Differences: An Example Study Using Amyotrophic Lateral Sclerosis. *IEEE Transactions on Medical Imaging*, 26(11), 1585–1597. *IEEE Transactions on Medical Imaging*. <https://doi.org/10.1109/TMI.2007.906784>
- Zhang, H., Hubbard, P. L., Parker, G. J. M., & Alexander, D. C. (2011). Axon diameter mapping in the presence of orientation dispersion with diffusion MRI. *NeuroImage*, 56(3), 1301–1315. <https://doi.org/10.1016/j.neuroimage.2011.01.084>
- Zhang, H., Schneider, T., Wheeler-Kingshott, C. A., & Alexander, D. C. (2012a). NODDI: Practical in vivo neurite orientation dispersion and density imaging of the human brain. *NeuroImage*, 61(4), 1000–1016. <https://doi.org/10.1016/j.neuroimage.2012.03.072>
- Zhang, H., Schneider, T., Wheeler-Kingshott, C. A., & Alexander, D. C. (2012b). NODDI: Practical in vivo neurite orientation dispersion and density imaging of the human brain. *NeuroImage*, 61(4), 1000–1016. <https://doi.org/10.1016/j.neuroimage.2012.03.072>

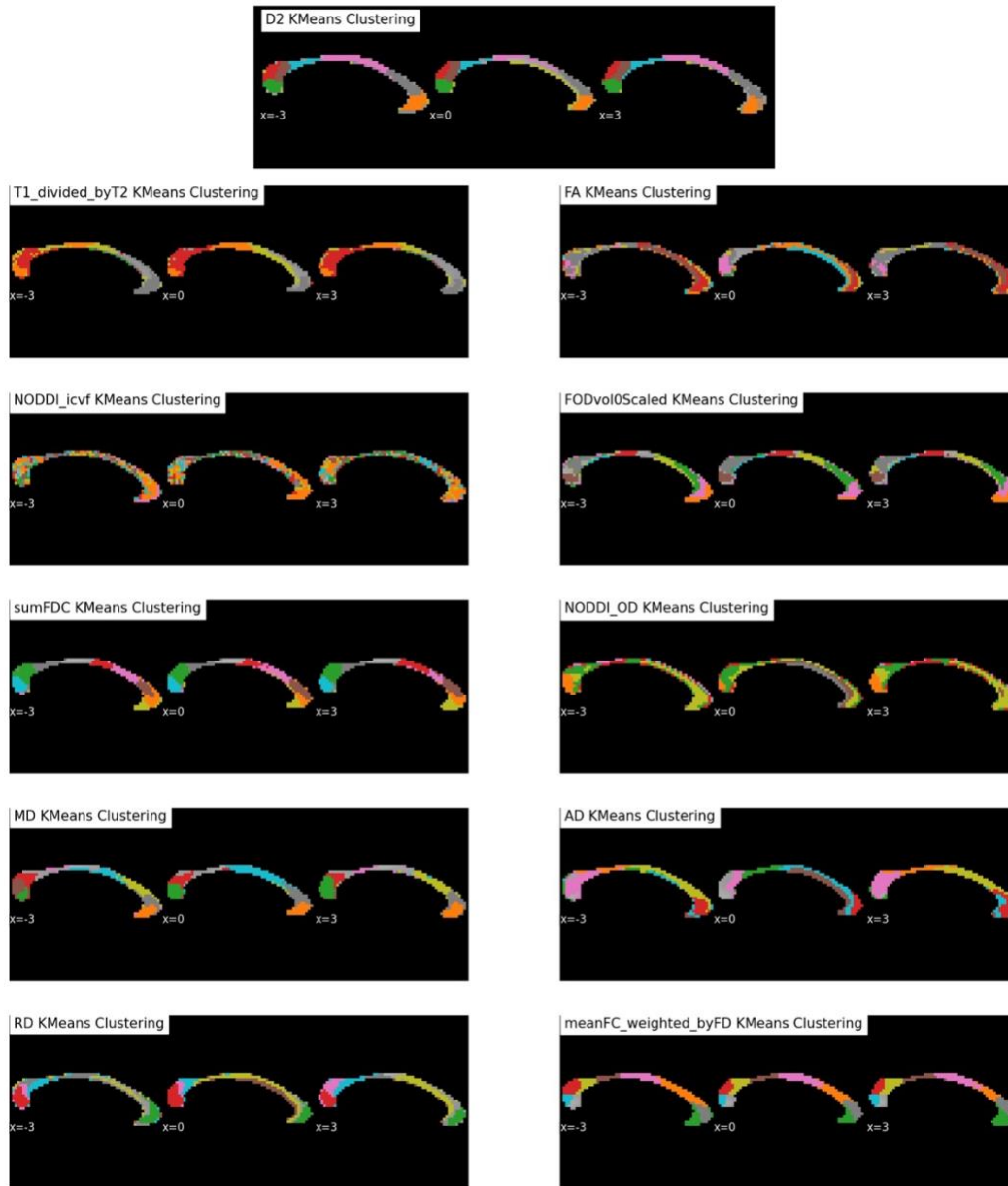
- Zhang, Y., Brady, M., & Smith, S. (2001). Segmentation of brain MR images through a hidden Markov random field model and the expectation-maximization algorithm. *IEEE Transactions on Medical Imaging*, *20*(1), 45–57. <https://doi.org/10.1109/42.906424>
- Zheng, L., Mack, W. J., Chui, H. C., Heflin, L., Mungas, D., Reed, B., DeCarli, C., Weiner, M. W., & Kramer, J. H. (2012). Coronary Artery Disease Is Associated with Cognitive Decline Independent of Changes on Magnetic Resonance Imaging in Cognitively Normal Elderly Adults. *Journal of the American Geriatrics Society*, *60*(3), 499–504. <https://doi.org/10.1111/j.1532-5415.2011.03839.x>
- Zhu, N., Jacobs, D. R., Schreiner, P. J., Launer, L. J., Whitmer, R. A., Sidney, S., Demerath, E., Thomas, W., Bouchard, C., He, K., Erus, G., Battapady, H., & Bryan, R. N. (2015). Cardiorespiratory fitness and brain volume and white matter integrity. *Neurology*, *84*(23), 2347–2353. <https://doi.org/10.1212/WNL.0000000000001658>

Appendix I – Supplementary material Study 1



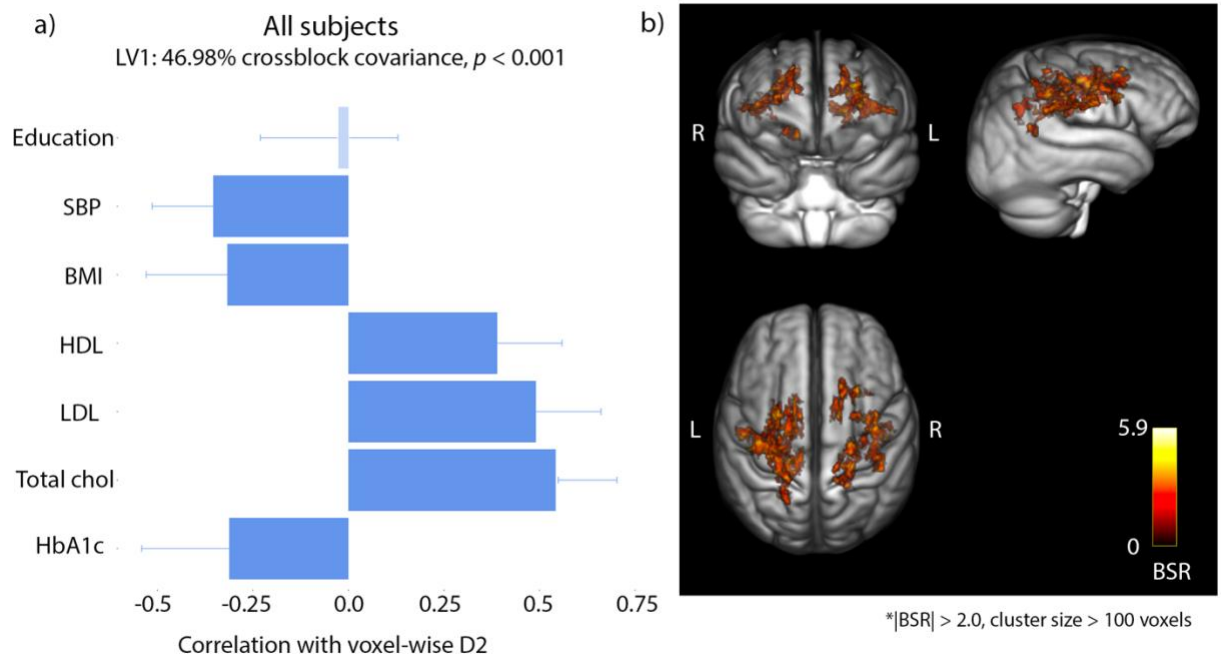
Supplementary Figure 1 (from Study 1). Time course of changes in FA across training days (d1-d5) and the retention session (d17) in each group. a) Decrease in FA in LRN group between d1-d5 in the right ascending sensorimotor tract connecting to the primary somatosensory cortex (S1). The change was not maintained at the retention session (d17). b) FA decreased in the LRN group and increased in the SMP group between d1-d5 in the left corticospinal tract connecting to the primary motor cortex (M1). FA changed significantly between d5 and d17 in the LRN group, but not in the SMP group. c) Increase in FA in both groups between d1-d2 in the right frontal inferior longitudinal (FIL) tract connecting to the pars opercularis (PO). FA then progressively decreased between d2 and d17 in both groups. d) Increase in FA in both groups between d1-d5 in the anterior corona radiata connecting to the right frontal eye field (FEF). FA then decreased significantly between d5-d17 in both groups (Tremblay et al., 2021).

Appendix II – Supplementary material Study 2



Supplementary Figure 1 (from Study 2). Comparison of corpus callosum segmentations obtained using k-means on D2 and on each individual MRI measures (Tremblay, Alasmar, et al., 2024b).

Appendix III – Supplementary material Study 3



Supplementary Figure 1 (from Study 3). Relationships between D2 in WM and risk factors in the whole sample (males and females). a) The strength and direction of the relationship that each risk factor has with D2 in the voxels shown on the brain images on the right. Error bars show 95% confidence intervals. Correlations are non-significant when confidence intervals overlap with zero. b) Colored voxels ($|BSR| > 2.0$) have a positive relationship with the patterns shown in (a). The BSR maps are overlaid on a MPAGE T1w group average image. Higher D2 in the WM regions shown on the right was associated with lower SBP, BMI and HbA1c and with higher HDL, LDL and total cholesterol (Tremblay, Spreng, et al., 2024).

Supplementary Table 1 (from Study 3). Results of the 2x2 ANOVA with sex and APOE4 groups as fixed factors and the brain scores (usc) as the dependent variable.

ANOVA

ANOVA - Brain scores

	Sum of Squares	df	Mean Square	F	p	η^2p
Sex	26681.7	1	26681.7	15.2741	<.001	0.107
APOE4	1629.3	1	1629.3	0.9327	0.336	0.007
Sex * APOE4	37.5	1	37.5	0.0215	0.884	0.000
Residuals	223598.6	128	1746.9			

[3]

Post Hoc Tests

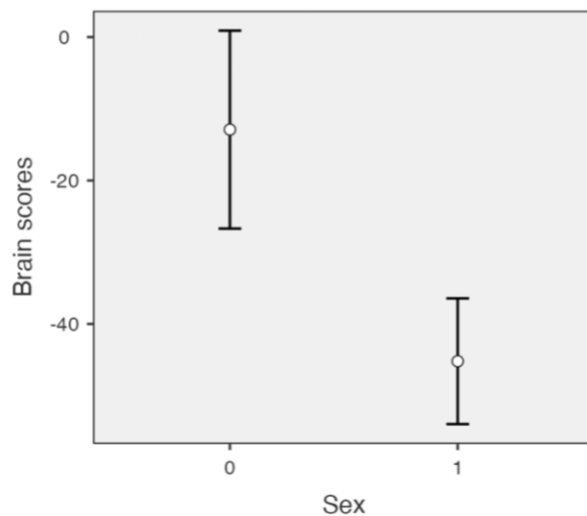
Post Hoc Comparisons - Sex

Comparison		Mean Difference	SE	df	t	Ptukey
Sex	Sex					
0	- 1	32.3	8.27	128	3.91	<.001

Note. Comparisons are based on estimated marginal means

Estimated Marginal Means

Sex



Supplementary figure 2 (from Study 3). Marginal means plot shows males expressed the pattern of the LV more strongly than females (errors bars = confidence intervals). Males = 0, Females = 1.